LBL-8305

MEASUREMENT OF INCLUSIVE PRODUCTION OF NEUTRAL PIONS AT HIGH TRANSVERSE MOMENTUM

Arthur Ogawa

October 1978

Prepared for the U. S. Department of Energy
under Contract W-7405-ENG-48

Measurement of Inclusive Production of Neutral Pions at High Transverse Momentum

By

Arthur Ogawa

Lawrence Berkeley Laboratory
University of California
Berkeley, California 94720

ABSTRACT

These are the results of a measurement of inclusive production at high transverse momentum ($P_\perp$) of neutral pions (π°) from protons by beams of proton (p), kaon (K), pion (π), and antiproton ($\bar{p}$) particles.

The experiment used the Fermilab M2 beam line at momenta of 100, 200 and 300 GeV/c striking a liquid hydrogen target. The data include center of mass (cm) production angles of the π° between 2° and 115° for $P_\perp$ greater than 1 GeV/c. A pair of differential Cerenkov counters distinguished the types of beam particles. The photon (γ) detector of a lead and scintillator sandwich measured both photons from the $\pi^\circ \rightarrow 2\gamma$ decay and enabled a reconstruction of the π° kinematics.

The measurements show several remarkable features distinguishing the production rates for these different beams, including a forward peak in the cm for πp collisions and much less π° production at high $P_\perp$ in pp than in πp or Kp collisions. A simple parametrization accurately represents the data over most of its range, showing approximate scaling in the radial variable $x_R = 2P/\sqrt{s}$ (in the cm). Several parton models are compared with the data. A heuristic picture in terms of the quark constituents of the interacting hadrons accounts for many features of the data in an intuitive way.

Dedicated to my father

Fremont T. Ogawa

my first teacher

ACKNOWLEDGEMENTS

I wish to acknowledge the contributions of the people who were most helpful to me in the course of this experiment and in the writing and preparation of my thesis.

The collaborators listed below were all important to the success of the experiment.

G. J. Donaldson, H. A. Gordon, K.-W. Lai, and I. Stumer
Brookhaven National Laboratory, Upton, New York 11973

and

A. V. Barnes, D. J. Mellema, A. V. Tollestrup, and R. L. Walker
California Institute of Technology, Pasadena, California 91125

and

O. I. Dahl, R. A. Johnson, A. Ogawa, M. Pripstein, and S. R. Shannon
Lawrence Berkeley Laboratory, Berkeley, California 94720

I would additionally like to thank the staff of Fermilab and the Meson Area in particular for their fine support and cooperation.

The data analysis was done by H.A. Gordon, G.J. Donaldson, I. Stumer and me at BNL, where I enjoyed the hospitality of the Omega Group. Some of the drawings in this thesis were originally prepared for publication at BNL.

A.C. Helmholtz and R. Kenney were my advisors and my source of support at LBL. They along with W. Fretter and L. Moretto comprised my thesis committee. I am grateful to them and to H.A. Gordon and G.J. Donaldson for reading the manuscript and for many helpful suggestions.

In the preparation of the manuscript, I thank Cita Symons for editing and typing and Tim Daly for drawing many of the figures.

This work was done with the financial support of the taxpayers of The United States of America through the High Energy Physics Division of the U.S. Department of Energy under Contract W-7405-ENG-48.

FOREWORD TO THE READER

It was my intention in writing this thesis that it be readable not only by the members of the thesis committee but also by a wider audience which may include beginning graduate students. To this end, I have included the definitions of the most important specialized concepts in the text and have written several supplements to introduce particularly specialized areas to the non-expert. Those very detailed discussions which I judged to be of interest only to specialists appear as appendices.

The style I have used may appear strange to those who like the use of the passive voice and avoid the use of the first person singular. Objective distance notwithstanding, however, I think that a statement like "Data were collected by polling a random sample of subjects at ..." does not serve as well as "I handed out questionnaires to people on the street". The result is, I believe, more natural, personal and easily understood.

This thesis is available as LBL-8305 from the author at the Lawrence Berkeley Laboratory, Berkeley, CA 94720

TABLE OF CONTENTS

Dedication i

Acknowledgements ii

Foreword iii

Table of Contents iv

References vi

List of Figures x

List of Tables xiv

1. Introduction 1

    1.1 Context of the Experiment 4

    1.2 Theoretical Issues 11

    1.3 Experimental Possibilities 15

2. Experiment 18

    2.1 Overview 18

    2.2 Apparatus 22

        2.2.1 Beam and Beam-Defining Counters 23

        2.2.2 Hydrogen Target 25

        2.2.3 Photon Detector 28

        2.2.4 PPERP Trigger 33

        2.2.5 Data Assembly 38

    2.3 Data Gathering 40

    2.4 Data Analysis 47

        2.4.1 PASS 1, Fitting Showers 48

        2.4.2 PASS 2, Matching Showers 50

        2.4.3 PASS 3, Calculating the Number of Pions 53

2.4.4 Monte Carlo Efficiencies 59

2.4.5 Cerenkov Analysis 63

2.5 Results 72

2.5.1 Cross sections 72

2.5.2 Features of the Data 85

3. The Physics of Hadron Interactions at High $P_\perp$ 91

3.1 Interpretation 91

3.1.1 Global Parametrization 92

3.1.2 Phenomenological Models 97

3.1.3 Pion Structure Function 108

3.1.4 Beam Ratio At Equal Quark Energies 110

3.2 Conclusions 116

Supplements

1 Fermilab Accelerator and M2 Transport 118

2 Shower Process and Detector Resolution 123

3 Decay Properties of the π^0 127

Appendices

1 Cerenkov Counters 133

2 Kinematic Formulae 144

3 Graphs of Cross Sections 153

REFERENCES

Ref. 1-1 R.P. Feynman, The Theory of Fundamental Processes (Benjamin, New York, 1962)

Ref. 1-2 R.P. Feynman, Quantum Electrodynamics (Benjamin, New York, 1962)

Ref. 1-3 S. Weinberg, Rev. Mod. Phys. 46 255 (1974)
A. Salam, Proc. Eight Nobel Symp. (Almqvist and Wiksells, Stockholm, 1968)

Ref. 1-4 M. Gell-man and Y. Ne'eman, The Eightfold Way (Benjamin, New York, 1965)
H.J. Lipkin, Phys. Reports 8C 173 (1973)

Ref. 1-5 O.W. Greenberg and C.A. Nelson, Phys. Reports 32C 69 (1977)

Ref. 1-6 J. Whitmore, Phys. Reports 10C 273 (1974)

Ref. 1-7 D.R. Nygren and J.N. Marx, Proposal for a PEP Facility (PEP-4), unpublished, was estimated to cost $6M.

Ref. 1-8 R.P. Feynman, Phys. Rev. Letters 23 1415 (1969)

Ref. 1-9 P. Bosetti et al., Nucl. Phys. B54 141 (1973)

Ref. 1-10 A.H. Mueller, Phys. Rev. D2 2963 (1970)
R. Hagedorn and J. Ranft, Nuovo Cimento Suppl. 6 169 (1968)
R. Hagedorn, Nuovo Cimento 56 1027 (1968)
S. Frautschi, Phys. Rev. D3 2821 (1971)

Ref. 1-11 J.D. Bjorken and E.A. Paschos, Phys. Rev. 185 1975 (1969)

Ref. 1-12 S.M. Berman, J.D. Bjorken and J.B. Kogut, Phys. Rev. D4 3388 (1971)

Ref. 1-13 B. Alper et al., Phys. Lett. 44B 521 (1973)
M. Banner et al., Phys. Lett. 44B 537 (1973)
and Ref. 1-14

Ref. 1-14 F.W. Büsser et al., Phys. Lett. 46B 471 (1973)

Ref. 1-15 E. Rutherford, Phil. Mag. 21 669 (1911)

Ref. 1-16 D. Sivers, S.J. Brodsky and R. Blankenbecler, Phys. Reports 23C 1 (1976), contains a review of hadronic and parton models

Ref. 1-17 S.J. Brodsky and G.R. Farrar, Phys. Rev. Letters, 31 1153 (1973)

Ref. 1-18 S.D. Ellis and M.B. Kislinger, Phys. Rev. D9 2027 (1974)

Ref. 1-19 P.V. Landshoff and J.C. Polkinghorne, Phys. Rev. D8 4157 (1973)

Ref. 1-20 S. Fredericksson, Phys. Rev. Letters 37 1373 (1976)

Ref. 1-21 J. Kuti and V.F. Weisskopf, Phys. Rev. D4 3418 (1971)

Ref. 1-22 A. Cacher, J. Kogut and L. Susskind, Phys. Rev. Letters 31 793 (1973)

Ref. 1-23 F. E. Taylor et al., Phys. Rev. D14 1217 (1976)

***

Ref. 2-1 R.A. Johnson, Ph.D. Thesis, University of California, Berkeley, LBL-4610 (1975)

Ref. 2-2 R.R. Wilson, "The NAL Proton Synchrotron", Proc. 8th Int. Conf. on High Energy Accelerators, CERN, 1971, 3-13 (1971)

Ref. 2-3 W.B. Atwood, Ph.D. Thesis, SLAC Report 185 (1975); based on a fit of LH_2 density versus pressure in

Ref. 2-4 D.C. Carey et al., Phys. Rev. Letters 33 327 (1974)

Ref. 2-5 Yu. B. Bushnin et al., Nucl. Inst. and Methods 120 391 (1974)

Ref. 2-6 R.L. Walker, CALT 68-348, Caltech (1972), unpublished

Ref. 2-7 A.V. Barnes, CEX note 1/17/75, Caltech, unpublished

Ref. 2-8 A.V. Tollestrup, private communication

Ref. 2-9 A.V. Barnes, CEX note 5/12/75, Caltech, unpublished

Ref. 2-10 P. Bosetti et al., Nucl. Phys. B54 141 (1973)

Ref. 2-11 K. Eggert et al., Nucl. Phys. B98 49 (1975)

Ref. 2-12 S.J. Brodsky, SLAC-PUB-2009, (9/77)

Ref. 2-13 F.E. Taylor et al., Phys. Rev. D14 1217 (1976)

Ref. 2-14 A.H. Mueller, Phys. Rev. D2 2963 (1970); it has been seen in the data of J. Erwin et al., Phys. Rev. Letters 33 1352 (1974)

***

Ref. 3-1 S.J. Brodsky, SLAC-PUB-2009, (9/77)

Ref. 3-2 P. Bosetti et al., Nucl. Phys. B54 141 (1973)

Ref. 3-3 T.-C. Meng, Phys. Rev. D9 3062 (1974); notwithstanding the comparison in K.-W. Lai and T.-C. Meng, Phys. Rev. Letters 37 241 (1976)

Ref. 3-4 D.C. Carey et al., Phys. Rev. Letters 33 327 1974

Ref. 3-5 D. Antreasyan et al., Phys. Rev. Letters 38 112 (1977)

Ref. 3-6 S.D. Ellis and M.B. Kislinger, Phys. Rev. D9 2027 (1974)

Ref. 3-7 J. Kuti and V. Weisskopf, Phys. Rev. D4 3418 (1971) relates the proton structure function to the νW_2 of ep deep inelastic scattering; A. Cacher, J. Kogut and L. Susskind, Phys. Rev. Letters 31 792 (1973)

Ref. 3-8 R.D. Field and R.P. Feynman, Phys. Rev. D15 2590 (1977)

Ref. 3-9 E. Fishbach and G.W. Look, Phys. Rev. D15 2576 (1977) and E. Fishbach, private communication (5/77)

Ref. 3-10 N.W. Biswas, Phys. Rev. D15 1420 (1977), and N.W. Biswas, private communication (7/77)

Ref. 3-11 R. Blankenbecler, S.J.Brodsky and J.F. Gunion, SLAC-PUB-2057 (12/77)

Ref. 3-12 F.T. Dao et al., Phys. Rev. Letters 39 1388 (1977)

Ref. 3-13 M.K. Chase and W.J. Stirling, DAMPT 77/15, University of Cambridge

Ref. 3-14 B.L. Combridge, private communication (6/77)

Ref. 3-15 H. Gordon, private communication (3/78)

Ref. 3-16 S. Fredriksson, Phys. Rev. Letters 37 1373 (1976)

Ref. 3-17 Published accounts of this experiment appear in:
G.J. Donaldson et al., Phys. Rev. Letters 36 1110 (1976);
G.J. Donaldson et al., Phys. Lett. 73B 375 (1978);
G.J. Donaldson et al., Phys. Rev. Letters 40 684 (1978);
G.J. Donaldson et al., Phys. Rev. Letters 40 917 (1978);
G.J. Donaldson et al., BNL #23844 (5/78), BNL, unpublished

Ref. 3-18 R.P. Feynman, R.D. Field and G.C. Fox, CALT-68-651 (5/78), Caltech, unpublished; for an application of QCD to high $P_\perp$ scattering

Ref. 3-19 P. Fayet and S. Ferrara, Phys. Reports 32C 249 (1977); see also D.Z. Freedman and P. van Nieuwenhuizen, Sci. Am. 238 no. 2, 126 (1978)

***

Ref. S1-1 Fermilab Staff, IEEE Trans. NS-22 929 (1975); R.R. Wilson, Sci. Am. 230 no. 2, 72 (1972)

Ref. S1-2 K.L. Brown and S.K. Howry, SLAC-91, unpublished

Ref. S2-1 B.B. Rossi, Cosmic Rays (McGraw-Hill, New York, 1964)

Ref. S3-1 Particle Data Group, Phys. Lett. 75B 1 (1978)

Ref. A1-1 P.A. Cerenkov, Phys. Rev. 52 378 (1937)

Ref. A1-2 International Critical Tables 7 7 (McGraw-Hill, New York, 1930)

LIST OF FIGURES

Fig. 1-1 Electromagnetic, weak and strong interactions.

Fig. 1-2 Scattering phenomena of high energy pp interactions versus beam momentum P_{BEAM}:
a) Total (σ_{TOT}) and elastic ($\sigma_{ELASTIC}$) cross sections;
b) Average multiplicity of final state particles;
c) Probability of producing n particles

Fig. 1-3 Examples of inclusive and exclusive interactions.
a) $\pi^- p \to \pi^0 n$; b) $\pi^- p \to \pi^0 \Delta^0 (\Delta^0 \to n\gamma)$; c) $\pi^- p \to \pi^0 \pi^0 n$; d) $\pi^- p \to \pi^0 \pi^- p$.
All of a), b), c) and d) contribute to the inclusive channel $\pi^- p \to \pi^0 X$.

Fig. 1-4 Acceleration of exchanged charge in an exclusive reaction.

Fig. 1-5 Inclusive $x_{\parallel}$ and $P_{\perp}$ spectra on logarithmic scale from Ref. 1-9.

Fig. 1-6 Electroproduction diagrams.

Fig. 1-7 Inclusive cross section at high $P_{\perp}$ on logarithmic scale versus $P_{\perp}$ from Ref. 1-14.

Fig. 1-8 Inclusive cross section at high $P_{\perp}$ with $P_{\perp}$ dependence divided out versus $x_{\perp}$ from Ref. 1-14.

Fig. 1-9 Scattering subprocesses with their s-dependences.
a) $qq \to qq$ subprocess; b) $qM \to qM$ subprocess.

Fig. 1-10 The three-step scattering process (see text).

Fig. 1-11 Reactions in the $q\bar{q}$ fusion model a) $\pi p \to \pi^0 X$ and b) $pp \to \pi^0 X$.

Fig. 2-1 Schematic diagram of the apparatus. Not to scale.

Fig. 2-2 Beam counters. Scale as shown.

Fig. 2-3 Photon detector. There are 70 hodoscope counters for each view of the detector. Each counter has 8 scintillation fingers interleaved in the lead sheets. The counters integrate the showers in longitude (z).

Fig. 2-4 Detail of a photon detector finger. The source button and Lucite cookie are glued to the face of the phototube.

Fig. 2-5 PPERP trigger. Both FLUX and DET signals must be present simultaneously for a trigger to occur.

Fig. 2-6a Trigger electronics, FLUX logic. In Boolean logic notation:
$FLUX = (M1 \cdot M2 \cdot M3) \cdot \overline{(2xMINM1 + 2xMINM2)} \cdot \overline{(A\emptyset)} \cdot \overline{(Late_{\pi} + EARLY_{\pi})} \cdot \overline{(A1A + A1B)}$

Fig. 2-6b Trigger electronics, DET logic. The signal Ex is proportional to the total $P_\perp$ of photons in the detector.

Fig. 2-7 Data assembly. See text.

Fig. 2-8 Bi^{207} spectrum as seen in the source buttons. Limits of summation for the Source Monitor program are shown.

Fig. 2-9 SRCAVG/SRCPK versus SRCAVG/PEAK. In the region of correction shown, the value of PEAK can be recovered from SRCAVG and the known value of SRCPK.

Fig. 2-10 Detector X-view for a typical event. The response to a minimum ionizing particle appears at finger 5.

Fig. 2-11a,b PASS 2, match.

Fig. 2-11c PASS 2, split.

Fig. 2-11d PASS 2, drop.

Fig. 2-12 Plots of data: a) $P_\perp$ spectra of data sets for three different trigger biases; b) the software $P_\perp$ cut used in the analysis; c) invariant mass spectrum for photon pairs with target empty data subtracted.

Fig. 2-13 Illustration of kinematic parameters used in Monte Carlo analysis.

Fig. 2-14 Geometric detection efficiency as determined by Monte Carlo analysis for 90° cm, 100 GeV/c beam momentum detector setting.

Fig. 2-15 Map of kinematic boundaries for three beam energies. The limits of detection efficiency appear in a Peyrou plot ($x_\parallel$, $x_\perp$ scales); a), b) and c) beam energy as shown.

Fig. 2-16 Invariant cross sections on a logarithmic scale versus $x_\parallel$: a) and c) $\pi^- p \to \pi^o X$; b) and d) $pp \to \pi^o X$; a) and b) @ 100 GeV/c; c) and d) @ 200 GeV/c. $P_\perp$ as indicated.

Fig. 2-17 Invariant cross sections on a logarithmic scale versus θ_{cm} for $\pi^- p \to \pi^o X$ @ 100 GeV/c. $P_\perp$ as indicated.

Fig. 2-18a Beam ratios from Tab. 2-11 at 100 GeV/c beam momentum and indicated cm angle. $R(p/\pi^-)$ is the ratio of invariant cross sections for $pp \to \pi^o X$ / $\pi^- p \to \pi^o X$.

Fig. 2-18b Beam ratios from Tab. 2-11 at 200 GeV/c beam momentum and indicated cm angle. $R(p/\pi^-)$ is the ratio of invariant cross sections for $pp \to \pi^o X$ / $\pi^- p \to \pi^o X$.

Fig. 2-19 Beam ratio from Tab. 2-10 for indicated reaction and beam energy versus x_R. Data from 90° and 30° cm appear overplotted.

Fig. 3-1 $Ed^3\sigma/dp^3 / (P_\perp^2 + M^2)^{-N}$ on a logarithmic scale versus x_D, for $\pi^- p \to \pi^0 X$. a) @ 100 GeV/c - 90°, 30° and 8° cm; b) @ 200 GeV/c - 90° and 30° cm.

Fig. 3-2 Three-step scattering process.

Fig. 3-3 Structure and decay function as used by Field and Feynman:
a) proton structure function for u-quark ($G_{p/u}$) and d-quark ($G_{p/d}$);
b) pion structure function for u, d, $\bar{u}$ or $\bar{d}$ quark, $G_{\pi/u}$;
c) decay function for u, d, $\bar{u}$ or $\bar{d}$-quark into π^0, $D_{\pi/u}$.

Fig. 3-4 Scattering in the CIM. H_A splits into a meson M plus $n_a = 3$ inactive quarks and H_B splits into a quark a plus $n_b = 2$ inactive quarks. In the reaction of $qM \to q\pi^0$ there are $n_A = 6$ active quarks.

Fig. 3-5 Scattering subprocess $qM \to qM$. Because two gluons g are exchanged, the cross section scales like $1/s^4$.

Fig. 3-6 Subprocess scattering diagrams and $d\hat{\sigma}/d\hat{t}$.

Fig. 3-7 Beam ratios as defined in Eq. 2-16 versus $x_\perp$ compared to predictions from various models: a) $R(p/\pi)$ at 90° cm; b) $r(p/\pi)$ at 30° cm; c) $R(\bar{p}/p)$ at 90° cm. Curve labels: (1) Ref. 3-8; (2) Ref. 3-12; (3) Ref. 3-9; (4) Ref. 3-10; (5) Ref. 3-13; (6) Ref. 3-8; (7) Ref. 3-11.

Fig. 3-8 Pion structure function from three sources.
a) Ref. 3-8; b) Ref. 3-12; c) This experiment.

Fig. 3-9 Comparison of π^0 production in πp and pp interactions.
a) Quark fusion process; b) $qq \to qq$ scatter plus quark decay.

Fig. 3-10 Beam ratios at equal quark energy versus $P_\perp$ as defined in Eq. 3-14, data at 133 GeV/c is interpolated:
a) pp @ 300 GeV/c / πp @ 200 GeV/c, at 90° cm;
b) pp @ 200 GeV/c / πp @ 133 GeV/c, at 90° cm;
c) pp @ 200 GeV/c / πp @ 133 GeV/c, at 30° cm.

Fig. S1-1 (A) Fermilab proton synchrotron and experimental areas. (B) M2 beam line optics (schematic).

Fig. S3-1 Symmetric decay of $\pi^0 \to \gamma\gamma$: a) rest frame of π^0; b) lab frame.

Fig. S3-2 Definition of decay angles θ_π, θ_1, θ_2.

Fig. A1-1 Relationship between particle speed $\beta = \eta/\gamma$, light velocity $1/n$ and Cerenkov angle θ_C.

Fig. A1-2 Cerenkov counter optics.

Fig. A1-3 Pressure curve for Cerenkov counter showing crosstalk and inefficiency on logarithmic scale for two alternative tipped mirror sizes. Larger mirror gives lower inefficiency at optimum operating point.

Fig. A2-1 Laboratory coordinates for an event.

Fig. A2-2 Kinematic parameters in a Peyrou plot. Lines of constant $x_\parallel$, $x_\perp$, x_1, x_2, x_R and θ_{cm} are shown.

Fig. A3-1 Legend of $P_\perp$ band labels.

Fig. A3-2 $Ed^3\sigma/dp^3$ ($\pi^+p \to \pi^0X$); a) and b) @ 100 GeV/c; c) and d) @ 200 GeV/c; a) and c) versus $x_\parallel$; b) and d) versus θ_{cm}. Curve is from fit to Eq. 3-2.

Fig. A3-3 $Ed^3\sigma/dp^3$ ($\pi^-p \to \pi^0X$); a), b), c) and d) as in Fig. A3-1.

Fig. A3-4 $Ed^3\sigma/dp^3$ ($pp \to \pi^0X$); a), b), c), e) and f) as in Fig. A3-1, but e) and f) @ 300 GeV/c.

Fig. A3-5 $Ed^3\sigma/dp^3/(P_\perp^2 + M^2)^{-N}$ ($\pi^-p \to \pi^0X$); a) @ 100 GeV/c; b) @ 200 GeV/c. Curve is from same fit as for Fig. A3-2.

Fig. A3-6 $Ed^3\sigma/dp^3/(P_\perp^2 + M^2)^{-N}$ ($pp \to \pi^0X$); a) @ 100 GeV/c, b) @ 200 GeV/c; c) @ 300 GeV/c. Curve is from same fit as for Fig. A3-3.

LIST OF TABLES

Tab. 2-1 Beam Counter Dimensions

Tab. 2-2 Hydrogen Target Data

Tab. 2-3 Photon Detector Properties

Tab. 2-4 Detector Positions

Tab. 2-5 Definitions and Distributions of Kinematic Parameters

Tab. 2-6 Resolution of the Apparatus

Tab. 2-7 CERBIT Distributions for 200 GeV/c Beam, 30° Data

Tab. 2-8 Counter Parameters and Efficiencies

Tab. 2-9 Flow Chart for Cerenkov Analysis

Tab. 2-10 Cross Sections for $\pi^{-}p$, $\pi^{+}p$, $pp \rightarrow \pi^{o}X$, @ 100, 200, 300 GeV/c

Tab. 2-11 Cross Sections for $\pi^{\pm}p$, $K^{\pm}p$, pp and $\bar{p}p \rightarrow \pi^{o}X$, @ 100 and 200 GeV/c

Tab. 3-1 Values of Best-Fit Parameters

Tab. 3-2 Quark Content of Hadrons

Tab. 3-3 Ratios of Cross Sections as Predicted by Various Models

Tab. S3-1 Decay Properties of the π^{o}

Tab. A1-1 Number of Photoelectrons Inferred from Two Methods

Tab. A2-1 Maximum CM Energy for Different Beams

Tab. A2-2 Kinematic Parameters in the Super Relativistic Limit

But just between us theoretical physicists:

What can we do with all these data?

We can't do anything.

- R. P. Feynman

1. Introduction

Physics concerns itself with understanding the nature of the physical world: the structure of space, time and matter. Particle physics deals with the most basic properties of matter - how the fundamental particles interact with one another. The "particles" involved are by definition the smallest divisions of matter known. We believe that by understanding the properties of these simple interactions, we can extend our understanding to more complex systems. Beginning with the electromagnetic interaction of electron and proton, we build the properties of all atoms.

Of the four fundamental interactions - gravity, electromagnetism, weak and strong - the last occupies a unique position in the present state of our understanding. There now exists an exact theory of electromagnetism (Ref. 1-2) and a candidate for a unified theory of weak - electromagnetism (Ref. 1-3), both based solidly on quantum mechanics and the theory of relativity. However, the strong force defies such an approach. We still cannot make precise calculations from first principles of such things as the relative masses of the hadrons (strongly interacting particles) and the dynamics of their interactions. Part of the problem is the strength of the interaction itself. We do not know how to make perturbation theory calculations with such a large coupling constant ($\cong 15$).

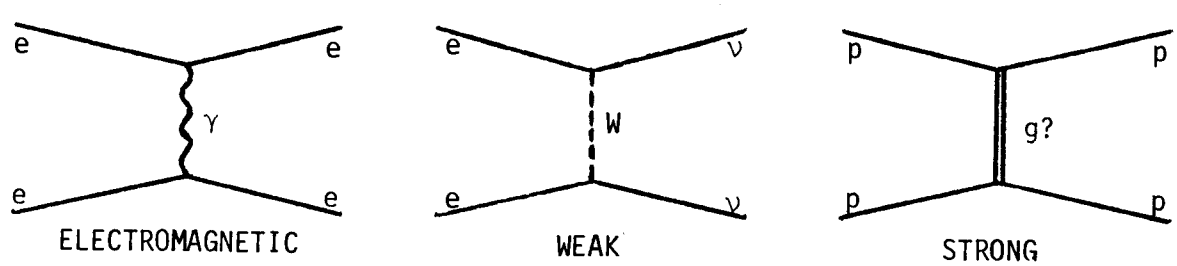

Fig. 1-1

We simply cannot view the interactions between hadrons as a small change from their free state (Ref. 1-1).

One very successful theory regards the hadrons as being composed of still smaller entities, quarks (Ref. 1-4) Even though free quarks have never been seen, the formalism makes very good account of the static properties of hadrons - quantum numbers, spins, etc. At present we have classified and cataloged more hadrons than there are chemical elements. Yet we still do not understand the interaction between quarks that binds them in hadrons. Saying that the interaction is mediated by "gluons" as in QCD (Ref. 1-5) provides a basis for further progress, but as before - precise calculations cannot be made.

As a consequence, we use models to study the strong interaction. These theories seek to predict - or mimic, as the case may be - the results of experiments in terms of phenomenological laws which the data are seen to follow. In this sense, we are in the position of the early atomic physicists confronted with their very baffling line spectra without the simple Schroedinger or Heisenberg quantum theory. It is not surprising that there are many complicated models.

It has been the pattern that as experimenters discover new phenomena, theorists develop new models to explain these phenomena. As the experimenters broaden the scope and refine the precision of their measurements, the weaker models are abandoned in favor of the more powerful ones. Then newer phenomena appear and the pattern repeats itself. Occasionally real progress is made in the theoretical realm when an integrated theory appears which is able to explain phenomena over a broad range, formerly covered by disparate models. This cyclical development is illustrated well by the history of hadron interactions at high energy

which lead to our experiment.

1.1 Context of the Experiment

The recent history of hadron scattering experiments is characterized by ever increasing interaction energy. From the familiar arguement based on the Heisenberg uncertainty principle, higher energy implies a smaller distance scale probed by the interaction, thus a more accurate picture of the interaction. Are these expectations borne out by experiment? We shall see that higher energy brings the hoped-for powerful probe of the finer structure of the hadrons, but in a way one would not naively expect.

Figure 1-2 shows some of the important phenomena observed. The total cross section, which measures the probability for any reaction to occur, is decreasing with energy for beam momenta below about 1 GeV/c. However, at higher energy it levels off and is nearly constant with energy. The cross section for elastic scattering $pp \rightarrow pp$, in which the identity of the original particles is preserved, is only about 10% of the total. The rest is inelastic, entailing the production of more or different particles than entered initially.

The average multiplicity measures the number of particles produced. Figure 1-2b shows the multiplicity increasing logarithmically with the energy of the interaction. It appears that the greater energy available to the interaction merely goes into the production of more particles.

The botton graph in the figure illustrates this in another way. The probability for having only two particles in the final state of an interaction P(2) is decreasing with energy. But the probability for producing three particles is increasing, eventually exceeding the former at very high energy.

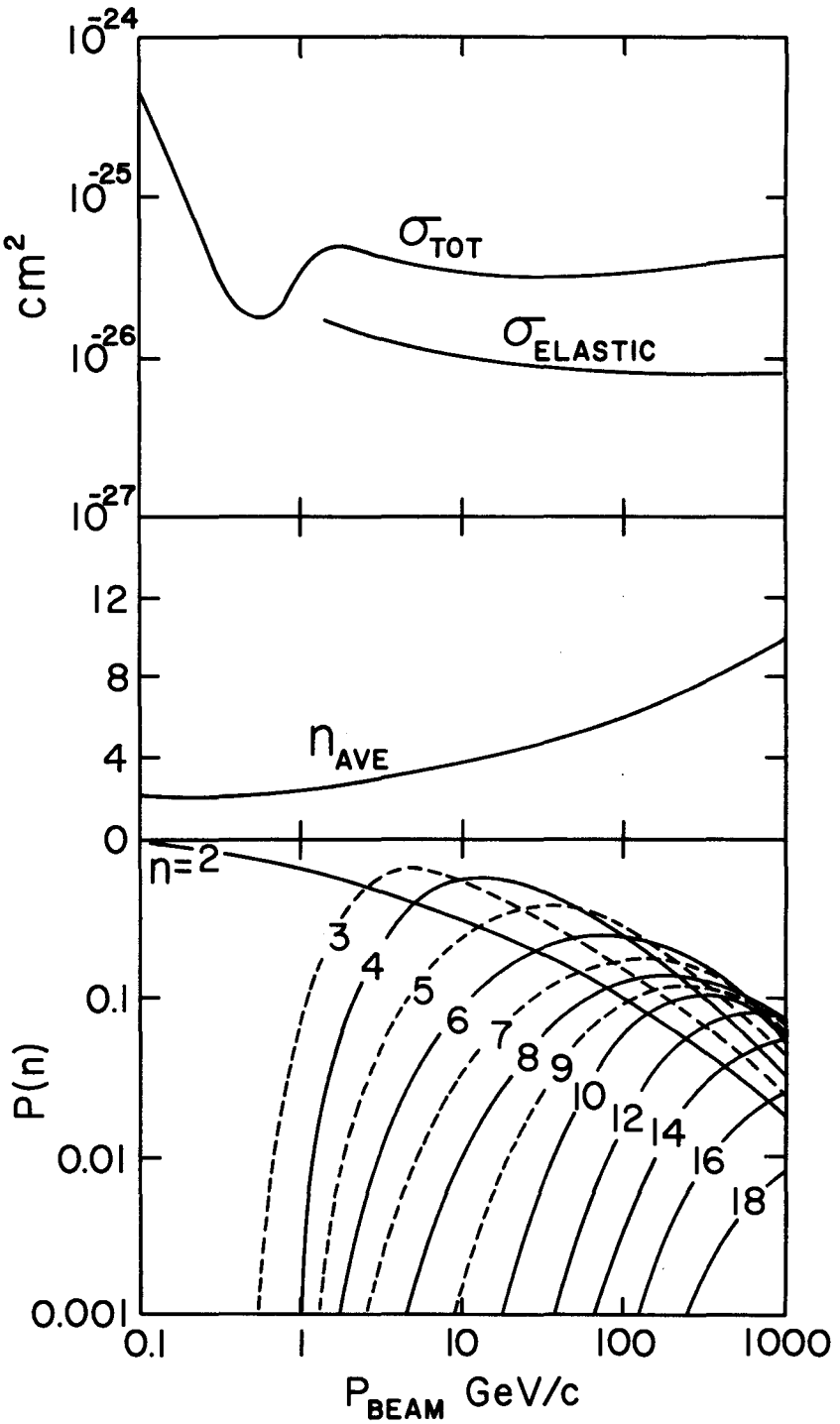

Fig. 1-2 Scattering phenomena of high energy pp interactions versus beam momentum P_{BEAM}:

a) Total (σ_{TOT}) and elastic ($\sigma_{ELASTIC}$) cross sections;

b) Average multiplicity of final state particles;

c) Probability of producing n particles

XBL 789-11371

Reactions producing five or seven particles are quite complicated compared to those making only two or three. To fully describe each interaction, one must specify the momentum and angles of each of the outgoing particles. The number of correlation between angles and momenta of the various different particles is staggering and, more importantly, overly expensive in the computer time to calculate them all. At this point, we are faced with a vast amount of data but have an only half vast idea of how to extract the truth from it.

Another impact of the increased multiplicity is that only very special detectors have a chance of detecting all the particles thus produced. Such a detector must literally surround the target and be able to distinguish between a wide variety of particles. These are the specifications for a very expensive detector indeed (Ref. 1-7).

At this point, R. P. Feynman showed a simple way out of the quandary. Making the distinction between <u>inclusive</u> and <u>exclusive</u> experiments, he made general predictions for the cross sections in both cases and showed a way to present the data in terms of a scaling variable (Ref. 1-8).

Exclusive experiments are ones which require specific particles to be produced <u>and no others</u>. Each reaction pictured in Fig. 1-3 is an example of an exclusive reaction. In the first, $\pi^- p \rightarrow \pi^0 n$, the π^0 and n must balance momenta and account for all the input energy of the π^- and p. The second $\pi^- p \rightarrow \pi^0 \Delta^0$ ($\Delta^0 \rightarrow N\gamma$) would be a possible background reaction to the first, if one detected the n from Δ^0 decay but missed the γ.

Inclusive experiments, on the other hand, require one specific particle to appear, <u>regardless of what accompanies it</u>. Thus all of the

reactions in the figure contribute to the π^0 inclusive reaction $\pi^- p \to \pi^0 X$.

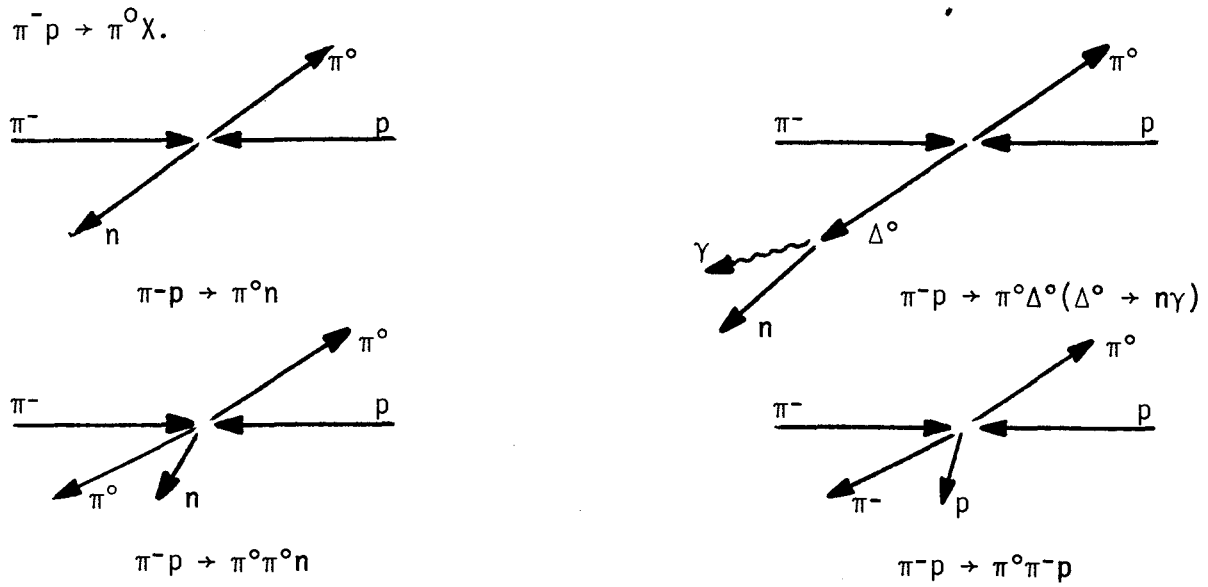

Fig. 1-3 Examples of inclusive and exclusive interactions.
a) $\pi^- p \to \pi^0 n$; b) $\pi^- p \to \pi^0 \Delta^0 (\Delta^0 \to n\gamma)$; c) $\pi^- p \to \pi^0 \pi^0 n$; d) $\pi^- p \to \pi^0 \pi^- p$. All of a), b), c) and d) contribute to the inclusive channel $\pi^- p \to \pi^0 X$.

According to Feynman, exclusive reactions in general must decrease with energy like a power law while inclusive interactions will approach a constant. It is possible to view the rise and leveling off of the inelastic cross section as simply a consequence of the appearance of more exclusive channels as the energy rises, and the power law decrease with energy of each such channel. The flat behavior of the inclusive reactions can be viewed in much the same way.

We can think about the power law fall of exclusive processes in the following way. Channels such as $\pi^- p \to \pi^0 n$ demand that the relevant quantum numbers (in this case the electrical charge) be exchanged without the production of more particles. At high energy this becomes increasingly less likely as the quantum exchanged tends to radiate (bremsstrahl) particles as it is accelerated, as in the figure below.

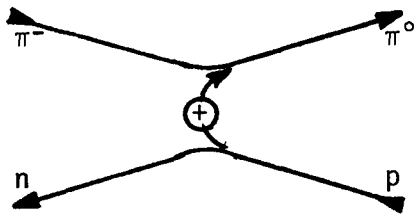

Fig. 1-4 Acceleration of exchanged charge in an exclusive reaction.

The scaling behavior predicted by Feynman is a very powerful concept and since I discuss variations on this concept later, it is well to explain it here. The invariant cross section for the inclusive reaction $a + b \rightarrow c$ + anything, denoted $Ed^3\sigma/dp^3(ab \rightarrow cX)$ is in general a function of the center of mass energy s, the transverse momentum of c, $P_\perp$ and the longitudinal momentum of c, $P_\parallel$. The variables $P_\perp$, $P_\parallel$ are by convention expressed in the center of mass system (cm) of a + b. So $\tan \theta_{cm} = P_\perp/P_\parallel$ with θ_{cm} the scattering angle of c in the cm. In this frame of reference, the maximum momentum available to c P_0 is approximately $\sqrt{s}/2$. Thus the invariant cross section is some function:

$$(1\text{-}1) \qquad \frac{Ed^3\sigma}{dp^3}(ab \rightarrow cX) = F(P_\perp, P_\parallel, P_0)$$

The scaling hypothesis is simply that for large s, F approaches a form:

$$(1\text{-}2) \qquad F(P_\perp, P_\parallel, P_0) = f\,(P_\perp, P_\parallel/P_0) = f(p_\perp, x_\parallel),\ x_\parallel = P_\parallel/P_0$$

where f is independent of P_0. In short, for large s, the invariant cross section depends on P_0 and $P_\parallel$, but in such a way that only the ratio $x_\parallel = P_\parallel/P_0$ matters. So $x_\parallel$ is the scaled longitudinal momentum.

Measurements of inclusive cross sections gave results as in Fig. 1-5a, which shows the cross section versus $x_\parallel$ in a given $P_\perp$ interval. Such plots for different values of s seem to lie on a universal curve,

substantiating the scaling hypothesis. The dependence on $P_\perp$ at $x_\parallel = 0$ appears in Fig. 1-5b, showing the exponential fall of the cross section versus $P_\perp$.

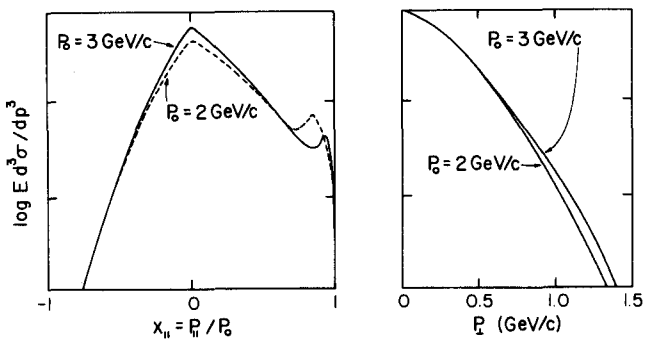

Fig. 1-5 Inclusive $x_\parallel$ and $P_\perp$ spectra on a logarithmic scale from Ref. 1-9.

Indeed the data are well parametrized by a form:

$$Ed^3\sigma/dp^3 = e^{-6P_\perp} f(x_\parallel) \qquad P_\perp \text{ in GeV/c} \tag{1-3}$$

The average transverse momentum of secondaries is very small -- about .160 GeV/c. At $x_\parallel = 0$ cross sections fall by over two orders of magnitude from $P_\perp = 0$ to $P_\perp = 1$.

The above form accurately represents the fall of the $P_\perp$ spectrum over several decades of cross section. Various phenomenological models can be fit to these data (Ref. 1-10). A typical picture of these models is that the two hadrons, colliding at high energy, create very massive excited states, "fireballs", which in cooling boil off hadrons. The momentum of these secondaries is limited by Boltzman statistics to values commensurate with some characteristic temperature giving a $P_\perp$ spectrum as in Fig. 1-5b. The longitudinal momentum of the fireball gives the secondaries an $x_\parallel$ spectrum like that shown in Fig. 1-5a. The characteristic temperature has a value of about 1/6 GeV/c.

So inclusive interations, at least at these value of momentum transfer, are characterized at large interaction energy by a constant cross section, rising average multiplicity and limited transverse momentum.

They seem to indicate that the kinetic energy of the interaction is being turned into the production of more particles. The concept of massive fireballs boiling off fragments would give the idea that the interal structure of the hadrons is being averaged out during the interaction. The high energy probe of fine hadron structure seems to be lost.

In contrast, deep inelastic electroproduction $ep \to eX$ and neutrino scattering $\nu p \to \mu X$ seemed to be sensitive to small transverse distances in the hadron. The very successful model (Ref. 1-11) of Bjorken and Paschos interprets these interactions in terms of the lepton scattering elastically at high $P_\perp$ from a single hadron constituent (parton) as in Fig. 1-6.

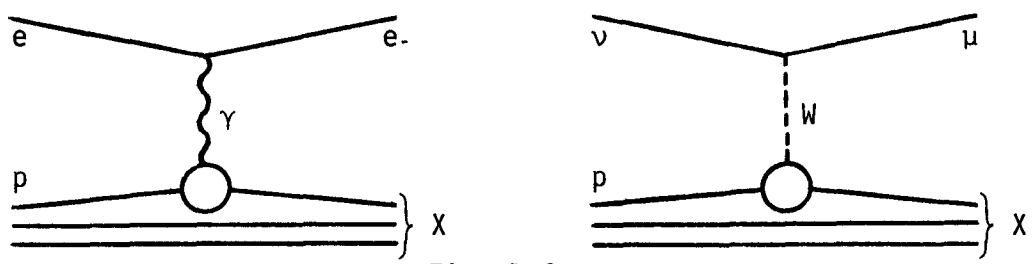

Fig. 1-6

By a simple extension Berman, Bjorken and Kogut expect a similar process to occur in purely hadronic scattering (Ref. 1-12), of the form:

(1-4) $$Ed^3\sigma/dp^3 = s^{-2}F(x_\perp, x_\parallel) \ , \qquad x_\perp = P_\perp/P_0 = P_\perp/(\sqrt{s}/2)$$

which is equivalent to:

(1-5) $$Ed^3\sigma/dp^3 = P_\perp^{-4} f(x_\perp, x_\parallel)$$

The expectation is that at sufficiently high $P_\perp$ hadronic processes give rise to the form Eq. 1-3 eventually fall below those that give rise to Eq. 1-4.

The above form exhibits a more specific form of Feynman scaling in that the $P_\perp$ dependence is separable from the dependence on the other

variables. It predicts that cross sections at high $P_\perp$, at fixed $x_\parallel$ and $x_\perp$, will behave like s^{-2} or $P_\perp^{-4}$ since $P_\perp = \sqrt{s}x_\perp/2$.

Several early experiments at the ISR (CERN) (Ref. 1-13) did measure this high $P_\perp$ region in inclusive hadronic interactions. What they saw was striking indeed. The cross section at high $P_\perp$ is several orders of magnitude larger than the extrapolation of $e^{-6P_\perp}$ as Fig. 1-7 illustrates.

Fig. 1-7 from Ref. 1-14

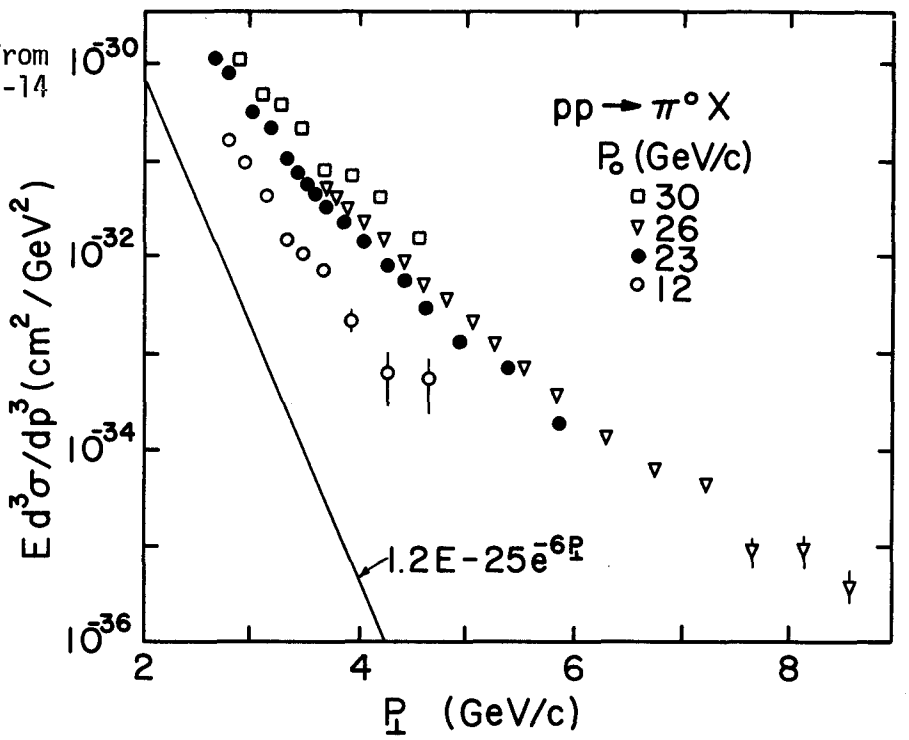

This phenomena may have the same significance as the famous Rutherford α-particle scattering experiments (Ref. 1-15). The low $P_\perp$ data indicate that hadron-hadron scattering is somehow "soft", leading to small average $P_\perp$. At high $P_\perp$, however, we must invoke some sort of parton - or quark - hard scattering, viewing the hadrons as clusters of these perhaps pointlike constituents.

1.2 Theoretical Issues

It seems that it is not feasible to view hadronic scattering at high $P_\perp$ as occuring between structureless matter distributions. Accord-

ly, even though purely hadronic models for high $P_\perp$ processes have been proposed, I do not discuss them here. As reviewed in Ref. 1-16, all are limited in the range of phenomena at high $P_\perp$ they are able to accommodate.

The parton models are an intuitively satisfying way of interpreting these phenomena, yet they too have their difficulties. An illustration is the scaling in $x_\perp$ and the $P_\perp$ dependence at fixed $x_\perp$. Figure 1-8 shows a plot of the cross section with the $P_\perp$ dependence at fixed $x_\perp$ divided out. A fit of the data of Ref. 1-13 to the form

$$(1\text{-}6) \qquad Ed^3\sigma/dp^3 = A\, P_\perp^{-N}\, e^{-bx_\perp} \qquad (x_\parallel = 0 \text{ or } \theta_{cm} = 90^0)$$

gives a value of N = 8.2. This is in some conflict with the conjecture of Berman, Bjorken and Kogut based on electroproduction as in Fig. 1-6 and Eq. 1-5.

Fig. 1-8 from Ref. 1-14

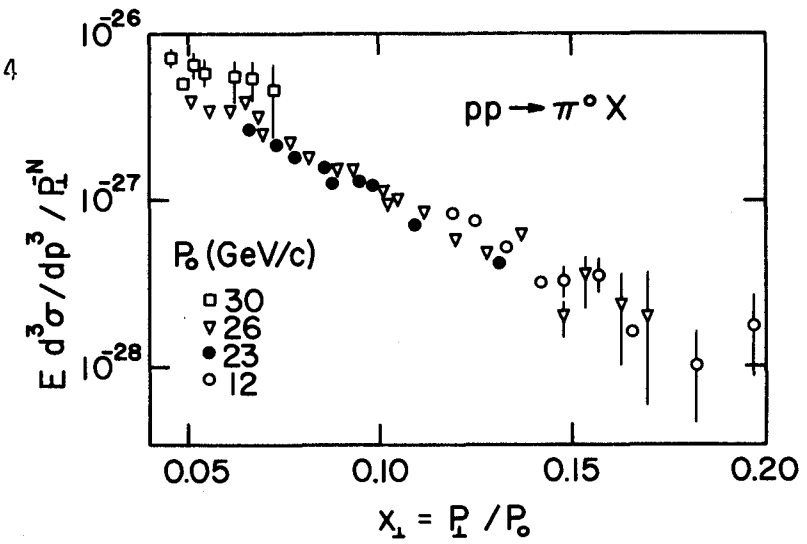

But the puzzle goes deeper because in the parton picture the dependence on s at fixed $x_\perp, x_\parallel$ is related to the number of partons (elementary fields) participating in the interaction (Ref. 1-17). If the high $P_\perp$ secondary in $\pi p \to \pi X$ is the result of simple quark-quark scattering ($qq \to qq$) as in Fig. 1-9a the fixed $x_\perp, x_\parallel$ behavior is like s^{-2} ($P_\perp^{-4}$). We say that there are four elementary fields active in the scattering. The

observed $P_\perp^{-8}$ behavior is better accounted for if one assumes that six partons are involved. With mesons composed of $q\bar{q}$ pairs as in the usual quark theory, the $qM \to qM$ diagram shown in Fig. 1-9b has a fixed $x_\perp x_\parallel$ behavior like s^{-4}.

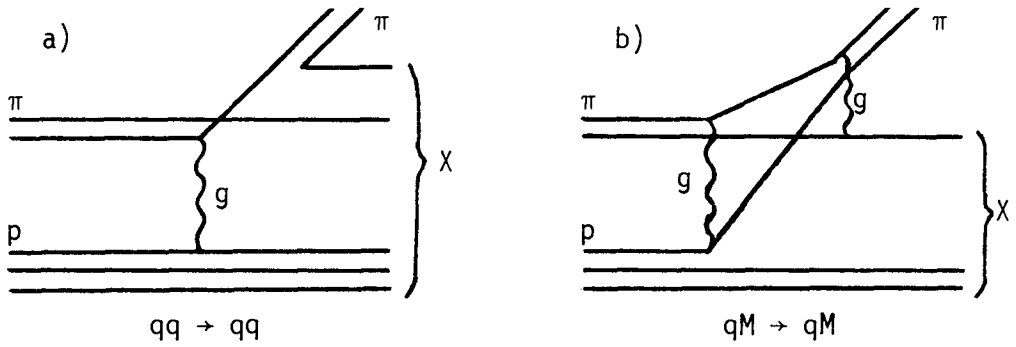

Fig. 1-9

Many parton models fit this data. It is these different models which show the current theoretical issues. All these models had to give a cross section which did not fall as fast an an exponential in $P_\perp$, but which did fall faster than the $P_\perp^{-4}$ power law. All had to take the apparent scale invariance of Fig. 1-5 into account.

The general approach shared by many models involves a very simple step-by-step process (Ref. 1-18). In the rare high $P_\perp$ scatter, (Fig. 1-10) each incoming hadron H_a, H_b fragments into a parton and a core. The partons α, β undergo a simple $2 \to 2$ scatter at high angle producing partons γ, δ. The parton γ gives rise to a real hadron H_c via an inverse fragmentation or decay, or perhaps γ is a hadron already.

I think of this process as the incoming hadrons "undressing" into their constituent partons, two partons undergoing a hard scatter with a strong recoil, and one of the scattered partons "dressing" back up as a real parton. The remaining pieces of the interaction become part of the

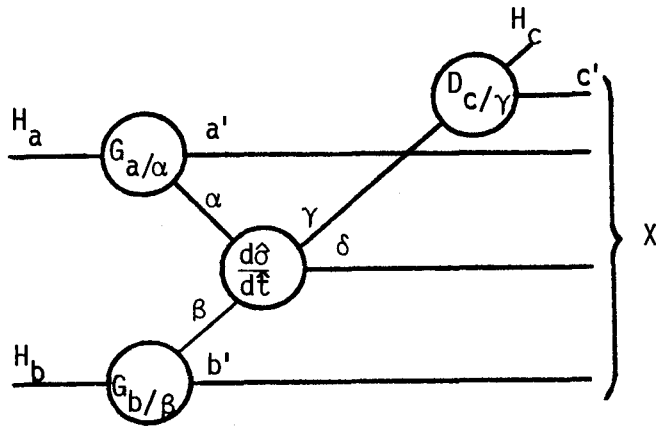

Fig. 1-10

inclusive X which is undetected in the experiment.

The cross section can be expressed as the basic subprocess cross section $d\hat{\sigma}/d\hat{t}$, folded into the structure functions $G_{a/\alpha}, G_{b/\beta}$ for the initial hadron undressing into partons and the fragmentation function $D_{\gamma/c}$ for the final parton dressing up into a hadron. As I will discuss in Chapter 4, Interpretations, the dependence on s at fixed $x_\perp, x_\parallel$ is primarily a result of the form of the subprocess cross section.

We can differentiate between the various models on the basis of the form of $d\hat{\sigma}/d\hat{t}$. A large class of models use qq scattering but doctor the $d\hat{\sigma}/d\hat{t}$ to fit the data. Others use qM scattering or other similar combinations which naturally scale like $P_\perp^{-8}$ (Ref. 1-6). These models receive a more detailed treatment in Chapter 4.

It would be interesting to resolve the puzzle of just what is the central process. An analogy due to Feynman states that studying hadron-hadron collisions is like smashing two watches together and watching the gears fly out. While not as simple to interpret as electroproduction, hadronic processes may permit us to study the perhaps fundamental "gear-gear" interaction. Particularly interesting is the possibility of a relationship between electroproduction as in Fig. 1-6 and high $P_\perp$ inclusive hadronic processes as in Fig. 1-10.

1.3 Experimental Possibilities

Our experiment could supplement the existing data in two important ways. In the previous experiments, all of the data had been taken at the CERN ISR in proton-proton collisions. All had been measured at cm angles near 90°. Our experiment would use a secondary beam including particles other than the proton - pions, kaons and antiprotons - and would investigate cm scattering angles from 110° to about 5°. These measurements would help to put constraints on models and perhaps answer some of the questions posed above.

Antiquarks in the Beam Particle

The quark fusion model rather restrictedly assumes the scattering subprocess to proceed only via the scattering of q and $\bar{q}$ into two mesons $q\bar{q} \rightarrow MM$, one of which is the detected π^{o} at high $P_{\perp}$ (Ref. 1-19). Since a pion consists of a $q\bar{q}$ pair and a proton of three quarks (qqq), the model predicts much more π^{o} production from pion beams than from proton beams. This is a consequence of the fact that the pion carries an antiquark into the reaction but the proton does not (Fig. 1-11). In the latter case, the $\bar{q}$ must be obtained from the "sea" of $q\bar{q}$ pairs accompanying the proton (the mesonic cloud). The $\bar{q}$ from the beam pion is much more energetic, on the average, than that from the sea, leading to a much higher probability of producing a π^{o} with large transverse momentum.

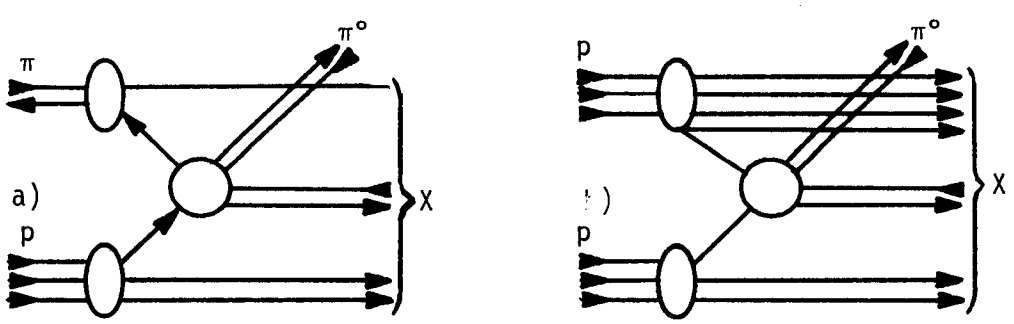

$\pi p \rightarrow \pi^{0} X$ Fig. 1-11 $pp \rightarrow \pi^{0} X$

Momentum of Quarks in the Beam Particle

The fact that there are only two quarks in the pion versus three in the proton might have an effect on the physics quite apart from the question of antiquarks. One reasons (Ref. 1-20) that the quarks, on the average, share equally in the momentum of the incoming hadron. This implies that, given a pion and a proton of equal momentum, the two quarks in the pion will each have about 50% more momentum than the three quarks in the proton. It is natural to compare the respective cross sections at the same value of quark-quark incoming energy. By the above argument, this condition is met when the proton beam momentum is 50% higher than the pion beam momentum. We might then expect the ratio of cross sections to be a constant, independent of s ($P_\perp$) and $x_\perp$, $x_\parallel$. Further, this constant would be the ratio of the number of respective beam quarks:

$$(1\text{-}7) \qquad Ed^3\sigma/dp^3(pp\to\pi^0X)\Big|_{@300\ \mathrm{GeV/c}} \Big/ Ed^3\sigma/dp^3(\pi p\to\pi^0X)\Big|_{@200\ \mathrm{GeV/c}} = 3(\mathrm{proton})/2(\mathrm{pion})$$

The Structure Function of the Pion

Having pion beam data would also put constraints on the structure function of the pion in the context of the parton model. That of the proton can be determined by an analysis of electroproduction data (Ref. 1-21), while data from experiments like $e^+e^-\to$hadrons (Ref. 1-22) can reveal the fragmentation function. Analysis of hadronic processes can never be so clean, but deep inelastic electroproduction of pions is a difficult experiment to realize. One way to use the hadron data would be to adjust a hypothetical pion structure function to fit the observed pion-induced cross section using a proton structure function and quark

fragmentation function as above.

Scaling Law

We have mentioned scaling in the two variables $x_{\parallel}$ (at low $P_{\perp}$) and $x_{\perp}$ (at 90°, or low $P_{\parallel}$). Is there an extension of these to the intermediate cm angles where both $P_{\perp}$ and $P_{\parallel}$ are not small? One idea is that scaling in the variable x_R could unify both (Ref. 1-23). This variable is the scaled radial momentum defined as:

(1-8) $$x_R = \sqrt{(x_{\perp}^2 + x_{\parallel}^2)} = P/P_o$$ where P is the total cm momentum of the secondary

Then the cross section at all angles would approximately follow:

(1-9) $$Ed^3\sigma/dp^3 = P_{\perp}^{-n} f(x_{\perp},x_{\parallel}) = P_{\perp}^{-n} g(x_R)$$

This is a very tempting simplification indeed, and our experiment could test it very well by providing data over a broad range of cm angles.

2. Experiment

This chapter contains a description of the experiment itself. It begins with an overview, which briefly introduces the experiment, discusses the apparatus, the types of data we gathered, and sets out the way we analyzed our data. The latter three topics each receive a more detailed treatment in the subsequent sections.

2.1 Overview

Fermilab E-268 came into being as a collaboration of the California Institute of Technology (CIT), Brookhaven National Laboratory (BNL) and Lawrence Berkeley Laboratory (LBL). The experiment closely followed Fermilab E-111 and employed much of the existing apparatus and personnel (Ref. 2-1). We used a beam of particles from the Fermilab accelerator (see Supplement 1) striking a hydrogen target and detected the high $P_\perp$ particles in a photon detector (Fig. 2-1).

General Features

The particle beam consisted of a mixture of pions (π), kaons (K), and protons (p). By identifying the beam particle in our Cerenkov counters, we were able to study the scattering of the three different particles in each of two (positive and negative) charge states. We hoped to measure the difference in the cross sections of the six respective particles. With a beam of positives, we would concurrently measure the inclusive rates: $\sigma(\pi^+ p \rightarrow \pi^0 x)$, $\sigma(K^+ p \rightarrow \pi^0 x)$, $\sigma(pp \rightarrow \pi^0 x)$. Ratios of these cross sections would be free from many systematic uncertainties (such as our precise knowledge of the detectors' acceptance) which would have to be taken into account in a presentation of the absolute cross sections. We used a target of hydrogen rather than a nuclear target,

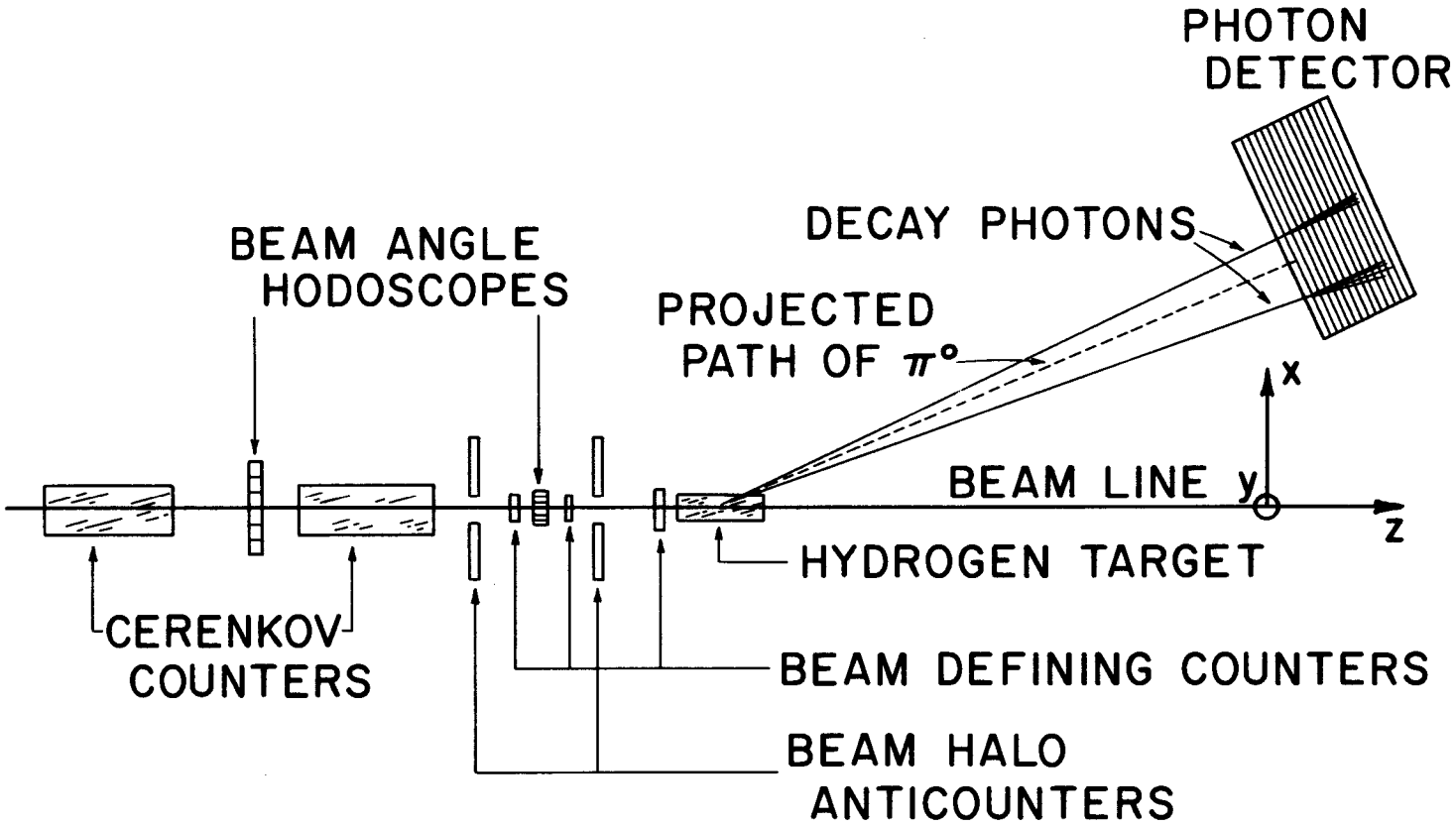

Fig. 2-1 Schematic diagram of the apparatus. Not to scale. XBL 789-11380

since the latter introduces many effects which complicate the analysis and interpretation of the data. The photon (γ) detector was already a proven device for detecting π^0's and other neutral particles through their 2γ decays. In principle any particle decaying into photons could be detected in the device. Since ours was an inclusive experiment, it was unnecessary to detect the other particles produced in the collision.

We also used the detector itself in the "PPERP" trigger of our apparatus, which was "beam particle in and high $P_\perp$ photons out". A special mixing circuit calculated in real time the total transverse momentum of the photons in the detector and decided if this was greater than a preset bias. This trigger requirement cut out the copious low $P_\perp$ events. Typically, requiring the detected $P_\perp$ to be greater than 2.5 GeV/c meant that we would have a trigger on only one out of a million beam particles.

The region of angular acceptance was set by our choice of detector positions. The combination of good two-photon discrimination and large size resulted in a large solid angle for detecting π^0's.

The event trigger signaled the data assembly portion of our apparatus to go into action. The signals from the detector were in the form of electrical impulses. The MPHA (Multi-Pulse Height Analyzer) converted these into digital form and retained them. Another device, the BPHA, performed a similar function on signals from the Cerenkov counters. The on-line computer (the SIGMAII read these data as well as the scalers and hydrogen target status. Eventually, the computer created a permanent record of the event by writing it on magnetic tape.

Types of Data

Several different types of data collection took place in this experiment. We calibrated the photon detector's energy response by using

an electron beam* of known momentum swept over the detector. The electron sweeps took place at the beginning and end of a (typically 4 week) data run. By repeatedly triggering the apparatus while the beam was off, we measured the response of the detector in the absence of any signal. These pedestal runs preceeded every other kind of data-taking and measured the null response of the detector. We triggered the apparatus on any beam particle during flux runs. This allowed a study of the beam composition. Using our $P_\perp$ trigger at several different biases allowed us to collect data for several intervals in $P_\perp$. These PPERP runs took up most of the time. Along with the PPERP runs, we took data using the identical triggers but with the target empty. Target empty runs allow a calculation of the contribution of the target flask walls, etc., to our measurements. Finally a special system employing radioactive sources within the detector allowed us to track the energy response of the detector between electron sweeps.

Our SIGMAII had a program which analyzed the data on-line, allowing us to get a first glimpse at the results. It also made it possible to carry out diagnostic analyses of the various counters in our experiment to detect possible errors in settings even while the data taking was in progress.

Analysis Plan

We analyzed the data using a CDC7600 computer at BNL to read the raw data tapes and perform the calculations. The first step was to derive the photon momenta from the detector information. The sum of detector pulse heights from a shower is proportional to the photon's energy; the

---

*The M2 beam at 100 GeV/c was about 7% electrons.

centroid of the pulse heights gives the photon's location in the detector. The direction of the photon is along a line between the target center and the shower location in the detector. We assumed the π^0 production and decay vertices coincided with the target center. Then, using conservation of (4-) momentum in the $\pi^0 \rightarrow 2\gamma$ decay we reconstructed the original π^0 momentum. After a simple transformation to the center of mass frame, we calculated all the relevant kinematic quantities, including the invariant mass of photon pairs.

A histogram of this quantity shows a large peak around the true π^0 mass. With the target-empty events subtracted, we estimated the amount of π^0's that made up the Gaussian shaped peak and the amount of "background" under the peak. The latter presumably consists of uncorrelated photon pairs.

We made many such mass plots, the events being grouped in bins of $P_\perp$ and $x_\parallel$. For each such bin we calculated the average cross section.

2.2 Apparatus

In the following section, I discuss the apparatus, consisting of the beam and beam counters and the target, which together make up the "initial state", the detector, which analyzes the "final state", the trigger, which causes the data assembly apparatus to record the event data.

This experiment used much of the existing, tried-and-true apparatus and methods of the previous experiment E-111 (Ref. 2-1) with change. The major differences lay in the Cerenkov counters, where we upgraded the one threshold counter to two differential counters, and the target, where we eliminated the charged particle anticounters and gamma veto system. Also, we place the detector not in the beam, but off to one side where the detector acceptance was in the neighborhood of 90^0 and 30^0 respectively

in the cm.

The trigger for this experiment was naturally quite different, since the E-111 trigger required no information from the detector. In the present experiment, the trigger required more than a certain amount of transverse momentum in the detector.

2.2.1 Beam and Beam Defining Counters

This experiment used the M2 beam at Fermilab, a secondary beam derived from targeting protons at 400 GeV/c momentum on a tungsten production target in the Meson Lab (Ref. 2-2).

Collimators defined a narrow beam of the the "spray" from this target, and a system of magnets called the beam transport then brought particles all of a certain momentum to the apparatus of our experiment. The momentum "bite" was selected by our choice of magnet currents and collimator settings. Collimators also controlled the intensity of the beam (see Supplement 1 for details).

The beam-defining counters (Tab. 2-1, Fig. 2-2) performed several functions which, in combination, signaled the presence of an incoming particle ready to interact in the hydrogen target.

The beam telescope consisted of M1, M2 and M3. M1 was a thick (1/4") counter for better efficiency and time resolution and provided the main timing information for the experiment. M2 was a smaller, thinner counter and limited the acceptance of the telescope. The thin M3 counter was specially situated within 2" of the target flask and coupled to a phototube by an air light pipe and mirror arrangement. This counter ensured that the target was correctly aligned with the beam and the other beam counters.

TABLE 2-1

BEAM COUNTERS

Counter	Thickness Height Width (dimensions in inches)	Longitude (relative to M1)	Function
M1	.250 .438 .438	0.0	primary timing
M2	.125 .312 .312	-13.75	limits aperture
M3	.063 1.0 (circular)	40 to 70	aligns target
AØ	.250 15 15 (.375 circular hole)	-16.5	"anti" for beam halo
A1A and A1B	.250 15 15 (.375 square hole)	8	"anti" for beam photons (.25" Pb sheet on face)
DX	.063 .125 .063(x6)	-9	position resolution horizontal
DY	.063 .063(x6) .125	-9	vertical
UX	.125 2.5 .375(x6)	-196 feet (90° data) and -236 feet (30° data)	angular resolution horizontal
UY	.125 .375(x6) 2.5		vertical

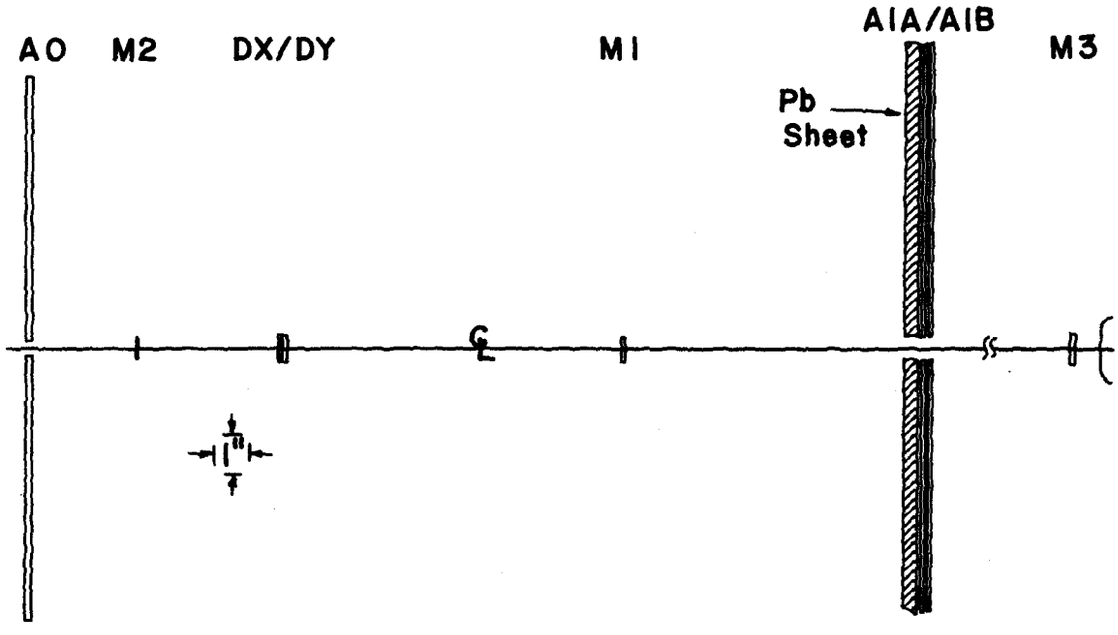

Fig. 2-2 Beam counters. Scale as shown.

The AØ counter with its 3/8" diameter beam hole vetoed any event with a beam particle outside of the normal beam size. The A1 counter with a 1/4" lead (Pb) sheet in front as a radiator served the same function for beam-associated photons. We were especially keen on eliminating any event accompanied by the products of an upstream interaction, since these could possibly produce spurious signals in the detector.

The two differential Cerenkov counters (upstream: CU, downstream: CD) each independently identified the beam particle. Each counter had two phototubes (outer: O, inner: I) which respectively registered large- and small-angle Cerenkov light. Pions count in the outer phototubes (CUO, CDO) while kaons count in the inner (CUI, CDI). Protons are below Cerenkov threshold in both counters (for more details see Appendix 1).

The upstream and downstream beam hodoscopes (UX, UY, DX, DY) provided position and angular information on the incoming beam particle.

A series of electronic circuits (the "fast logic") analyzed in real time the signals from these counters (see 2.2.4 PPERP Trigger). An output from these circuits indicated that a beam particle had arrived and that it was not accompanied by any other particles. The Cerenkov counters and beam hodoscopes were not anlayzed in real time, but were simply "read out" to the computer as part of the event data.

2.2.2 Hydrogen Target

The target used in this experiment was a double flask of liquid hydrogen (LH_2), the scattering of interest taking place between the beam particles and the (proton) nuclei of the hydrogen atoms. The length of the flasks (60 cm) was such that about 1/10 the beam particles would interact upon passing through the target. As we shall see later the mass resolution of the experiment increases with the length L of the target.

Ideally then, we would want a material with as high a density ρ as possible to give the required density of scattering centers, $n = \rho L$, in as short a length as possible. Why did we pick LH_2 over lead (Pb), where the equivalent target length would have been less than 1 cm? The answer lies in the fact that the hydrogen nucleus is simply a proton, while the Pb nucleus contains over two hundred total protons and neutrons. Thus a scattering on lead would involve a complicated interaction indeed, perhaps able to mask the effect we are interested in. Rather than grapple with this thorny problem, we chose the LH_2.

Besides its low density, this material has other properties which make it problematic. It boils at 21K, one of the lowest b.p.'s of any material, and it is flammable. The first property makes it necessary for the target to be a cryogenic refrigerator with all parts enclosed in a high quality vacuum for insulation. The second property requires that the cryogenic system be surrounded by a specially ventilated tent.

The closed hydrogen cryosystem employed two continuously running twelve watt helium refrigerators to condense bottled hydrogen gas into a large reservoir located above the target flasks, at which point the fill line from the bottle was closed. Three liters of LH_2 were enough to operate the target for several days. The refrigerator recondensed the hydrogen which boiled in the target flasks, thus returning it to the LH_2 reservoir. A feedback loop between a sense resistor and two heating resistors in the reservoir regulated the LH_2 temperature. In this way, we held the reservoir pressure at about 5 PSI (absolute) where LH_2 has a density of .0694 gm/cc. A change of about 1.5 PSI in the pressure produces only 1% change in the LH_2 density (Ref. 2-3).

The tent, vacuum jacket, and flask windows through which the beam

TABLE 2-2

HYDROGEN TARGET DATA

	LENGTH (or THICKNESS)	DIAMETER	IL#*	MATERIAL
	(Dimensions in Inches)			
UPSTREAM FLASK	15.8	2.5	.00025	.005 Mylar wall
DOWNSTREAM FLASK	8.0	3.0	.00025	.005 Mylar wall
SUPERINSULATION	.00025 (x90)		.00114	.00025 aluminized Mylar
BEAM WINDOWS -				
UPSTREAM	.005		.00025	.005 Mylar
DOWNSTREAM	.014		.00071	.014 Mylar
M3 COUNTER	.0625	1.0	.00318	Scintillation plastic
TENT WINDOWS	.1		.00508	Treated cotton
HYDROGEN	23.8		.08851	H_2 (liquid)

* Nuclear interaction lengths

passes constitute material from which the beam may scatter, just as from the LH_2 itself. This means that the target will scatter beam particles even if it is empty of LH_2. Typically only 3/4 of our event triggers originated in the LH_2 itself. By taking data with the target flasks full and empty of LH_2, we were able to correct for this effect.

Table 2-2 contains a summary of relevant dimensions of the hydrogen target. Included is a calculation of the number of nuclear interaction lengths (IL) of the various materials in the beam. There is a total of .0994 IL including the LH_2, of which .0885 IL is hydrogen. The remaining .0109 IL is made up of contributions from beam windows, insulation and so on. From this we can calculate the expected ratio of trigger rates for target-empty vs. target-full. The ratio of .11 is consistent with that found in the analysis of π^0 events, but not with the trigger rates above (see 2.4.3 PASS III Analysis).

2.2.3 Photon Detector

The novel feature of this apparatus was the photon detector (see Fig. 2-3). It enabled us to measure the momentum and energy of each individual photon striking it, making possible the exclusion of much of the background found in some π^0 production experiments (Ref. 2-4).

The detector was a series of horizontal (X) and vertical (Y) scintillation hodoscopes sandwiched between sheets of lead radiator. A high energy photon striking the front of the detector would develop into a shower of electrons, positrons and photons which was entirely consumed in the 19 radiation lengths (RL) of lead in the detector. The 70 element hodoscopes "sampled" the shower at 16 intervals in longitude (z), eight each in x and y. Light pipes combined the light of the eight longitudinal samples of each hodoscope into "fingers", yielding 140 (70 X

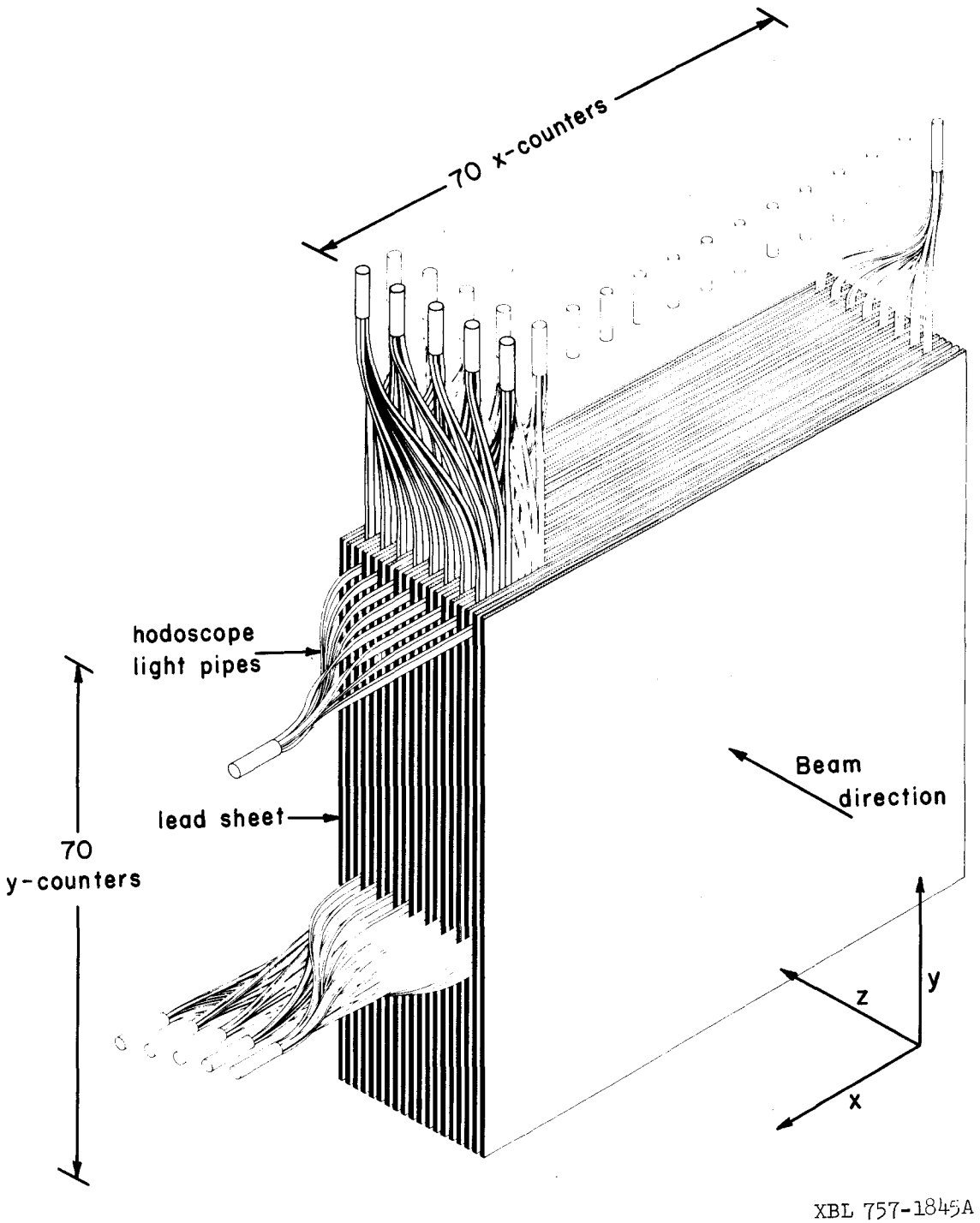

Fig. 2-3 Photon detector. There are 70 hodoscope counters for each view of the detector. Each counter has 8 scintillation fingers interleaved in the lead sheets. The counters integrate the showers in longitude (z).

and 70 Y) independent signals for each event. Each finger of the detector performed a two-fold integration: the X fingers integrate in y (the elements are vertical) and in z (eight scintillators go to one phototube).

Table 2-3 contains a summary of the detector dimensions and properties. Sampling the showers in fine gradations in depth, i.e., in 1 RL, yields the good energy resolution we obtained. Also, since each shower was sampled by several fingers transversely, we obtained good position resolution as well. (A shower centered in a finger typically put 60% of its energy in that finger and most of the balance in the adjacent fingers. However there was a trade-off here in that two showers centered in two adjacent fingers could not be separately resolved (see Supplement 2, Shower Process and Detector Resolution).

TABLE 2-3

PHOTON DETECTOR PROPERTIES

	PROPERTIES
POSITION RESOLUTION	.2 cm
TRANSVERSE SHOWER SPREAD (sigma)	1.4 cm
TWO-SHOWER SEPARATION	1.5 cm
ENERGY RESOLUTION	$.25/\sqrt{E[\mathrm{GeV}]}$
ENERGY RESPONSE UNIFORMITY	
- ALONG EACH FINGER	2%
- FINGER TO FINGER	2%

	LENGTH X WIDTH	THICKNESS
HODOSCOPE PLANE	73.5 cm x 1.05 cm (x70 fingers)	.7 (x8 fingers)
LEAD RADIATOR	75 cm x 75 cm	.64 (x19 layers)

Since we used the detector in the trigger it was extremely important that the energy response be as uniform as possible, both finger-to-finger and along each finger. This was not easy to obtain as others have experienced (Ref. 2-5). Pains taken in the construction of the detector ensured uniform response along the fingers, while the electron sweeps and source monitor system (see 2.3 Gathering Data) enabled us to set the gains of the counters and track their gain drift during the runs to an accuracy of about 2%.

The flat response of the detector along the length of the fingers was the result of four techniques worked out during the construction (Fig. 2-4). As is the usual practice, the surfaces of the plastic scintillators and light pipes were polished to give a good surface for total internal reflection, and a mirror was placed at the far end of the scintillator as a first step toward equalizing the response of the counter.

First, a yellow filter (Wratten 2E) at the phototube eliminated the effect of the short absorption length of blue light in the scintillator. Second, an angle filter (a black painted plastic bar) between the scintillator and the light pipe equalized the response by absorbing the wide-angle internally reflected light, probably because such light was especially susceptible to scattering by surface irregularities. Third, the small-angle light selection of the angle filter was preserved by the use of very gently curving light pipes of constant cross section, as opposed to wedge light pipes.

The fourth technique is unique: silkscreening a graded black pattern onto the aluminized Mylar wrapping fine-tuned the response. A local diminution of the scintillator response of up to 15% could be obtained by this method. It probably worked by absorbing some of the ultraviolet

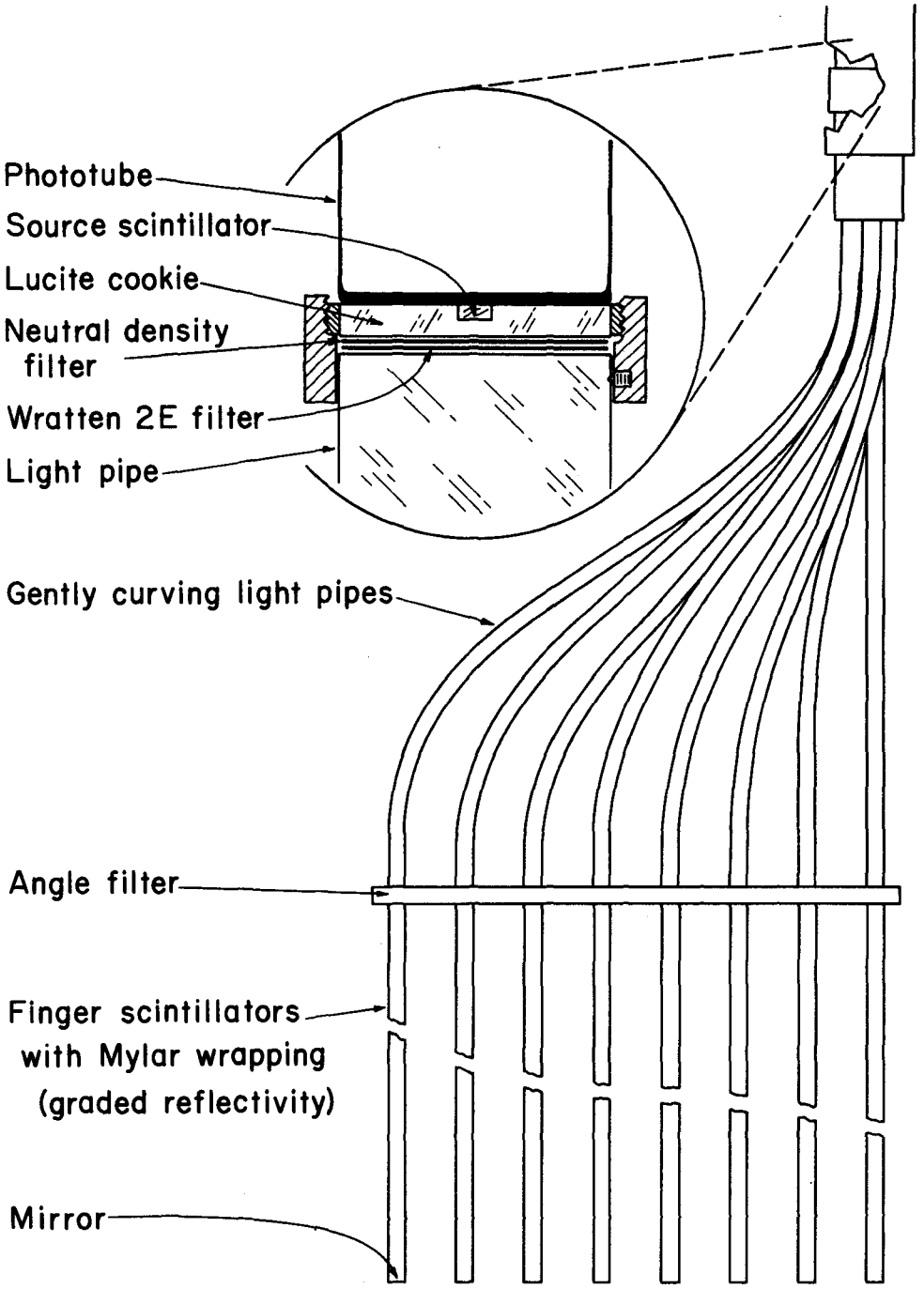

XBL 789-11375

Fig. 2-4 Detail of a photon detector finger. The source button and Lucite cookie are glued to the face of the phototube.

scintillation light which the wrapping would otherwise reflect back into the scintillator to be wave-shifted and re-emitted as visible light into the angular acceptance of the phototube. That we were able to equalize the response of scintillation rods 1 cm square and 70 cm long to 2% speaks for the power of this method (Ref. 2-6).

2.2.4 PPERP Trigger

As mentioned earlier, the trigger is a signal indicating that an event of interest has occurred, which we used to initiate the data-gathering equipment. It consisted of two parts; when both were present simultaneously, we had an event trigger. One part was the beam signal, "FLUX", which meant that a "clean" beam particle had entered the target. The second was the "DET" signal which indicated that the event had deposited more than a certain (threshold) amount of transverse momentum in the detector in the form of γ rays.

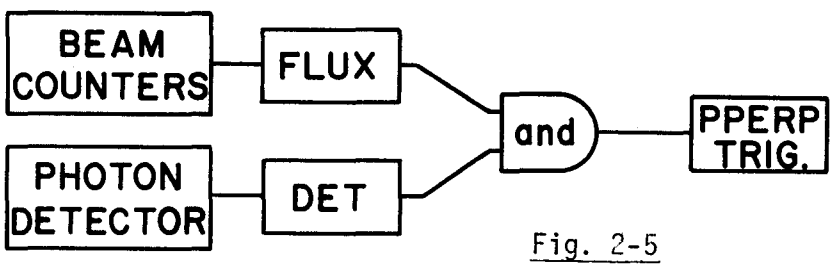

Fig. 2-5

The signal FLUX required first a three-way coincidence between M1, M2, and M3 called BEAM (see Fig. 2-6a). Double-sized pulses from either M1 or M3 indicated that two charged particles had passed through the respective counter. Discriminators marked 2xMIN were set to detect such pulses and vetoed the BEAM pulse at the coincidence ONEπ . It was important to exclude such events from the trigger since we wished to study only those events in which a single beam species (π, K or p) interacted in the target. There was naturally a high probability of receiving

ambiguous tagging information from the Cerenkov counters when two beam particles arrived simultaneously. Beam halo was detected by the AØ counter -- good beam particles passed through the hole -- and vetoed ONEπ at $1\pi\overline{A\emptyset}$. Beam particles within 50 ns before or after the particle of interest caused signals (EARLYπ and LATEπ respectively) which vetoed BEAM signals at the DTPI coincidence. This was done to ensure that the MPHA, which integrated signals from the detector over a 50 ns time span, did not also receive signals from events resulting from beam particles earlier or later than the one of interest. Photons in the beam halo (which might otherwise have caused spurious triggers by striking the detector) were vetoed by the A1 counter at the FLUX coincidence.

The radio frequency (RF) structure of the beam was such that the particles arrived in groups called "buckets", separated in time by 18 ns. Inside each bucket, they were bunched to within 1 ns of each other. Since our electronics could resolve pulses to much better than 10 ns, we could treat each bucket separately.

This made it simple to implement the 2xMIN vetoes, since these were invariably in tight time coincidence with the M1 (and therefore BEAM) signal. We also took advantage of the RF structure in the DT signal, which was made to, in effect, exclude events where there was a signal from M1 in any of the three buckets preceeding or following the BEAM coincidence.

In summary, the requirement for a FLUX signal can be expressed by the simple Boolean logic equation:

$$\text{(2-1)}\quad \text{FLUX} = (\text{M1}\cdot\text{M2}\cdot\text{M3})\cdot\overline{(2\text{xMINM1}+2\text{xMINM3})}\cdot\overline{\text{A}\emptyset}\cdot\overline{(\text{EARLY}\pi+\text{LATE}\pi)}\cdot\overline{(\text{A1A}+\text{A1B})}$$

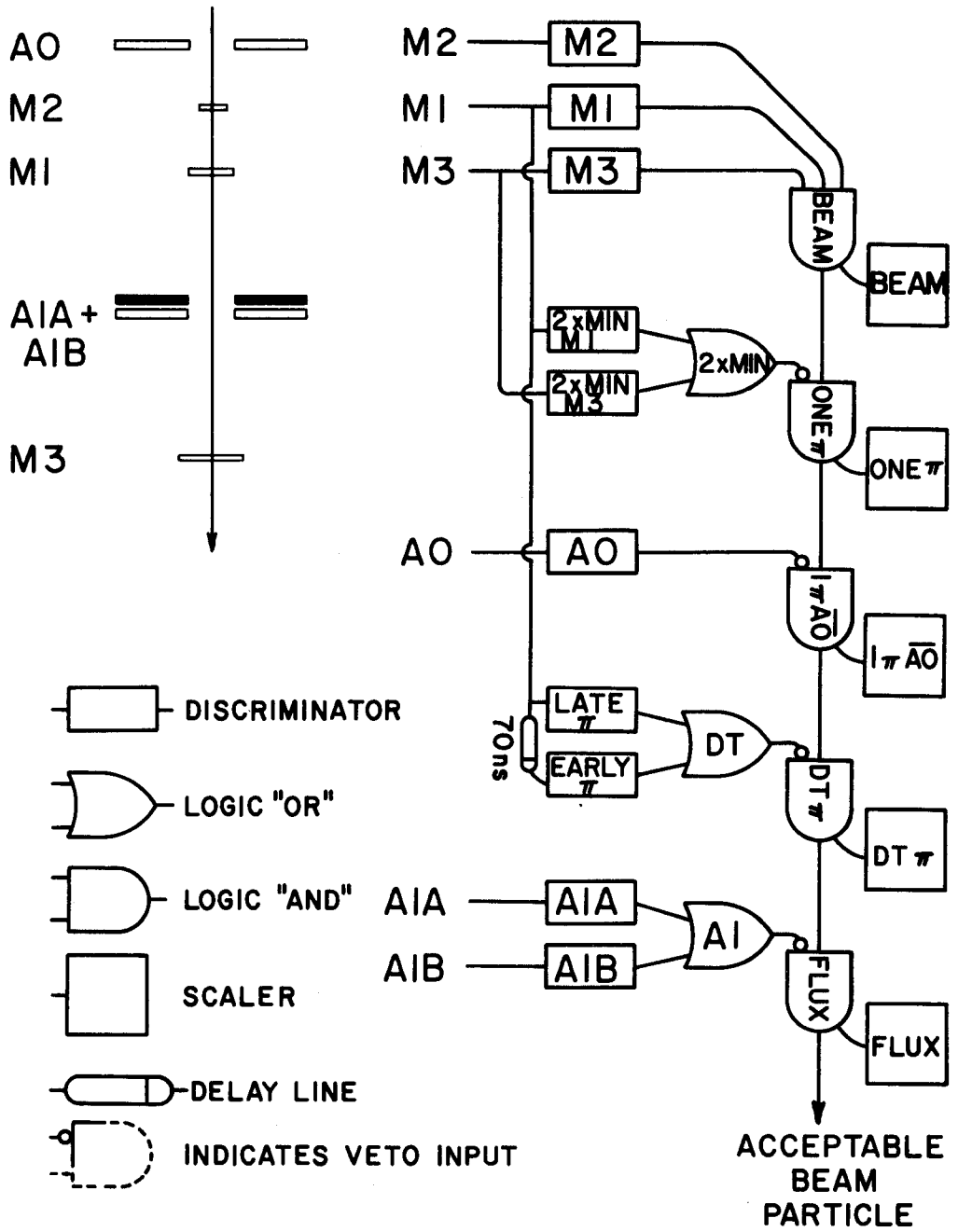

TRIGGER ELECTRONICS
FLUX LOGIC

XBL 789-11369

Fig. 2-6a Trigger electronics, FLUX logic. In Boolean logic notation:

$$FLUX = (M1 \cdot M2 \cdot M3) \cdot \overline{(2xMINM1 + 2xMINM2)} \cdot \overline{(A\emptyset)} \cdot \overline{(Late_{\pi} + EARLY_{\pi})} \cdot \overline{(A1A + A1B)}$$

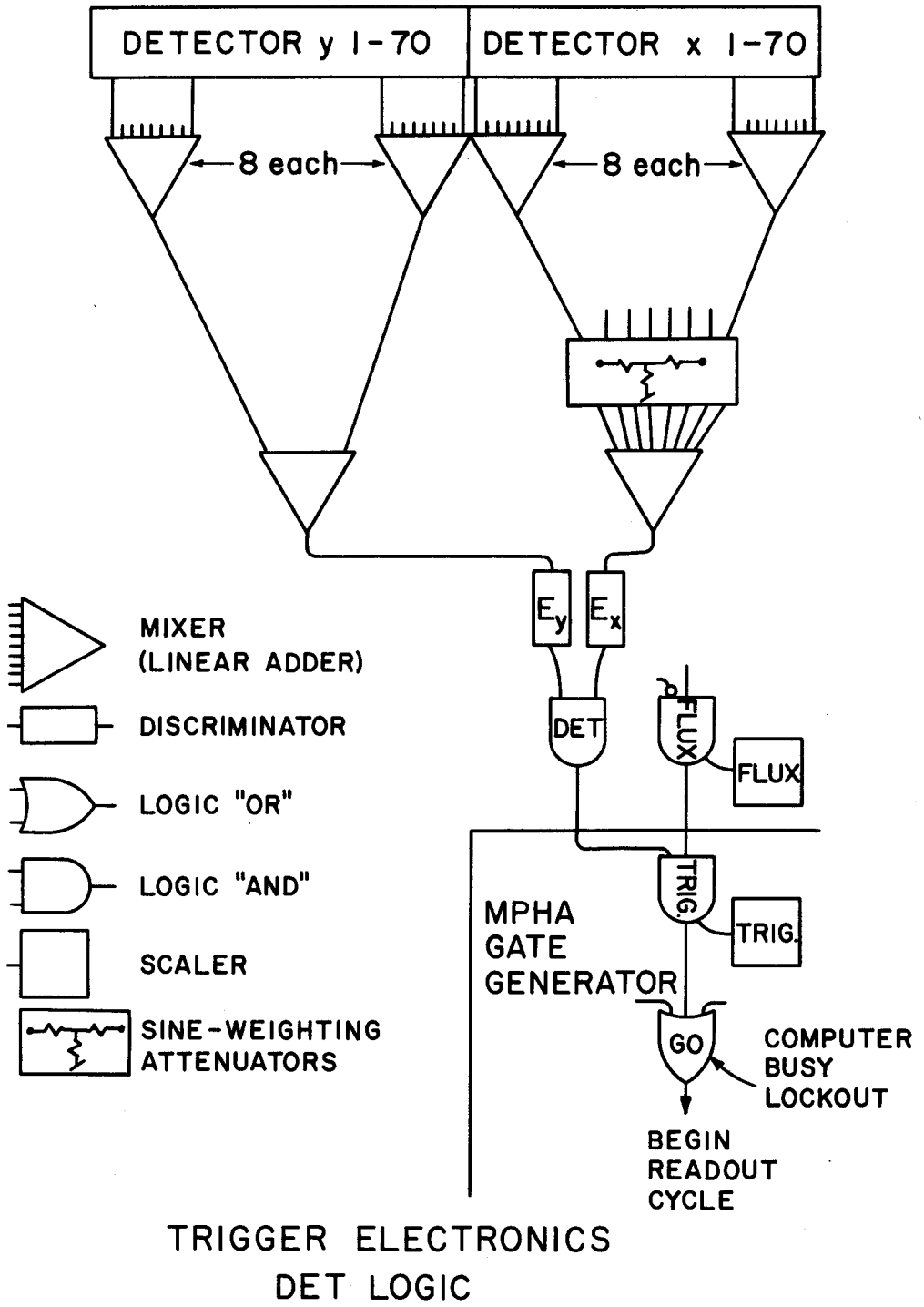

XBL 789-11377

Fig. 2-6b Trigger electronics, DET logic. The signal Ex is proportional to the total $P_\perp$ of photons in the detector.

The "DET" half of the trigger (see Fig. 2-6b) worked in the following way. Signals from each counter in the detector are proportional to the energy E_γ of photon striking that counter. The 70 X counters in the detector were summed in eight groups (seven groups of 9 counters plus one group of 7 counters). Each of these signals then passed through an attenuator which effectively weighted the pulse with the average sine of the laboratory angle $\sin\theta_L$ of that group of counters in the detector. Since $P_\perp = E_\gamma \sin\theta_L$, these pulses are proportional to the transverse momentum of the photons in the respective group. Then another summing circuit (MIXER) added the eight resulting pulses, yielding a single pulse E_x, whose height was roughly proportional to the total transverse momentum of photons in the detector.

At the same time, and in a similar way, all 70 Y counters were summed to form E_y, proportional to the total energy of photons in the detector. We required both E_x and E_y to be greater than a preset bias. The E_y signal was used in addition to the E_x signal to eliminate events in which the energy seen in the Y view was far less than the energy in the X view. We believe that such events were due to charged particles striking the source buttons (see Section 2.3, Gain Monitor System) in the X counters nearest the beam line.

The two components of the trigger, FLUX and DET, combined in the MPHA Gate Generator to produce a trigger. If the computer was not busy (e.g., reading in a previous event), a readout cycle would begin. At low biases, however, the trigger rate would saturate the computer's data-handling capacity. In this case, only a sample of the potential triggers would be recorded.

A bank of scalers totalized pulses from the fast electronics, as shown in Fig. 2-6a and 2-6b. Scaling at each successive stage of coincidence enabled us to see how much each cut down our counting rate. We monitored the ratios of successive scalers from run to run as a check on the stability of our apparatus. The ratio of TRIGGERS/FLUX was the raw trigger rate of the experiment and entered into the eventual calculation of the cross section. This permitted us to compensate for the computer dead time at low biases (see 2.4.3, PASS 3).

2.2.5 Data Assembly

The data for each event consisted of several parts from the various counters in the apparatus (see Fig. 2-7). The detector information, in the form of pulses from the phototubes, went to the MPHA (Multi-Pulse Height Analyzer) which digitized the pulse integral. We derived two signals from each phototube by splitting the signal at the anode. One went via the MIXERS to the trigger electronics while the other, appropriately delayed by an additional length of coaxial cable, went to the MPHA for digitization. The anode signal was integrated on a capacitor over a 50 ns time interval, then digitized by the standard constant-current run-down method. A similar device, the BPHA* did the same job the Cerenkov counter signals.

The UX/Y and DX/Y hodoscopes simply set bits in "Bit Boxes", while the scaler information was already in digital form. On a signal from the SIGMA II computer, these data were assembled by a Data Assembly Box which then transferred the data to the SIGMA II. Event data (including

---

* for historical reasons dubbed the "Banana" Pulse Height Analyzer

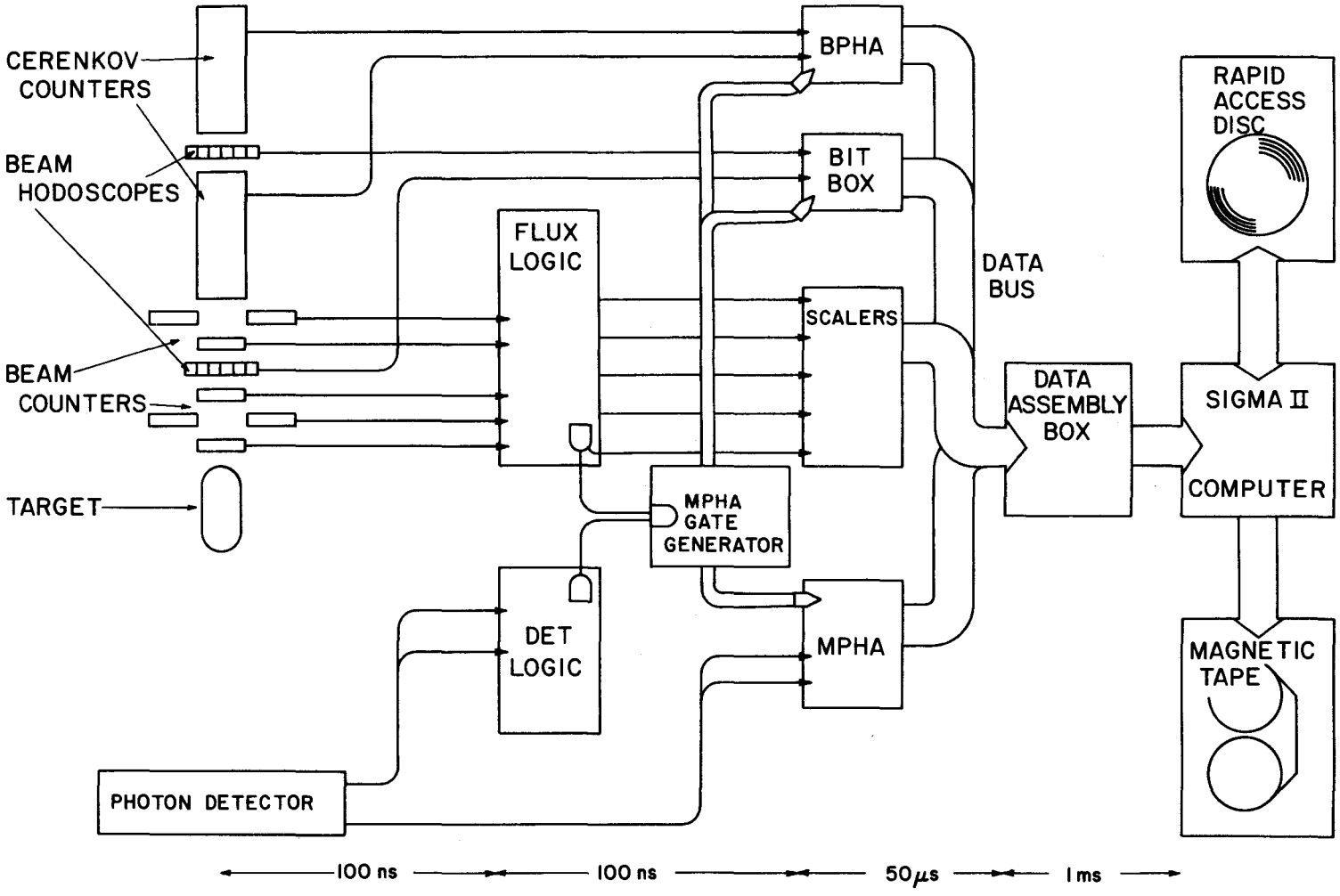

Fig. 2-7 Data assembly. See text. XBL 789-11381

date-time, run number and event number) were then stored on a Rapid Access Disc (RAD) during the beam spill, then spooled to magnetic tape at the end of spill. About 80 events could be recorded for each spill in this way. Figure 2-7 also shows the approximate time delays associated with each step. There was a progressive reduction in the data transfer rate as the information proceeded from the counters to the computer to the magnetic tape.

2.3 Data Gathering

This section discusses the various types of data-taking involved in the experiment. Calibration of the detector gains, the correspondence between pulse height and energy in the detector, took place in Electron Sweeps at the beginning and end of each - typically 4-week - data-taking session. Periodic Flux runs revealed the relative amounts of the various particle types in the beam. Naturally most of the time was spent in taking scattering data with the PPERP trigger previously described. By setting the discriminator biases of E_x and E_y at three different levels, we took data covering overlapping ranges in $P_\perp$. Concurrent with the above, we accumlated data on the pedestal response of the detector and, with a special gain monitoring system, on the gain drifts of the detector.

We calibrated the detector by sweeping an electron beam over its face both horizontally and vertically for X- and Y views. The electron beam was obtained by triggering the apparatus on the approximately 7% electron content of the 100 GeV/c negative beam. For this we filled the downstream Cerenkov counter with helium to just below pion threshold; thus only electrons* were sensed. The trigger further required a count

* The small amount of muons in the beam was not important.

in either an X- or Y counter of a special survey hodoscope placed directly in front of the detector. The detector itself was moved in one-finger increments and data taken with the beam centered on each finger of each view. An on-line program written by Alan Barnes (Ref. 2-7) gave the relative gains of each counter at the end of the sweep. Typically at the beginning of a data session, we ran the sweeps several times for each view, adjusting the individual counter gains via the phototube high voltages until the gains were all within a few percent of a target figure. We then re-ran the sweeps at the end of the session to determine the gains once more and relied on the gain monitor system as described below to track individual counter gains during the intervening data-taking.

Once every data tape, we took a short Flux run, the trigger of which was identical to that of a PPERP run except no detector signal was required. We triggered on every good beam particle regardless of whether or not it scattered in the target. Later we analyzed the Cerenkov counter information (see 2.4.5, Cerenkov Analysis) to determine the beam fraction of each type of beam particle for use in calculating the cross sections.

We selected in general three $P_\perp$ biases for our regular data-taking. In the 90° region, the lowest gave useful data above a $P_\perp$ of about 1 GeV/c; the middle bias filled in between the region where the low bias data was statistics-limited and where the high bias data was useable. We selected the high $P_\perp$ bias so that at the largest beam rates (1-3MHz), the computer was just barely saturated. Later in the analysis, we combined the data from different biases, averaging the points where they overlapped (Fig. 2-15).

Aside from proton beam data at 300 GeV/c at 90°, we took data at both beam polarities at 100 and 200 GeV/c in two kinematic regions, 90°- and 30°. At 100 GeV/c, we also took data near 10° (see Tab. 2-4).

TABLE 2-4

DETECTOR SETTINGS

Beam momentum [GeV/c]	Detector angle in cm	Angular range in cm	Detector-to-target L [m]	Detector-to-beam D [m]	Integrated luminosity, FT (Eq.2-8) [events/1E-32cm^2] $p/\bar{p}$	K^+/K^-	π^+/π^-
100	90°	48° - 116°	5.	.69	18. / 0.96	1.6 / 1.0	46. / 41.
	30°	15° - 52°	16.4	.68	57. / 2.2	4.4 / 2.5	160. /100.
	10°	2° - 20°	16.4	.10	8.6/ 1.5	0.7 / 1.7	23. / 61.
200	90°	51° - 114°	7.7	.74	180. / 2.8	5.0 / 7.5	46. /160.
	30°	16° - 55°	22.	.68	290. / 1.9	6.7 / 6.0	77. /190.
300	90°	43° - 121°	7.5	.61	6.8		

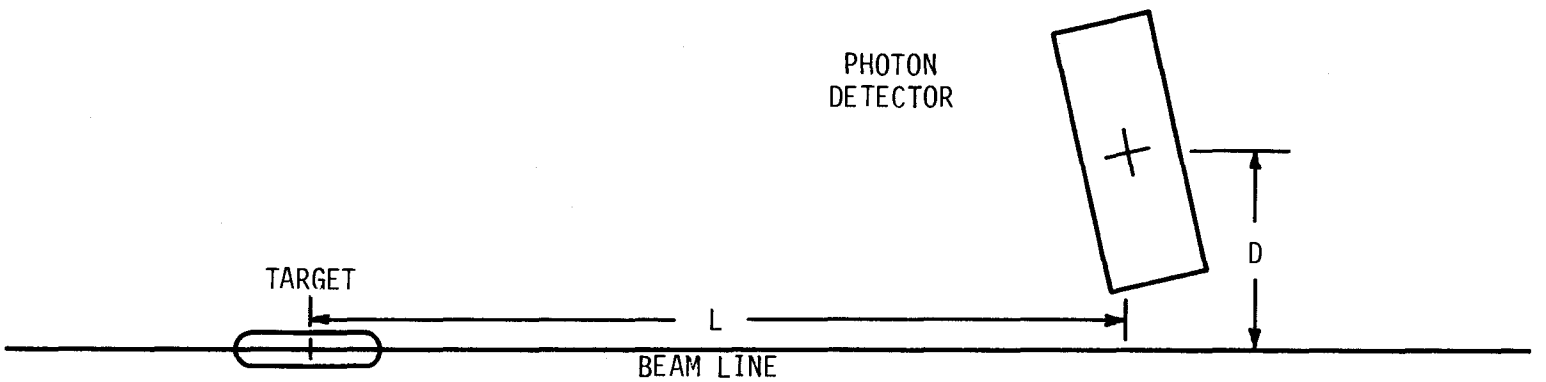

As Fig. 2-15 shows, these angular regions nearly overlap, thus giving our experiment good coverage of the forward-scattering region for two beam energies.

Pedestal Monitor

The gain monitor and pedestal data accumulated concurrently with other kinds of data-taking. Triggers were accepted during the monitor period - the first one or two seconds after the spill ended - when the detector was quiescent. The time between spills was usually from 7-10 seconds. Pedestal triggers were generated by an oscillator, showing the MPHA's response in the absence of a pulse from the detector. A built-in current source at each MPHA channel input, which was always present in order to give a more linear response for very small signals, caused a non-zero output from the MPHA, typically about 40 MPHA "units". Pedestal drift usually reflected a change in the respective MPHA channel, due to temperature change or malfunction. The width of the pedestal pulse height distribution for a single channel was about 1/2 unit; a larger width usually could be traced to 60Hz-induced noise ("hum"). As the pedestal was "added on" to the pulse from the detector, it was necessary to subtract this before the data was analyzed. Pedestal runs, which occurred several times on each data tape, provided us with the information we needed to make this subtraction.

Gain Monitor System

The gain monitor system served to track the gains of the individual phototubes as a function of time. The gains did change noticeably due to a number of factors, the most important of which seemed to be the repeated exposure of the phototube to the large amounts of light from the

photon showers themselves (Ref. 2-8). What we hypothesized is that in the phototubes the individual electrodes accumulated slowly dissipating stray charges which distorted the phototube's electric fields. We have noted both a fall and rise of several percent as the gains drift.

The heart of the gain monitor system was a small source-and-scintillator-button arrangement glued to the front of each phototube in the detector (see Fig. 2-4). The source (Bi^{207}) is a beta-ray emitter and gives a pulse height spectrum with a large peak (Fig. 2-8). For each counter, the approximate location of the peak, SRCPK was stored in a table on the RAD and was used to supply limits, as shown, between which the pulse heights were averaged (Ref. 2-9).

We implemented the SOURCE trigger by combining the sixteen first-stage MIXER signals (each MIXER had two outputs) in an independent pair of MIXERs. A special pair of discriminators with amplified inputs then detected the tiny pulses due to the source buttons and triggered the apparatus during the monitor period. Figure 2-8 shows the trigger bias to be well below the peak. After enough SOURCE triggers were accumulated, the averages were calculated and written to the magnetic tape to be processed off-line. Any drift in the gain of a phototube would be reflected in a like change in the position of that counter's source peak and thus in the value of the source average SRCAVG.

Figure 2-9 shows the correspondence between SRCAVG and PEAK, where PEAK is the location of the maximum in Fig. 2-8. As the shape of the BI^{207} spectrum is independent of the counter, this curve applied to all counters. Over the region of good correction shown, it is possible to infer the value of PEAK by inverting the function. We find the following formula is valid to better than 2%:

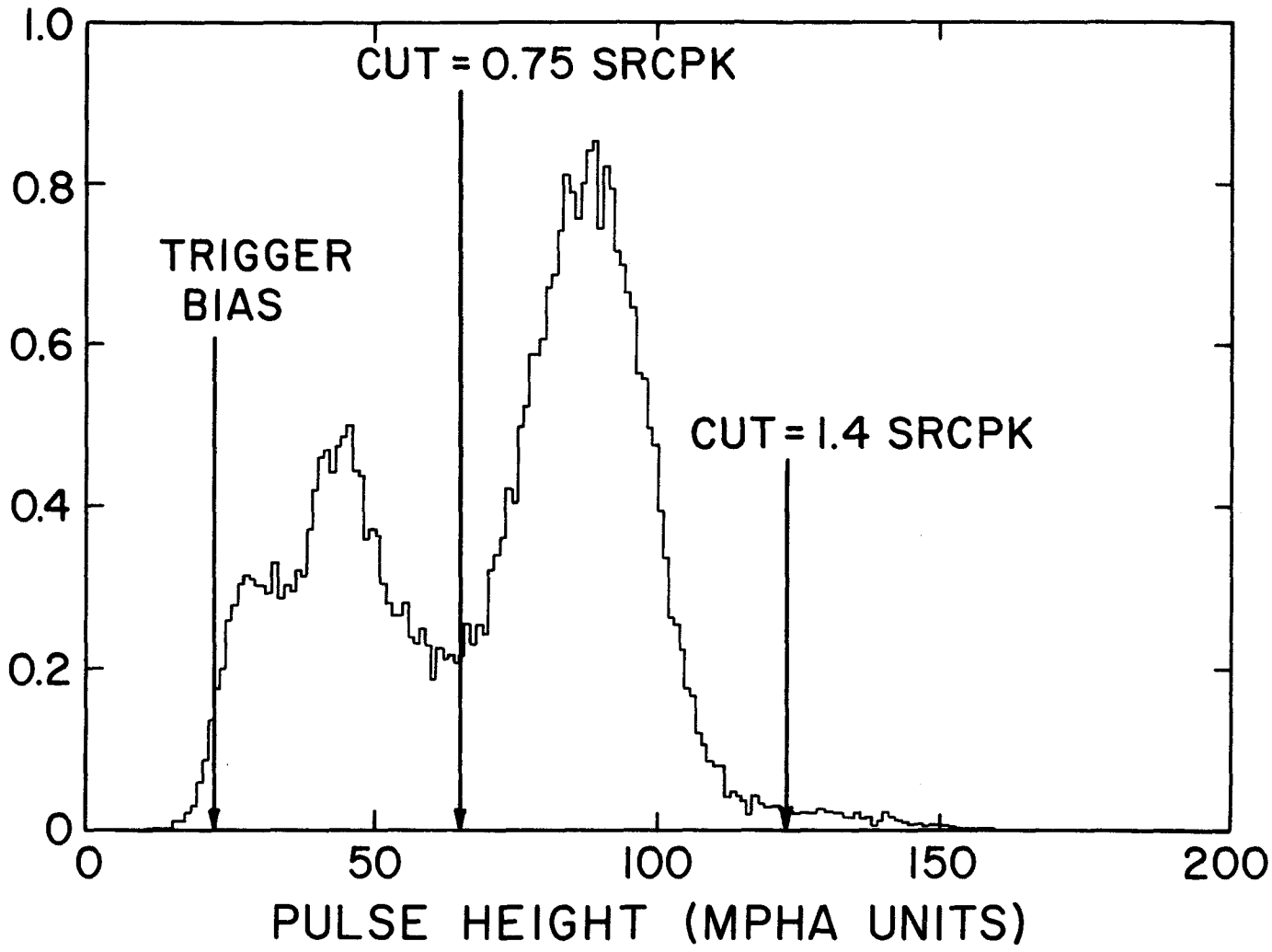

Fig. 2-8 Bi^{207} spectrum as seen in the source buttons. Limits of summation for the Source Monitor program are shown. XBL 789-11367

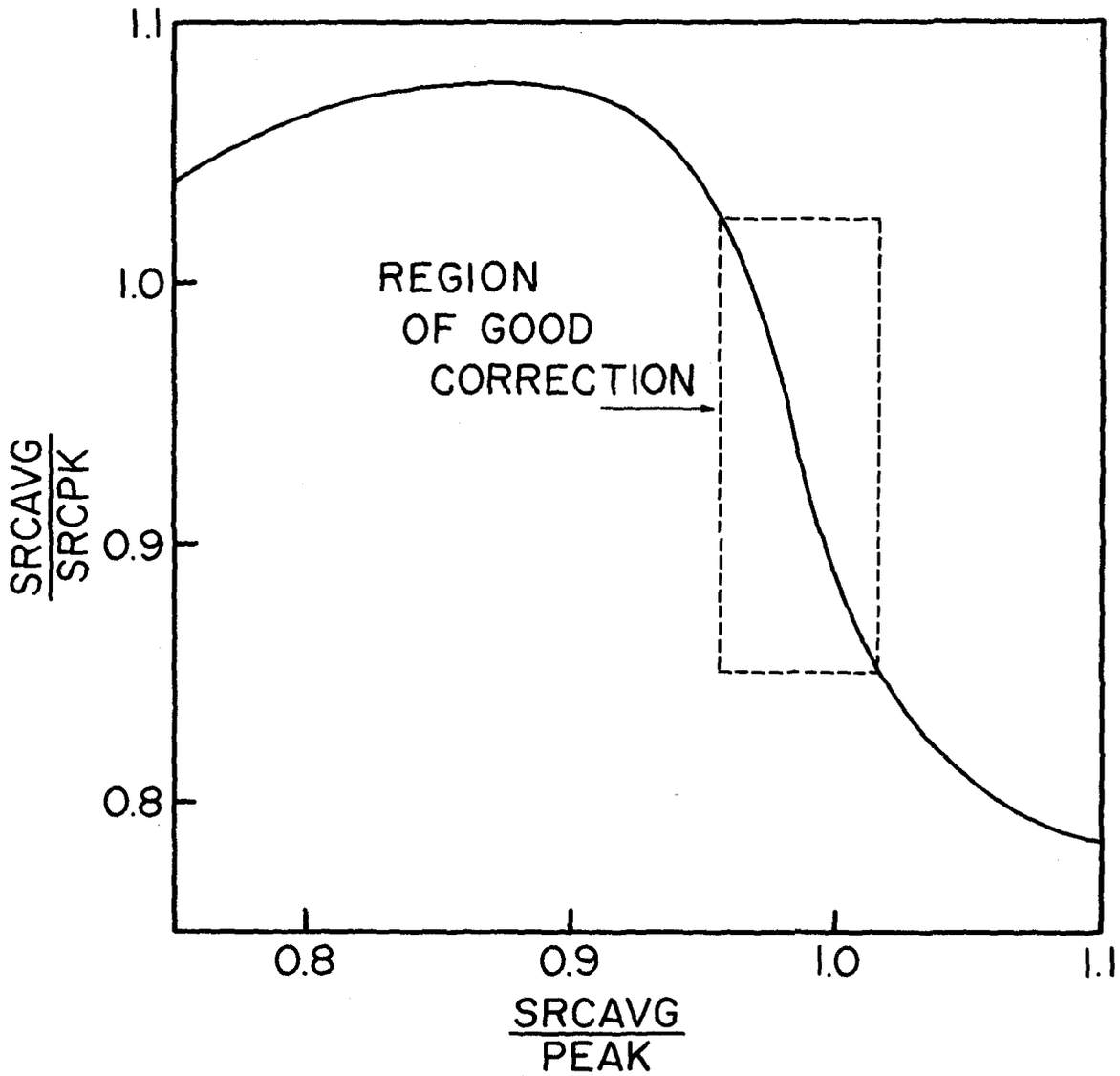

XBL 789-11376

Fig. 2-9 SRCAVG/SRCPK versus SRCAVG/PEAK. In the region of correction shown, the value of PEAK can be recovered from SRCAVG and the known value of SRCPK.

(2-2) PEAK/SCRAVG = .324*SRCAVG/SRCPK + .711

The off-line analysis consisted of finding for each counter the value of PEAK using the known values of SRCPK which were on the RAD and SRCAVG which was on the tape. Thus each counter had a history of PEAK values, starting with those recorded during the first electron sweep PEAKØ and ending with those recorded during the last. For any intermediate in the data session, we would compensate for the gain drift of each counter by using the current value of PEAK for that counter. Before each event was analyzed, we subtracted the current pedestals and then multiplied the pulse heights by the current values of PEAKØ/PEAK. Thus the counter gains in effect return to those values obtained during the first sweeps. By comparing the compensated gains of the counters as determined by the last sweeps in the data-taking session to the gains determined by the first sweep, we can gauge the effectiveness of this prescription. Typically, they agreed to within 2%.

2.4 Data Analysis

As this was an inclusive experiment, we wished to carry out the analysis in as general a way as possible in order to detect π^0's and other neutral particles such as η and ω, even amidst the multiphoton background. Our goal was to reconstruct completely the positions and energies of the photons in the detector and only then construct a hypothesis as to the type of parent particle which may have decayed into them.

The data analysis proceeded in several steps or passes. The input to the entire process was the raw data tapes and the output was the invariant cross sections. PASS 1 determined the position and energy of the showers seen in each view of the detector. PASS 2 matched the two views and calculated the four-vectors of the photons in the lab frame.

PASS 3 histogrammed the mass of photon pairs for the bins in P and $x_{\parallel}$, then calculated the number of π^0's in each bin by fitting the histograms. In the final calculation of the cross sections, we used the results of the Monte Carlo program to correct for the apparatus efficiency and the results of the Flux analysis to calculate the flux of each beam particle.

2.4.1 PASS 1, Fitting Showers

PASS 1 considered each view of the detector separately. Before any processing, the pedestals were subtracted and the gains compensated as described in Section 2.3. Figure 2-10 shows the X-view of the detector for a typical event. The prominent peaks are photon showers as seen from the top of the detector. Near finger #5 is the signal which a typical minimum ionizing charged particle would leave.

As a first step, PASS 1 searched out the peaks - defined as a local maximum above a pulse height threshold - and obtained a preliminary estimate of the shower energy, proportional to the integrated size of the peak and its position in the detector. The energy E was approximately proportional to the sum of the largest pulse height h_0 plus those of the two adjacent counters h_{-1}, h_1:

(2-3) $$E = k_E(h_{-1}+h_0+h_1), \qquad \text{where } k_E \text{ is a constant}$$

The position was estimated by taking the shower to be centered on the finger with the pulse height h_0 with a correction Δx amounting to:

(2-4) $$\Delta x = (h_1-h_{-1})/h_0, \qquad \text{in finger units}$$

The next step was to fit the entire view with showers of canonical shape but adjustable height and position, using as preliminary values

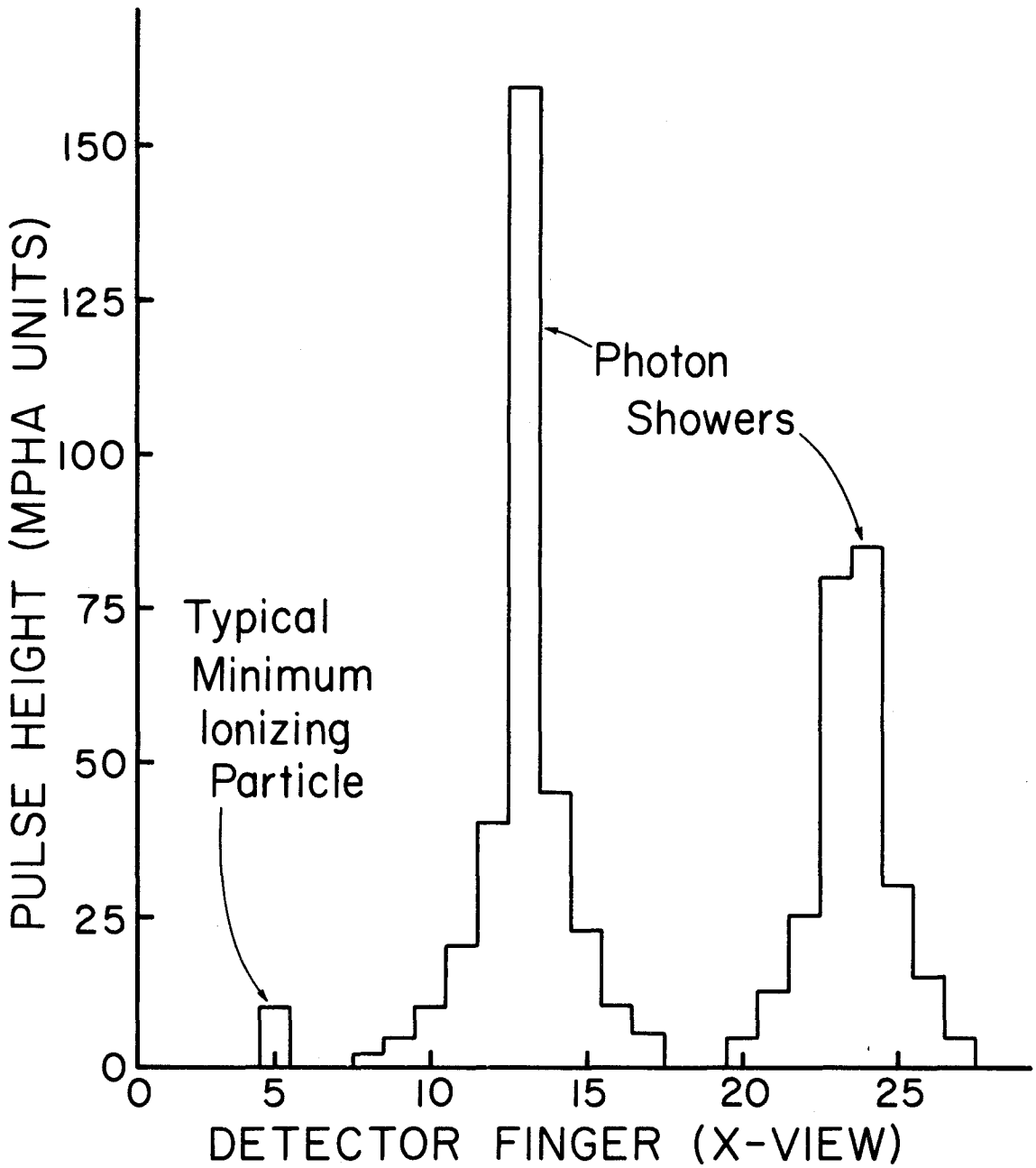

XBL 789-11379

Fig. 2-10 Detector X-view for a typical event. The response to a minimum ionizing particle appears at finger 5.

those estimated above*. The goodness of fit is measured by the χ^2:

(2-5) $\chi^2_{fit} = \sum_i (h_i - f_i)^2/f_i$, f_i is the value from the canonical shower, i ranges over all counters in the view

The heights and positions of the showers were adjusted to minimize the χ^2.

It was important to reject signals induced by charged particles in the detector. In the case of minimum ionizing particles as shown in Fig. 2-10, PASS 1 would not find a shower since the pulse height is too small. Particles which interact in the detector generally left fairly small showers which were eliminated in PASS 2 by the photon energy cut.

At this point, the detector information, which comprised the bulk of the information in an event, was summarized briefly as a list of shower heights and positions as determined by PASS 1. For each event, this list plus some beam information was written to a second tape for later processing by PASS 2.

2.4.2 PASS 2, Matching Showers

We did several cuts before proceeding in order to clean up the data. The border cuts rejected all showers within two fingers of the detector's edges. Since the showers were spread out in the detector over several fingers, there were, understandably, systematic errors in PASS 1's reconstruction of showers which spilled out of the detector.

Similarly, we determined from Monte Carlo simulations that showers separated by less than 1.5 fingers in a view (close pairs) had a large chance of being reconstructed by PASS 1 as a single shower. For this

---

* The canonical shape was $EXP(-2.04*c^2) + .278*EXP(-.618*|c|)$, with c = distance from center of shower in finger units.

reason, PASS 2 combined all shower pairs within two fingers of each other into single showers, but only in one view. We relied on the splitting process described below to correctly recover the original information if there had actually been two showers.

Matching

Nearly all of the events had either one or two photons. In an event with only two photons, there are two hypotheses for a match as pictured below. The figure of merit for a prospective match was:

(2-6) $\chi^2_{match} = \sum_i (EX_i - EY_i)^2 / (EX_i + EY_i)$ EX_i, EY_i - energy of shower i in X and Y views

i ranges over all showers in the event

From the figure it is clear that the better match gives the lower χ^2.

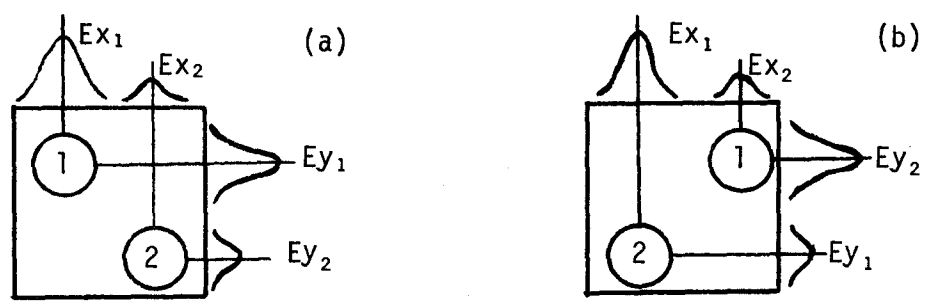

good match- low χ^2 poor match- high χ^2

Fig. 2-11a,b PASS 2, match

Splitting

In some cases the photons coalesced in one view as in the figure below. For these cases, PASS 2 would split the composite shower in proportion to the energies as seen in the opposite view. Since there is a minimum opening angle in π^0 decay (see Supplement S4), the photons should always be distinct in at least one view.

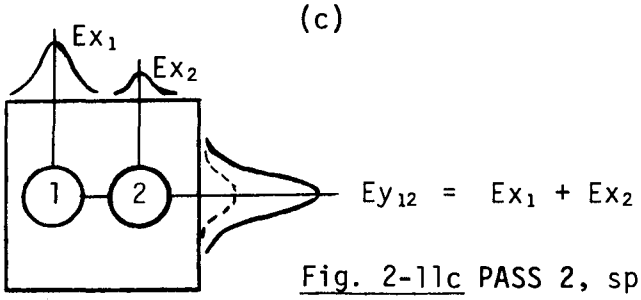

Fig. 2-11c PASS 2, split

Dropping

A third case to consider occurs when there is an extra shower in one view that cannot be accommodated either by matching or splitting. In this case the best course is often to simply drop the shower. Usually the shower had been seen quite well in one view but had been eliminated by the border cut in the other view as illustrated below. Sometimes, too, the extra shower was very small, probably an artifact of the peak-finding routines in PASS 1.

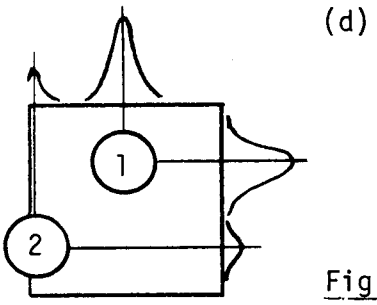

Fig. 2-11d PASS 2, drop

In cases where there were many photons in the event, this matching process could become quite complex. PASS 2 considered all different combinations of matches for three categories: (1) all showers in each view are matched with exactly one shower in the other view, a "complete" match; (2) one or more showers in one view are split between shower pairs in the other view; and (3) one or more showers are dropped. For each split or drop invoked, it "penalized" the χ^2_{match} by adding an appropriate amount to compensate for the attendant inevitable decrease in the χ^2_{match}.

We chose this penalty to maximize our overall efficiency for reconstructing π^0's. In all of the above combinations, it formed the χ^2_{match} for the entire event as in Eq. 2-6 and then chose the match with the best χ^2_{match}. In most events, the best match was a complete match; in a fair fraction of the events there were one or more splits or drops.

Once there was a complete picture of the showers in the detector, PASS 2 calculated the direction and energy (4-momentum) of the photons in the event. For this the program used its knowledge of the position of the detector relative to the beam and target for the run in question to extrapolate the photon's path from the target to the detector (details in Appendix 2, Kinematic Formulae.

At this point, all showers of energy less than 2.5 GeV were cut from the data. This had the effect of eliminating the π^0's with very asymmetric decays in a predictable way for the sake of the apparatus detection efficiency calculation (see 2.4.4, Monte Carlo).

2.4.3 PASS 3, Calculating the Number of Pions

The PASS 3 program determined the number of π^0's in each of the bins in $P_\perp$, $x_\parallel$. Typically, there were 30 such bins for each detector setting. We then used these numbers to calculate the final cross sections averaged over the bins.

For each event, PASS 3 calculated the necessary kinematic parameters (as described in Appendix 2). For the cross section calculation, these were the invariant mass m, transverse momentum $P_\perp$ and scaled longitudinal momentum $x_\parallel$ of all photon pairs in the event.

Since the data were taken with a $P_\perp$ trigger bias, we needed to figure out at what value of $P_\perp$ the trigger was fully efficient for each trigger bias. We did this by comparing the $P_\perp$ spectra of the data sets as in Fig. 2-12a. This led to the choice of a software $P_\perp$ cut for each bias

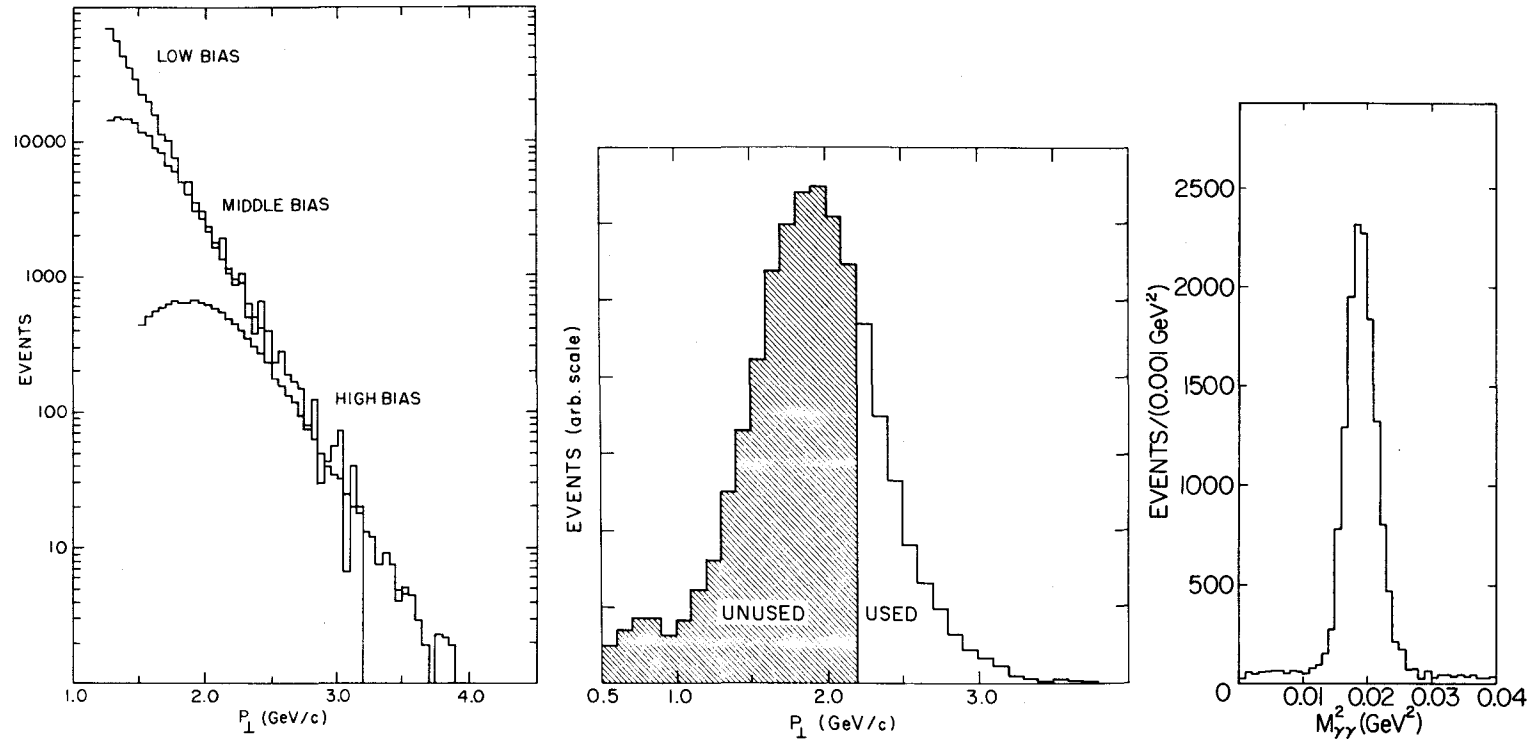

XBL 789-11436

Fig. 2-12 Plots of data: a) $P_\perp$ spectra of data sets for three different trigger biases; b) the software $P_\perp$ cut used in the analysis; c) invariant mass spectrum for photon pairs with target empty data subtracted.

such that the data above the cut agreed with the data from the next lower bias. Figure 2-12b illustrates the $P_\perp$ cut for a typical high bias data set. Unfortunately, the effect was to eliminate about two-thirds of the data at each bias.

We selected the photon pair with the highest $P_\perp$ as most likely to be a π^0. This was done to reduce the combinatorial complexities in events with high photon multiplicities. Events with two photons, of course, present only one choice for the photon pair. Events with higher multiplicity represent between .25 to .05 of the total events depending on the detector setting. For these, the efficiency of the selection averaged about .75. The overall inefficiency of reconstructing π^0's using the high $P_\perp$ pair selection was between .005 and .10, averaging .03.

The high $P_\perp$ pairs were then entered in invariant mass histograms, one for each $P_\perp$, $x_\parallel$ bin for which we wish to calculate the cross section. Each event was compensated for apparatus inefficiency by weighting it with the quantity $1/E_{ff}$, as described in 2.4.4, Monte Carlo. In addition, PASS 3 weighted the events by certain kinematic factors in order to effect the calculation of the average cross section. Data taken with the target empty of hydrogen were entered with negative weights in order to correct for the events originating in the target flasks. Their weights are in proportion to the effective flux taken with target full versus target empty: F_{FULL}/F_{EMPTY} as in Eq. 2-10.

The resulting mass plots show a large Gaussian shaped peak corresponding to the π^0 (see Fig. 2-12c). We determined the number of weighted π^0's $N^W_{\pi^0}$ by fitting with a Gaussian, plus a quadratic polynomial to represent the background. Thus we have:

$$(2\text{-}7) \quad N^W_{\pi^0} = N_{FULL} - N_{EMPTY} - N_{BKGD} \pm \sqrt{(\sigma^2_{FULL} + \sigma^2_{EMPTY} + \sigma^2_{BKGD})}$$

Where N_{FULL} represents the number of weighted events for target full running in the π^0 region ($.010 < m^2[GeV^2] < .025$) with uncertainty σ_{FULL}. The corresponding numbers for target empty running are N_{EMPTY}, σ_{EMPTY} N_{BKGD}, σ_{BKGD} give the events and uncertainty for the background.

Typically, N_{EMPTY}/N_{FULL} was from .10 to .25 depending on the detector setting and bias. The target empty/target full raw trigger rate ratio of .25 and ratio of material interaction lengths of .11 (see 2.2.2, Target) each fall somewhere in the range of N_{EMPTY}/N_{FULL} but we cannot reconcile the three figures with each other. We do not completely understand what is happening here, but part of the explanation may lie in triggers caused by interactions upstream of the target. Supposedly, these would occur whether or not there was hydrogen in the target and would not need a large production angle if the vertex were upsteam in one of the beam counters. Of course, π^0's produced by upstream interactions would be reconstructed with a mass systematically higher than that of the π^0 since the decay vertex would be so much farther upstream than the target.

The value N_{BKGD}/N_{FULL} ranged from .05 to .10 and was systematically lower at higher $P_\perp$. We believe that much of this background came from decay photons each coming from two different π^0's. Such uncorrelated photon pairs would give a fairly flat mass spectrum.

The final cross section calculation was carried out for over 250 different $P_\perp$, $x_\parallel$ bins for each of three different beam particles of each beam polarity. The formula we used was:

$$\text{(2-8)} \qquad \left.\frac{Ed^3\sigma}{dp^3}\right|_{AV} = N_{\pi^0} < \frac{E}{2\pi P \; P_0 E_{ff}} > /(FT\Delta x_\parallel \Delta P)$$

$\left.\frac{Ed^3\sigma}{dp^3}\right|_{AV}$ - invariant cross section, averaged over the bin [$cm^2/(GeV^2/c^3)$]

N_{π^o} - number of π^o events under the mass peak (target empty and background subtracted)

$N_{\pi^o} < \frac{E}{2\pi P_\perp P_o E_{ff}} >$ - number of weighted π^o's, $N^W_{\pi^o}$ (Eq. 2-7)

F - effective flux of beam particle (see Eq. II.D-7)

T - density of scattering centers in target (see Eq. II.D-7) [$1/cm^2$]

$\Delta x_{\parallel}\Delta P$ - area of $x_{\parallel}$ P bin

< weight > - average weight of the events - [$1/(GeV/c^2)$] $N^W_{\pi^o}/N_{\pi^o}$

Factors in the event weight:

E - π^o energy in the cm [GeV]

$P_\perp$ - π^o transverse momentum [GeV/c]

P_o - π^o maximum momentum in the cm [GeV/c]

E_{ff} - apparatus detection efficiency for the P and $x_{\parallel}$ of the event

In this formula the target density is:

(2-9) $T = N_{AV}\, DL/A$

N_{AV} - Avogadro's number (= 6.0221 E23) [1/gm]

D - mass density of liquid hydrogen (= .0694) [gm/cm^3]

L - length of target (= 60) [cm]

A - atomic weight of hydrogen = 1.007

The effective flux F is defined by:

(2-10) $$F = f \cdot N_{EVENT} N_{FLUX} / N_{TRIG}$$

f - fraction of this type of beam particle in beam (see 2.4.5, Flux Analysis)

N_{FLUX} - total beam flux for this data set (from FLUX scaler, see 2.2.4, Trigger)

N_{EVENT} - total number of events recorded by the SIGMAII for this data set

N_{TRIG} - total triggers for this data set

This formula shows how we compensated for computer dead time. The raw trigger rate is N_{TRIG}/N_{FLUX}, while N_{π^o}/N_{EVENT} represents the fraction of good π^o events in a random sample of triggers. Thus the cross section should be proportional to the product of these two ratios.

The effect of our analysis was to compute the invariant cross section averaged over the $P_\perp$ $x_\parallel$ bin in the following way:

(2-11) $$\left.\frac{Ed^3\sigma}{dp^3}\right|_{AV} = \int_{bin} dx_\parallel dP_\perp \frac{Ed^3\sigma}{dp^3} / (\Delta x_\parallel \Delta P_\perp)$$

Note that $dx_\parallel dP_\perp$ is not an invariant volume element, although $dx_\parallel P_\perp dP_\perp$ is.

2.4.4 Monte Carlo Efficiencies

In our experiment, it was necessary to know the detection efficiency E_{ff} in order to calculate the cross sections. We calculated this by using a computer model of the apparatus and a Monte Carlo method of averaging over the kinematic parameters for many fine bins in $P_\perp$ and $x_\parallel$. Typically these bins were several times smaller than those used to bin the data for the cross section calculation. The computer model was based on the known positions and sizes of the components of the apparatus including the beam hodoscopes, target, and detector.

Apparatus Acceptance

To perform the Monte Carlo averaging, we selected the kinematic parameters of many events independently and according to appropriate distributions. We then determined whether each event would have been detected and whether it would have passed all the software cuts of our analysis. Table 2-5 shows the kinematic parameters and their distributions. In order to obtain an accurate average, we made the distributions a close approximation to the "correct" physics, except for those of $P_\perp$ and $x_\parallel$ since we wanted to calculate the detection efficiency as a function of precisely these two variables.

The ratio of π^0's surviving the analysis versus the number generated is the detection efficiency. The largest E_{ff} must be no bigger than the maximum azimuth subtended by the detector, typically .25 of 2π. The detector geometry also limits the range of cm polar scattering angle θ_{cm} which can be detected. The lab angles of the inner and outer edges of the detector correspond to values of θ_{cm} where the apparatus acceptance falls to zero. Figure 2-14 shows plots of E_{ff} for the apparatus geometry

TABLE 2-5

DISTRIBUTIONS OF KINEMATIC QUANTITIES

BEAM PARTICLE PARAMETERS	
UX, UY, DX, DY	flat across the hodoscope fingers
Beam energy	fixed, nominal beam energy
INTERACTION PARAMETERS	
Interaction vertex in target	flat along target length
$P_\perp$, $x_\parallel$	flat over the relevant bin
Azimuth, ϕ	flat over a sector including the detector solid angle
DECAY PARAMETERS OF THE π°	
$\cos\theta_{\gamma\gamma}$	flat, 0 to 1
decay azimuth, $\phi_{\gamma\gamma}$	flat, 0 to π

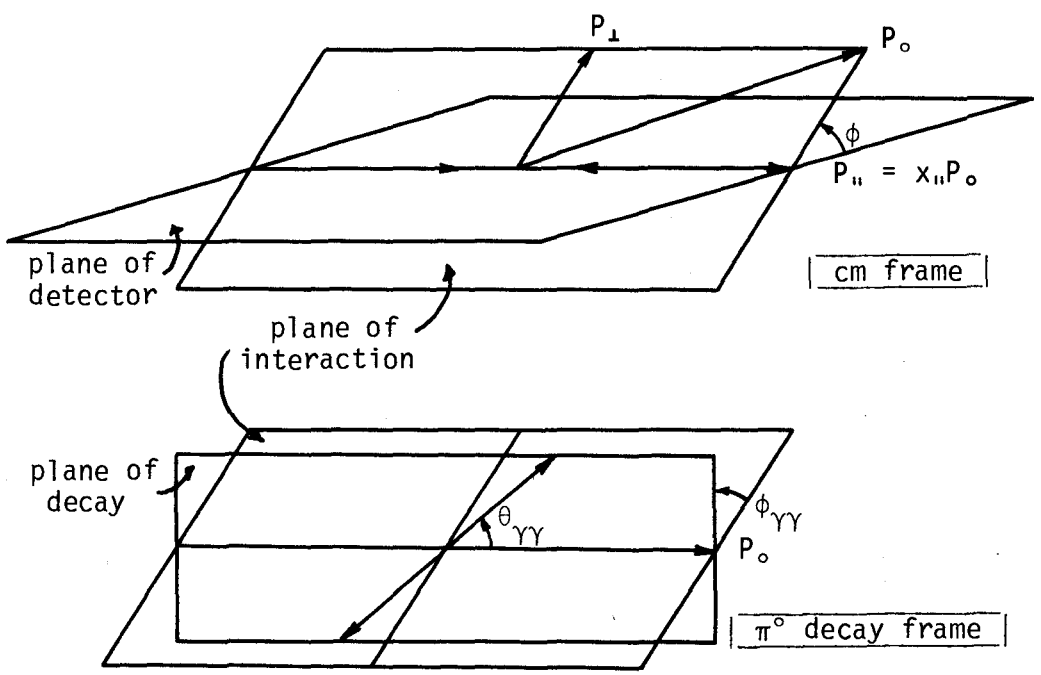

Fig. 2-13 Illustration of kinematic parameters used in Monte Carlo analysis.

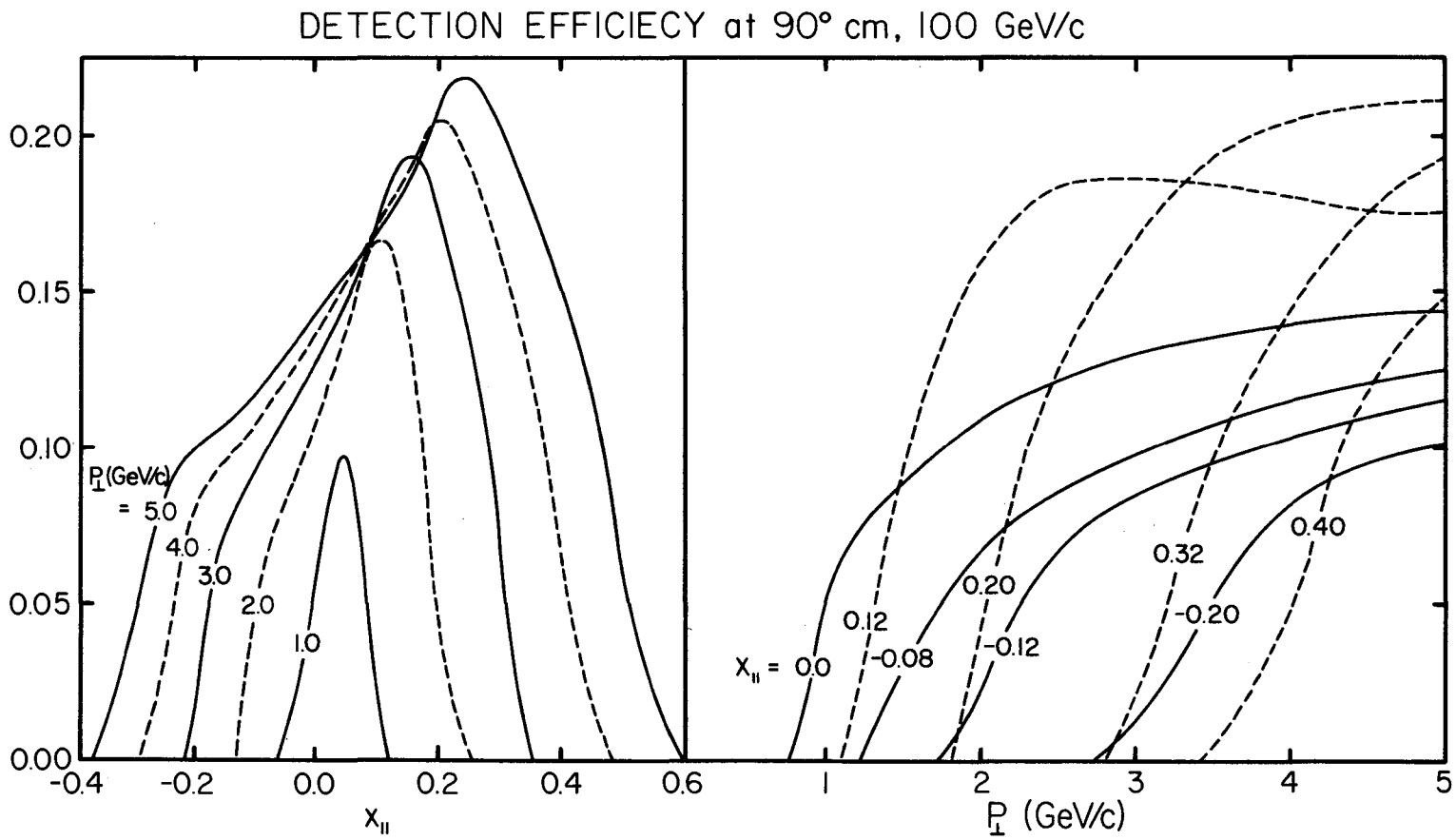

XBL 789-11385

Fig. 2-14 Geometric detection efficiency as determined by Monte Carlo analysis for 90° cm, 100 GeV/c beam momentum detector setting.

at 90° cm detector setting and 100 GeV/c beam momentum.

The maximum value of the efficiency E_{max} is about .22, consistent with the azimuthal angular range of the detector. At these values of E_{ff}, its uncertainty σ_E is about 2%. For lower values of E_{ff}, σ_E can be as high as 10 to 15%. In general $\sigma_E/E_{ff} = \sqrt{((E_{max}/E_{ff}-1)/N)}$ where N = 1000, the number of events generated for each bin. To find the E_{ff} at particular values of $P_\perp$ and $x_\parallel$, we interpolated between neighboring points. This introduced an error of - at most - 3%.

Apparatus Resolution

We also used an extension of this method to study the resolution of our experiment. We wanted to know how the $P_\perp$, $x_\parallel$ and mass were affected by various properties of the apparatus such as uncertainty in the production vertex position, beam hodoscope element size and statistical fluctuations of the showers in the detector. For this, the Monte Carlo generated the actual pulse heights as would be seen in real events in the detector using a canonical shower shape with Poisson-like fluctuations. These events passed through the analysis programs as would real events.

Table 2-6 shows the size of $P_\perp$, lab energy P_E, and 2γ mass^2 resolutions with various possible sources of finite resolution turned off or turned on. Case 1 is for zero target length and zero beam hodoscope width and no shower fluctuations; Case 2 for finite-size target and beam hodoscope; Case 3 for shower fluctuations and Case 4 for both. The mean $P_\perp$ was 1.2 GeV/c, the cm angle was 90°, and the beam momentum was 100 GeV/c. It is clear that shower fluctuation, which was the source of our finite photon energy resolution, was also the dominant source of our finite $P_\perp$ and mass resolution.

It was also possible to check for systematic shifts in the values of the kinematic quantities caused by the reconstruction programs themselves. We found these to be much less than the respective resolutions in all cases. The overall efficiency for two-photon events was consistent with that found by the simpler geometric Monte Carlo program.

TABLE 2-6

RESOLUTION OF THE APPARATUS
(100 GeV/c Beam, 90° cm)

	$\Delta P_{\perp}/P_{\perp}$	$\Delta P_E/P_E$	$\Delta m^2/m^2$	Sources of Resolution
Case 1	.015	.015	.035	None
Case 2	.043	.015	.059	Target length, Hodoscope width
Case 3	.043	.048	.130	Shower Fluctuations
Case 4	.10	.10	.17	Both

Average values $< P_{\perp} > = 1.2$ GeV/c, $< P_E > = 12$ GeV/c, $< m^2 > = .0182 \text{GeV}^2$

2.4.5 Cerenkov Analysis

The Cerenkov counters provided the identification of the beam particles in this experiment. Each of the two counters operated independently, and each counter could tag a beam particle as π, K or p. In all but one data set, a consensus between the counters was required; thus the beam particles were twice-tagged. The flux runs were analyzed to find the flux of twice-tagged particles and the respective contaminations.

These data also gave a value of the actual beam yeild for each beam particle (see Appendix 1, Cerenkov Counters).

Since each counter (CU-upstream, CD-downstream) had two phototubes (Inner and Outer), each event could have one of sixteen (2^4) signatures, depending on whether or not each phototube "saw" Cerenkov light for the event. The signature of an event CERBIT is an integer between 0 and 15 from the weighted sum:

$$\text{CERBIT} = \text{CUI} + 2 * \text{CUO} + 4 * \text{CDI} + 8 * \text{CDO} \tag{2-12}$$

where the value of each C-variable on the right side is 0 or 1 corresponding to a respective phototube pulse height less or more than 1/4 the level of the one photoelectron peak.

In the standard configuration, pions counted in CUO and CDO, kaons counted in CUI and CDI, and protons were below Cerenkov threshold. Thus the signature for twice-tagged particles were CERBIT = 10 for π, 5 for K and 0 for p. Certain other signatures have ready interpretations. For instance, a π event with CUO inefficient would give CERBIT = 8; a K event with stray light in CDO would give 13 and so on.

A histogram of CERBIT for the 200 GeV/c beam, 30° data, triggering on any beam particle, appears in Tab. 2-7, columns 1 and 5. The numbers $N^{+/-}(0,5,10)$ are large, while those corresponding to other signatures are small, as expected. The tagged beam fraction for π^+, for example, is simply the ratio of the tag sample $N^+(10)$ to the histogram total N^+_{TOT}. These numbers are the f's of Tab. 2-8 used in the cross section calculation (see Eq. 2-10). For instance, $f_{\pi^+} = N^+(10)/N^+_{TOT}$.

The tagged beam fraction f is equal to the actual beam yield F times the tagging efficiency P_{TOT}. To obtain these latter numbers requires the

TABLE 2-7

CERBIT DISTRIBUTIONS FOR 200 GeV/c Beam, 30° cm DATA

	COLUMN	1	2	3	4	5	6	7	8
	i	$N^{+}(i)$	$N_p(i)$	$N_K{}^{+}(i)$	$N_{\pi}+(i)$	$N^{-}(i)$	$N_{\bar{p}}(i)$	$N_K-(i)$	$N_{\pi}-(i)$
p	0	59848	59848	34	34	710	514	46	150
	1	907	639	266	1	432	6	422	5
	2	1135	652	2	481	2133	6	4	2123
	3	196	166	13	17	89	1	37	70
	4	136	0	133	3	195	0	182	13
K	5	1063	0	1063	0	1686	0	1686	0
	6	61	0	6	38	292	0	16	177
	7	52	0	51	1	151	0	145	6
	8	1457	303	11	1143	5053	3	13	5040
	9	164	3	86	41	291	0	121	168
π	10	16144	3	0	16144	71210	0	1	71210
	11	585	0	4	581	2378	0	11	2367
	12	115	0	42	91	443	0	51	422
K	13	342	0	339	3	493	0	479	14
	14	1288	0	2	1286	5970	0	5	5965
	15	68	0	16	46	335	0	41	198
	N_{TOT}	83561	61509	2042	19943	91870	527	3217	87967

more detailed analysis described below. This analysis yields the contamination of our tagged beam samples G_i as well as the probability of a counter to detect its assigned particle and the probability to register the wrong particle. These probabilities are P(1) for CUI, P(2) for CUO , P(4) for CDI, P(8) for CDO corresponding to the weight in Eq. 2-12. The subscript indicates the beam particle in question, e.g., $P_{\pi}+(8)$ is the probability for a π^+ to register in CDO. Note that $P_{\pi}(10)$, $P_{\pi}(8)$, $P_K(1)$ and $P_K(4)$ should be ~ 1, so they appear in the form $1-\varepsilon$ in Tab. 2-8 where ε is the inefficiency.

The numbers in columns 2-4 and 6-8 in Tab. 2-7 are the amounts of respective beam particles in each histogram bin, as inferred from the analysis. For instance the number of π^+'s in bin 10 is $N_{\pi}+(10) = 16144$.

The method used to calculate the probabilities in Tab. 2-8 and the self-consistent values for N_P, N_K, N_{π} in Tab. 2-7 used the $N^{\pm}(j)$ of Tab. 2-7, Eq. 12-13a and 2-13b following the steps outlined in Tab. 2-9. In short, Eq. 2-13a shows how to calculate the P's from the entries in the table where there is little or non contamination, e.g., signatures 1, 2, 4, 8, 10 are all π's. Then Eq. 2-13b enables a calculation of entries of Tab. 2-7 from the $P_i(n)$'s. For example, all the $N_{\pi}+(i)$ were calculated from $N_{TOT\pi}+$, $P_{\pi}+(1)$, $P_{\pi}+(2)$, $P_{\pi}+(4)$, $P_{\pi}+(8)$. The fact that some samples contaminated others dictated the special assumptions used in the method.

The first analyzed were the π and K samples between which there was little cross talk. The probabilities P_{π} and P_K were calculated from Eq. 2-13a and Tab. 2-7. As the protons represented a non-negligible fraction of $N^+(1)$, $N^+(2)$ and $N^+(8)$, it was impossible to independently determined $P_K+(4)$, $P_{\pi}+(8)$ and $P_{\pi}+(2)$, respectively. These probabilities are assumed equal to that of the corresponding negative particle (i.e.,

(2-13a)

$$P_\pi(1) = 1/(1 + N_\pi(10)/N_\pi(11)),\ P_\pi(2) = 1 - 1/(1 + N_\pi(10)/N_\pi(8))$$

$$P_\pi(4) = 1/(1 + N_\pi(10)/N_\pi(14)),\ P_\pi(8) = 1 - 1/(1 + N_\pi(10)/N_\pi(2))$$

$$P_{TOT\pi} = (1 - P_\pi(1))\ P_\pi(2)\ (1 - P_\pi(4))\ P_\pi(8),\ N_{TOT\pi} = N(10)/P_{TOT\pi}$$

$$f_\pi = N(10)/N_{TOT},\ F_\pi = N_{TOT\pi}/N_{TOT} = f_\pi/P_{TOT\pi}$$

$$P_K(1) = 1 - 1/(1 + N_K(5)/N_K(4)),\ P_K(2) = 1/(1 + N_K(5)/N_K(7))$$

$$P_K(4) = 1 - 1/(1 + N_K(5)/N_K(1)),\ P_K(8) = 1/(1 + N_K(5)/N_K(13))$$

$$P_{TOTK} = P_K(1)\ (1 - P_K(2))\ P_K(4)\ (1 - P_K(8)),\ N_{TOTK} = N(5)/P_{TOTK}$$

$$f_K = N(5)/N_{TOT},\ F_K = N_{TOTK}/N_{TOT} = f_K/P_{TOTK}$$

$$P_p(1) = 1/(1 + N_p(0)/N_p(1)),\ P_p(2) = 1/(1 + N_p(0)/N_p(2))$$

$$P_p(4) = 1/(1 + N_p(0)/N_p(4)),\ P_p(8) = 1/(1 + N_p(0)/N_p(8))$$

$$P_{TOTp} = (1 - P_p(1))\ (1 - P_p(2))\ (1 - P_p(4))\ (1 - P_p(8))$$

$$N_{TOTp} = N(0)/P_{TOTp},\ f_p = N(0)/N_{TOT},\ F_p = N_{TOTp}/N_{TOT} = f_p/P_{TOTp}$$

(2-13b)

$$N_i(\ 0) = N_{TOTi}\ (1 - P_i(1))\ (1 - P_i(2))\ (1 - P_i(4))\ (1 - P_i(8))$$

$$N_i(\ 1) = N_{TOTi}\ (\quad P_i(1))\ (1 - P_i(2))\ (1 - P_i(4))\ (1 - P_i(8))$$

$$N_i(\ 2) = N_{TOTi}\ (1 - P_i(1))\ (\quad P_i(2))\ (1 - P_i(4))\ (1 - P_i(8))$$

$$N_i(\ 3) = N_{TOTi}\ (\quad P_i(1))\ (\quad P_i(2))\ (1 - P_i(4))\ (1 - P_i(8))$$

$$N_i(\ 4) = N_{TOTi}\ (1 - P_i(1))\ (1 - P_i(2))\ (\quad P_i(4))\ (1 - P_i(8))$$

$$N_i(\ 5) = N_{TOTi}\ (\quad P_i(1))\ (1 - P_i(2))\ (\quad P_i(4))\ (1 - P_i(8))$$

$$N_i(\ 6) = N_{TOTi}\ (1 - P_i(1))\ (\quad P_i(2))\ (\quad P_i(4))\ (1 - P_i(8))$$

$$N_i(\ 7) = N_{TOTi}\ (\quad P_i(1))\ (\quad P_i(2))\ (\quad P_i(4))\ (1 - P_i(8))$$

$$N_i(\ 8) = N_{TOTi}\ (1 - P_i(1))\ (1 - P_i(2))\ (1 - P_i(4))\ (\quad P_i(8))$$

$$N_i(\ 9) = N_{TOTi}\ (\quad P_i(1))\ (1 - P_i(2))\ (1 - P_i(4))\ (\quad P_i(8))$$

$$N_i(10) = N_{TOTi}\ (1 - P_i(1))\ (\quad P_i(2))\ (1 - P_i(4))\ (\quad P_i(8))$$

$$N_i(11) = N_{TOTi}\ (\quad P_i(1))\ (\quad P_i(2))\ (1 - P_i(4))\ (\quad P_i(8))$$

$$N_i(12) = N_{TOTi}\ (1 - P_i(1))\ (1 - P_i(2))\ (\quad P_i(4))\ (\quad P_i(8))$$

$$N_i(13) = N_{TOTi}\ (\quad P_i(1))\ (1 - P_i(2))\ (\quad P_i(4))\ (\quad P_i(8))$$

$$N_i(14) = N_{TOTi}\ (1 - P_i(1))\ (\quad P_i(2))\ (\quad P_i(4))\ (\quad P_i(8))$$

$$N_i(15) = N_{TOTi}\ (\quad P_i(1))\ (\quad P_i(2))\ (\quad P_i(4))\ (\quad P_i(8))$$

where $i = p, K$ or π and $N(j) = N_p(j) + N_K(j) + N_\pi(j)$, for $j=0,15$

XBL 789-11439

$P_K+(4) = P_K-(4)$. Note the close agreement between the corresponding independently determined P's. With these probabilities known, Eq. 2-13b determined the entries in Tab. 2-7, columns 3, 4, 7, 8.

The next step was to calculate the N's for p and $\bar{p}$. We assumed the protons constitute the balance of the counts, i.e., $N^+ = N_p + N_K + N_\pi+)$. Then we calculated the P_p's. The corresponding probabilities for $\bar{p}$ were assumed to be the same as there was not sufficient information to determine them independently. This enables a new determination of $N_\pi-(2)$, $N_\pi-(8)$ and $N_K-(1)$, taking into account the amount of $\bar{p}$ in these categories.

The iteration proceeded by returning to the first step and carrying through the process again and again until the values stabilized. This took about three passes in all.

Table 2-8 presents the results of this analysis. The output of the calculations is the tagged beam fractions f_i, tagging efficiency P_{TOTi}, beam yield F_i and the contaminations g_i. The g_i are computed as a fraction of f_i, e.g., for the $\bar{p}$ beam $\pi_{\bar{p}} = N_\pi-(0)/N^-(0)$.

In considering the contaminations, we note that for all but the 200 GeV/c data at 90°, where the counter configuration was different, the only beam sample which was appreciably contaminated was the $\bar{p}$'s and in all but the 200 GeV/c data at 30°, only by K^-. A larger contamination at higher beam momentum was inevitable, since the counter configuration was squeezed between two conflicting criteria (large Cerenkov angle for π's and K's versus large separation between π's and K's). However a comparison of the 'cross over' possibilities $P_\pi(1)$, $P_\pi(4)$, $P_K(2)$, $P_K(8)$ between the two beam energies shows that the performance of the counters at higher beam energies was better for some and worse for others instead of being uniformly worse for all. We probably could have run with a

larger tipped mirror, giving better π and K detection probabilities, and still gotten good π/K separation (we certainly could have improved $P_K(8)$) and also better π/p separation (see Appendix 1).

All in all, we operated the counters fairly well, but there was room for improvement at 200 GeV/c beam momentum. Later users E-350 benefitted from our experience, obtaining even better results.

TABLE 2-9

FLOW CHART FOR CERENKOV ANALYSIS

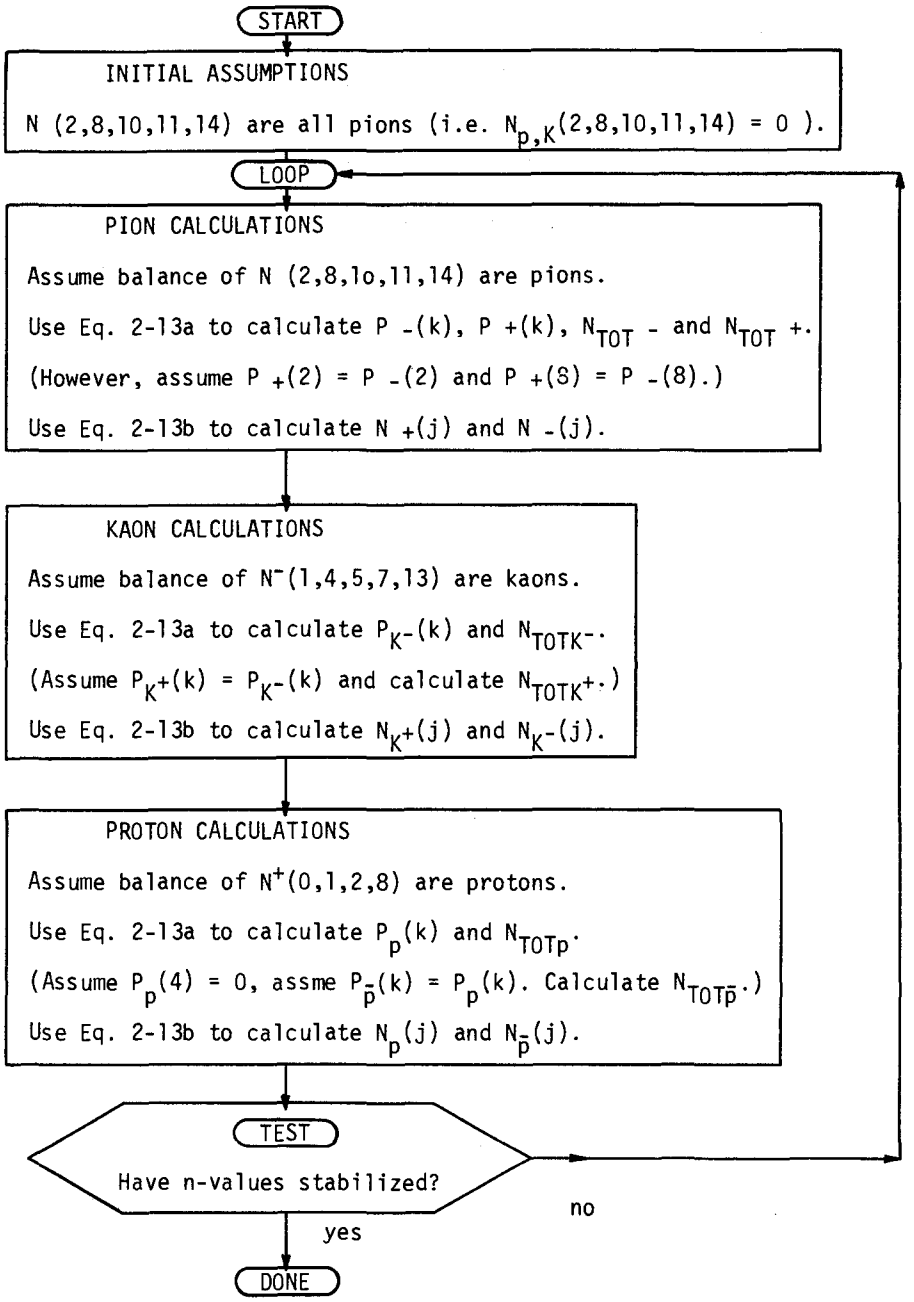

XBL 789-11438

TABLE 2-8

COUNTER PARAMETERS AND EFFICIENCIES

BEAM/ ANGLE	BEAM PARTICLE i	CERBIT	PROBABILITY TO COUNT IN: CUI $P_i(1)$	CUO $P_i(2)$	CDI $P_i(4)$	CDO $P_i(8)$	TAGGING EFFI-CIENCY P_{TOTi}	BEAM YIELD F_i	TAGGED BEAM FRACTION f_i	CONTA-MINATION g_i
	p	0	.0374	.1826	.0005	.0240	.768	.296	.222(2)	
	K^+	5	1-.0516	.1935	1-.1767	.0393	.605	.0327	.0197(5)	
100 GeV/c	π^+	10 or 8	.1141	1-.0123	.0160	1-.0107	.857	.670	.574(3)	
90°cm	p	0	.0374	.1826	.0005	.0240	.760	.0253	.0192(6)	$.013(2)K_{\bar{p}}$
	K^-	5	1-.0516	.1935	1-.1767	.0350	.608	.0350	.0212(7)	
	π^-	10 or 8	.0882	1-.0123	.0160	1-.0107	.881	.940	.828(4)	
	p	0	.0184	.1054	.0000	.0665	.820	.279	.229(2)	
	K^+	5 or 13	1-.2492	.1221	1-.1888	.0541	.535	.0329	.0176(5)	
100 GeV/c	π^+	10	.0531	1-.0126	.0151	1-.0037	.917	.689	.632(3)	
30°cm	p	0	.0184	.1054	.0000	.0665	.820	.0226	.0185(8)	$.08(1)K_{\bar{p}}$
	K^-	5 or 13	1-.2574	.1285	1-.1888	.0660	.525	.0400	.0210(8)	
	π^-	10	.0447	1-.0126	.0141	1-.0037	.927	.940	.871(5)	
	p	0 or 4	.012	.035	1-.246	.046	.910	.752	.684(3)	
	K^+	9	1-.175	.039	.022	1-.021	.759	.025	.0188(5)	$.050(5)\pi_{K^+}$
200 GeV/c	π^+	10	.054	1-.086	.051	1-.006	.816	.214	.175(2)	
90°cm	p	0 or 4	.012	.039	1-.437	.046	.906	.015	.0132(4)	$.08(1)\pi_{\bar{p}}$
	K^-	9	1-.175	.039	.022	1-.021	.759	.047	.0356(7)	$.20(1)\pi_{K^-}$
	π^-	10	.072	1-.108	.010	1-.012	.819	.947	.767(4)	
	p	0	.011	.011	.0003	.005	.973	.736	.716(3)	
	K^+	5 or 13	1-.111	.0458	1-.200	.242	.688	.0244	.0168(5)	
200 GeV/c	π^+	10	.0347	1-.066	.0738	1-.0290	.810	.239	.193(2)	
30°cm	p	0	.011	.011	.0003	.005	.973	.0079	.0077(3)	$.211(5)\pi_{\bar{p}}$ $.065(3)K_{\bar{p}}$
	K^-	5 or 13	1-.097	.0792	1-.200	.229	.073	.0352	.0237(6)	
	π^-	10	.0322	1-.066	1-.0773	1-.0290	.810	.958	.775(3)	

XBL 789-11440

2.5 Results

This section presents the results of this experiment, both absolute cross sections and beam ratios (ratio of π^0 production for different beams). There follows a discussion of various features of the data with an eye toward the interpretation of these features in the next chapter.

2.5.1 Cross Sections

Tables 2-10 and 2-11 give the value of the invariant cross section for the indicated beam particle and region of $P_\perp$, $x_\parallel$. Note that these represent the averaged cross sections as in Eq. 2-11. Where there existed data with commensurate errors from more than one bias setting, we averaged the numbers to obtain the tabulated result; otherwise we chose the data with the smaller error.

Cross sections for π^+,π^- and p beams appear on Tab. 3-10, while Tab. 3-11 sets forth those of all six beam particles but in much wider bins in $x_\parallel$. This was necessitated by our lower statistical sample of K and $\bar{p}$ beam events. In a given $P_\perp$ bin, the $x_\parallel$ ranges over the entire useable acceptance for the particular detector setting.

We corrected the data for some of the beam particles for a known amount of beam contamination. This correction amounted to solving a simple equation. If beam particle i has a measured cross section I_i with a beam contamination g_i, and the contaminant g has a cross section I_g, then the true cross section I_i' must satisfy:

$$(1-g_i)I_i' + g_i I_g = I_i \tag{2-14}$$

with a corresponding error σ_i' satisfying:

$$(1-g_i)\sigma_i' = \sqrt{((g_i\sigma_g)^2 + \sigma_i^2)} \tag{2-15}$$

The quoted errors combine the statistical error (based mainly on the counting statistics of N_{π^o}) with a floor relative error of 14% which is our estimate of the error due to triggering stability, error in the beam flux, etc. We used comparisons of data at adjacent $P_\perp$ bias settings as well as fluctuations in the ratio of π^+p and π^-p cross sections to give an indication of how large this error was. In cases where the statistical error was larger than 14%, we quoted only the statistical error.

An additional error not specified in the tables is the $P_\perp$ scale error. The source of this is largely the absolute energy calibration of the detector (2.5%) and to a smaller extent of the detector position survey (1%).

Figure 2-15 is a map of the kinematic boundaries of our experiment. It shows for each beam momentum, the approximate limits of each detector setting. Inside these limits appear the bins where we quote values for the cross sections. Each map is in the form of a Peyrou plot ($x_\perp$, $x_\parallel$ axes) with the equivalent $P_\perp$ shown to the right. Statistics limits our $P_\perp$ acceptance. We only approach the kinematic limit in the forward angle data where the cross sections are large.

Figure 2-16 shows the cross sections for $\pi^-p \rightarrow \pi^oX$(a and c) and $pp \rightarrow \pi^oX$ (b and d) for beam momenta 100 GeV/c(a and b) and 200 GeV/c(c and d). The data are plotted on a logarithmic scale versus $x_\parallel$ in bands of $P_\perp$. The smooth curves on the plots serve for the present to guide the eye. I discuss these in detail in the next chapter.

Figure 2-17 depicts the data for $\pi^-p \rightarrow \pi^oX$ at 700 GeV/c versus θ_{cm}. For this plot, we did not re-bin the data. The θ_{cm} bin corresponds, center and width, to the respective $x_\parallel$, $P_\perp$ bin. See Appendix 3 for a more complete set of $\pi\pm p$ and pp plots.

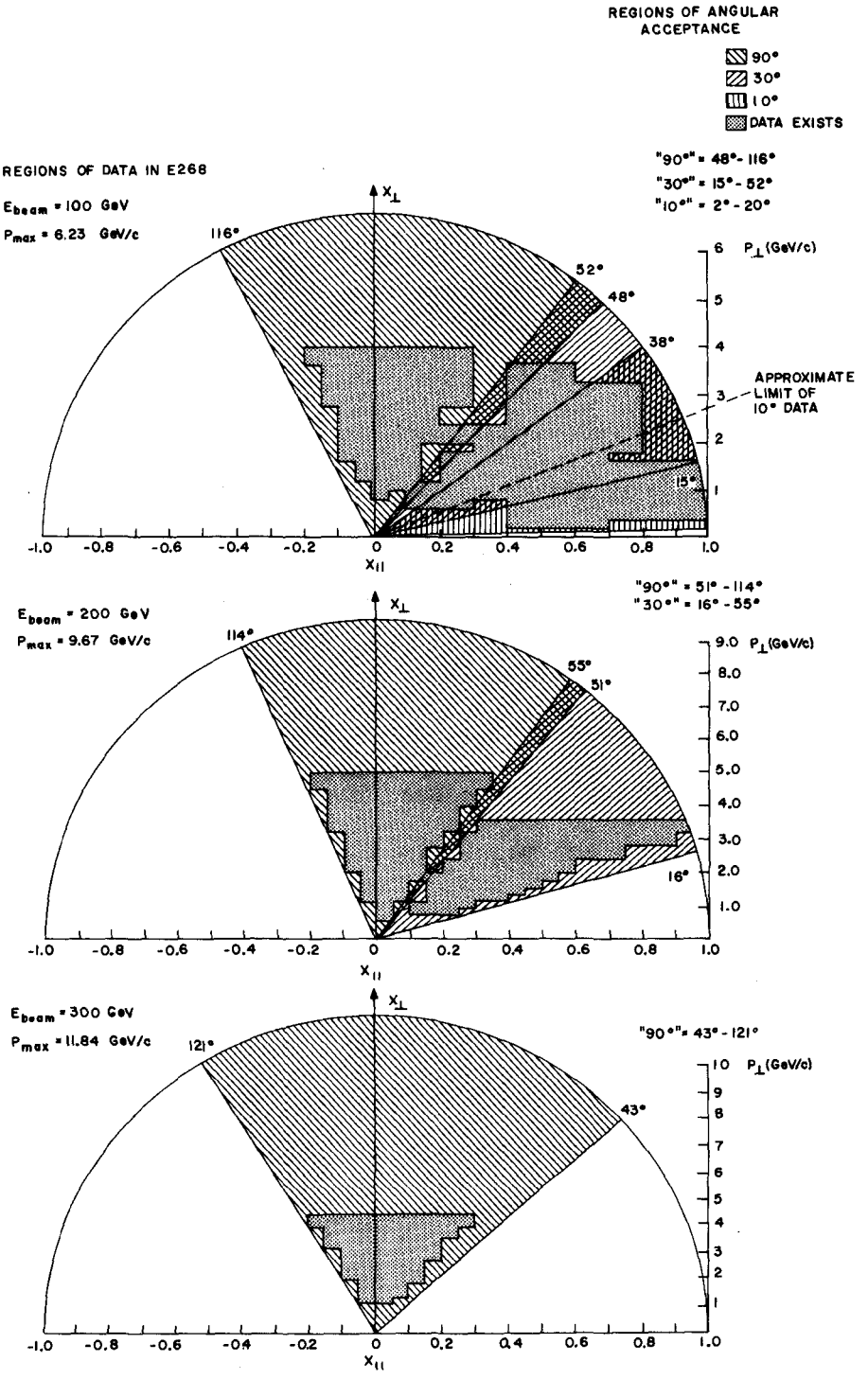

Fig. 2-15 Map of kinematic boundaries for three beam energies. The limits of detection efficiency appear in a Peyrou plot ($x_{\parallel}$, $x_{\perp}$ scales); a), b) and c) beam energy as shown.

TABLE 2-10 #1

$E \frac{d\sigma}{dp^3} \left(\frac{cm^2}{GeV^2}\right)$ for Beam + p → π^0 + X @ 100 GeV/c

$p_\perp$ (GeV/c)		$X_{\parallel}$		π^+	π^-	p
.2	.4	.40	.50	2.47(.35)E-27	2.06(.29)E-27	1.53(.24)E-27
		.50	.60	1.42(.20)E-27	1.71(.24)E-27	1.02(.14)E-27
.4	.6	.40	.50	1.01(.14)E-27	1.22(.17)E-27	4.59(.64)E-28
		.50	.60	6.76(.95)E-28	6.10(.85)E-28	3.21(.45)E-28
		.60	.70	3.68(.52)E-28	3.73(.52)E-28	1.58(.26)E-28
		.70	.80	2.39(.34)E-28	2.63(.37)E-28	1.58(.22)E-29
		.80	.90	1.77(.25)E-28	2.00(.28)E-28	3.46(.61)E-30
		.90	1.00	6.94(.97)E-29	9.17(1.28)E-29	
.6	.8	.15	.25	1.01(.14)E-27	1.20(.17)E-27	1.10(.15)E-27
		.40	.50	5.53(.77)E-28	6.80(.95)E-28	3.00(.42)E-28
		.50	.60	3.23(.45)E-28	3.95(.55)E-28	1.07(.17)E-28
		.60	.70	1.95(.27)E-28	2.15(.30)E-28	
		.70	.80	7.42(1.04)E-29	8.71(1.22)E-29	8.70(1.22)E-30
		.80	.90	4.14(.58)E-29	5.00(.70)E-29	2.59(.65)E-30
		.90	1.00	1.11(.16)E-29	1.22(.17)E-29	
.8	1.0	0.00	.05	2.31(.32)E-28		7.13(1.00)E-28
		.20	.30	3.14(.44)E-28	3.74(.52)E-28	3.13(.44)E-28
		.30	.40	2.75(.39)E-28	4.20(.59)E-28	1.99(.28)E-28
		.40	.50	2.27(.32)E-28	2.30(.32)E-28	8.32(1.47)E-29
		.50	.60	1.44(.20)E-28	1.88(.26)E-28	5.24(.73)E-29
		.60	.70	1.05(.15)E-28	1.15(.16)E-28	
		.70	.80	3.18(.45)E-29	3.75(.53)E-29	3.13(.44)E-30
		.80	.90	1.65(.23)E-29	2.07(.29)E-29	8.27(2.40)E-31
		.90	1.00	2.79(.39)E-30	3.37(.47)E-30	
1.0	1.2	0.00	.05	9.62(1.35)E-29	1.16(.16)E-28	1.84(.26)E-28
		.05	.10	1.11(.16)E-28	1.28(.18)E-28	1.78(.25)E-28
		.20	.30	8.58(1.20)E-29	1.10(.15)E-28	8.60(1.20)E-29
		.30	.40	8.86(1.24)E-29	7.43(1.05)E-29	6.46(.90)E-29
		.40	.50	7.34(1.03)E-29	7.94(1.11)E-29	3.00(.62)E-29
		.50	.60	5.87(.82)E-29	5.35(.75)E-29	
		.60	.70	3.18(.45)E-29	3.66(.53)E-29	
		.70	.80	1.20(.17)E-29	1.51(.21)E-29	1.12(.28)E-30
		.80	.90	6.40(.90)E-30	8.44(1.18)E-30	3.09(1.55)E-31
		.90	1.00	6.04(.96)E-31	1.10(.18)E-30	
1.2	1.4	-.05	0.00	2.15(.33)E-29	2.59(.36)E-29	4.55(.64)E-29
		0.00	.05	2.84(.40)E-29	3.20(.45)E-29	5.72(.80)E-29
		.05	.10	4.23(.59)E-29	4.78(.67)E-29	5.33(.75)E-29
		.20	.30	2.37(.33)E-29	3.29(.46)E-29	2.66(.37)E-29

Figures in parentheses are the one-σ error in the mantissa.

TABLE 2-10 #2

$E \frac{d\sigma}{dp^3} \left(\frac{cm^2}{GeV^2}\right)$ for Beam + p → π^0 + X @ 100 GeV/c

$p_\perp$ (GeV/c)		$X_{\parallel}$		π^+	π^-	p
1.2	1.4	.30	.40	2.38(.33)E-29	2.92(.41)E-29	1.74(.24)E-29
		.40	.50	1.94(.27)E-29	2.58(.36)E-29	9.60(1.34)E-30
		.70	.80	4.08(.57)E-30	4.64(.65)E-30	1.83(.92)E-31
		.80	.90	2.11(.30)E-30	2.07(.29)F-30	
		.90	1.00	1.81(.55)E-31	3.74(.94)F-31	
1.4	1.6	-.05	0.00	1.01(.30)E-29	6.06(2.00)E-30	1.49(.37)E-29
		0.00	.05	8.26(1.60)E-30	1.12(.16)E-29	1.37(.30)E-29
		.05	.10	1.10(.15)E-29	1.24(.23)E-29	1.81(.25)E-29
		.10	.15	1.33(.24)E-29		1.50(.48)E-29
		.20	.30	1.08(.15)E-29	1.58(.22)E-29	7.92(1.11)E-30
		.30	.40	8.39(1.18)E-30	1.04(.15)F-29	6.97(2.00)E-30
		.40	.50	5.84(.82)E-30	6.99(.98)E-30	3.27(.46)E-30
		.50	.60	4.86(.68)E-30	3.10(.43)E-30	9.99(4.00)E-31
		.70	.80	1.33(.19)E-30	1.76(.25)E-30	1.12(.68)E-31
		.80	.90	6.31(.88)E-31	6.14(.86)E-31	
		.90	1.00	5.20(3.12)E-32	6.51(3.91)F-32	
1.6	1.8	-.10	0.00	4.31(.60)E-30	3.53(.49)E-30	6.82(.96)E-30
		0.00	.05	4.63(.65)E-30	3.59(.50)E-30	6.60(.92)E-30
		.05	.10	4.26(1.20)E-30	3.96(.55)E-30	6.47(.91)E-30
		.10	.15	4.60(2.30)E-30	4.41(.62)E-30	7.74(1.08)E-30
		.30	.40	3.06(.43)E-30	3.12(.44)E-30	1.88(.26)E-30
		.40	.50	2.08(.29)E-30	2.15(.30)E-30	8.22(1.15)E-31
		.50	.60	1.21(.17)E-30	1.24(.17)E-30	2.43(.34)E-31
		.60	.70	9.21(1.29)E-31	1.15(.16)E-30	1.46(.23)E-31
1.8	2.0	-.10	0.00	1.69(.24)E-30	1.62(.44)E-30	2.77(.39)E-30
		0.00	.05	2.06(.29)F-30	1.87(.26)F-30	2.97(.42)F-30
		.05	.10	2.17(.30)E-30	1.63(.23)E-30	2.59(.36)E-30
		.10	.15	2.39(.34)E-30	2.01(.28)E-30	2.81(.39)E-30
		.30	.40	1.33(.19)E-30	1.31(.18)E-30	7.61(1.07)E-31
		.40	.50	9.50(1.33)E-31	9.74(1.36)E-31	3.33(.47)E-31
		.50	.60	5.43(.76)E-31	5.31(.74)E-31	1.16(.16)E-31
		.60	.70	2.99(.42)E-31	3.36(.47)E-31	2.98(.89)E-32
		.70	.80	1.39(.20)E-31	1.78(.25)E-31	2.38(1.19)E-32
2.0	2.4	-.10	0.00	5.21(.73)E-31	4.34(.94)E-31	5.85(.82)E-31
		0.00	.10	5.39(.76)E-31	4.85(.68)E-31	6.15(.86)E-31
		.10	.20	5.92(.83)E-31	6.53(.91)E-31	6.01(.84)E-31
		.30	.40	3.66(.51)E-31	3.94(.55)E-31	2.14(.30)E-31
		.40	.60	2.03(.29)E-31	2.03(.29)E-31	4.59(.64)E-32

Figures in parentheses are the one-σ error in the mantissa.

TABLE 2-10 #3

$E \frac{d\sigma}{dp^3} \left(\frac{cm^2}{GeV^2}\right)$ for Beam + p → π^0 + X @ 100 GeV/c

$p_\perp$ (GeV/c)		$X_{\parallel}$		π^+	π^-	p
2.0	2.4	.60	.80	5.19(.73)E-32	6.09(.85)E-32	4.92(1.72)E-33
2.4	2.8	-.10	0.00	7.22(1.01)E-32	9.33(1.31)E-32	9.49(1.33)E-32
		0.00	.10	9.26(1.30)E-32	8.91(1.25)E-32	1.00(.14)E-31
		.10	.20	9.80(1.37)E-32	8.21(1.15)E-32	6.74(.94)E-32
		.40	.60	3.15(.44)E-32	3.76(.53)E-32	6.85(2.06)E-33
		.60	.80	5.62(.90)E-33	1.13(.16)E-32	
2.8	3.2	-.15	.30	1.70(.24)E-32	1.78(.25)E-32	9.40(1.96)E-33
		.40	.60	4.70(.66)E-33	6.46(1.42)E-33	
		.60	.80	1.46(.51)E-33		
3.2	3.6	-.15	.30	2.89(.83)E-33	5.56(2.00)E-33	2.59(.52)E-33
		.40	.60	1.34(.67)E-33		
3.6	4.0	-.20	.30		9.04(3.98)E-34	

Figures in parentheses are the one-σ error in the mantissa.

TABLE 2-10 #4

$E \frac{d\sigma}{dp^3} \left(\frac{cm^2}{GeV^2}\right)$ for Beam + p → π^0 + X @ 200 GeV/c

$p_\perp$ (GeV/c)		$X_{\parallel}$		π^+	π^-	p
.6	.8	0.00	.05	1.57(.22)E-27	1.40(.20)E-27	1.96(.27)E-27
.8	1.0	0.00	.05	4.87(.68)E-28	4.03(.56)E-28	7.43(1.04)E-28
		.10	.20	4.50(.63)E-28	4.66(.65)E-28	4.88(.68)E-28
1.0	1.2	0.00	.05	1.80(.25)E-28	1.68(.24)E-28	2.15(.30)E-28
		.10	.20	1.70(.24)E-28	1.58(.22)E-28	2.11(.30)E-28
		.20	.30	1.55(.22)E-28	1.61(.23)E-28	1.41(.20)E-28
1.2	1.4	-.05	0.00	3.38(.47)E-29	3.12(.44)E-29	5.40(.76)E-29
		0.00	.05	3.68(.52)E-29	3.39(.47)E-29	5.25(.74)E-29
		.05	.10	5.04(.71)E-29	4.77(.67)E-29	5.60(.78)E-29
		.15	.20	4.02(.56)E-29	6.65(.93)E-29	
		.20	.30	4.67(.66)E-29	4.60(.65)E-29	4.06(.57)E-29
		.30	.40	3.99(.56)E-29	4.28(.60)E-29	2.43(.34)E-29
1.4	1.6	-.05	0.00	1.92(.27)E-29	1.63(.23)E-29	2.59(.36)E-29
		0.00	.05	2.11(.30)E-29	1.77(.25)E-29	2.55(.36)E-29
		.05	.10	2.12(.30)E-29	2.27(.32)E-29	2.70(.38)E-29
		.15	.20	1.65(.23)E-29	2.51(.35)E-29	
		.20	.30	1.69(.24)E-29	1.83(.26)E-29	1.60(.22)E-29
		.30	.40	1.41(.20)E-29	1.84(.26)E-29	8.36(1.17)E-30
		.40	.45	1.31(.18)E-29	1.48(.30)E-29	
1.6	1.8	-.05	0.00	5.63(.79)E-30	6.55(.92)E-30	9.18(1.29)E-30
		0.00	.05	8.13(1.14)E-30	8.35(1.17)E-30	1.02(.14)E-29
		.05	.10	7.55(1.06)E-30	8.73(1.22)E-30	1.03(.14)E-29
		.20	.30	7.39(1.03)E-30	8.65(1.21)E-30	6.07(.85)E-30
		.30	.40	6.32(.89)E-30	5.41(.76)E-30	3.22(.45)E-30
		.40	.50	3.98(.80)E-30	3.95(.55)E-30	1.17(.17)E-30
1.8	2.0	-.05	0.00	2.50(.63)E-30	3.14(.44)E-30	5.05(.71)E-30
		0.00	.10	3.81(.53)E-30	2.96(.41)E-30	4.54(.64)E-30
		.10	.15		2.59(.36)E-30	3.12(.44)E-30
		.20	.30	2.44(.34)E-30	2.16(.30)E-30	1.91(.27)E-30
		.30	.40	1.62(.23)E-30	1.44(.20)E-30	8.80(1.23)E-31
		.40	.50	1.20(.17)E-30	1.15(.16)E-30	4.31(.60)E-31
2.0	2.4	-.10	0.00	7.05(.99)E-31	6.39(.89)E-31	9.26(1.30)E-31
		0.00	.10	6.43(.90)E-31	6.77(.95)E-31	8.25(1.16)E-31
		.10	.15	1.11(.34)E-30		9.30(2.79)E-31
		.20	.30	7.63(1.07)E-31	7.39(1.03)E-31	6.01(.84)E-31
		.30	.40	5.68(.80)E-31	5.35(.75)E-31	3.04(.43)E-31
		.40	.50	3.38(.47)E-31	3.56(.50)E-31	1.30(.18)E-31
		.50	.60	2.45(.34)E-31	2.59(.36)E-31	4.61(.65)E-32

Figures in parentheses are the one-σ error in the mantissa.

TABLE 2-10 #5

$E \frac{d\sigma}{dp^3} \left(\frac{cm^2}{GeV^2}\right)$ for Beam + p → π^0 + X @ 200 GeV/c

$p_\perp$ (GeV/c)		$X_{\parallel}$		π^+	π^-	p
2.4	2.8	-.10	0.00	1.93(.58)E-31	1.73(.24)E-31	2.25(.32)E-31
		0.00	.10	1.73(.24)E-31	1.85(.26)E-31	2.00(.28)E-31
		.10	.15	1.86(.26)E-31	2.46(.34)E-31	1.89(.26)E-31
		.30	.40	1.14(.16)E-31	1.11(.16)E-31	5.47(.77)E-32
		.40	.50	9.01(1.26)E-32	7.69(1.08)E-32	2.66(.37)E-32
		.50	.60	4.83(.68)E-32	5.44(.76)E-32	8.96(1.37)E-33
2.8	3.2	-.10	0.00	4.03(.61)E-32	3.71(.52)E-32	4.02(.56)E-32
		0.00	.10	3.66(.51)E-32	4.26(.60)E-32	4.57(.64)E-32
		.10	.20	5.38(.75)E-32	4.26(1.28)E-32	4.01(.56)E-32
		.30	.40	2.35(.33)E-32	2.55(.36)E-32	1.02(.14)E-32
		.40	.50	1.88(.26)E-32	1.82(.26)E-32	5.06(1.01)E-33
		.50	.60	1.00(.20)E-32	1.31(.18)E-32	1.38(.28)E-33
		.60	.70		6.83(.96)E-33	1.08(.44)E-33
3.2	3.6	-.15	0.00	1.10(.50)E-32	9.23(2.01)E-33	7.53(1.05)E-33
		0.00	.10	8.87(1.80)E-33	1.18(.17)E-32	8.72(2.62)E-33
		.10	.20	6.67(2.00)E-33	9.80(1.37)E-33	7.29(1.46)E-33
		.30	.50	6.83(1.57)E-33	4.36(.61)E-33	1.66(.37)E-33
		.50	.70	2.46(.86)E-33	1.78(.25)E-33	4.70(2.35)E-34
3.6	4.0	-.15	.25	1.34(.67)E-33	2.27(.32)E-33	1.37(.34)E-33
		.35	.55	9.85(5.91)E-34	1.21(.43)E-33	3.38(2.03)E-34
		.55	.75		2.15(1.72)E-34	
4.0	4.5	-.15	.30		6.08(1.82)E-34	4.39(1.10)E-34
		.35	.55		2.15(2.16)E-34	
4.5	5.0	-.20	.35		2.69(1.35)E-34	

Figures in parentheses are the one-σ error in the mantissa.

TABLE 2-10 #6

$E \frac{d\sigma}{dp^3} \left(\frac{cm^2}{GeV^2}\right)$ for Beam + $p \rightarrow \pi^0 + X$ @ 300 GeV/c

$p_\perp$ (GeV/c)		$X_{\parallel}$		π^+	π^-	p
1.2	1.4	-.05	0.00			5.84(.82)E-29
		0.00	.05			6.61(.93)E-29
		.05	.10			5.96(.83)E-29
1.4	1.6	-.05	0.00			1.97(.28)E-29
		0.00	.05			2.67(.37)E-29
		.05	.10			2.43(.34)E-29
1.6	1.8	-.05	0.00			7.19(1.01)E-30
		0.00	.05			1.11(.16)E-29
		.05	.10			1.17(.16)E-29
1.8	2.0	-.05	0.00			4.72(.66)E-30
		0.00	.05			3.97(.56)E-30
		.05	.10			3.67(.51)E-30
		.10	.15			3.72(.93)E-30
2.0	2.4	-.10	0.00			1.04(.15)E-30
		0.00	.10			8.70(1.22)E-31
		.10	.15			9.94(1.39)E-31
2.4	2.8	-.10	0.00			1.97(.28)E-31
		0.00	.10			2.27(.32)E-31
2.8	3.2	-.10	0.00			5.47(.77)E-32
		0.00	.10			4.67(.66)E-32
		.10	.20			3.08(.43)E-32
3.2	3.6	-.10	0.00			1.32(.28)E-32
		0.00	.10			1.63(.23)E-32
		.10	.20			1.14(.16)E-32
3.6	4.0	-.10	0.00			5.52(2.05)E-33
		0.00	.10			5.03(1.18)E-33
4.0	4.5	-.10	.30			7.93(2.86)E-34

Figures in parentheses are the one-σ error in the mantissa.

TABLE 2-11 #1

$E \frac{d\sigma}{dp^3} \left(\frac{cm^2}{GeV^2}\right)$ for Beam + p → π^0 + X @ 100 GeV/c

$p_\perp$ (GeV/c)		$X_{\parallel}$		p	K^+	π^+	$\bar{p}$	K^-	π^-
.4	.6	.70	.95	9.40(1.32)E-30	7.09(.99)E-29	1.83(.26)E-28			
.6	.8	.15	.25	1.10(.15)E-27	6.86(2.13)E-28	1.01(.14)E-27	2.99(.42)E-27	1.08(.32)E-27	1.20(.17)E-27
		.70	.95	4.84(.68)E-30	2.80(.42)E-29	4.91(.69)E-29	8.18(2.62)E-30	3.98(.60)E-29	5.79(.81)E-29
.8	1.0	0.00	.05	7.13(1.00)E-28	2.95(1.48)E-28	2.76(.41)E-28			
		.15	.40	2.82(.40)E-28	2.07(.41)E-28	3.02(.42)E-28	4.48(1.12)E-28	6.25(1.88)E-28	4.12(.58)E-28
		.70	.95	1.83(.26)E-30	5.84(1.75)E-30	2.01(.28)E-29	5.02(1.86)E-30	1.28(.26)E-29	2.41(.34)E-29
1.0	1.2	0.00	.10	1.87(.26)E-28	8.83(2.21)E-29	1.04(.15)E-28	1.97(.43)E-28	8.07(3.23)E-29	1.20(.17)E-28
		.15	.50	7.79(1.09)E-29	8.73(2.18)E-29	8.43(1.18)E-29	1.62(.73)E-28		9.37(1.31)E-29
		.70	.95	6.37(1.34)E-31	1.12(.45)E-30	7.51(1.05)E-30	1.39(.84)E-30	3.91(1.17)E-30	9.79(1.37)E-30
1.2	1.4	-.05	.10	5.39(.76)E-29	2.00(.80)E-29	3.18(.45)E-29		4.59(2.07)E-29	3.72(.52)E-29
		.20	.55	1.54(.22)E-29	1.11(.16)E-29	2.24(.31)E-29	1.75(.61)E-29	1.64(.58)E-29	2.98(.42)E-29
		.70	.95	7.86(3.93)E-32	1.03(.52)E-30	2.56(.36)E-30		1.78(.80)E-30	2.83(.40)E-30
1.4	1.6	-.05	.15	1.50(.21)E-29	7.07(3.54)E-30	1.06(.15)E-29		1.08(.65)E-29	1.20(.17)E-29
		.20	.65	4.31(.60)E-30		7.05(.99)E-30	1.21(.42)E-29		9.10(1.27)E-30
		.70	.95					6.25(4.38)E-31	9.76(1.37)E-31
1.6	1.8	-.10	.15	6.67(.93)E-30	3.73(.52)E-30	4.68(.66)E-30	5.52(1.11)E-30	2.41(.72)E-30	3.75(.53)E-30
		.25	.75	9.54(1.34)E-31	1.08(.15)E-30	1.95(.27)E-30	1.30(.18)E-30	1.31(.18)E-30	1.99(.28)E-30
1.8	2.0	-.10	.15	2.78(.39)E-30	1.50(.21)E-30	1.96(.28)E-30	1.11(.28)E-30	1.11(.28)E-30	1.63(.23)E-30
		.25	.85	3.17(.44)E-31	4.55(.64)E-31	6.73(.94)E-31	2.82(.42)E-31	4.22(.59)E-31	6.94(.97)E-31
2.0	2.4	-.10	.20	7.97(1.12)E-31	4.67(.65)E-31	6.11(.86)E-31	4.63(.74)E-31	6.87(1.24)E-31	5.33(.75)E-31
		.30	.95	4.88(.68)E-32	6.22(2.49)E-32	1.35(.19)E-31	3.78(1.14)E-32	1.66(.30)E-31	1.44(.20)E-31
2.4	2.8	-.15	.25	7.09(.99)E-32	5.66(2.27)E-32	8.82(1.24)E-32	1.12(.29)E-31	8.93(1.34)E-32	9.64(1.35)E-32
		.35	.95	3.92(.78)E-33	1.40(.70)E-32	1.57(.22)E-32			1.79(.25)E-32
2.8	3.2	-.15	.30	1.58(.29)E-32	2.23(1.12)E-32	1.56(.22)E-32	4.16(1.69)E-32	3.77(1.13)E-32	1.94(.27)E-32
3.2	3.6	-.15	.30	2.59(.52)E-33		2.89(.83)E-33			5.56(2.00)E-33
		.40	.60			1.34(.67)E-33			
3.6	4.0	-.20	.30						9.04(3.98)E-34

Figures in parentheses are the one-σ error in the mantissa.

TABLE 2-11 #2

$E \frac{d\sigma}{dp^3} \left(\frac{cm^2}{GeV^2}\right)$ for Beam + p → π^0 + X @ 200 GeV/c

$p_\perp$ (GeV/c)		$X_{\parallel}$		p	K^+	π^+	$\bar{p}$	K^-	π^-
.6	.8	0.00	.05	1.96(.27)E-27		1.57(.22)E-27		8.11(1.30)E-28	1.40(.20)E-27
.8	1.0	0.00	.05	7.43(1.04)E-28	4.58(1.37)E-28	4.87(.68)E-28		4.76(.72)E-28	4.03(.56)E-28
		.10	.25	4.53(.64)E-28	2.36(.59)E-28	4.46(.62)E-28	7.20(1.01)E-28	3.83(.54)E-28	4.69(.66)E-28
1.0	1.2	0.00	.05	2.15(.30)E-28		1.80(.25)E-28		1.56(.39)E-28	1.68(.24)E-28
		.10	.30	1.75(.25)E-28	6.80(2.72)E-29	1.58(.22)E-28	2.53(.51)E-28	1.18(.17)E-28	1.55(.22)E-28
1.2	1.4	-.05	.10	5.76(.81)E-29	5.06(.71)E-29	5.29(.74)E-29		3.42(.48)E-29	3.60(.51)E-29
		.15	.40	3.63(.51)E-29	2.66(.37)E-29	4.74(.66)E-29	4.19(.59)E-29	4.11(.58)E-29	4.48(.63)E-29
1.4	1.6	-.05	.10	2.56(.36)E-29	1.79(.25)E-29	1.93(.27)E-29		1.34(.19)E-29	1.87(.26)E-29
		.15	.45	1.24(.17)E-29	1.01(.21)E-29	1.63(.23)E-29	1.68(.28)E-29	1.61(.23)E-29	1.92(.27)E-29
1.6	1.8	-.05	.10	9.86(1.38)E-30	8.15(1.14)E-30	7.49(1.05)E-30		5.84(.82)E-30	7.92(1.11)E-30
		.15	.50	4.43(.62)E-30	8.78(2.20)E-30	6.47(.91)E-30	5.60(1.23)E-30	4.34(.70)E-30	6.89(.96)E-30
1.8	2.0	-.05	.15	4.33(.61)E-30	2.85(.57)E-30	3.77(.53)E-30	3.74(1.68)E-30	1.47(.44)E-30	2.90(.41)E-30
		.15	.55	1.30(.18)E-30	1.32(.19)E-30	1.76(.25)E-30	1.74(.24)E-30	1.29(.18)E-30	1.64(.23)E-30
2.0	2.4	-.10	.15	1.02(.14)E-30	9.59(1.34)E-31	9.70(1.36)E-31	5.59(.78)E-31	4.29(.60)E-31	8.23(1.15)E-31
		.20	.60	2.66(.37)E-31	3.00(.42)E-31	4.75(.67)E-31	3.14(.44)E-31	3.94(.55)E-31	4.69(.66)E-31
2.4	2.8	-.10	.15	1.85(.26)E-31	1.38(.25)E-31	1.84(.26)E-31	1.51(.21)E-31	1.08(.15)E-31	1.90(.27)E-31
		.25	.75	2.85(.40)E-32	4.04(.57)E-32	7.27(1.02)E-32		5.48(.77)E-32	6.70(.94)E-32
2.8	3.2	-.10	.20	4.20(.59)E-32	6.53(1.44)E-32	4.63(.65)E-32	4.23(1.27)E-32	3.87(.58)E-32	4.16(.58)E-32
		.25	.90	4.12(.58)E-33	1.09(.33)E-32	9.62(1.35)E-33		4.67(1.87)E-33	1.27(.18)E-32
3.2	3.6	-.15	.25	5.81(.87)E-33		1.03(.21)E-32		9.00(1.80)E-33	1.11(.16)E-32
		.30	.95	7.01(1.05)E-34		2.78(.42)E-33			
3.6	4.0	-.15	.25	1.37(.34)E-33		1.34(.67)E-33			2.27(.34)E-33
4.0	4.5	-.15	.30	4.39(1.10)E-34					6.08(1.82)E-34
4.5	5.0	-.20	.35						2.69(1.35)E-34

Figures in parentheses are the one-σ error in the mantissa.

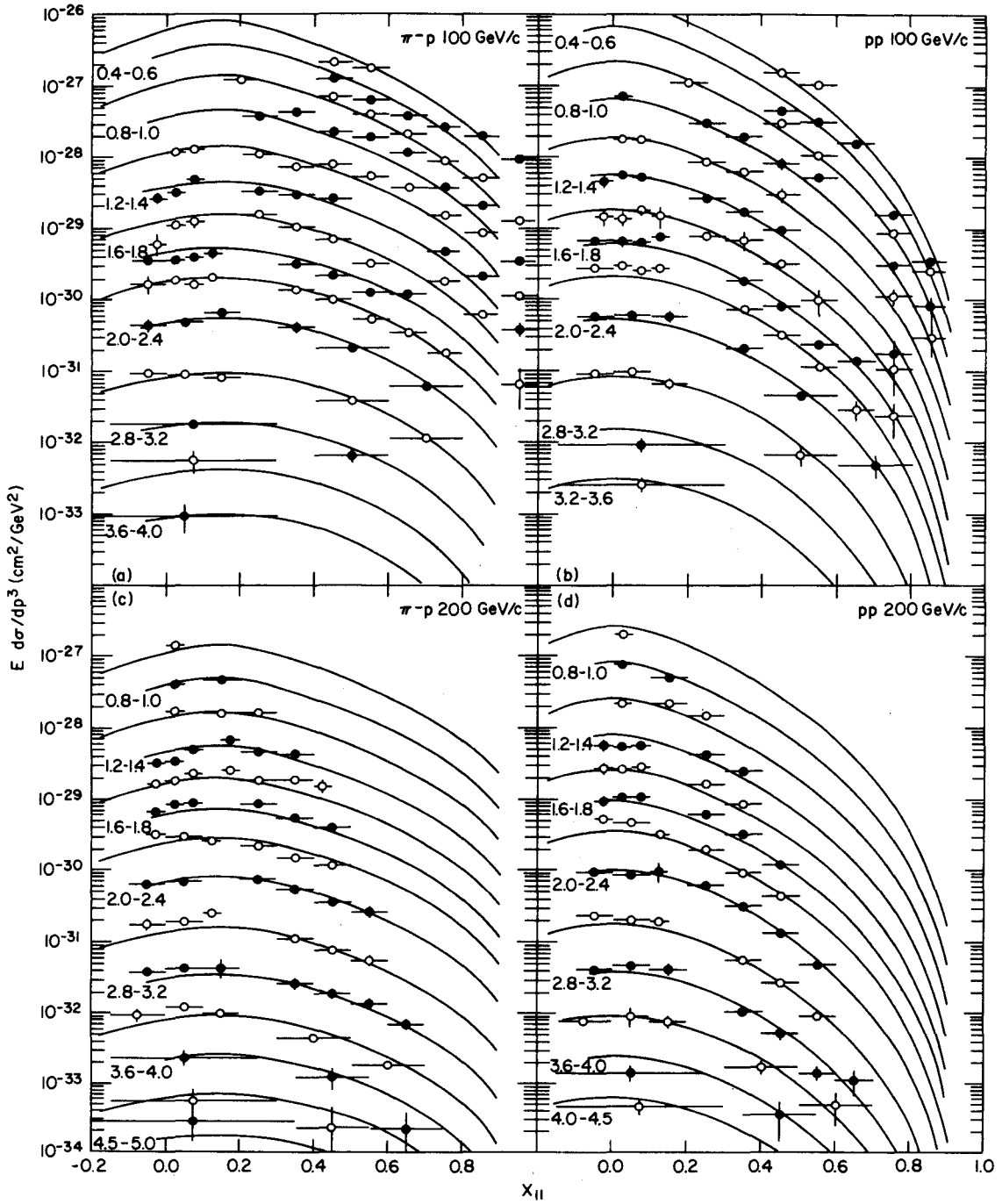

Fig. 2-16 Invariant cross sections on a logarithmic scale versus $x_{\parallel}$: a) and c) $\pi^- p \to \pi^0 X$; b) and d) $pp \to \pi^0 X$; a) and b) @ 100 GeV/c; c) and d) @ 200 GeV/c. $P_{\perp}$ as indicated.

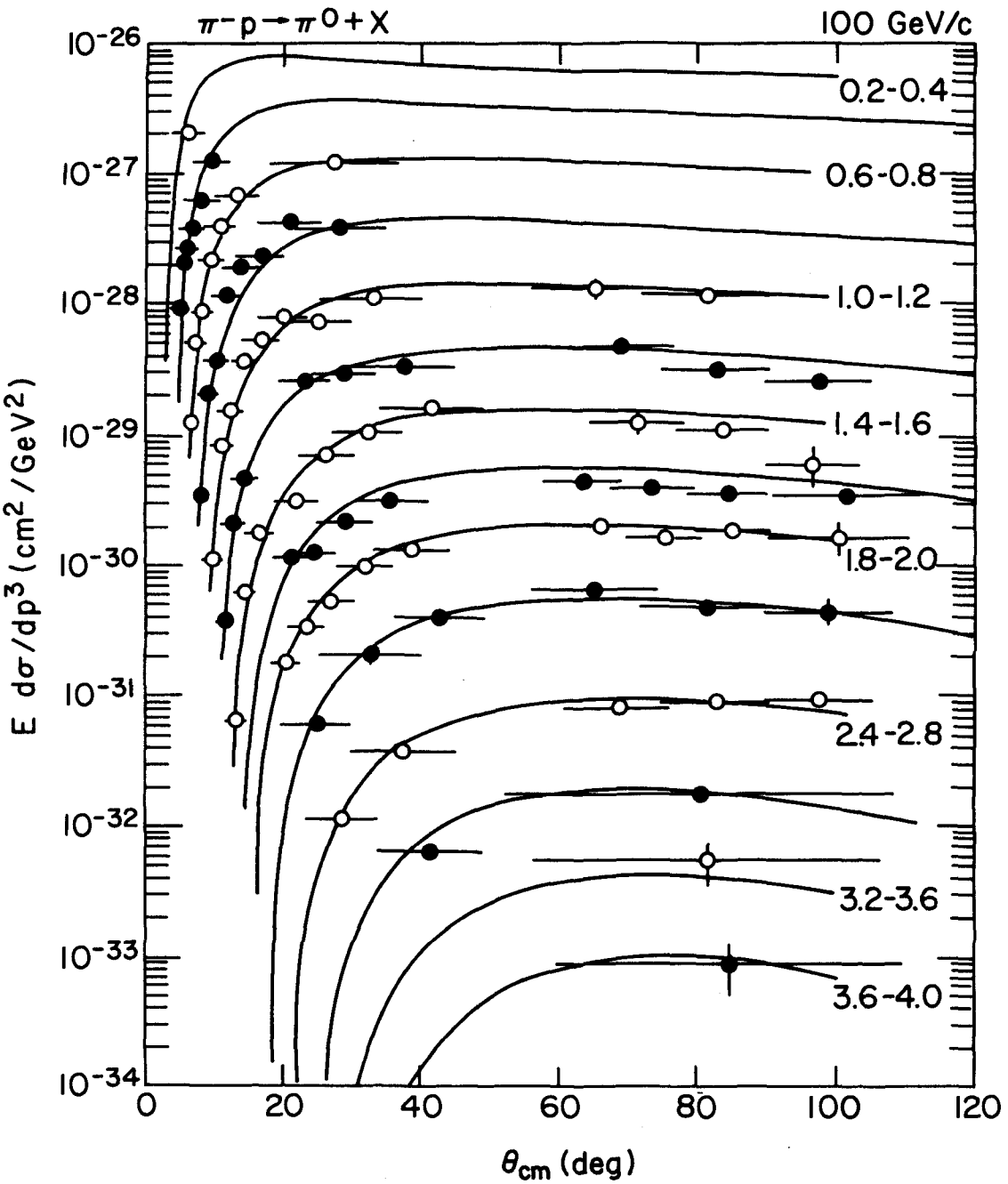

Fig. 2-17 Invariant cross sections on a logarithmic scale versus θ_{cm} for $\pi^- p \to \pi^0 X$ @ 100 GeV/c. $P_\perp$ as indicated.

2.5.2 Features of the Data - Absolute Cross Sections

Some features of the data in Fig. 2-16 and 2-17 continue trends of the low $P_\perp$ data. First is the obvious steep fall of the cross section with $P_\perp$ at fixed $x_\parallel$. This amounts to about 5 orders of magnitude for $P_\perp$ ranging from 1 to 4.5 GeV/c. Also note the less steep fall of the cross section with $x_\parallel$ at fixed $P_\perp$. Finally, there is a plateau in the central region in θ_{cm} at fixed $P_\perp$ even at $P_\perp$ = 2 GeV/c.

Interestingly enough, differences in the πp and pp spectra are visible to the eye. The fall in $P_\perp$ at $x_\parallel = 0$ is slower for πp than for pp. The same is true for the fall in $x_\parallel$ at fixed $P_\perp$. Note that although the pp cross section peaks at $x_\parallel = 0$, as it must from symmetry, that of the πp seems to peak more forward. This phenomena has been observed at lower $P_\perp$ (Ref. 2-10).

The central plateau in θ_{cm} (Fig. 2-17) shows the same contrast. At a $P_\perp$ of about 1, the cross section is flat from 90° to 30°. Data from the ISR (Ref. 2-11) and our own data (see Appendix A3, Graphs of Cross Sections) on the corresponding pp interaction show the plateau to be narrower from 90° to 50°.

The Beam Ratios

Earlier it was pointed out that the ratios of the cross sections for different beams (but with $P_\perp$, $P_\parallel$, and P_0 the same) would be a result less susceptible to systematic error. Beam ratios are specified:

$$R(p/\pi^-) = \frac{Ed^3\sigma/dp^3(pp \rightarrow \pi^o X)}{Ed^3\sigma/dp^3(\pi^- p \rightarrow \pi^o X)} \tag{2-16}$$

Seen this way, in Fig. 2-18 the data exhibit more subtle features. $R(p/\pi)$

displays the largest variation with $P_\perp$ and θ_{cm}, dropping by more than one order of magnitude over the range of the data. The predictions of the CIM (Ref. 2-12) are (for $\theta_{cm} = 90^o$) that the beam ratio should be a simple function of $x_\perp$:

(2-17) $$R(P/\pi) \simeq (1 - x_\perp)^2$$

It is interesting to compare our data not only at 90°, but at 30° as well, to this prediction. We can follow a suggestion of Taylor et al (Ref. 2-13) by plotting $R(\pi/p)$ versus x_R (as in Eq. 1-8) which reduces to $x_\perp$ at 90° ($x_\parallel = 0$). Figure 2-19 shows such a plot for 200 GeV/c beam data along with the form $1.75\ (1-x_R)^2$. In the next chapter, I interpret the striking agreement illustrated here in terms of a scaling hypothesis.

The fact that the ratio $R(p/\pi)$ at low $P_\perp$ and $\theta_{cm} = 90_o$ is near the ratio of the respective total cross sections is reminiscent of a low $P_\perp$ inclusive interaction conjecture (Ref. 2-14):

(2-18) $R(p/\pi) = \sigma_{TOT}(pp)/\sigma_{TOT}(\pi p)$, σ_{TOT} is the total cross section

The dashed lines in Fig. 2-18 illustrate this comparison by showing in each case the ratio of total cross sections for the respective beam particles. It is also tantilizingly close to the 3:2 ratio of the number of quarks in the respective hadrons.

The ratio $R(\pi/K^-)$ is unity to within errors. It is also in agreement with the ratio of total cross sections predictions as above. The only unusual feature is a possible increase at 10° which may be due to beam fragmentation of the π. The behavior of $R(p/K^-)$ is consistent with $R(p/\pi^-)$, as it has to be if $R(\pi^-/K^-$ is unity.

Finally, there is the $R(\bar{p}/p)$ which is also a constant slightly larger than 1. Since some theories predict a radically different behavior than this, we were quite interested in this data, and I will deal with the point in the following chapter.

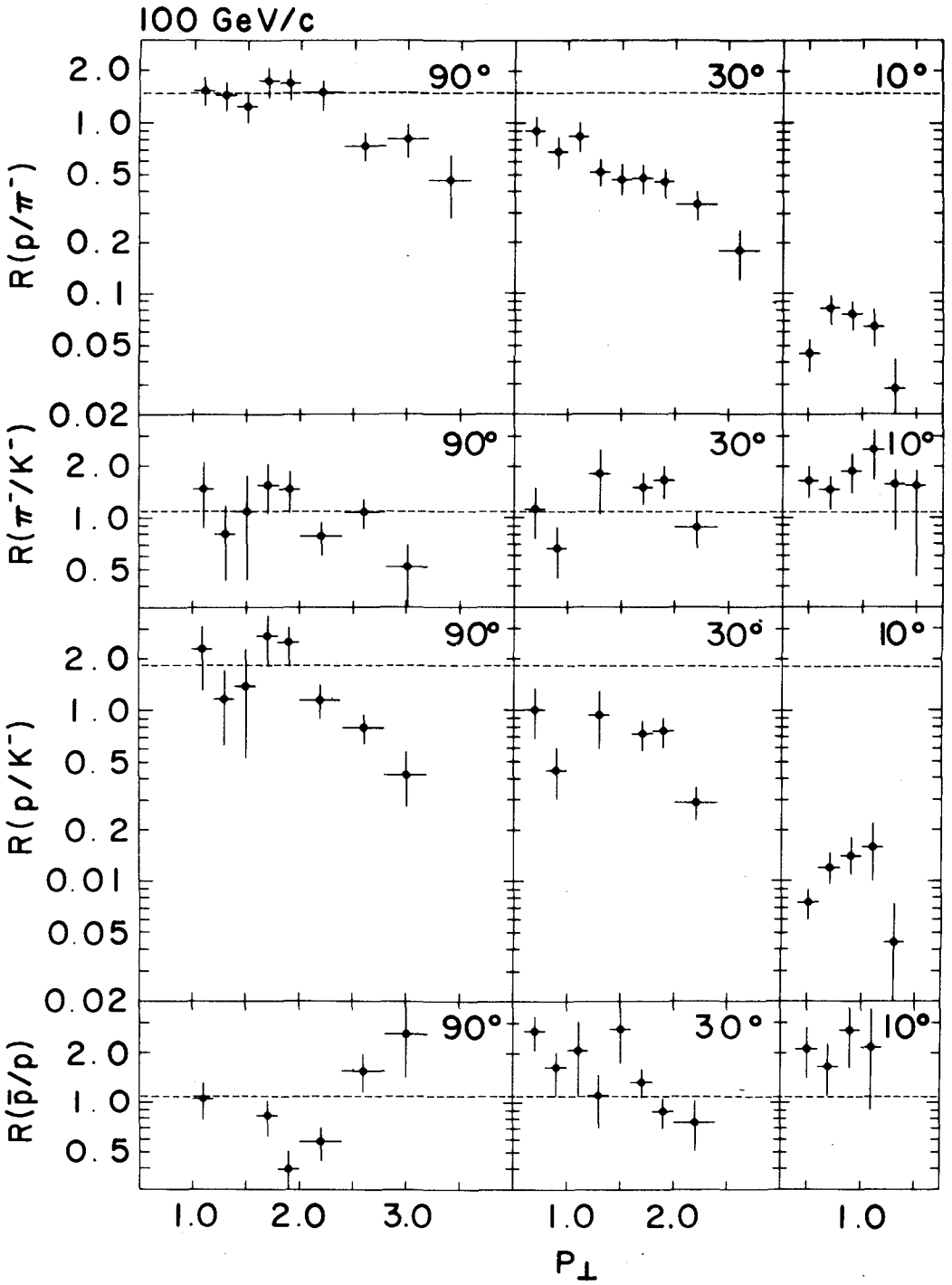

XBL 789-11382

Fig. 2-18a Beam ratios from Tab. 2-11 at 100 GeV/c beam momentum and indicated cm angle. $R(p/\pi^-)$ is the ratio of invariant cross sections for $pp \to \pi^o X$ / $\pi^- p \to \pi^o X$.

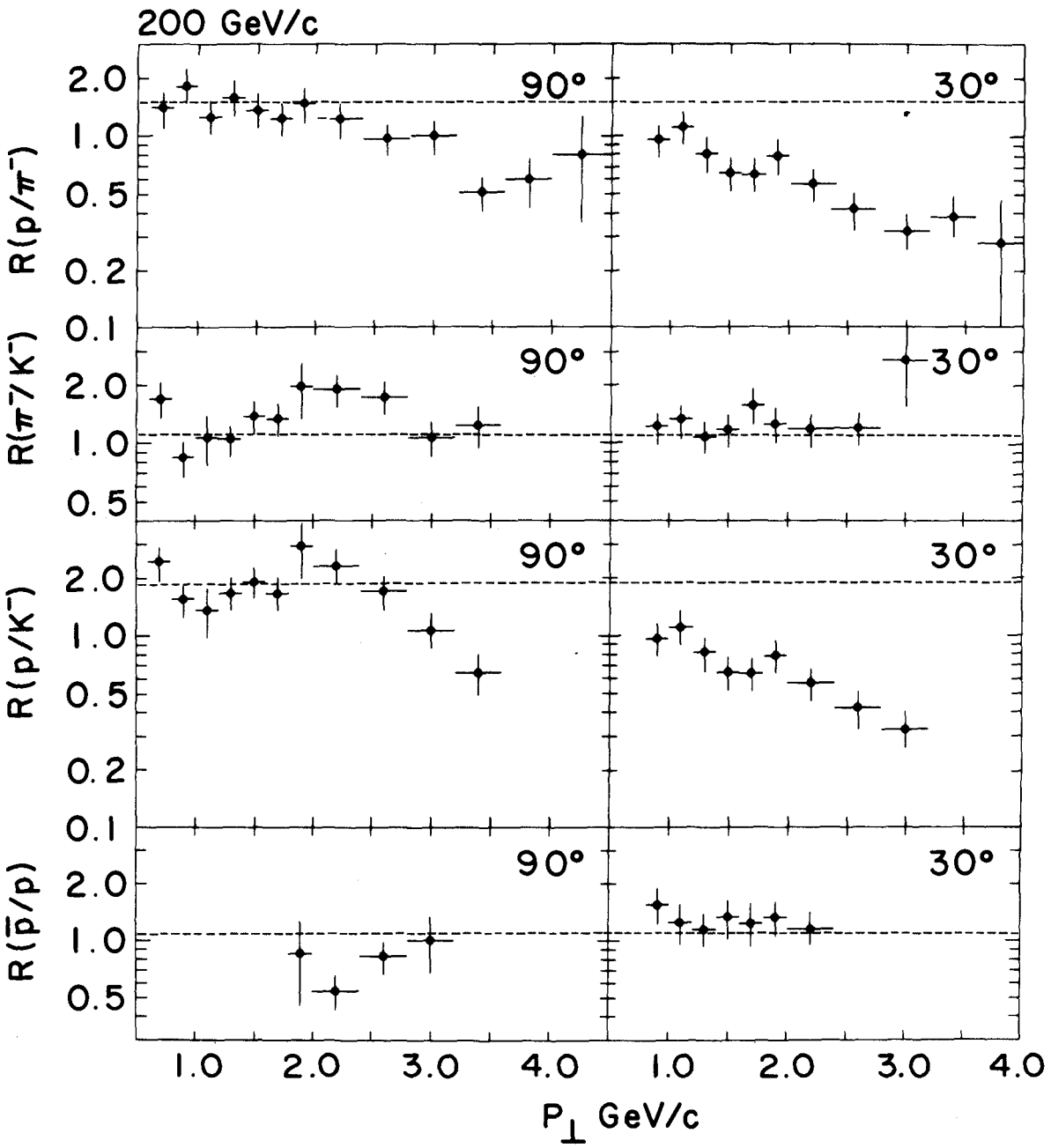

XBL 789-11383

Fig. 2-18b Beam ratios from Tab. 2-11 at 200 GeV/c beam momentum and indicated cm angle. $R(p/\pi^-)$ is the ratio of invariant cross sections for $pp \to \pi^0 X$ / $\pi^- p \to \pi^0 X$.

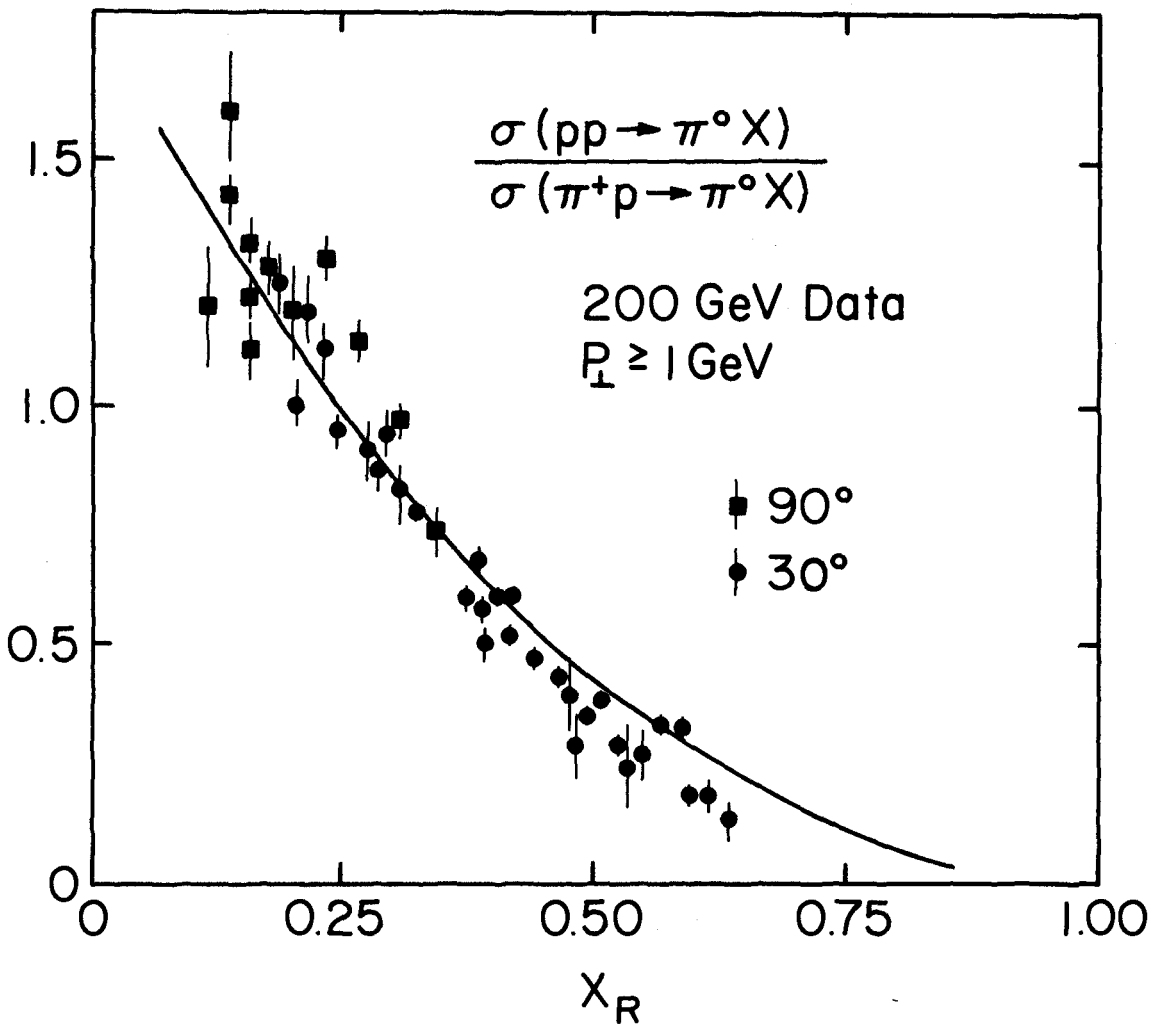

XBL 789-11374

Fig. 2-19 Beam ratio from Tab. 2-10 for indicated reaction and beam energy versus x_R. Data from 90° and 30° cm appear overplotted.

3. Physics of Hadron Interactions at High $P_\perp$

This experiment was carried out in order to shed light on some issues relevant to hadron physics, namely the phenomena of scattering at high transverse momentum. An interpretation of the data in terms of these phenomenological issues appears in this chapter, followed by conclusions drawn from the data.

3.1 Interpretation

We tried several ways of interpreting these data, some of which I discuss in this chapter. One must bear in mind that with no exact theory to make predictions, one is left with very little solid basis from which to interpret the large amount of data at hand. Although there are some underlying relationships between the following approaches, their diversity points up this fact quite clearly.

Global Parametrization

The first method is fairly primitive. A simple functional form can be adjusted to obtain a good global fit to the data. I discuss the results of this parametrization in terms of the model which suggested the form.

Phenomenological Models

The second method is complex by comparison. Hard scattering models predict the cross section in terms of an integral over the structure functions of the hadrons and the cross section for quark-quark scattering. This formalism is applicable to a large class of models, some of which I discuss in this section. Here, I present the predictions of these and other models against our measured results.

Pion Structure Function

Our data can be used in the context of parton models to extract the structure function of the pion. I present our preliminary results and those of other analyses for comparison.

Beam Ratio at Equal Quark Energy

The last approach is quite simple in concept though surprisingly consistent with our data. This heuristic conjecture, briefly explained in the Introduction, tells us to take the ratio of cross sections at different beam energies but such that the average quark-quark scattering energy is the same. This ratio at equal quark energy should be a constant versus $P_\perp$, equal in magnitude to the ratio of the numbers of quarks in the respective beams. This approach enables one to gain an intuitive grasp of the physics behind our data.

3.1.1 Global Parametrization

As pointed out in the Introduction, the earlier data exhibited scaling in the $x_\perp$ variable - a prediction of the CIM model (Ref. 3-1). the 90^0 cross sections are expressed as a function of $P_\perp$ and $x_\perp$, the dependence on s, the cm energy, disappears:

$$\frac{Ed^3\sigma}{dp^3}(P_\perp, x_\parallel, s) = A(P_\perp^2)^{-N}(1-x_\perp)^F \qquad (3\text{-}1)$$

$$x_\perp = 2P_\perp/\sqrt{s} \quad , \quad x_\parallel = 0$$

In this model, the values of N and F are predicted by counting rules to be N = 4 and F = 7 for πp and N = 4 and F = 9 for pp.

Guided by this model, we fit the data for each beam particle with the functional form:

$$\frac{Ed^3\sigma}{dp^3}(P_\perp, x_\parallel, s) = A(P_\perp^2 + M^2)^{-N}(1 - x_D)^F \tag{3-2}$$

$$x_D^2 = x_\perp^2 + (x_\parallel - x_0)^2$$

A, M^2, N, x_0, and F are adjustable parameters in the fit. The results of these fits for π and p beams appears in Tab. 3-1, and the predictions of this fit appear as curves drawn over the data in Fig. 2-16 and 2-17. Note that we do not include data for $x_\parallel > .8$ in the fit. In this region, Eq. 3-2 fits the data very poorly -- probably because the data are showing beam fragmentation or triple Regge behavior, neither of which are well integrated into the CIM.

The functional form fits the steeply falling $P_\perp$ dependence to a power law (modified by an effective mass term, M^2) at fixed x_D for all beam momenta, while giving the remainder of the kinematic dependence in terms of a universal function of x_D.

We noticed quite early in our analysis that having an M^2 term increased the goodness of the fit at lower $P_\perp$ by quite a bit. Similarly, the inclusion of data at angles other than 90^0 cm prompted us to generalize the CIM scaling variable $x_\perp$ to $x_R = \sqrt{(x_\perp^2 + x_\parallel^2)}$ as $x_\perp$ scaling makes no sense algebraically in the forward (0^0 cm) direction.

Finally, we noticed that the π^-p data at fixed $p_\perp$ peaks at a positive value of $x_\parallel$ (about .15). We accommodated this behavior by taking $x_\parallel$ into $x_\parallel - x_0$. The case of pp must, by symmetry, have $x_0 = 0$, but in the hitherto unexplored πp reaction, no such symmetry constraint exists. This phenomenon appears in low $P_\perp$ inclusive data (Ref. 3-2). Such was the tortuous path from $x_\perp$ to x_D scaling.

TABLE 3-1

VALUES OBTAINED FOR LEAST-SQUARES FIT TO THE FORM

$$Ed^3\sigma/dp^3 = A(P_\perp^2 + M^2)^{-N}(1 - x_D)^F \ , \quad \text{where } x_D^2 = x_\perp^2 + (x_\parallel - x_o)^2 \text{ and } x_\parallel < .8$$

Reaction Fit (Beam Momenta) [GeV/c]	A [E-26 cm^2/GeV^2]	F	x_o	N	M [GeV^2]	χ^2/DOF
$p\ p \rightarrow \pi^o X$ (100,200,300)	1.22(15)	4.42(5)	0.02(1)	4.90(6)	0.81(4)	306/142
$\pi^- p \rightarrow \pi^o X$ (100,200)	1.13(10)	3.13(10)	0.14(1)	5.06(6)	0.97(4)	271/132
$\pi^+ p \rightarrow \pi^o X$ (100,200)	1.02(15)	3.29(10)	0.14(1)	5.00(7)	0.95(4)	325/130
CIM Predictions for $x_\parallel = 0$ (Ref. 3-1)						
$p\ p \rightarrow \pi^o X$		9		4		
$\pi^\pm p \rightarrow \pi^o X$		7		4		

Figures in parenthesis correspond to the one-standard-deviation uncertainty in the last digits of the main number.

Appendix 3 has a more complete set of graphs showing the fit plotted on the data. It is visually apparent that the fit agrees with the data over a wide range in beam energy and scattering angle.

It is well to remember some implicit assumptions of Eq. 3-2. One is the non-trivial factorization of the cross section into $F(P_\perp)G(x_\perp,x_\parallel)$, which implies scaling in the sense of Eq. 1-5. Another is the precise form of $F(P_\perp)$, namely a power law in $P_\perp^2 + M^2$. Finally, there is the simplification of $G(x_\perp,x_\parallel)$ to a function of x_D.

Fits to a simple exponential in total π^0 momentum in the cm P like e^{-bP}, although quite good for each detector setting (beam energy and cm angle), require quite different values of slope parameter b for each fit. This rules out thermodynamic models such as Meng's (Ref. 3-3) as in these, the slope parameter is generally the same for all cm angles.

Figure 3-1 shows the cross section with the $P_\perp$ dependence divided out as in Fig. 1-8. Here we show, at each energy, the values for each different angular region versus x_D. In every graph, the smooth curve is the fit value: the two curves are identical. This plot illustrates the agreement between the data at different cm angles and different energies with the form Eq. 3-2. Appendix 3 has plots like Fig. 3-1 for $\pi\pm p$ and pp reactions at all energies. The pp data scale in x_R.

What does this fit tell us about the physics? One observation concerns the non-zero value of x_0 for the πp data which accommodates the peaking of the $x_\parallel$ spectrum in the forward direction. It makes sense that if the quarks of the π are fewer in number than those of the p, they would each carry a larger fraction of the beam momentum. Then the center of mass frame of the quark-quark scattering (in which the cross section would presumably be symmetric) is actually moving forward in the overall

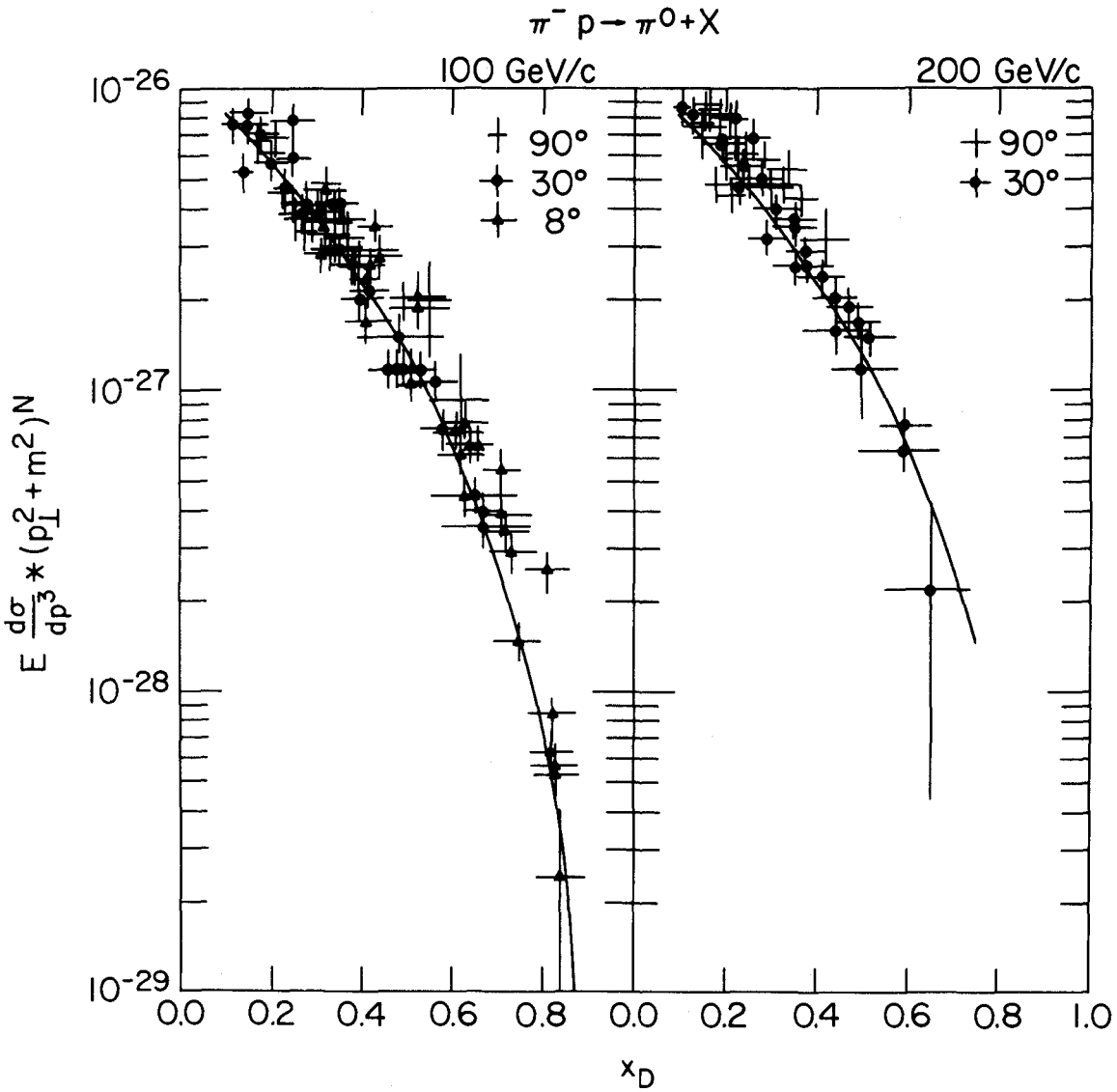

Fig. 3-1 $Ed^3\sigma/dp^3 \; / \; (P_\perp^2 + M^2)^{-N}$ on a logarithmic scale versus x_D, for $\pi^- p \rightarrow \pi^0 X$. a) @ 100 GeV/c - 90^0, 30^0 and 8^0 cm; b) @ 200 GeV/c - 90^0 and 30^0 cm.

cm. We will see other evidence for this point of view in the later discussions.

Another observation concerns the values of F, the power of $1-x_D$, in the fit (see Tab. 3-1). Our values are much smaller than those predicted by the CIM (Ref. 3-1). Another π^0 inclusive experiment in a $P_\perp$ range similar to ours also sees a small value, F = 4 for pp data (Ref. 3-4). It is the belief from quark theory that the average of π^+ and π^- inclusive rates should be equal to the π^0 rates. One such measurement (Ref. 3-5) agrees with the CIM result and disagrees with ours. There is something of a puzzle here, and no clear resolution has been found. One speculation is that the $P_\perp$ values over which our measurements have been taken are not sufficiently high for the exact validity of the CIM counting rules. On the other hand, our fit determines F mainly through the angular dependence of the data at fixed $P_\perp$ and s. It is clear that a form like $(1-x_R)^9$ cannot fit the data at fixed beam energy for all angles.

Finally, there is the great similarity between the values for N (the power of $(P_\perp^2 + M^2)$) in the pp and πp case. It is the property of most hard scattering models that the N value is determined mainly by the form of the scattering law for the particular subprocess in question. If this is the case, our fit seems to indicate that the form is the same for pp and πp scattering. The N values we obtain, however, are not consistent with those predicted by the CIM; in fact they are uniformly one unit larger. As in the case of the F values, this could be due to the kinematic region of our data.

3.1.2 Phenomenological Models

There are now several models which make predictions for the beam ratios which we measure. In this section, I discuss a class of these

models, which I am calling "three step models", and show how they calculate the cross section in terms of the simple ideas set forth in the introduction. Then I show how their predictions compare with the data.

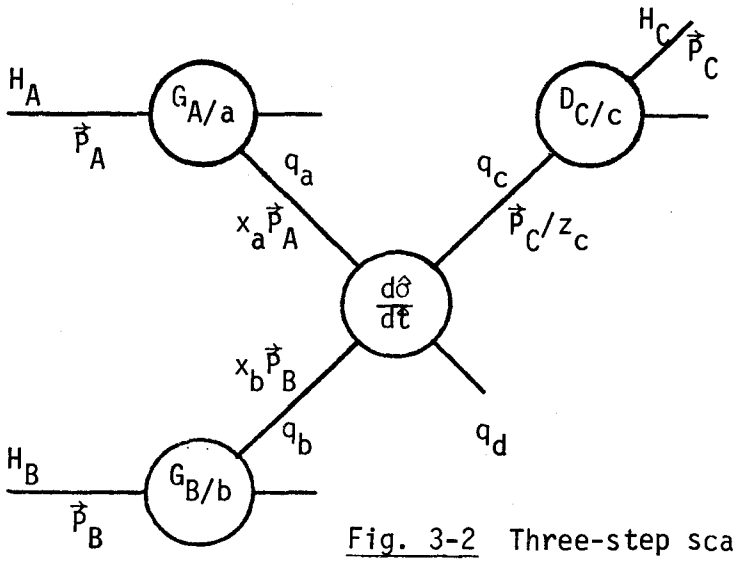

Fig. 3-2 Three-step scattering process

$G_{A/a}(x_a)$ - Probability for q_a at x_a, likewise for $G_{B/b}$

$D_{C/c}(z_c)$ - Probability for q_a at x_a

$d\hat{\sigma}/d\hat{t}$ - Elastic cross section for $q_a q_b \rightarrow q_c q_d$

We picture the production of a high transverse momentum hadron (in our case the π^o) as proceeding by three steps as illustrated in Fig. 3-2 (Ref. 3-6). We start with the two incoming hadrons, H_A and H_B, with momentum P_A and P_B in the center of mass. In our case, H_A is the beam particle and H_B is the target particle, a proton. We picture the hadron H_A as being composed of quarks, each carrying a fraction of the hadron's momentum with a probability distribution we call $G_{A/a}(x_a)$. The value of the function $G_{A/a}$ at some value of the argument x_a is the probability for the quark to have fractional momentum x_a of the hadron H_A.

In the second step, the two quarks scatter by some mechanism with a cross section given by $d\hat{\sigma}/d\hat{t}$ $(\hat{s}, \hat{t}, \hat{u})$. In this expression, we implicitly view the scatter as occurring in the center of mass frame of qa and

qb, which is not necessarily the same as the center of mass of the incoming hadrons (the overall cm).

(3-3)

Hadron Kinematic Variables	Parton Kinematic Variables
$s = (P_A^2 + P_B^2)$	$\hat{s} = (x_a P_A + x_b P_B)^2 = x_a x_b s$
$t = (P_A^2 - P_C^2)$	$\hat{t} = (x_a P_A - P_C/z_c)^2 = x_a t/z_c$
$u = (P_B^2 - P_C^2)$	$\hat{u} = (x_b P_B - P_C/z_c)^2 = x_b u/z_c$
$x_1 = -u/s$	$\hat{x}_1 = -\hat{u}/\hat{s} = \cos^2\hat{\theta}/2 = x_1/(x_a z_c)$
$x_2 = -t/s$	$\hat{x}_2 = -\hat{t}/\hat{s} = \sin^2\hat{\theta}/2 = x_2/(x_b z_c)$
$x_{\parallel} = (x_1 - x_2)/2$	$\hat{\theta}$ is the angle of q_c in the $q_a q_b$ cm frame
$x_R = (x_1 + x_2)/2$	$z_c = x_1/x_a + x_2/x_b$
$x_{\perp} = \sqrt{(x_1 x_2)}$	
θ is the cm angle of C	

Thus the kinematic parameters $\hat{s}$, $\hat{t}$, $\hat{u}$ defined in the Eq. 3-3 refer to the Mandelstam variables for the qaqb interaction. The crucial assumption is that qa and qb scatter elastically. This makes the subprocess cross section $d\hat{\sigma}/d\hat{t}$ at fixed s a function only of the scattering angle in the qaqb frame. In general, we have the formula:

(3-4) $$\hat{s} + \hat{t} + \hat{u} = m_a^2 + m_b^2 + m_c^2 + m_d^2$$ (m_a, m_b, etc. are the quark masses)

The simplification that the quark masses m_a, m_b are all zero:

(3-5) $$\hat{s} + \hat{t} + \hat{u} = 0$$

implies elastic scattering. This is also implicit in Eq. 3-3 . Equation 3-5 is approximately true if $\hat{s}$, $\hat{t}$ and $\hat{u}$ are all much larger than the quark masses squared, which would be the case in sufficiently high energy, high

transverse momentum interactions. Since we do not really know how large the quark masses really are, we cannot know if this assumption is correct, but for better or for worse we assume so.

The third step is that one of the scattered quarks qc gives rise to the hadron which we detect, H_c, in our case a π^0. Some like to think of this as a "decay" of a quark into a hadron. Presumably then the other decay products carry away any excess quantum numbers - such as charge and quark number - and go undetected. In this transformation, we picture the hadron H_c to be carrying away a fraction z_c of the momentum of q_c, with an associated probability $D_{C/c}(z_c)$, much like the $G_{A/a}(x_a)$.

So the entire process is one of hadrons H_A, H_B undressing into their constituent quarks, the quarks q_a, q_b interacting and the scattered quark q_c dressing up as the hadron H_c.

The cross section for the inclusive production of H_c is then given by the integral:

$$(3\text{-}6) \qquad Ed^3\sigma/dp^3 = \int_{x_{am}}^{1} dx_a \int_{x_{bm}}^{1} dx_b \, \frac{1}{\pi} \frac{d\hat{\sigma}}{d\hat{t}} (\hat{s},\hat{t},\hat{u}) \; G_{A/a}(x_a) \; G_{B/b}(x_b) \; D_{C/c}(z_c)/z_c \, ,$$

$$x_{am} = x_1/(1 - x_2) \text{ and } x_{bm} = x_2/(1 - x_1/x_a)$$

This represents a convolution of $d\hat{\sigma}/d\hat{t}$ over the functions $G_{A/a}$, $G_{B/b}$ and $D_{C/c}$.

In order to make calculations one must determined the structure functions $G_{p/q}$, $G_{\pi/q}$, $D_{q/\pi}$ and the subprocess cross section $d\hat{\sigma}/d\hat{t}$. As discussed in the Introduction, for the proton structure function and the π^0 decay function, there are independent data which the phenomenologists use (Ref. 3-7). But in the case of the π structure function and the subprocess cross section, we have no such data. For the latter,

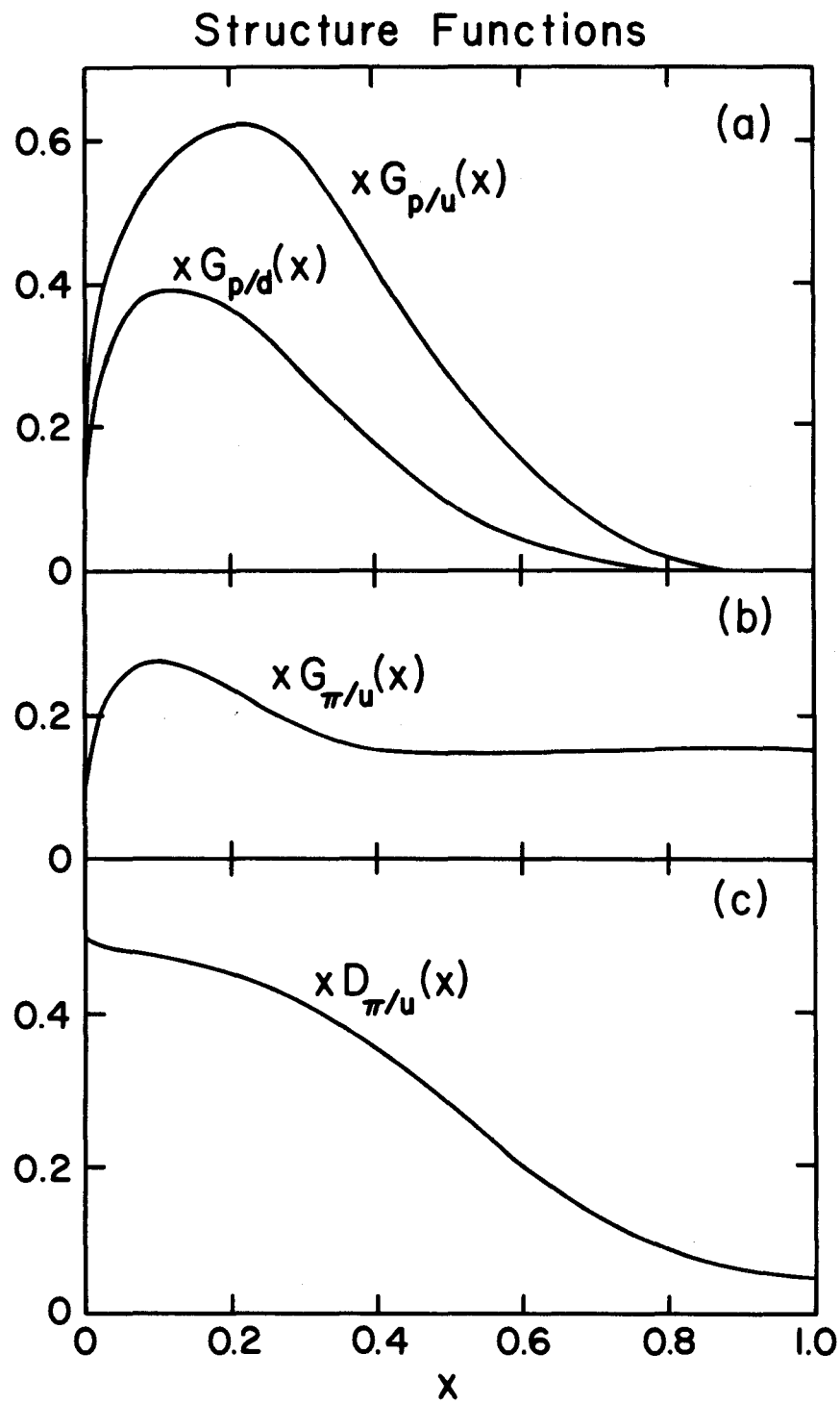

Fig. 3-3 Structure and decay function as used by Field and Feynman:
a) proton structure function for u-quark ($G_{p/u}$) and d-quark ($G_{p/d}$);
b) pion structure function for u, d, $\bar{u}$ or $\bar{d}$ quark, $G_{\pi/u}$;
c) decay function for u, d, $\bar{u}$ or $\bar{d}$-quark into π^0, $D_{\pi/u}$.

XBL 789-11368

Feynman and Field (Ref. 3-8) hypothesize $d\hat{\sigma}/d\hat{t} = A/(\hat{s}\hat{t}^3)$. For the structure function, they adjust a form to give the best fit to the pion beam data of this experiment. Figure 3-3 shows the structure function of protons $G_{p/u}$ and $G_{p/d}$ and pions $G_{\pi/u} = G_{\pi/\bar{d}}$ as well as the decay function of quarks into π^0 $G_{\pi/u} = G_{\pi/d}$ as used in Ref. 3-8.

Other phenomenologists (Ref. 3-9 and 3-10) use similar structure and decay functions but account for the observed $P_\perp$ dependence by using a different form of $d\hat{\sigma}/d\hat{t}$. The simple Dirac scattering form for one gluon exchange, $(1 + \hat{u}^2/\hat{s}^2)/\hat{t}^2$ times an <u>ad hoc</u> quark from factor $1/(1 + \hat{s}^2/\Lambda^4)$, also gives an acceptable fit to the early high $P_\perp$ data.

The CIM model (Ref. 3-11) differs from the above models by picturing the scattering as occuring through the exchange of a hadron constituent. A typical subprocess would be $qM \rightarrow qM$ elastic scattering in which the detected π^0 comes directly from the interaction as in Fig. 3-4 below.

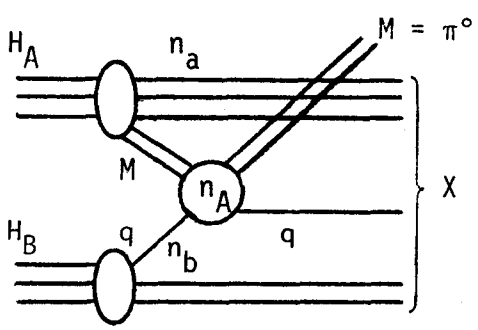

<u>Fig. 3-4</u> Scattering in the CIM. H_A splits into a meson M plus $n_a = 3$ inactive quarks and H_B splits into a quark a plus $n_b = 2$ inactive quarks. In the reaction of $qM \rightarrow q\pi^0$ there are $n_A = 6$ active quarks.

This quark-meson scattering will, in general, have a $P_\perp^{-8}$ spectrum. One may think of the scattering of quark and M ($q\bar{q}$ pair) as proceeding via the exchange of two gluons or the interchange of one quark:

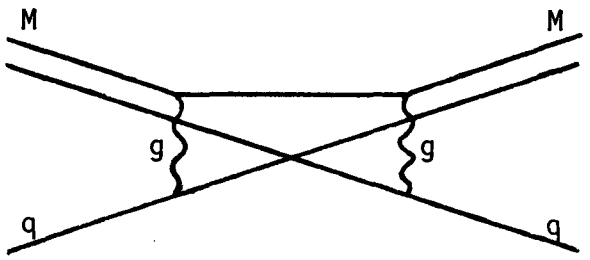

$$\frac{d\hat{\sigma}}{d\hat{t}} \sim \frac{1}{\hat{s}\hat{u}^3} \sim \frac{1}{(P_\perp^2)^4}$$

Fig. 3-5 Scattering subprocess $qM \to qM$. Because two gluons g are exchanged, the cross section scales like $1/s^4$.

Note the similarity between this form of $d\hat{\sigma}/d\hat{t}$ and that of Feynman and Field.

In the CIM, the cross section at 90° is:

(3-7) $$ED^3\sigma/dp^3 = A(P_\perp^2)^{-N}(1 - x_\perp)^F \quad , \text{ at } \theta_{cm} = 90^o$$

N and F are related by two counting rules to the numbers of "active" and "inactive" quarks. In this expression, $P_\perp^2$ may be replaced with $P_\perp^2 + M^2$ (where $M \sim 1$ GeV) to accommodate possible scale breaking behavior. The power of $P_\perp$ is related to the number of quarks active in the scatter by the first counting rule:

(3-8) $$N = (n_A - 2)$$

For example, $n_A = 6$ for the subprocess $qM \to qM$ in Fig. 3-5.

The second counting rule is a consequence of the assumed form of the structure functions:

(3-9) $$G_{A/a}(x) \sim (1 - x)^{G_a} \text{ with } g_a = 2n_a - 1$$

n_a is the number of spectators - inactive quarks - from H_A. This is the result of an underlying scale-invariant theory (Ref. 3-10). In the above example, H_A is a proton which contributes a meson to the interaction, thus $n_a = 3$ and $g_a = 5$. Note that there must be 3 spectators in this case because of quark number conservation. The power of $(1 - x_\perp)$ for 90° cm cross section F is simply expressed by the second counting rule:

$$F = 1 + g_a + g_b = 2(n_a + n_b) - 1 \tag{3-10}$$

To summarize, the inclusive cross section at 90° cm is:

$$\frac{E d^3\sigma}{dp^3} = (P_\perp^2 + M^2)^{-N}(1 - x_\perp)^F = (P_\perp^2 + M^2)^{n_A-2}(1 - x_\perp)^{2(n_a+n_b)-1} \tag{3-11}$$

The CIM prediction for $\pi p \to \pi^o X$ and $pp \to \pi^o X$ is simple to derive. If one assumes that the dominant subprocess is $qM \to qM$, then there are six elementary fields in the subprocess; thus $n_A = 6$ and $N = 4$. Furthermore, the number of inactive quarks in the target will be $n_b = 3$. In the case of πp scattering, the beam will have only one inactive quark, so $n_a = 1$ and $F = 7$. In the case of pp scattering, there will be two inactives; thus $n_a = 2$ and $F = 9$. This line of reasoning gives rise to the values quoted in Tab. 3-1 and the prediction that the ratio of cross sections versus $x_\perp$ at 90° will be $\sim(1 - x_\perp)^2$, as set forth in Eq. 2-17.

The pedagogical virtue of the CIM is that the cross section can be expressed in this simple form. We see, as alluded to in the previous section, that the N value is a consequence of the scattering subprocess, while the F value is due to the form of the structure functions. This enables one to separate out the two different aspects of the physics in a concise manner.

The integral Eq. 3-6 is applicable to the CIM (Ref. 3-11) by taking modified structure functions $G_{A/a}(x_a)$ which approach the form $(1 - x_a)^{G_a}$ as $x_a \to 1$ and by using the subprocess cross sections as in Fig. 3-6. To do this, one simply constrains $z_c = 1$ in the integral. As no decay takes place, there is no third step. The integral then becomes equivalent to:

$$\frac{E d^3\sigma}{dp^3} = \frac{2}{\pi} \int_{-(1-2x_1)}^{(1-2x_2)} \frac{dz}{1-z^2} \frac{d\hat{\sigma}}{d\hat{t}} (\hat{s},\hat{t},\hat{u})\ G_{A/a}(x_a)\ G_{B/b}(x_b) \quad , \text{ with } z = \cos\hat{\theta}, \tag{3-12}$$

$$x_a = 2x_1/(1+z), \quad x_b = 2x_2/(1-z), \text{ and with } \hat{s},\hat{t},\hat{u}, \text{ as in Eq. 3-3}$$

This integral reduces to Eq. 3-11 in the limit of high $P_\perp$ at 90^0 cm thus giving rise to Eq. 3-1. It also allows one to extend the CIM to angles other than 90^0 and to lower values of $P_\perp$.

SUBPROCESS $qM \to qM$

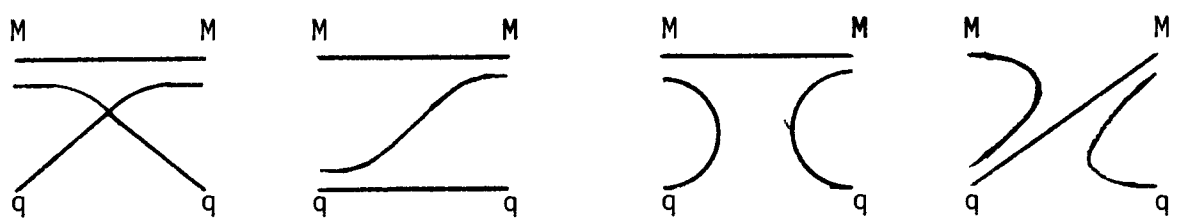

$\frac{d\hat{\sigma}}{d\hat{t}} = 1/(\hat{s}\hat{u}^3)$ $\quad 1/(\hat{s}\hat{t}^3)$ $\quad \hat{u}/\hat{s}^5$ $\quad \hat{t}/\hat{s}^5$

SUBPROCESS $q\bar{q} \to MM$

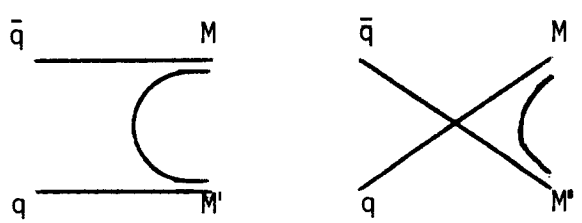

$\frac{d\hat{\sigma}}{d\hat{t}} = \hat{u}/(\hat{s}^2\hat{t}^3)$ $\quad \hat{t}/(\hat{s}^2\hat{u}^3)$

Fig. 3-6 Subprocess scattering diagrams and $d\hat{\sigma}/d\hat{t}$.

Figure 3-7 presents our measured beam ratios against the predictions of selected models. Shown are the $R(p/\pi)$ for 90° - a), 30° - b) and $R(\bar{p}/p)$ for 90° - c). By showing $R(p/\pi)$ at both 90° and 30°, we can test the angular dependence of some models. Many model-makers have had the opportunity to fit their predictions to our 90° data, so the agreement here is not surprising. However, at 30° some deficiencies appear. In particular, the Feynman-Field model (1) (Ref. 3-8) is greatly improved by the use of a different pion structure function (2) (Ref. 3-12). Other similar models, such as (3) (Ref. 3-9) and (4) (Ref. 3-10) may benefit from such a change. This illustrates the ability of our data at various cm angles to supply constraints for models.

The antiproton/proton beam ratio, however, shows up an interesting difference between theories. In both the quark fusion (5) (Ref. 3-13) and quark annihilation (6) (Ref. 3-8) theories, the dominant production mechanism is assumed to be one where an anti-quark from the beam and a quark from the target - or <u>vice versa</u> - combine to eventually produce the high $P_\perp$ π^o. This would be something like the CIM theory (7) (Ref. 3-11) with only the $q\bar{q} \rightarrow MM$ diagrams of Fig. 3-6 e) and f) contributing. As briefly discussed in the introduction, this is a case where the $\pi(\bar{q}q)$ beam would have an advantage over the p(qqq) beam, given the proton (qqq) target. Furthermore, the $\bar{p}(\bar{q}\bar{q}\bar{q})$ beam would, presumably, have an even greater production cross section than the π beam. As the figure shows, our $R(\bar{p}/p)$ is very difficult to accommodate in the quark fusion model as presently formulated (Ref. 3-14). Models which assume quarks to be as effective as antiquarks for producing π^o's, such as Feynman-Field, would predict $R(\bar{p}/p) = 1$. This along with (3) and (4) are basically in agreement with the data. The CIM (2) adds $qM \rightarrow qM$ subprocesses to quark fusion,

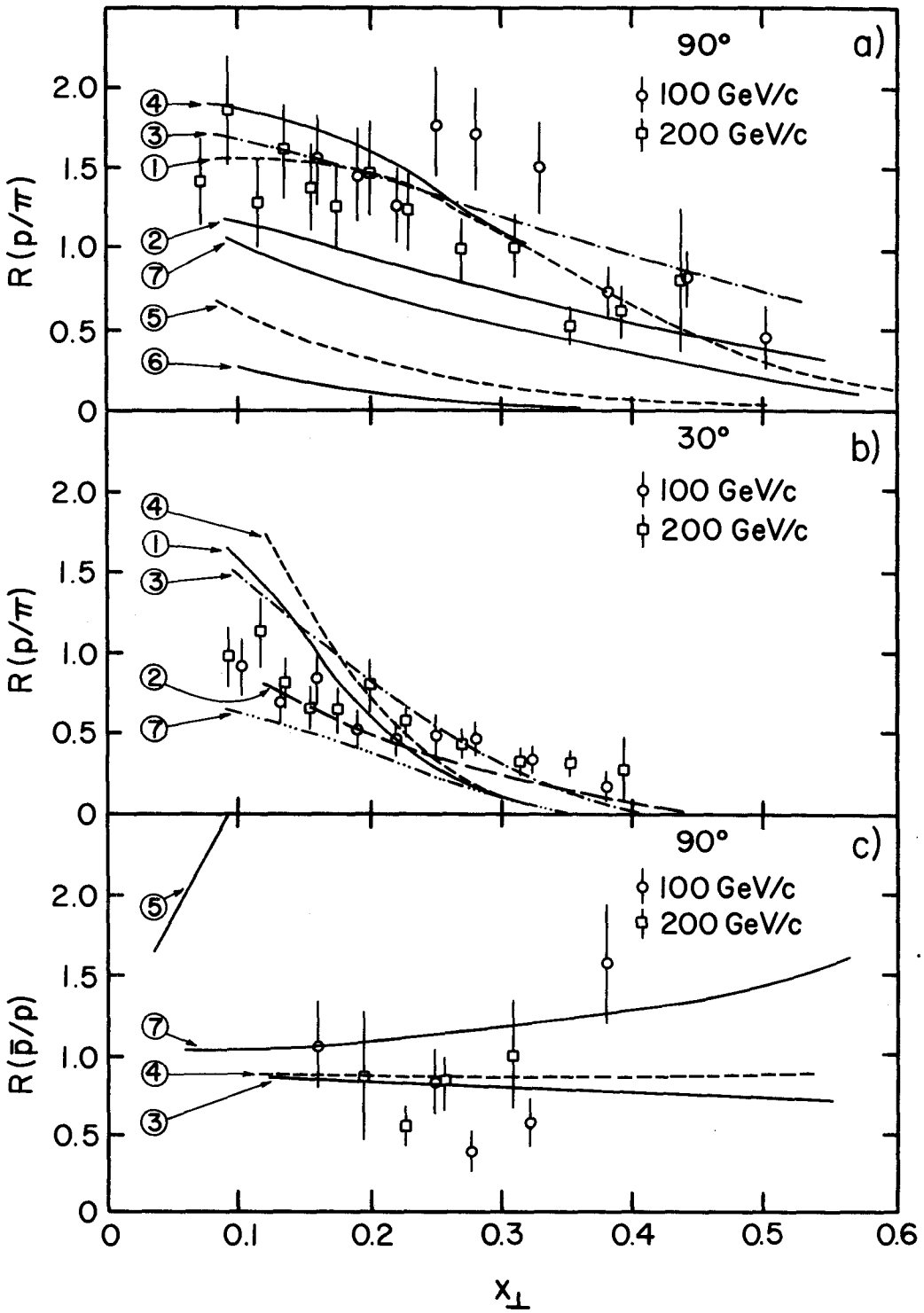

Fig. 3-7 Beam ratios as defined in Eq. 2-16 versus $x_\perp$ compared to predictions from various models: a) $R(p/\pi)$ at 90° cm; b) $r(p/\pi)$ at 30° cm; c) $R(\bar{p}/p)$ at 90° cm. Curve labels: (1) Ref. 3-8; (2) Ref. 3-12; (3) Ref. 3-9; (4) Ref. 3-10; (5) Ref. 3-13; (6) Ref. 3-8; (7) Ref. 3-11. XBL 789-11383

necessary from crossing relations, thus diluting the effect of the latter except at high $x_\perp$ where quark fusion begins to favor $\bar{p}p$.

3.1.3 Pion Structure Function

The structure functions of the hadrons are an essential ingredient in the parton models of the previous section. However, knowledge of the pion's structure is lacking. The proton's structure function was determined primarily from electroproduction data in the reaction $ep \rightarrow eX$. The analogous technique for pions would require a pion target which is not available at the present. With certain assumptions, data of the reaction $\pi p \rightarrow \mu^+\mu^- X$ has been used by Dao et al. to derive the pion structure function $G_{\pi/q}$ (Ref. 3-12).

Our own data can also shed light on this question. The technique is to create a function $G_{\pi/q}$ which gives the best fit to our $R(pp/\pi p)$ in the context of the Feynman-Field model. We first assure ourselves that the model provides an acceptable fit to the pp data. With the already determined $G_{p/q}$, the model has little flexibility in this regard, but the fit is reasonable. Preliminary results of the fit to $R(pp/\pi p)$ using the form of Eq. 3-13 yields a best value for α of 1.52±.03 (Ref. 3-15):

$$xG_{\pi/q}(x) = \sqrt{x}(1 - x)^{\alpha} \tag{3-13}$$

Figure 3-8 shows the pion structure functions $xG_{\pi/q}(x)$, a) as employed by Feynman and Field (Ref. 3-8); b) as derived by Dao, et al. (Ref. 3-12); and c) as derived from our data. A common feature of all is the slower fall with x than that of the proton structure function (see Fig. 3-3a).

Feynman and Field derived $G_{\pi/q}$ in order to fit our data at 90° cm and assumed that $G_{\pi/q}(x)$ is a constant (not zero) at x - 1. Both we and

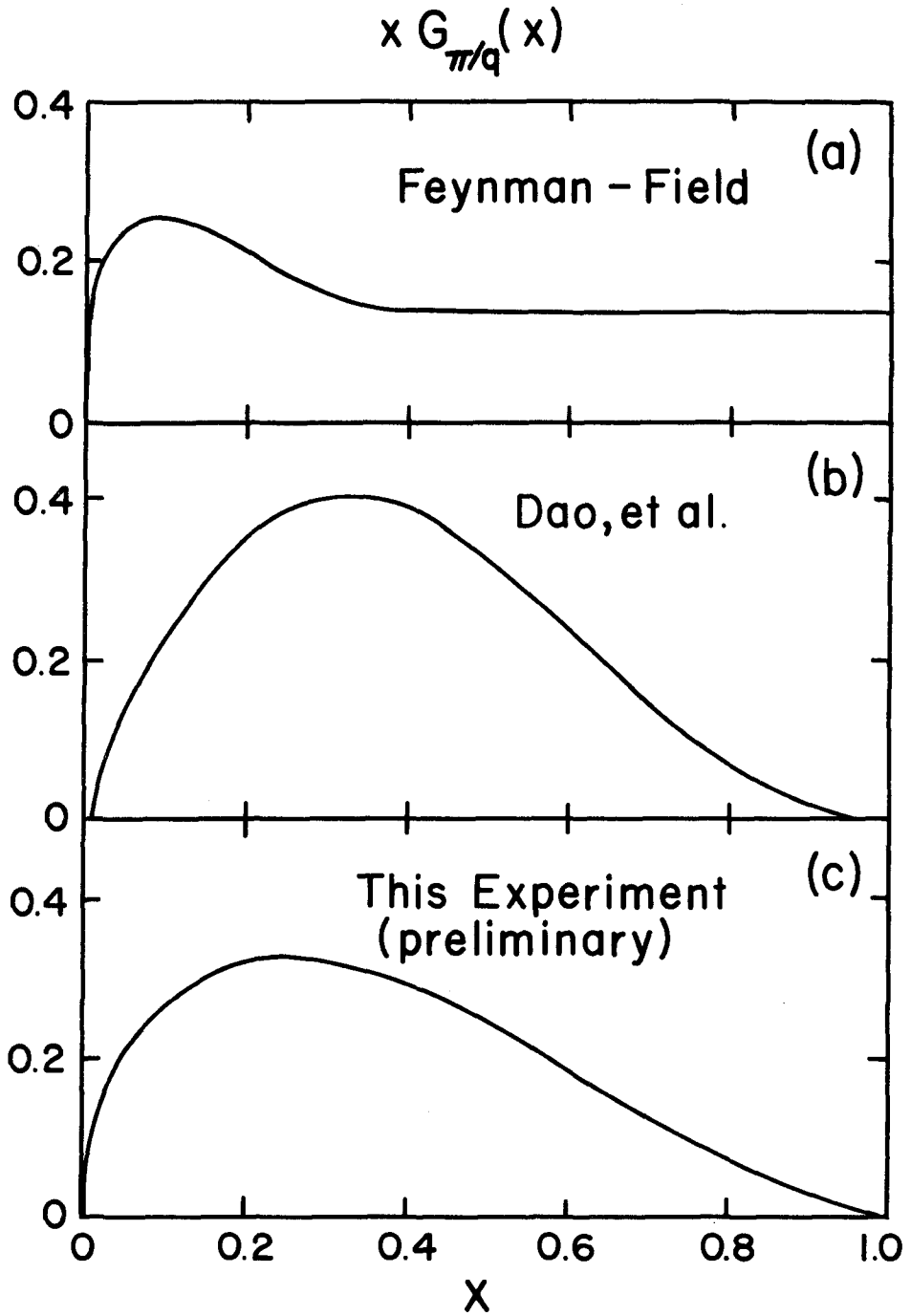

XBL 789-11372

Fig. 3-8 Pion structure function from three sources. a) Ref. 3-8; b) Ref. 3-12; c) This experiment.

Dao et al. assume a power law dependence $(1 - x)^{\alpha}$ near $x = 1$.

3.1.4 Beam Ratio at Equal Quark Energies

In the preceeding sections, our results were compared with the predictions of several theories. These predictions, however, are mainly derived from very complicated formalisms which tend to hinder one's understanding. In the following, I discuss our results from the simple point of view of the quark content of the hadrons (Tab. 3-2).

TABLE 3-2

QUARK CONTENT OF HADRONS

$p - \|uud)$	$\pi^+ - \|u\bar{d})$	$K^+ - \|u\bar{s})$
$\bar{p} - \|\bar{u}\bar{u}\bar{d})$	$\pi^0 - \|u\bar{u} - d\bar{d})/\sqrt{2}$	$K^- - \|\bar{u}s)$
	$\pi^- - \|\bar{u}d)$	

First, we look at the data from a plausible but, I believe, incorrect angle. We hypothesize that the main mechanism for creating a π^0 at high $P_\perp$ is one of quark fusion: an antiquark from the beam hadron fuses with a quark from the target hadron. A π^0 can be built from either a $u\bar{u}$ or $d\bar{d}$ pair, so that in a $\pi^- p$ collision the π^- supplies the $\bar{u}$ and the proton supplies the u. In a pp collision, however, the necessary antiquark must come from the sea of $q\bar{q}$ pairs; thus the reaction is suppressed (Fig. 3-9 a).

Checking the rough quantitative predictions of this model against the data shows some serious discrepancies. We can calculate the beam ratios $R(\pi^+/\pi^-)$, $R(p/\pi^-)$ as shown in Tab. 3-3. In each case, we take the ratio of the total number of combinations of beam and target quarks which

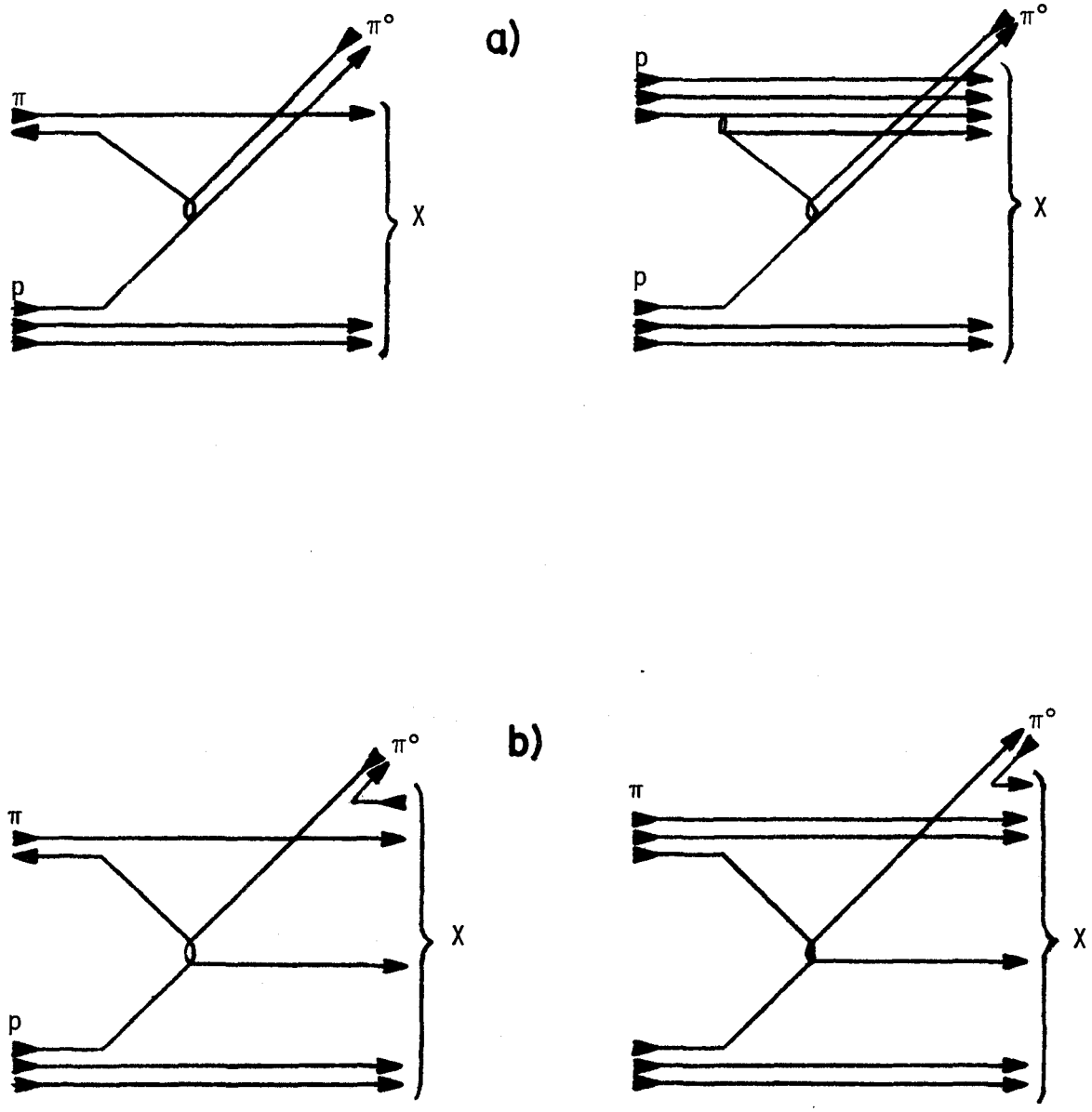

Fig. 3-9 Comparison of π^0 production in πp and pp interactions.
a) Quark fusion process; b) $qq \rightarrow qq$ scatter plus quark decay.

TABLE 3-3

RATIO OF CROSS SECTIONS

Reaction	Quark fusion	Quark scatter (with decay)	Ratio of total cross sections	Ratio of beam quarks	Data (*@ 90°, low $P_\perp$)
$\frac{\pi^+ p}{\pi^- p}$	$\frac{1}{2}$	$\frac{12}{12}$	1.0	$\frac{2}{2}$	1.
$\frac{\pi^- p}{K^- p}$	$\frac{2}{2}$	$\frac{12}{9}$	1.1	$\frac{2}{2}$	1.
$\frac{p\ p}{\pi^+ p}$	$\frac{0}{1}$	$\frac{18}{12}$	1.6	$\frac{3}{2}$	1.5*
$\frac{\bar{p}\ p}{p\ p}$	$\frac{5}{0}$	$\frac{18}{18}$	1.1	$\frac{3}{3}$	1.3

could make a π^0. For instance, the ratio $R(\pi^+/\pi^-)$ shows the difference in a very simple way. The fact that the proton has two u quarks and one d quark gives the 1:2 ratio. Quite dramatic is the $R(\bar{p}/p) \sim 5:0$. The main problem with this model seems to be the overly stringent requirement on the two quark components of the π^0 that one comes from the beam and the other from the target.

Another possibility is that the incoming hadrons scatter with just one quark being kicked out at high $P_\perp$. This one then finds a companion from the $q\bar{q}$ sea with which to make a π^0. We might even say that the high $P_\perp$ quark "decays" into a π^0. The other decay products then go into the inclusive "X" and are not detected as in Fig. 3-9b.

Table 3-3 shows the prediction for the beam ratios in the case of "qq scatter plus decay". Now that the requirements for making a π^0 are simply that one scatter a u, $\bar{u}$, d or $\bar{d}$ quark at large angle, the ratios are much closer to the ratio of total cross sections. It is interesting to note that the numbers we obtain by this method are also consistent with the ratio of total cross sections. It is unclear why this is the case, as the total cross sections are dominated by the low $P_\perp$ behavior where the cross sections are large and practically insensitive to the high $P_\perp$ behavior where the cross sections are small.

Another idea to try is the ratio at equal quark energy, as discussed in the Introduction. The reasoning is simply that the quarks in the pion and proton on the average share equally in the hadron momentum. With 50% more quarks in the proton than in the pion, the quark-quark scattering energy will be the same if the momentum of the proton beam is 50% greater than the momentum of the pion beam P_B (Ref.3-16). Thus the ratio of cross sections would be a constant equal to the ratio of the number of

beam quarks:

$$(3\text{-}14) \qquad Ed^3\sigma/dp^3(pp \to \pi^0 X)\Big|_{1.5\,P_B} \Big/ Ed^3\sigma/dp^3(\pi p \to \pi^0 X)\Big|_{P_B} = n_q(p)/n_q(\pi)$$

We take the idea of equal quark energy to be in the sense of the average over all x as in Eq. 3-6, since the quarks apparently share the momentum of the hadron over a broad range of momenta as in Fig. 3-3 and 3-8.

We show this ratio for 90^0 data in Fig. 3-11a plotted versus $P_\perp$. It is instructive to compare this p/ ratio at equal quark energy with $R(p/\pi)$ in Fig. 2-18 taken at equal hadron energy. Where the latter is falling dramatically with $P_\perp$, the former is nearly flat in $P_\perp$. We have also interpolated between our 100 GeV/c and 200 GeV/c beam data by assuming x_D scaling to a beam energy of 133 GeV/c in order to make the comparison pp at 200 GeV/c versus πp at 133 GeV/c. This appears in Fig. 3-11b and is also nearly constant.

We can use this same interpolation to effect a comparison at 30^0 scattering angle: σ_{pp}(200 GeV/c) / $\sigma_{\pi p}$(133 GeV/c) at 30^0 cm. This ratio appears in Fig. 3-11c. Our ratio at 30^0 strongly suggests that the equal quark energy comparison is not limited to the 90^0 cm region.

The regularity shown by these comparisons suggests that the difference in πp and pp scattering may be compensated for by a change in the beam momentum to bring the quark-quark scattering energies to the same value. Once this is done, the cross sections per incident quark are identical. This is consistent with the idea that quarks scatter from each other independent of the kind of hadron they came from, and that the pion's quarks have a 50% larger momentum fraction per quark than the proton's quarks.

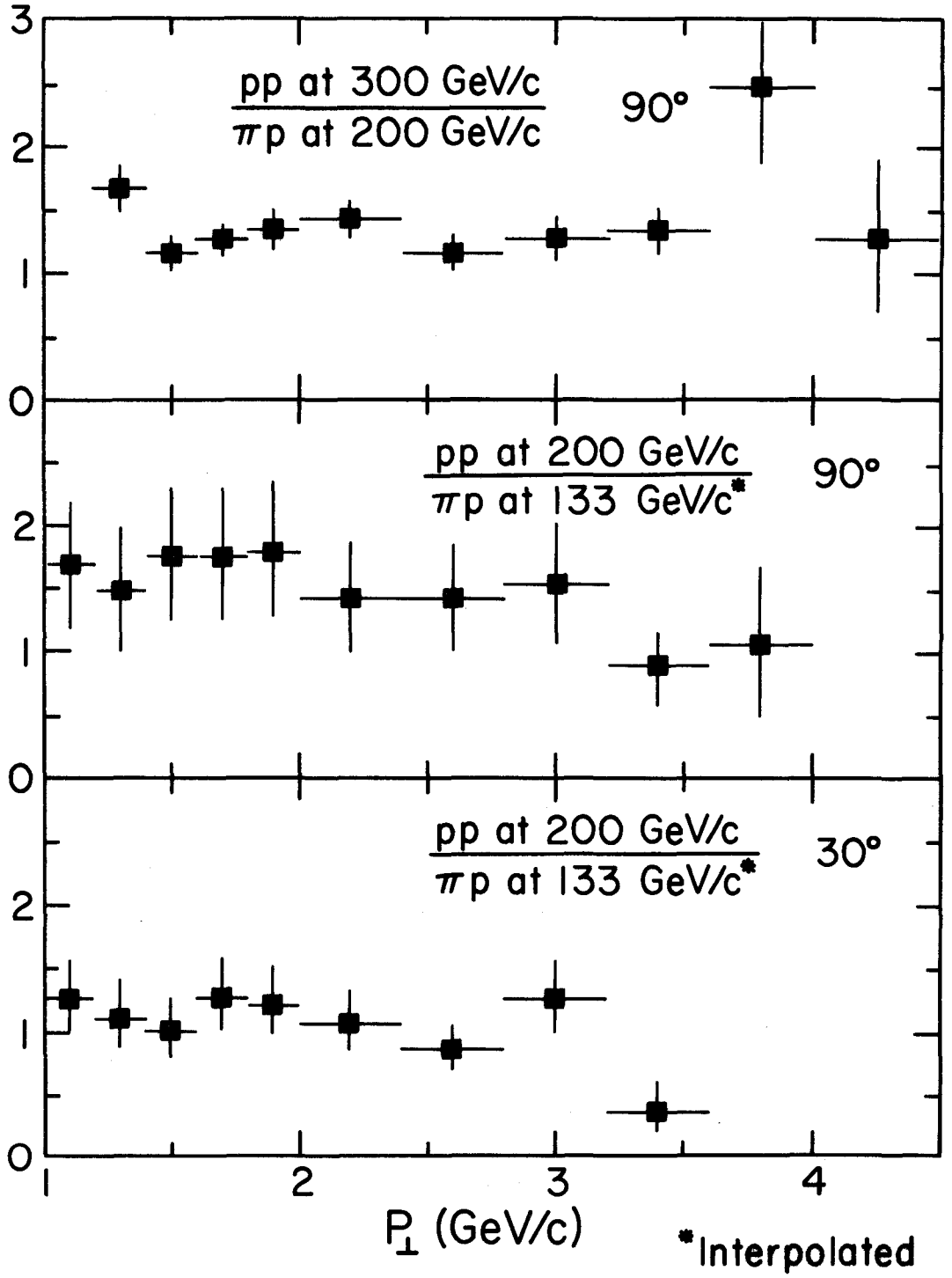

Fig. 3-10 Beam ratios at equal quark energy versus $P_\perp$ as defined in Eq. 3-14, data at 133 GeV/c is interpolated: XBL 789-11378
a) pp @ 300 GeV/c / πp @ 200 GeV/c, at 90° cm;
b) pp @ 200 GeV/c / πp @ 133 GeV/c, at 90° cm;
c) pp @ 200 GeV/c / πp @ 133 GeV/c, at 30° cm.

These simple, intuitive concepts yield a surprisingly consistent picture of the data. This does not constitute a model *per se*. I have discussed these ideas to illustrate the more formal interpretations developed previously.

3.2 Conclusions

Notwithstanding the difficulties with strong interaction theory mentioned in the Introduction, I draw two tentative conclusions from the data of this experiment (Ref. 3-17). They are a synthesis of the interpretations discussed previously, in which partons in the hadrons undergo a hard scatter to produce the high $P_\perp$ π^0.

A pion structure function with an appropriate quark momentum fraction seems to account for the features of the π/p ratio. A momentum fraction of quarks in the pion half again greater than that of quarks in the proton is consistent with the data and with the quark model picture of the pion as a pair of quarks and the proton as a trio of quarks.

Also, it seems to not matter in π^0 production at high $P_\perp$ whether the beam quarks are made of matter or antimatter. There appears to be a common subprocess in the all-hadronic reactions seen in this experiment in which quarks and antiquarks participate equally.

Of course, final conclusions are inappropriate. Indeed, experiments such as this represent more of a beginning than an end. Experimental work in hadronic interactions will continue, since this will be the testing ground for any candidate for a theory of strong interactions such as quantum chromodynamics (Ref. 3-18). With the recent introduction of supersymmetry (Ref. 3-19) which seeks to unify the large-scale phenomena of gravity with the short-scale phenomena of quantum particle physics,

and the promising picture of QCD as a theory for strong interactions, the theoretical picture of the four fundamental interactions may be close to the long-sought unity underlying all the laws of physics.

SUPPLEMENT 1

Fermilab Accelerator and M2 Transport

The Meson area is one of several experimental areas at Fermilab which receive the intense, high-energy proton beam from the main proton synchrotron (Ref. S1-1). The protons begin their trip at the Cockcroft-Walton electrostatic pre-accelerator (see Fig. A1-1a), pass through the radio-frequency (RF) powered linear accelerator, then into the booster synchrotron. At each of these preliminary stages, the protons receive more energy. By the time they pass from the booster into the main ring, they have a momentum of 8 GeV/c. Thirteen pulses from the booster accumulate in the 2 km diameter main ring, after which the beam begins its 10-second acceleration to 400 GeV/c. At this point, about 10^{13} protons are circulating in the main ring, tightly bunched by the main ring RF field used to accelerate them. In a period of about one second (the flat top), the protons are smoothly extracted to the experimental area. The Meson area receives a fraction of these proton on its target. The path of these protons is within a very high vacuum, as any air molecules present would quickly destroy the intensity of the beam through scattering.

The production target itself is a tungsten rod in which about 2/3 of the protons interact. Most of the interactions result in a proton's simply changing its direction slightly. However, some score a more direct hit on a target nucleus, shattering it. The resulting debris contains all kinds of particles at differing momenta.

The task of the beam line is to collect and transport particles of a particular momentum and polarity to the experimental target. There are six beam lines in the Meson area, each "looking at" the Meson target.

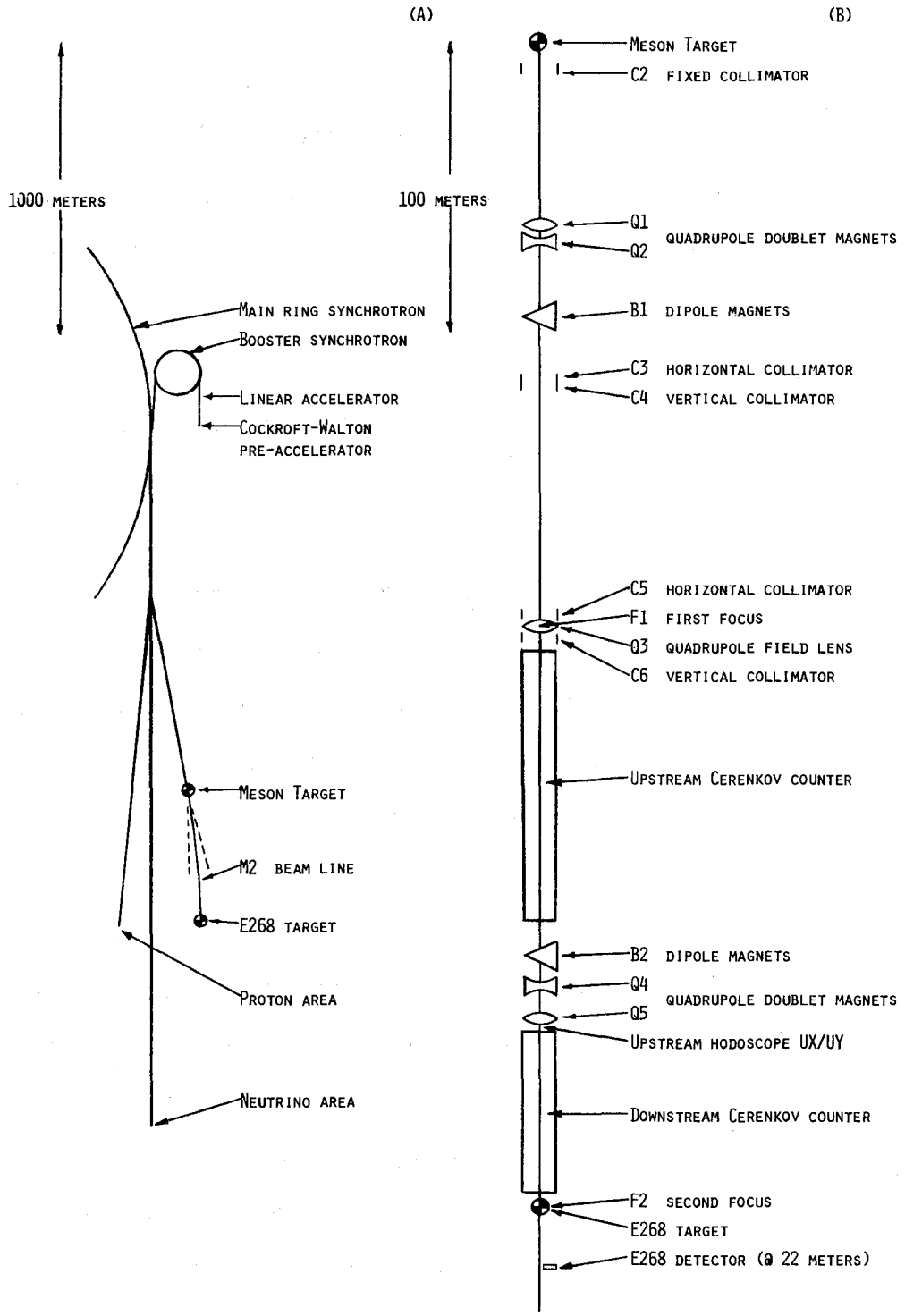

XBL 7810-11703

Fig. S1-1 (A) Fermilab proton synchrotron and experimental areas. (B) M2 beam line optics (schematic).

The M2 beam looks almost head-on at the target; particles need only scatter by 1 milliradian (mr) to pass through the collimator.

The arrangement of the magnets along the M2 line (see Fig. A1-1b) approximately follows a classic configuration consisting of quadrupole doublet focussing magnets Q1 and Q2, followed by dipole bending magnets B1 creating an image of the target at the first focus F1 followed by a repetition of the entire thing in mirror symmetry*.

The fixed collimator (C2) just downstream of the production target as well as movable collimators (C3, C4, C6) control the acceptance of the beam line and consequently the intensity of the beam. We maintained this typically at 2 million particles per spill.

The horizontal collimator (C5) at the first focus, however, controls the size of the momentum acceptance of the beam line. It works as follows: The dipole magnet B1 set at a certain excitation current has just enough impulse to cause a 100 GeV/c momentum positive particle to bend as it passes through, so that it is accepted by the rest of the beam line. A 101 GeV/c particle will not bend as much, and at the first focus will therefore be one inch to the right of the beam center line. At this point, the jaws of the C5 collimator, set at ±1 inch will block any beam not in the momentum interval 101-99 GeV/c. The dispersion of the first focus is the change in beam position divided by the percent change in momentum, i.e., 1"/($\Delta P/P$)%. In fact, controlling the momentum acceptance of the beam is the purpose of the dipole magnets. The focussing magnets work in conjunction with this momentum definition since with a given excitation current, their focussing properties only hold for a given

---

* "Time" symmetry would be more precise. All the bends are in the same direction.

momentum.

The symmetry of the beam lines gives the second focus F2 a special property, namely that the dispersion here is zero. The second set of bending magnets exactly cancels the dispersion of the first set. In reality, our beam line was not perfectly symmetrical.

The quadrupole magnet at the first focus Q3 acts as a field lens. The action of this magnet is to focus rays emanating from the center of the front dipoles B1 to the center of the rear dipoles B2. This effectively increases the acceptance of the beam line.

At the second focus F2, which coincides with the downstream beam hodoscope, the 200 GeV/c beam is typically 3 mm X 3 mm in size, while the angular divergence is .5 mr X .2 mr (FWHM). We usually operated with $\Delta P/P = 1\%$.

The bunching of the main ring beam in "RF buckets" causes the secondary beam to be similarly bunched. All the particles in the secondary beam arrive in groups separated by 18 nanoseconds (ns) (18×10^{-9} seconds), the period of the main ring RF. In each bunch there may be one or more particles or none at all. Within each bunch, the particles are close together indeed - about 1 ns apart. This bunching of the secondary beam played an important part in the way we set up our trigger electronics, as discussed in 2.2.4, PPERP Trigger.

To determine the proper magnet currents for a desired beam momentum, we used a model of the beam (TRANSPORT) (Ref. S1-2) on the Fermilab CDC6600 computer and the measured excitation functions of the magnets. In practice, we first set the dipole currents from the excitation curve, then set the quadrupole currents to minimize the spot size of the beam in the downstream hodoscope. For the latter task, we found "tune curves"

derived from TRANSPORT to be of aid. These are sets of quadrupole settings which move one focus (for instance, the horizontal) upstream or downstream while keeping the other focus fixed. This allowed us to minimize the spot size in each dimension independently.

We controlled all these beam line elements by means of a computerized control system. The Fermilab serial CAMAC system allowed us to control the magnet power supplies and the motors for the collimator jaws remotely from a console at the experiment.

SUPPLEMENT 2

Shower Process and Detector Resolution

Neutral particles leave no track of ionization as do charged particles, so a special detector is generally needed. In this experiment, the photons were detected by causing them to shower in a series of lead plates. Interleaved planes of scintillation counters in a hodoscope array then detected the cascade of charged particles. This supplement describes the shower process and discusses the energy and position resolution of the photon detector.

When a high-energy photon traveling through lead passes near a nucleus, it may undergo conversion or pair production. It turns into an electron-positron pair which carries off practically all the photon's energy and momentum. An electron or positron passing near a nucleus in turn may bremsstrahlen or shake off a photon. The electron continues on but shares its original energy with the photon. These electrons, positrons and photons continue to multiply in a cascade resulting in a shower of many much lower energy particles. The total energy of all these particles equals that of the original photon E_o and, due to the small angle nature of pair production and bremsstrahlung, the original direction is preserved as well.

The formation process of the shower outlined above competes with various absorption processes which cause the daughter particles to stop before they can multiply. The photon may lose energy through Compton scattering and the electron through ionization loss. The formation processes predominate at high energy while absorption dominates at low energy. The dividing line occurs at the critical energy E_{cr} characteristic

of the material. For lead, E_{cr} = 8 MeV. The shower develops until there are N_{max} particles, each of energy E_{cr}:

(S2-1) $$N_{max} = E_o/E_{cr}$$

The characteristic distance for conversion and for bremsstrahlung is about the same and is known as the radiation length χ_o. For lead, χ_o = 5.6 mm. For any material, the number of charged particles N_{ch} increases exponentially, approximately doubling every successive radiation length, until the maximum number N_{max} is present. This occurs at a depth $t\chi_o$ where:

(S2-2) $$t = 1.01 \ln(E_o/E_{cr}) + .8$$

Then, as absorption takes over, N_{ch} drops exponentially by a factor of about 2 every radiation length (Ref. S2-1). For typical photons in our detector, $t \simeq 8$, so the shower peaks at half the depth of the detector.

Energy Resolution

A sampling shower counter such as ours measures the photon's energy by repeatedly measuring N_{ch} and adding up the samples over the depth of the entire counter. This sum is called the charged particle crossings N_{cc} and, like N_{max}, is proportional to the photon energy:

(S2-3) $$N_{cc} = \sum N_{ch} \propto E_o$$

The energy resolution is governed by fluctuations in N_{cc} and by fluctuations in the phototube response. Poisson statistics then specify for the energy resolution:

(S2-4) $$\sigma_E^2 \propto N_{cc}$$

and for our detector:

(S2-5) $$\sigma_E/E = k/\sqrt{E_0}, \quad \text{with } k = .25\sqrt{(\text{GeV})}$$

Thus, the energy resolution is inversely proportional to the square root of the photon energy and, for our detector, is about 25% at 1 GeV.

Energy resolution is also affected by the amount of the shower leaking out the back of the detector. This process has non-Gaussian fluctuations but can be reduced by making the detector sufficiently deep in radiation length. The last scintillator in our detector was 17 χ_0 deep, about two times deeper than shower maximum. The detector provided fine protection against leakage up to the maximum π^0 energy encountered in the experiment.

Position Resolution

The position resolution σ_x for a hodoscope shower counter is determined primarily by the fluctuations in the wings of the shower. Let us calculate σ_x for a shower centered on one finger, with energy P_0 in that finger and with approximately equal shower energies P_1 and P_{-1} in adjacent fingers. With the shower position determined by Eq. 2-4:

(S2-6) $$\Delta x = (P_1 - P_{-1})/P_0$$

and with energy fluctuations on each P_i given by:

(S2-7) $$\sigma_i^2 = k^2 P_i, \text{ with k as in Eq. S2-5}$$

It is simple to derive the relation:

(S2-8) $$\sigma_x = \frac{k}{\sqrt{P_0}} \sqrt{((P_1 + P_{-1})/P_0)}$$

For showers in our detector, $(P_1 + P_{-1})/P_0 \sim 1/2$ so the position

resolution in finger units is approximately equal to the energy resolution σ_E/E as in Eq. S2-4. Thus, for a 2.5 GeV photon, the minimum accepted in the data analysis, the position resolution is about 2 mm.

SUPPLEMENT 3

Decay Properties of the π^0

Since this experiment was based on the detection of the π^0 through its decay, we should keep in mind several of its decay properties (see Table S3-1). The most important are decay length, minimum decay angle, decay energy distribution and branching fraction.

Decay Length

The decay length is the parameter used to characterize the lifetime of an unstable particle such as the π^0. Due to relativistic effects, the decay length in the lab L for a π^0 of momentum P depends on its velocity $\eta = P/m_{\pi^0}$ and on the mean life, $c\tau$:

$$L = \eta c\tau \tag{S3-1}$$

For P = 1 GeV/c, L = .18μm and for P = 100 GeV/c, L = 18μm. It is clear that even for the highest energy π^0, the decay length is much smaller than our target length of .6 m.

Minimum Decay Angle

In the rest frame of the π^0, the photons from the $\pi^0 \rightarrow 2\gamma$ decay are always back-to-back and of equal energy. This is the only photon configuration that can conserve momentum and energy, and it fixes the energy of the two photons $k^* = m_{\pi^0}/2$ (see Fig. S3-1a). In the laboratory, however, the energies of the two photons can be quite different from each other and will be about half the lab energy of the π^0 (see Fig. S3-1b). The angle of the photons in the π^0 rest frame relative to the π^0 lab momentum is the helicity angle θ_π. It is related to the lab momentum of the two photons k_1 and k_2 by the relation:

TABLE S3-1

DECAY PROPERTIES OF THE π^o

Mass	m_{π^o}	.1349 GeV
Mass	$m^2_{\pi^o}$	.0182 $(GeV)^2$
Mean Life	$c\tau$	2.5E-8 m
Spin/Parity	J^P	0^-

Decay Rates

$\gamma\gamma$	.9885
γe^+e^-	.0115
$e^+e^-e^+e^-$	3.32E-5
$\gamma\gamma\gamma$	(5E-6)
$\gamma\gamma\gamma\gamma$	(6E-6)
e^+e^-	(2E-6)

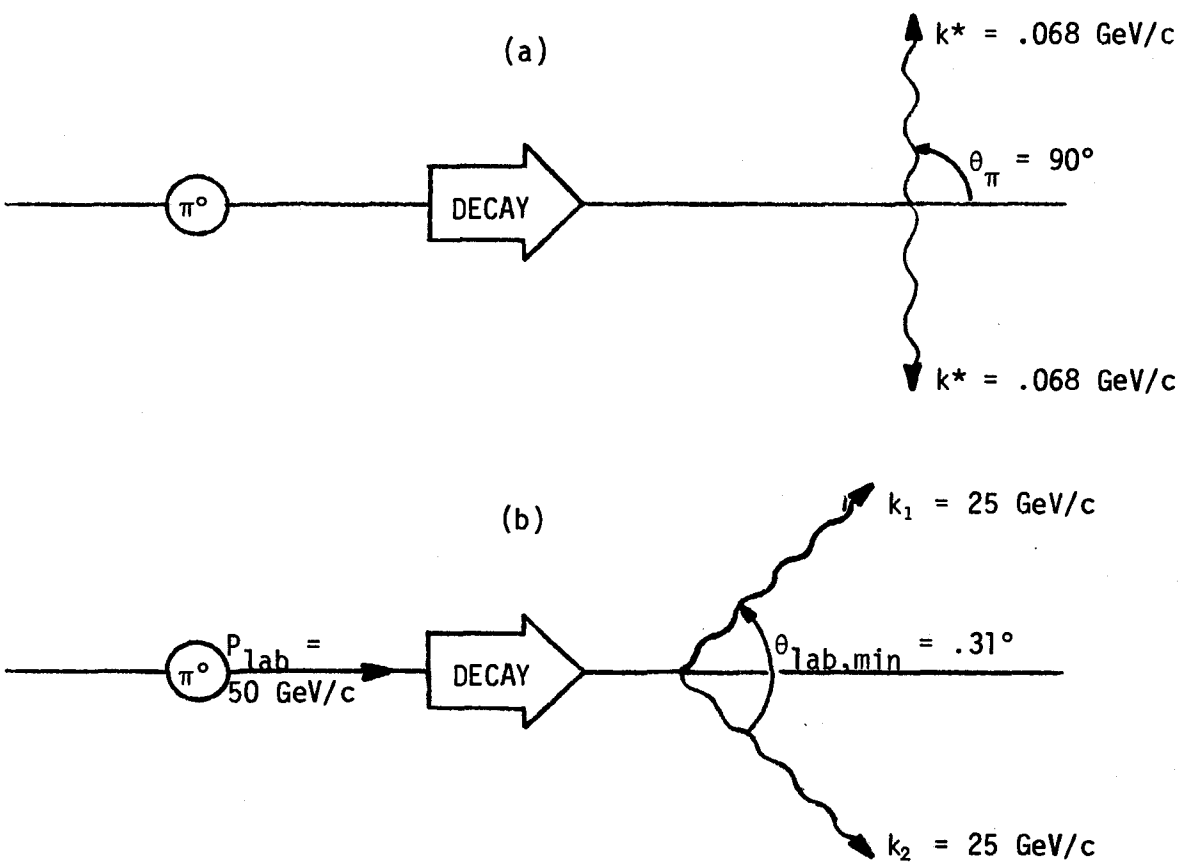

Fig. S3-1 Symmetric decay of $\pi^o \to \gamma\gamma$: a) rest frame of π^o; b) lab frame.

(S3-2) $$\frac{k_1 - k_2}{k_1 + k_2} = \frac{\eta}{\gamma} \cos\theta_\pi \text{ , where } \eta = P/m_{\pi^o} \text{ and } \gamma = E/m_{\pi^o}$$

Since $P/E \simeq 1$, this is approximately:

(S3-3) $$\frac{k_1 - k_2}{k_1 + k_2} \simeq \cos\theta_\pi$$

The lab angle between the two photons θ_{lab} is related to θ_π and η through the equation:

(S3-4) $$\sin\theta_{lab} = 2/(\eta\cos\theta_\pi + 1/(\eta\cos\theta_\pi))$$

and since $\eta >> 1$ and $\theta_{lab} << 1$,

(S3-5) $$\theta_{lab} \simeq 2/(\eta\cos\theta_\pi)$$

We obtain the minimum decay angle in the case where $\cos\theta_\pi = 1$.

(S3-6) $$\theta_{min} \simeq 2/\eta = 2m_{\pi^o}/P$$

This formula shows that for a given π^o lab momentum P, there is a minimum angular separation between the decay photons in the lab.

To see how this effect manifests itself in our detector, which has a two-photon resolution of 1.5 fingers, consider a π^o produced at a lab angle of 100 mr with a $P_\perp$ of 5 GeV/c. The lab momentum would be 50 GeV/c corresponding to θ_{min} = 5.4 mr. With a target to detector length of 5 m, this corresponds to a separation in the detector of 2.7 cm, well in excess of the minimum separation needed for resolution.

Photon Energy Distribution

Another concern is the distribution of energy seen in the detector. Given a π^o of momentum P in the lab, what are the highest and lowest lab

energies seen for the photons? Are there more events at higher energy or at lower?

The key to resolving these questions is to note that since the π^o has no angular momentum, it must decay isotropically in its rest frame. Let $P(\cos\theta_\pi)$ represent the probability for the π^o to decay with helicity angle θ_π. Since all values of $\cos\theta_\pi$ are equally likely:

(S3-7) $$P(\cos\theta_\pi) = 1$$

If the corresponding lab photon momentum is k, then we want to know what P'(k) is. We know from the relativistic transformation from π^o rest frame to the lab frame that:

(S3-8) $$k = (\gamma + \eta\cos\theta_\pi)m_{\pi o}/2$$

Using the simple relation between $P(\cos\theta_\pi)$ and P'(k):

(S3-9) $$P(\cos\theta_\pi)d\cos\theta_\pi = P'(k)dk$$

to obtain:

(S3-10) $$P'(k) = 2/(\eta m_{\pi o}) = 2/P$$

This tells us that the decay energy distribution is also flat. The limits for k are approximately:

(S3-11) $$m_{\pi o}/(2\gamma)^2 < k < E, \text{ where } E = \sqrt{(P^2 + m_{\pi o}^2)}$$

The result is that there are no more photons at the high end than at the low end of the energy spectrum. Therefore, our photon detector must be good at resolving photons of all energies. Since the two photon energies must add up to E, we will be seeing photon pairs of energy.

(S3-12) $$\begin{aligned} k_1 &= E/2 + k \\ k_2 &= E/2 - k \end{aligned}$$, where k is a parameter giving the asymmetry of energies

The case of $\theta_\pi = 90^o$ gives the case of symmetric decay (as in Fig. S3-1):

(S3-13) $$k_1 = k_2 = E/2$$

Another question is how large the detector must be to capture a given fraction of the π^o decays. One half of the π^o's decay with $\cos\theta_\pi$ in the range $|\cos\theta_\pi| < 1/2$. Let us see where these decay photons go in the lab (see Fig. S3-2). The photon lab angles θ_1 and θ_2 are given by:

(S3-14) $$\sin\theta_1 = \sin\theta_\pi/(\gamma + \eta\cos\theta_\pi)$$
$$\sin\theta_2 = \sin\theta_\pi/(\gamma - \eta\cos\theta_\pi)$$

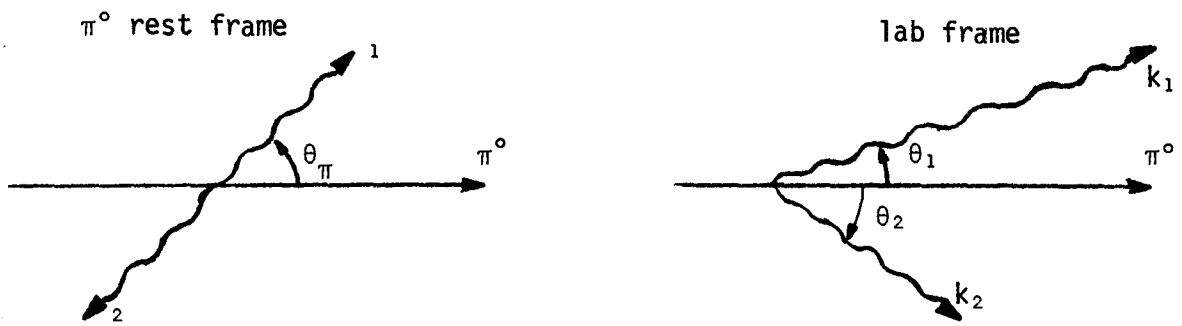

Fig. S3-2 Definition of decay angles θ_π, θ_1, θ_2.

For $\cos\theta_\pi = 1/2$ and for $\eta >> 1$, this simplifies to:

(S3-15) $$\sin\theta_1 \simeq \sqrt{3}/\gamma \text{ and } \sin\theta_2 \simeq 1/(\sqrt{3}\gamma)$$

Taking the larger of the two angles, we calculate the diameter D of a disc which, when placed L = 5 m away from the decay vertex, would subtend this angle:

(S3-16) $$D \simeq 2L\sin\theta_1 \simeq 2\sqrt{3}L/\gamma$$

For a π^o of lab momentum 5GeV/c, the γ is 37 and D is $\sim$.5 m. Thus, our .7 m square detector will have a geometric efficiency of greater than

1/2 for such pions aimed at its center. For π^0's with greater lab energy the probability of detection is correspondingly greater.

Branching Fraction

As Table S3-1 shows, fully 99% of π^0 decays go through the channel $\pi^0 \rightarrow 2\gamma$. Our detector is therefore sensitive to the most common decay mode of the π^0. Other modes are also possible to detect, but with poorer efficiency.

APPENDIX 1

Cerenkov Counters

This appendix treats the basics of the Cerenkov counters, beginning with some simple Cerenkov formulae as apply to our super-relativistic beam, the optics of the counter, counter efficiency and π/K discrimination. I discuss how we went about tuning and using the counter and the kinds of trade-offs involved in choosing the operating parameters.

Formulae

The phenomenon of Cerenkov radiation, discovered only in 1937 (Ref. A1-1) is now a well-established laboratory tool in particle physics for distinguishing between particles on the basis of velocity. When a charged particle passes through matter, the electrons in the medium can oscillate coherently (Fig. A1-1). If the speed of light (the reciprocal

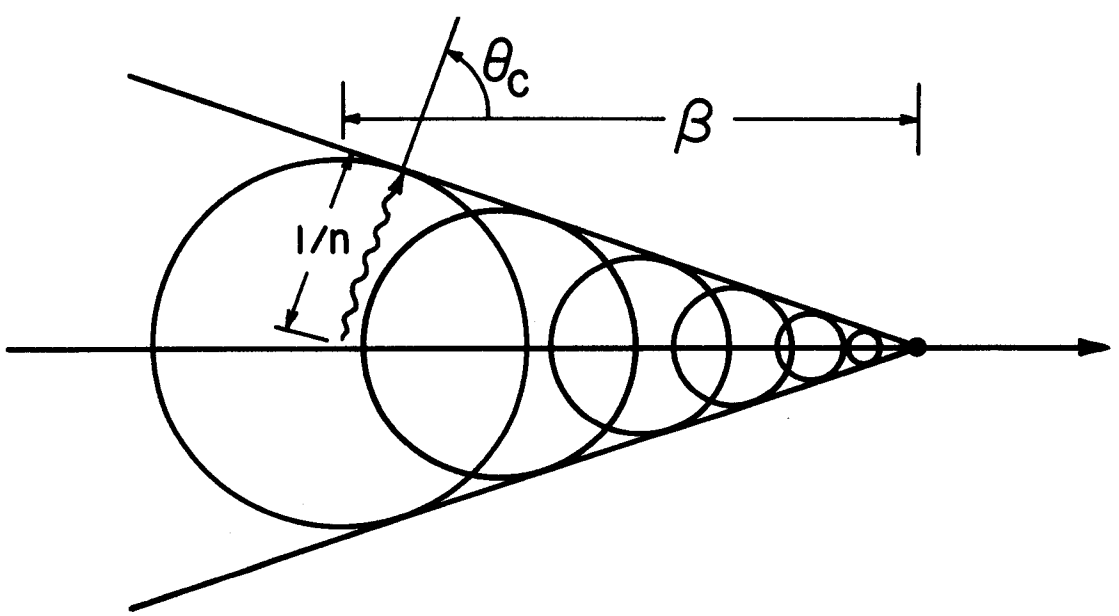

Fig. A1-1 Relationship between particle speed $\beta = \eta/\gamma$, light velocity $1/n$ and Cerenkov angle θ_C.

of the refractive index n of the medium) is less than the speed of the charged particle β, the coherent oscillations will add together to form a uniform wavefront - radiated light. The light emanates from the particle's path in a cone of fixed angle θ_C, given by

(A1-1) $$\cos\theta_C = 1/(n\beta)$$

At the high beam momenta common at Fermilab, Cerenkov light can be produced even in rarified gasses. For these, the index of refraction is

(A1-2) $n = 1 + a_G A$, where A is the absolute pressure of the gas and a_G is a constant, called the optical activity of the gas.

The β of these particles is, in terms of the beam momentum p and particle mass m:

(A1-3) $$\beta = \sqrt{(1 - (m/P)^2)} \simeq 1 - (m/P)^2/2$$

At high beam momentum ($m/P \ll 1$) and for small Cerenkov angles ($\theta_C \ll 1$), we can give an approximate formula for the latter:

(A1-4) $$\theta_C{}^2 = 2a_G P - (m/P)^2$$

Thus, there is a threshold pressure A_{th} below which no Cerenkov light is produced and which depends on the velocity of the particle:

(A1-5) $$A_{th} = \frac{1}{2a_G}(m/P)^2$$

And, independent of particle type, the Cerenkov angle is a function of the pressure above threshold $\Delta A = A - A_{th}$:

(A1-6) $$\theta_C{}^2 = 2a_G \Delta A$$

In a particle beam of fixed momentum, the particles of different masses can be distinguished by their different Cerenkov angles. In particular, we have the following formula:

(A1-7) $$\theta_\pi^2 - \theta_K^2 = (m_\pi^2 - m_K^2)/P^2, \quad \text{independent of pressure}$$

Also, if the average of the two angles $\theta_m = (\theta_\pi + \theta_K)/2$ is known, then the difference will be inversely proportional to the beam momentum squared:

A1-8) $$\Delta\theta_{\pi K} = \theta_\pi - \theta_K = \frac{1}{2\theta_m}(m_\pi^2 - m_K^2)/P^2$$

We see, then, that the job of π/K separation becomes more difficult as the beam momentum increases and as the average angle increases.

However, we want the Cerenkov angle to be as large as possible from the standpoint of efficiency. The counter inefficiency decreases exponentially with the number of Cerenkov photons. In fact, if n_{ph} represents the number of photoelectrons liberated at the photocathode, the inefficiency is:

(A1-9) $$\text{Ineff} = \exp(-n_{ph})$$

This number is in turn related to the Cerenkov angle:

(A1-10) $$n_{ph} = 2\pi\alpha\frac{\Delta f}{c}\ l_{eff}\ \sin\theta_C$$

In this formula, α is the fine structure constant ($\sim 1/137$), Δf represents the integrated bandwidth of the phototube (with the photocathode quantum efficiency folded in), l_{eff} is the effective length of the counter, and θ_C is the Cerenkov angle.

By using the small-angle approximation ($\sin\theta \simeq \theta$) and Eq. A1-6, we

can give n_{ph} as a universal function of $n_o = 2\pi\alpha(\Delta f/c)l_{eff}$, a function only of the properties of the counter, and a_G which depends only on the refractive index of the medium, and A the pressure above threshold:

(A1-11) $$n_{ph} = n_o\ 2\ a_G\ A$$

It is interesting to see just how stringent the requirements on a counter can become. If we require the difference $\Delta\theta_{\pi K}$ to be greater than the beam angular divergence θ_B for π/K separation and also require the number of photons to be greater than some minimal number n_{min} for the sake of efficiency, then we can use Eq. A1-8 and A1-10 to obtain the inequality:

(A1-12) $$n_o = 2\pi\alpha\frac{\Delta f}{c}\ l_{eff} > n_{min}\ (2\theta_B)^2\ P^4/(m_K^2 - m_\pi^2)^2$$

Thus the effective length of the counter must increase like the fourth power of the beam momentum. In fact, our counters used drift lengths in the beam line each greater than 50 meters in length. We also used a special phototube for one of the counters (CDO) with a very wide Δf, an RCA 3100M.

We can derive from the individual counters' efficiencies ε the number of photoelectrons given off the photocathode, normalized to the number produced at θ_o = 1mr, using Eq. A1-9 and A1-10:

(A1-13) $$n_p = -\ln(1 - \varepsilon)\frac{\sin^2\theta_o}{\sin^2\theta_C}\ ,\ \theta_o = 1\text{mr for normalization}$$

Table A1-1a shows n_p inferred in this way for each of the counters at each running configuration. These compare well with n_p = .34 derived from Cerenkov pressure curves for CDO taken during running and using Eq. A1-11.

It is also possible to derive an expected value of n_p' from knowledge of the effective bandwidth of the photocathode Δf and the known length of the Cerenkov counter l_{eff} (Eq. A1-9):

(A1-14) $$n_p' = 2\pi\alpha\frac{\Delta f}{c}\, l_{eff} \sin^2\theta_o \quad , (\theta_o = 1mr)$$

With l_{eff} = 56 m, we obtain the values for n_p' for each of the two phototubes used in the counter as shown in Tab. A1-1b.

Note that these differ from the results actually obtained in practice, as in Tab. A1-1a, by a clear factor of 10. This discrepancy is due in part to our not taking into account the efficiency of the optics of the counters and the vignetting of the Cerenkov light by the beam tube itself. But there is still a large factor not accounted for.

TABLE A1-1a

NUMBER OF PHOTOELECTRONS

n_p', number of photoelectrons normalized to θ_C = 1mr

COUNTER	200 GeV/c @ 90°cm	200 GeV/c @ 30°cm	100 GeV/c @ 90°cm	100 GeV/c @ 30° cm
CUI	.191	.256	.177	.081
CUI	.149	.182	.162	.161
CDI	-	.177	.103	.099
CDO	-	.237	.167	.206

TABLE A1-1b

NUMBER OF PHOTOELECTRONS

PHOTOTUBE RCA #	$2\pi\alpha\Delta f/c$ [1/m]	n_p
8850	21,400	1.2
3100M	56,900	3.2

Cerenkov Counter Configuration

The optics of the counters was simple in principle (see Fig. A1-2). A flat mirror, inclined 45° to the beam and with a hole for the beam, reflected the Cerenkov light to the telescope mirror. The latter focussed the light ($f = 2.4$ m) outside the gas volume of the counter. On its way, it passed through another cut out in the 45° mirror and through a quartz window for best UV light transmission into a light-tight box which housed the phototubes. In the focal plane lay a small tipped mirror, cut out in such a way that it presented a circle to the telescope mirror. Several tipped mirrors were available in a choice of radius r_m.

It was here the π/K separation took place. Cerenkov light of angle θ became a ring of light with radius $r = \theta f$. Light with a Cerenkov angle greater than $\theta_m = r_m/f$ passed by the tipped mirror and into the outer phototube. The face of the tipped mirror was curved to match the telescope mirror to the inner phototube much like a field lens.

Here can be seen the significance of Eq. A1-8. The angle of the tipped mirror θ_m will be close to the average of θ_π and θ_K. So in choosing the tipped mirror, we made it large enough to give a large n_{ph} for good counter efficiency and yet not so large that the π/K separation was compromised.

It was also important to have a gas medium with low dispersion, as the light rings were blurred by the dispersion of the gas. Table A1-2 presents the properties of several gasses, showing helium to be the best choice in this regard. Other contributors to blurring of the rings were the finite angular spread of the beam (.5 mr) and the precision of the optics.

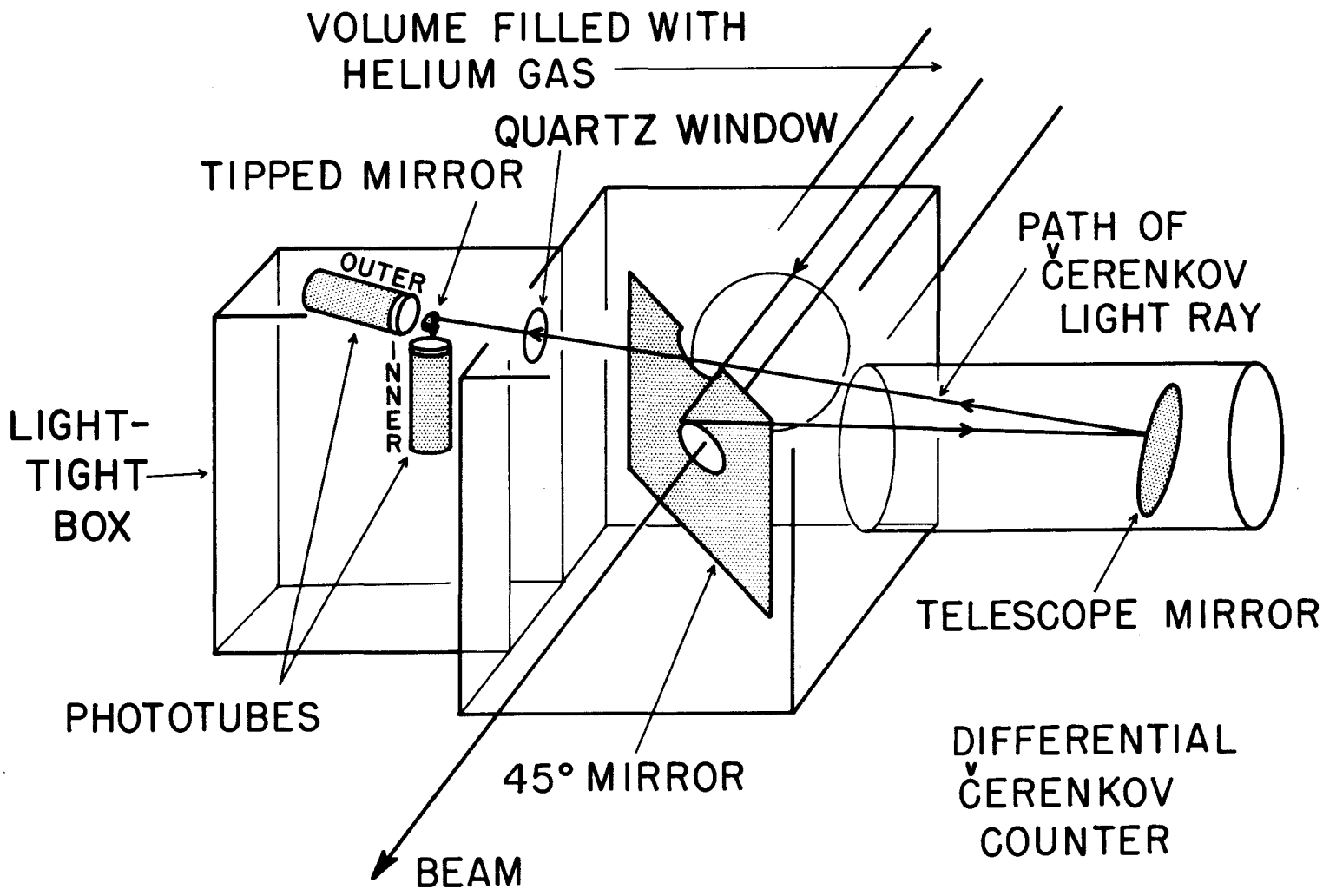

Fig. A1-2 Cerenkov counter optics.

XBL 789-11384

TABLE A1-2

PROPERTIES OF GASSES

GAS	OPTICAL ACTIVITY a_G [1/mmHg]	DISPERSION $(\Delta a_G/a_G)/(\Delta\nu/\nu)$
He	46.4E-9	.0324
H_2	190.0E-9	.1107
N_2	403.0E-9	.0770
CO_2	463.0E-9	.0899

Tuning

At the beginning of a data session, we tuned the Cerenkov counters. This entailed choosing the appropriate tipped mirror, aligning the optics of the counters, and filling them with the proper amount of helium gas. The 45° flat mirror was made to match the beam pipe with the telescope mirror, while the latter had two angle adjustments (pitch in the vertical plane and yaw in the horizontal plane), so as to properly align it with respect to the image of the beam pipe in the 45° flat mirror and the tipped mirror. After selecting and installing the tipped mirror in the light-tight box, we adjusted it and the phototubes so that the outer phototube's light collection cone nearly reached the plane of the tipped mirror, and so that the inner phototube was in the path of light from the telescope mirror reflected from the tipped mirror.

The pitch and yaw adjustments as well as the counter pressure were remotely adjustable through a control-and-readout box in the experimenter's area. In this way, the fine-tuning of the counters was carried out without necessitating access to the beam area.

We usually began by running pressure curves in the counters, showing the π and K thresholds. This provided us with a rough idea of the

correct counter pressure at which to operate. Next, the pitch and yaw had to be adjusted. The object was to center the π and K rings on the circular outline of the tipped mirror. For this, we used an iterative procedure. At the end, the counter would be at its best operating point.

In the fine-tuning, we found it helpful to have a real-time readout of the CERBIT distribution (see 2.4.5, Cerenkov Analysis). This was done by a specially built 1 of 16 decoder and scaler bank combination. Each scaler registered the counts of one bin in the 16 bin CERBIT histogram. We could thus study every possible counter signature. Our object was to minimize the ones indicating inefficiency or crosstalk.

The most important indicators of π/K separation were N(7), N(13) and N(11), N(14). The former indicated K's crossing over to the π sample and the latter π's crossing over to the K sample. Presumably these would indicate a poorly-adjusted pitch or yaw for one of the Cerenkov counters: N(7), N(11) for the upstream, N(13), N(14) for the downstream. Our procedure was to adjust the pitch and yaw of each counter to minimize the cross over rate. This had the effect of centering the K and π rings on the circular outline of the tipped mirror.

Important for a pure $\bar{p}$ sample was minimizing the inefficiencies of the counters, indicated by low N(1), N(4) for K's and N(2), N(8) for π's. Figure A1-3 illustrates how the counter pressure influences kaon efficiency in the upstream counter. As the pressure rises, the Cerenkov angle increases and the inefficiency rate N(1) falls. Eventually, the kaon ring of light exceeds the size of the tipped mirror, so we started getting stray light in CUQ and the crosstalk rate N(7) rises. This limits the pressure, and we are forced to use the lower pressure operating point

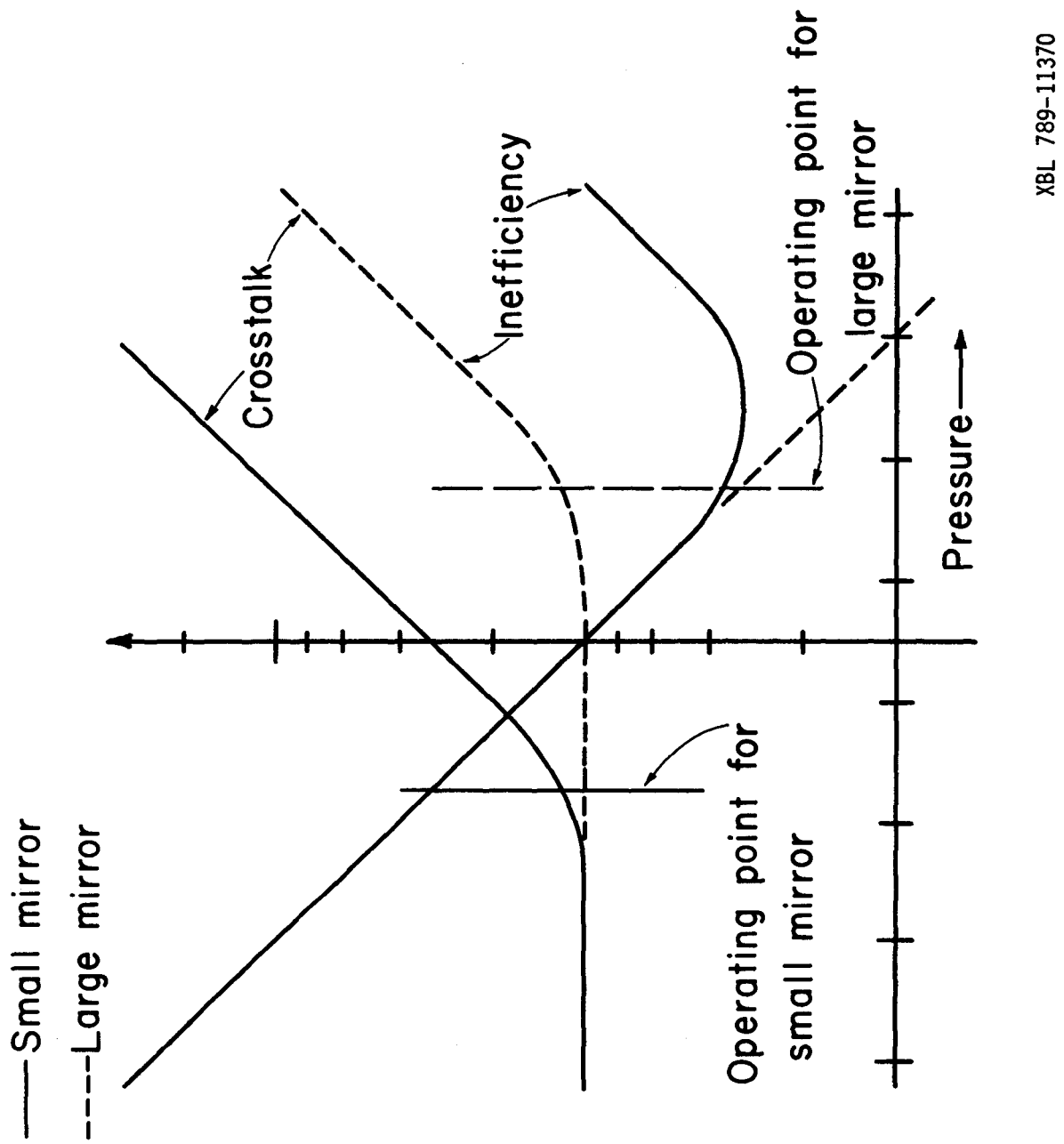

Fig. A1-3 Pressure curve for Cerenkov counter showing crosstalk and inefficiency on logarithmic scale for two alternative tipped mirror sizes. Larger mirror gives lower inefficiency at optimum operating point.

indicated. However, using a slightly larger mirror could obtain improved efficiency, as shown by the dashed curves. In this case, the higher pressure was the optimum. The mirror size is, of course, limited by considerations of π/K separation.

Thus by adjusting pitch, yaw and pressure of the two counters, and by using the various signatures as indicators, we would close in on the final operating parameters of the counter. At this point, recording the scalers provided a standard to use in monitoring the continued good performance of the counters.

APPENDIX 2

Kinematic Formulae

This appendix sets forth in greater detail the formulas used to reconstruct the lab momenta of the beam, target and detected photons. It also discusses the kinematic variables peculiar to this experiment, such as the scaling variables $x_{\parallel}$ and $x_{\perp}$.

Figure A2-1 illustrates the determination of the lab momenta. We note them as:

(A2-1)
$$P_B^{\mu} = (E_B, \vec{P}_B) = (E_B, P_{Bz}, P_{By}, P_{Bx}) \quad \text{Beam}$$
$$P_T^{\mu} = (E_T, \vec{P}_T) = (M_p, 0, 0, 0) \quad \text{Target}$$
$$k^{\mu} = (k, \vec{k}) = (k_o, k_z, k_y, k_x) \quad \text{Photon}$$

where the target is assumed to be a proton at rest in the lab.

The beam coordinates in the hodoscopes (z_{up}, y_{up}, x_{up}) and (z_{dn}, y_{dn}, x_{dn}) respectively, determined the angle of the beam particle, denoted (z_B', y_B', x_B') and the interaction and decay vertex (z_T, y_T, x_T):

(A2-2)
$$z_B = z_{up} - z_{dn} \qquad z_B' = z_B/r_B$$
$$y_B = y_{up} - y_{dn} \qquad y_B' = y_B/r_B$$
$$x_B = x_{up} - x_{dn} \qquad x_B' - x_B/r_B$$
$$r_B = \sqrt{z_B^2 + y_B^2 + x_B^2}$$
$$z_T = 0$$
$$y_T = y_{dn} - z_{dn} y'/z'$$
$$x_T = x_{dn} - z_{dn} x_B'/z_B'$$

The Cerenkov information determines the type of the beam particle, and therefore its mass M_B. Taking the momentum as the nominal beam momentum P, the beam 4-vector becomes:

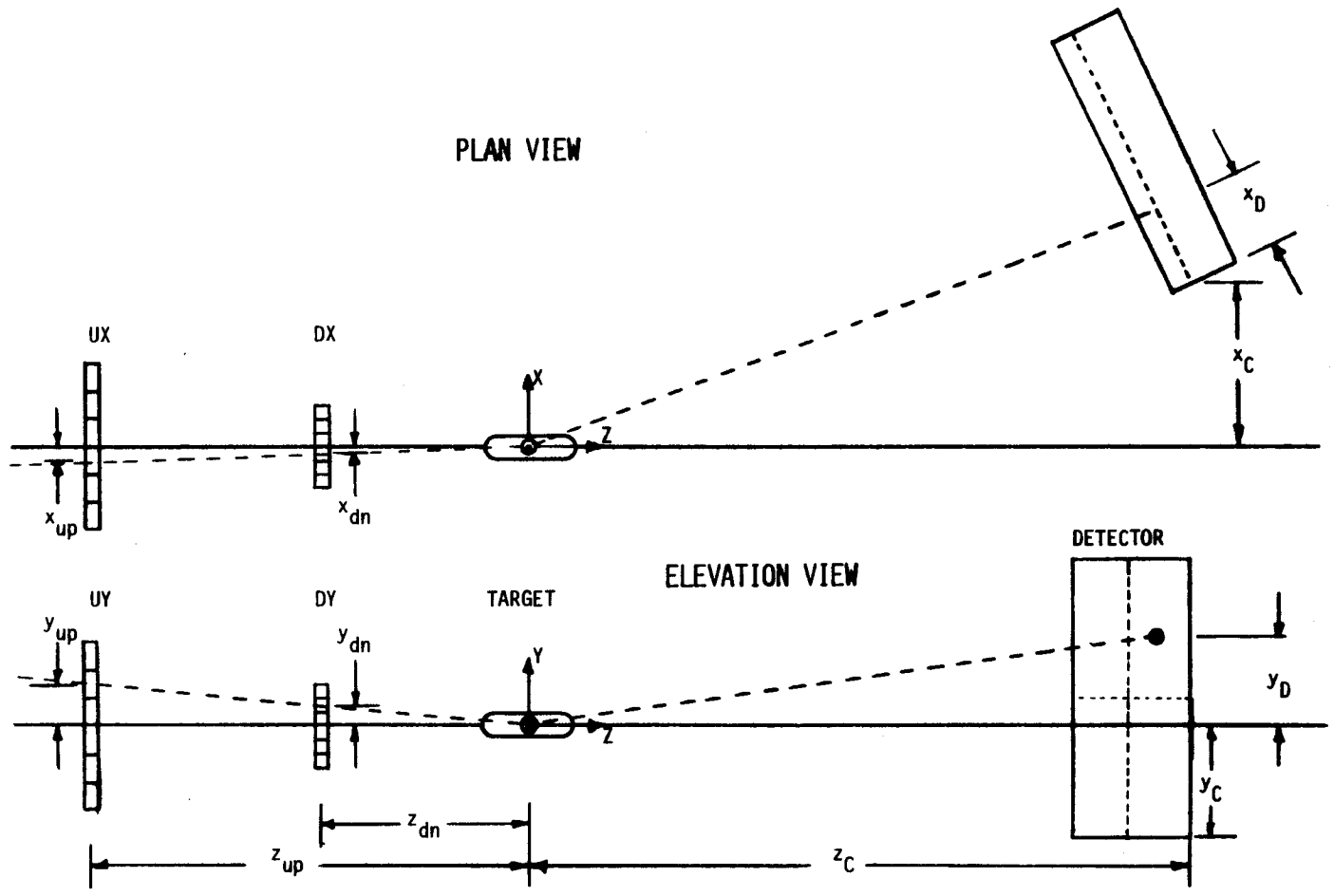

Fig. A2-1 Laboratory coordinates for an event.

(A2-3)
$$E_B = \sqrt{(P^2 + M_B^2)}$$
$$P_{Bz} = z_B' P$$
$$P_{By} = y_B' P$$
$$P_{Bx} = x_B' P$$

Thus the total momentum of the initial state, the cm momentum is:

(A2-4)
$$P^{\mu}_{cm} = P^{\mu}_B + P^{\mu}_T \underset{lab}{=} (E_B + M_T, \vec{P}_B)$$

A photon's momentum is calculated from its position in the detector (y_D, x_D) in finger units and energy E_D in MPHA units. The coordinates of the detector at $x_D = y_D = 0$ in the lab are (z_C, y_C, x_C). At each detector setting, we rotated the detector to face the target by an angle noted θ_C. For the conversion to lab coordinates, there is a constant k_f (= .0105) to convert from finger units to meters and a constant k_E to convert from MPHA units to GeV. The lab coordinates are:

(A2-5)
$$z_\gamma = z_C - z_T - k_f x_D \sin\theta_C \qquad z_\gamma' = z_\gamma / r_\gamma$$
$$y_\gamma = y_C - y_T + k_f y_D \qquad y_\gamma' = y_\gamma / r_\gamma$$
$$x_\gamma = x_C - x_T + k_f x_D \cos\theta_C \qquad x_\gamma' = d_\gamma / r_\gamma$$
$$r_\gamma = \sqrt{(z_\gamma^2 + y_\gamma^2 + x_\gamma^2)}$$

The photon momentum is then:

(A2-6)
$$k_o = k_E E_D$$
$$k_z = k_o z_\gamma'$$
$$k_y = k_o y_\gamma'$$
$$k_x = k_o x_\gamma'$$

and the momentum of a photon pair is noted:

(A2-7) $$P_C^\mu = (E_C, \vec{P}_C) = k_1^\mu + k_2^\mu$$

Kinematic Parameters

For the discussion of the kinematic parameters, it is important to recall the definition of the scalar product of two 4-vectors, P and Q:

(A2-8) $$PQ = P^\mu Q_\mu = P_o Q_o - \vec{P}\cdot\vec{Q}$$

which implies the definition of invariant length:

(A2-9) $$P^2 = P^\mu P_\mu = P_o^2 - |\vec{P}|^2$$
$$|P| = \sqrt{P^2}$$

The invariant mass of the cm system is:

(A2-10) $$W^2 = s = P_{cm}^2 \underset{lab}{=} 2E_B M_T + M_B^2 + M_T^2$$

The covariant velocity is defined as:

(A2-11) $$\eta^\mu = (\gamma, \vec{\eta}) = P/|P|$$
$$\beta = |\vec{\eta}|/\gamma$$

Recall that $\eta^2 = \gamma^2 - \vec{\eta}^2 = 1$, be definition.

All the lab vectors $P^\mu = (E, \vec{P})$ are transformed to the cm frame $p*^\mu = (E*\vec{P}*)$ by the usual relativistic transformation determined by:

(A2-12) $$\eta_{cm}^\mu = (\gamma_c, \vec{\eta}_{cm}) = P_{cm}^\mu/|P_{cm}|$$

The transformation is:

(A2-13) $$E* = \eta_{cm}^\mu P_\mu = \gamma_{cm} E - \vec{\eta}_{cm}\cdot\vec{P}$$
$$p* = \vec{P} - \vec{\eta}(E* + E)/(\gamma_{cm} + 1)$$

In this frame $P_{cm}^\mu = (W, \vec{0})$ by definition.

The beam, target and photon pair vectors take the form:

(A2-14)
$$P^{\mu}_{B} \underset{cm}{=} (E^{*}_{B}, P^{*}_{B}, 0, 0)$$
$$P^{\mu}_{T} \underset{cm}{=} (E^{*}_{T}, -P^{*}_{B}, 0, 0)$$
$$P^{\mu}_{C} \underset{cm}{=} (E^{*}_{C}, \vec{P}^{*}_{C}) = (E^{*}_{C}, P^{*}_{C}\cos\theta^{*}_{C}, P^{*}_{C}\sin\theta^{*}_{C}, 0)$$

where we now take the beam direction as the new spatial z-axis.

In the cm frame the $P_{\parallel}$ and $P_{\perp}$ are easy to calculate:

(A2-15)
$$P_{\parallel} = P^{*}_{C}\cos\theta^{*}_{C}$$
$$P_{\perp} = P^{*}_{C}\sin\theta^{*}_{C}$$

The maximum momentum available to C, P_o, as used in Eq. 1-1, is precisely given by:

(A2-16)
$$P_o = \sqrt{(s/4 - (M_C^2 + M_M^2)/2 + (M_C^2 - M_M^2)^2/(4s))} \simeq \sqrt{s}/2$$

where M_M is the mass of the lightest possible particles which can recoil against C, consistent with conservation laws. Table A2-1 shows the quantity P_o scaled by the approximate value of $\sqrt{s}/2 \simeq \sqrt{(P_B M_T/2)}$, for all the beams and momenta in our experiment.

In our data analysis, we calculated the scaling parameters according to the formula:

(A2-17)
$$x_R = P^{*}_{C}/P_o$$
$$x_{\parallel} = P^{*}_{\parallel}/P_o = x_R\cos\theta^{*}_{C}$$
$$x_{\perp} = P^{*}_{\perp}/P_o = x_R\sin\theta^{*}_{C}$$

Table A2-2 gives the definitions of the many interrelated kinematic parameters along with their values in the super relativistic limit where all particle masses are negligible.

Figure A2-2 illustrates the correspondence of the different coordinate systems in a Peyrou plot (axes $x_{\parallel}, x_{\perp}$). Lines of constant $x_{\parallel}$ and

$x_\perp$ are vertical and horizontal, respectively. Lines of constant x_R are circles concentric at the origin while those of constant $\theta_{cm} = \theta_C^*$ are rays from the origin.

Lines of constant x_1 and x_2 are parabolas cofocal at the origin. The equations for lines of constant x_1 or x_2 are:

(A2-18)
$$x_\parallel = ((x_\perp/2)^2/x_1 - x_1)$$
$$x_\parallel = -((x_\perp/2)^2/x_2 - x_2)$$

TABLE A2-1

MAXIMUM CM ENERGY FOR DIFFERENT BEAMS

Beam Particle and Mass (Gev)	Target Particle and Mass (GeV)	Detected Particle and Mass (GeV)	Minimum Recoil Particle and Masses (Gev)	$P_o/\sqrt{(P_B M_T/2)}$ @ 100 GeV/c $\sqrt{(P_B M_T/2)} = 6.849$	$P_o/\sqrt{(P_B M_T/2)}$ @ 200 GeV/c $\sqrt{(P_B M_T/2)} = 9.68$
p .9383	P .9383	π^o .1350	pp 1.8766	.9859	.9930
K^+ .4937	"	"	K^+p 1.4320	.9920	.9960
π^+ .1396	"	"	π^+p 1.0779	.9961	.9981
$\bar{p}$ .9383	"	"	π^o .1350	1.0045	1.0023
K^- .4937	"	"	Λ 1.1156	.9963	.9981
π^- .1396	"	"	n .9396	.9976	.9988

TABLE A2-2

KINEMATIC PARAMETERS AND VALUES

IN THE SUPER-RELATIVISTIC LIMIT

Parameter and Definition	Value in cm Frame	Value in Lab Frame
$s = (P_B + P_T)^2$	$(2E_B^*)$	$2E_BM_T$
$t = (P_B - P_C)^2$	$-4E_B^*E_C(1 - \cos\theta_C^*)/2$	$-4E_BE_C(1 - \cos\theta_C)/2$
$u = (P_B - P_C)^2$	$-4E_B^*E_C^*(1 + \cos\theta_C)/2$	$-2M_TE_C$
$M_X = (P_B + P_T - P_C)^2$	$s(1 - E_C^*/E_B^*)$	
$\varepsilon = M_X^2/s$	$1 - E_C^*/E_B^*$	
$x_R = 1 - \varepsilon$	E_C^*/E_B^*	
$\sqrt{(t/u)}$	$\tan\theta_C^*/2$	
$x_1 = -t/s$	$x_R(1 - \cos\theta_C^*)/2$	
$x_2 = -u/s$	$x_R(1 + \cos\theta_C^*)/2$	
$x_\perp = 2\sqrt{(x_1x_2)}$	$x_R\sin\theta_C^*$	
$x_\parallel = x_2 - x_1$	$x_R\cos\theta_C^*$	

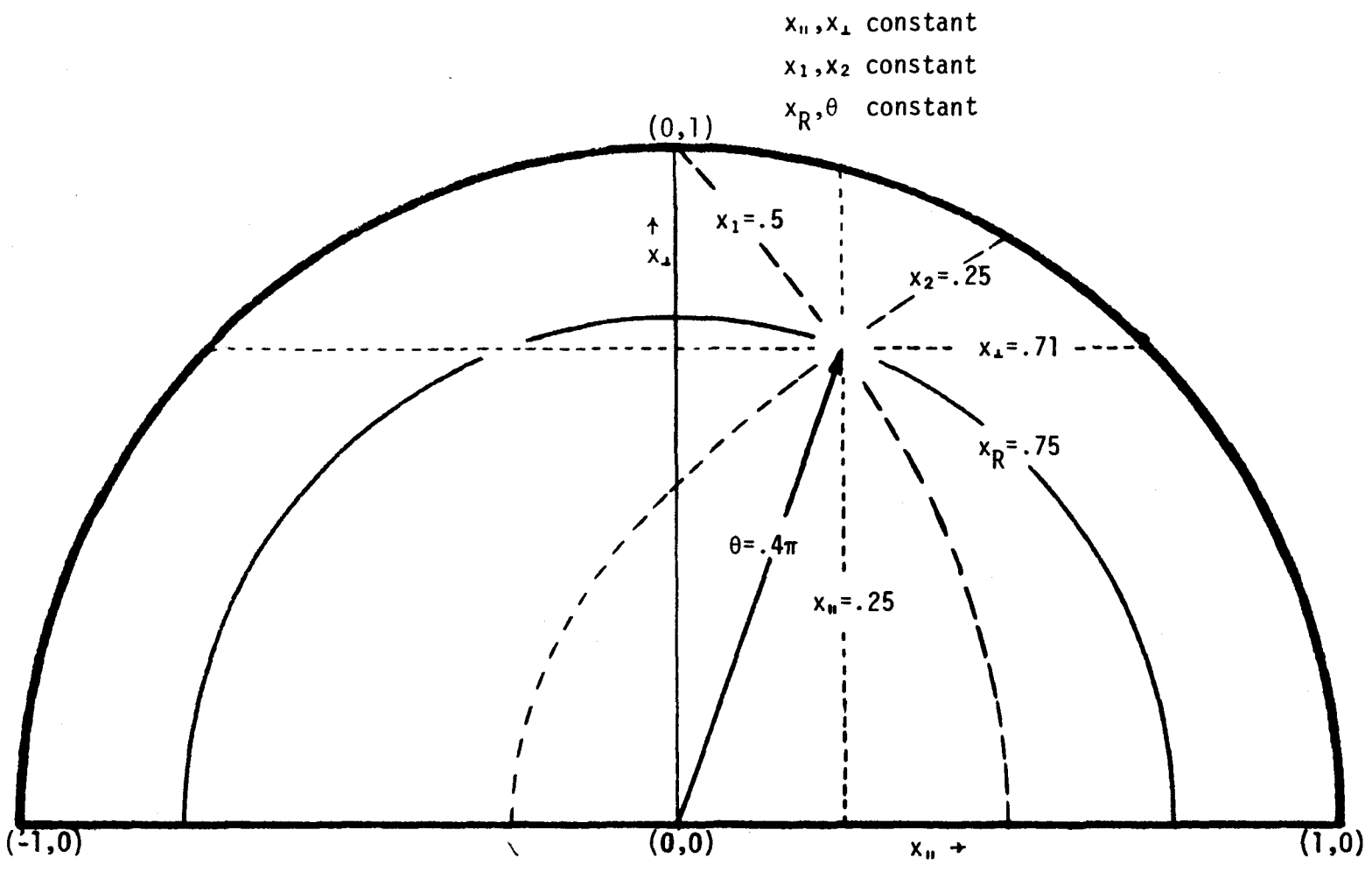

Fig. A2-2 Kinematic parameters in a Peyrou plot. Lines of constant $x_{\parallel}$, $x_{\perp}$, x_1, x_2, x_R and θ_{cm} are shown.

APPENDIX 3

Graphs of Cross Sections

This appendix presents computer-generated graphs of the data. They are organized by beam particle; Fig. A3-2 for π^+p, Fig. A3-3 for π^-p, and Fig. A3-4 for pp cross sections. In each figure a) and b) are at 100 GeV/c; c) and d) are at 200 GeV/c; and in Fig. A3-4, e) and f) are at 300 GeV/c beam momentum. The data appear in a), c) and e) versus $x_{\parallel}$; and in b), d) and f) versus θ_{cm}. Fig. A3-1 is a legend of the labels of the bands of $P_{\perp}$ in Fig. A3-1, 2 and 3.

Data with $P_{\perp}$ dependence from the fit divided out versus x_D appear in Fig. A3-5 for π^-p, and Fig. A3-6 for pp. In these plots, a) is at 100 GeV/c; b) is at 200 GeV/c; and Fig. A3-6c is at 300 GeV/c. The curves from the fit are independent of $P_{\perp}$ except near the kinematic limit.

□	$.2 < P_\perp < .4$
○	$.4 < P_\perp < .6$
△	$.6 < P_\perp < .8$
+	$.8 < P_\perp < 1.0$
×	$1.0 < P_\perp < 1.2$
◇	$1.2 < P_\perp < 1.4$
▽	$1.4 < P_\perp < 1.6$
⊠	$1.6 < P_\perp < 1.8$
✳	$1.8 < P_\perp < 2.0$
⌖	$2.0 < P_\perp < 2.4$
⊕	$2.4 < P_\perp < 2.8$
⧈	$2.8 < P_\perp < 3.2$
⊞	$3.2 < P_\perp < 3.6$
⊠	$3.6 < P_\perp < 4.0$
⧈	$4.0 < P_\perp < 4.5$
□	$4.5 < P_\perp < 5.0$
○	$5.0 < P_\perp < 5.5$
△	$6.0 < P_\perp < 6.5$

XBL 789-11437

Fig. A3-1 Legend of $P_\perp$ band labels.

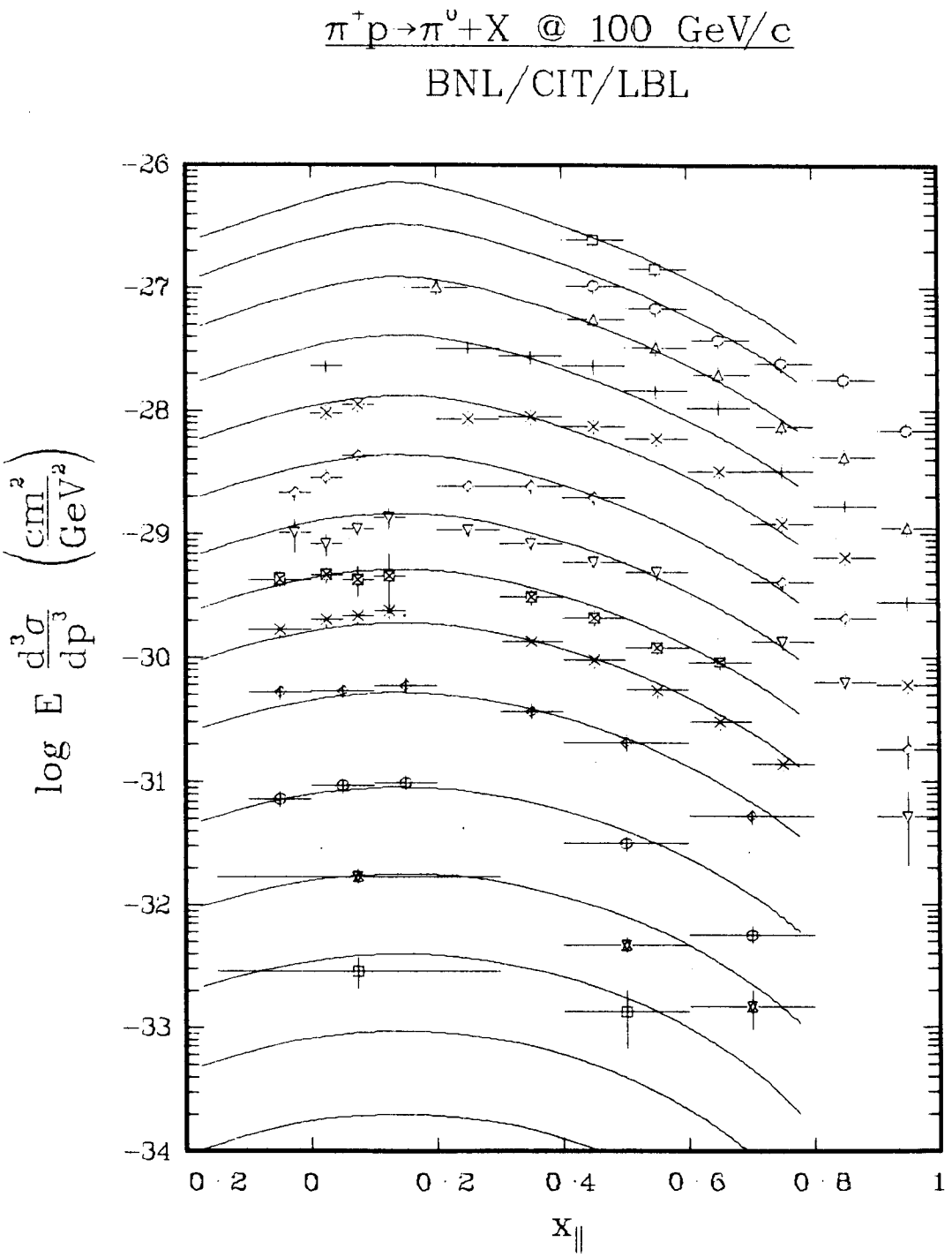

Fig. A3-2a.

XBL 789-11422

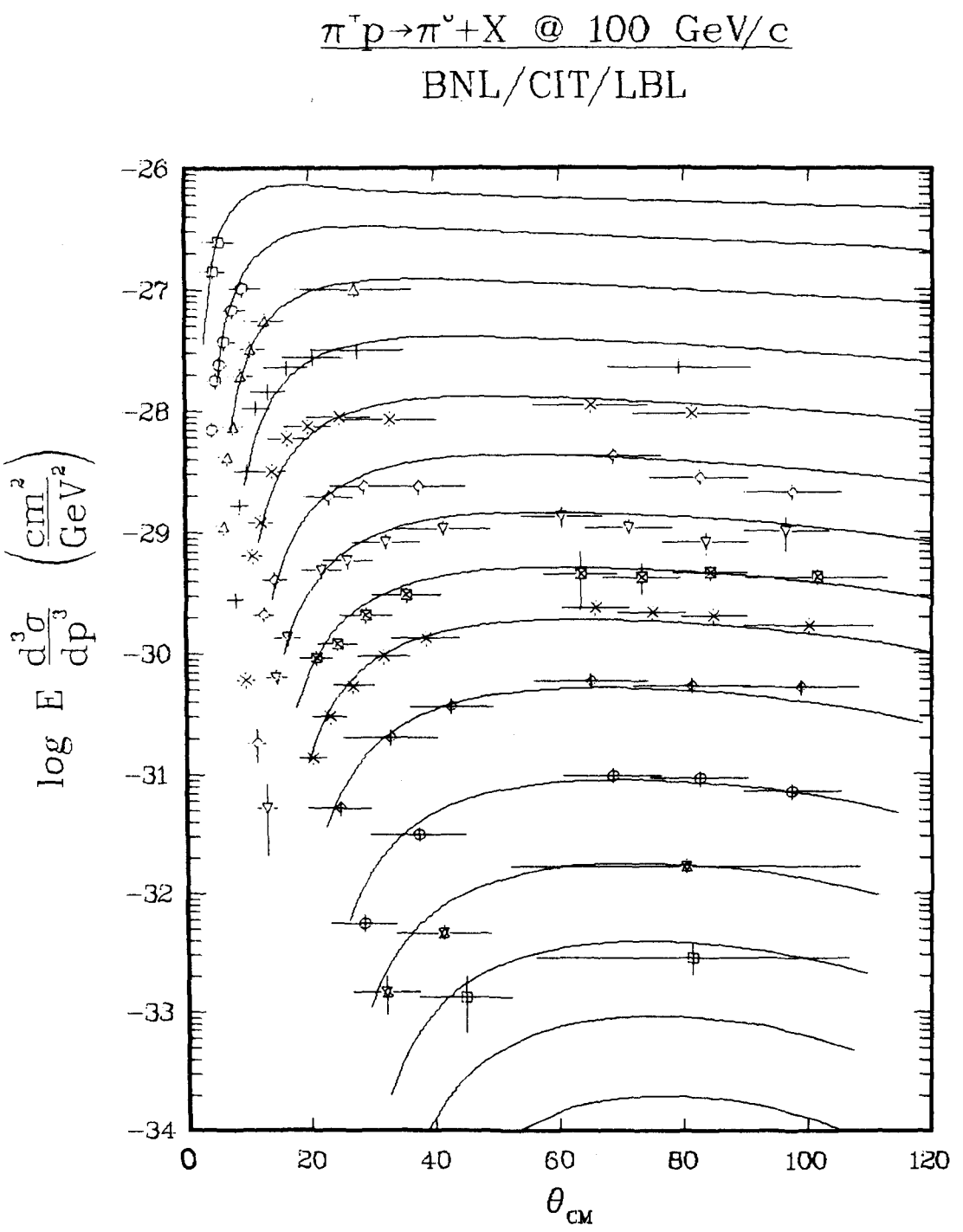

Fig. A3-2b.

XBL 789-11423

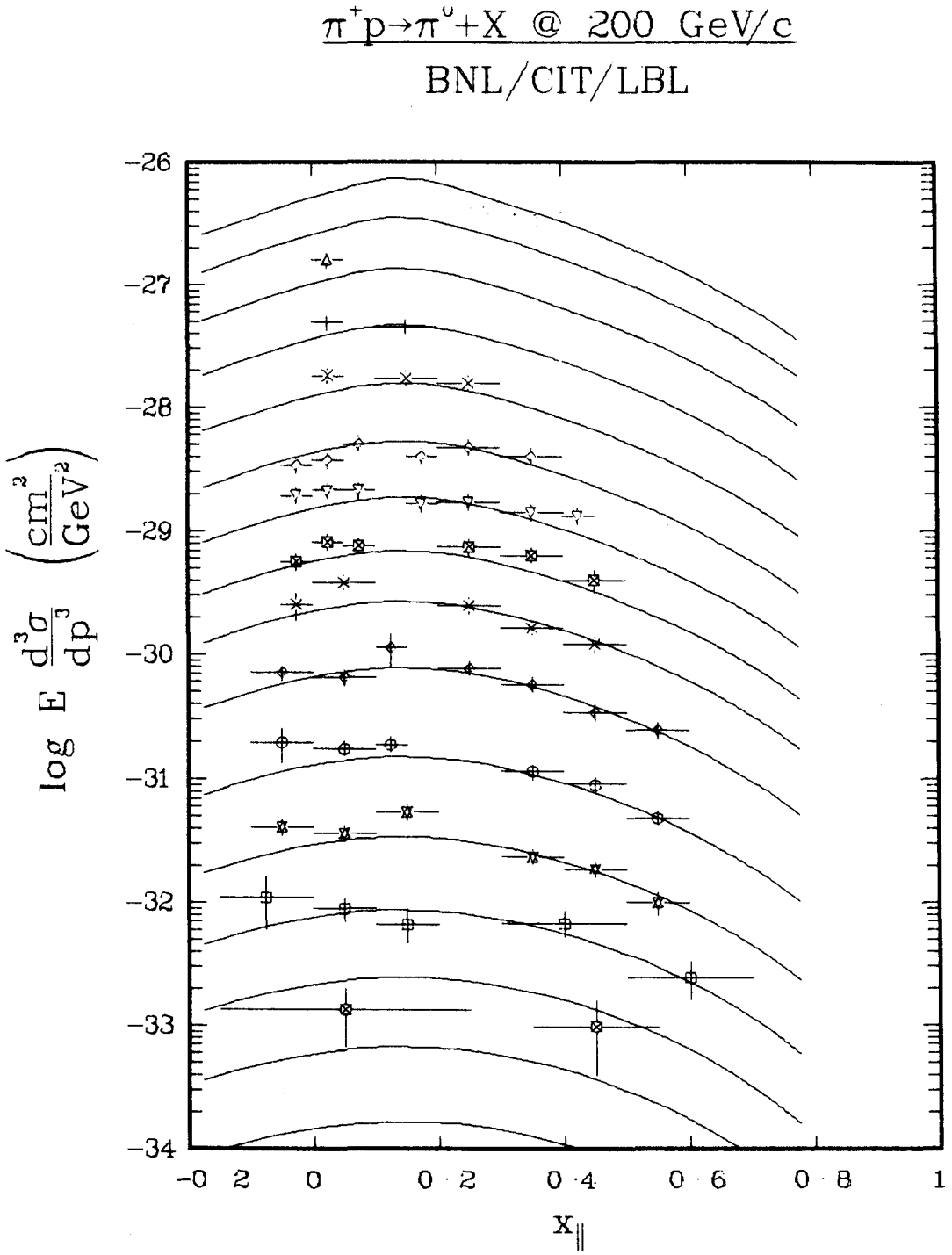

Fig. A3-2c.

XBL 789-11424

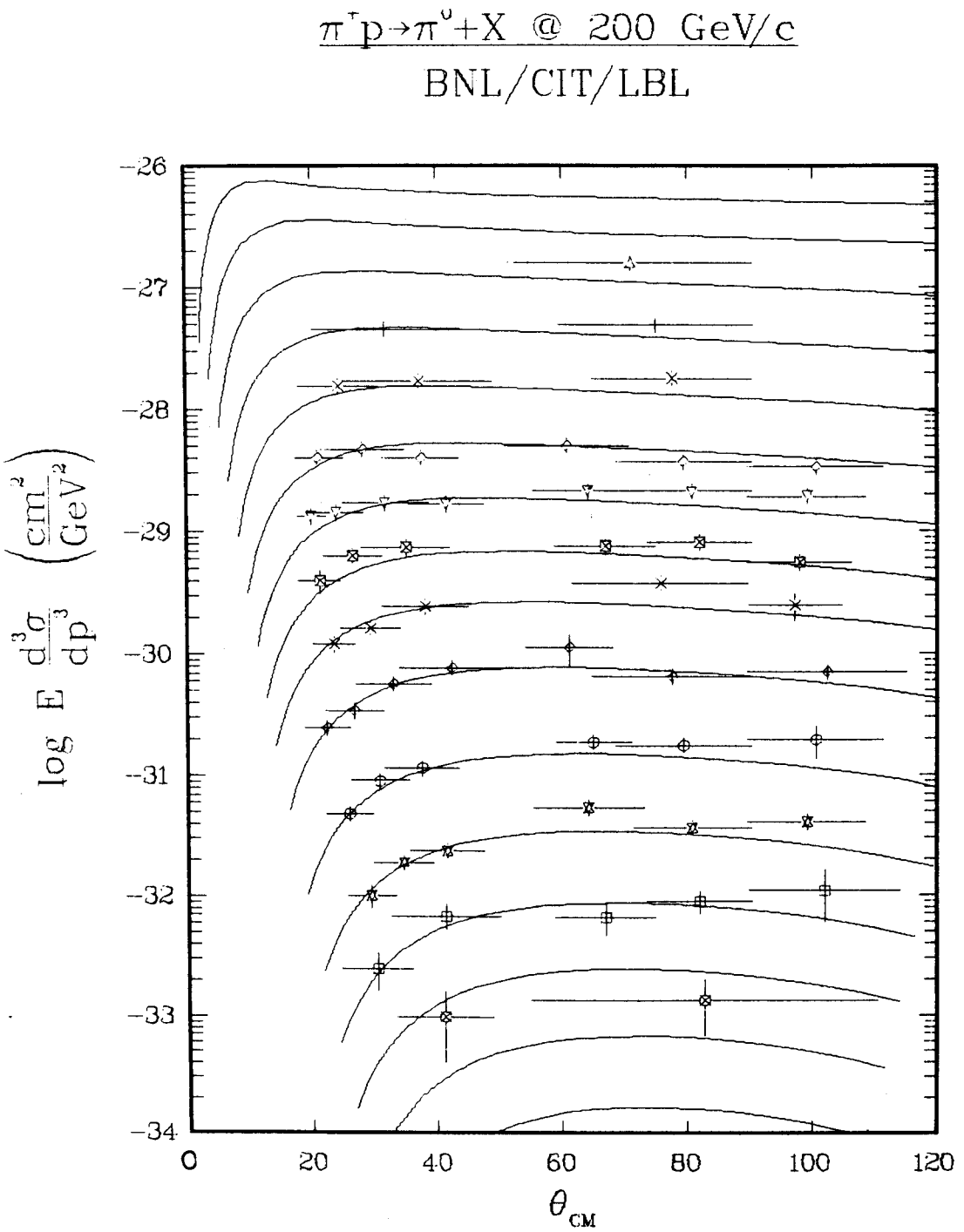

Fig. A3-2d.

XBL 789-11425

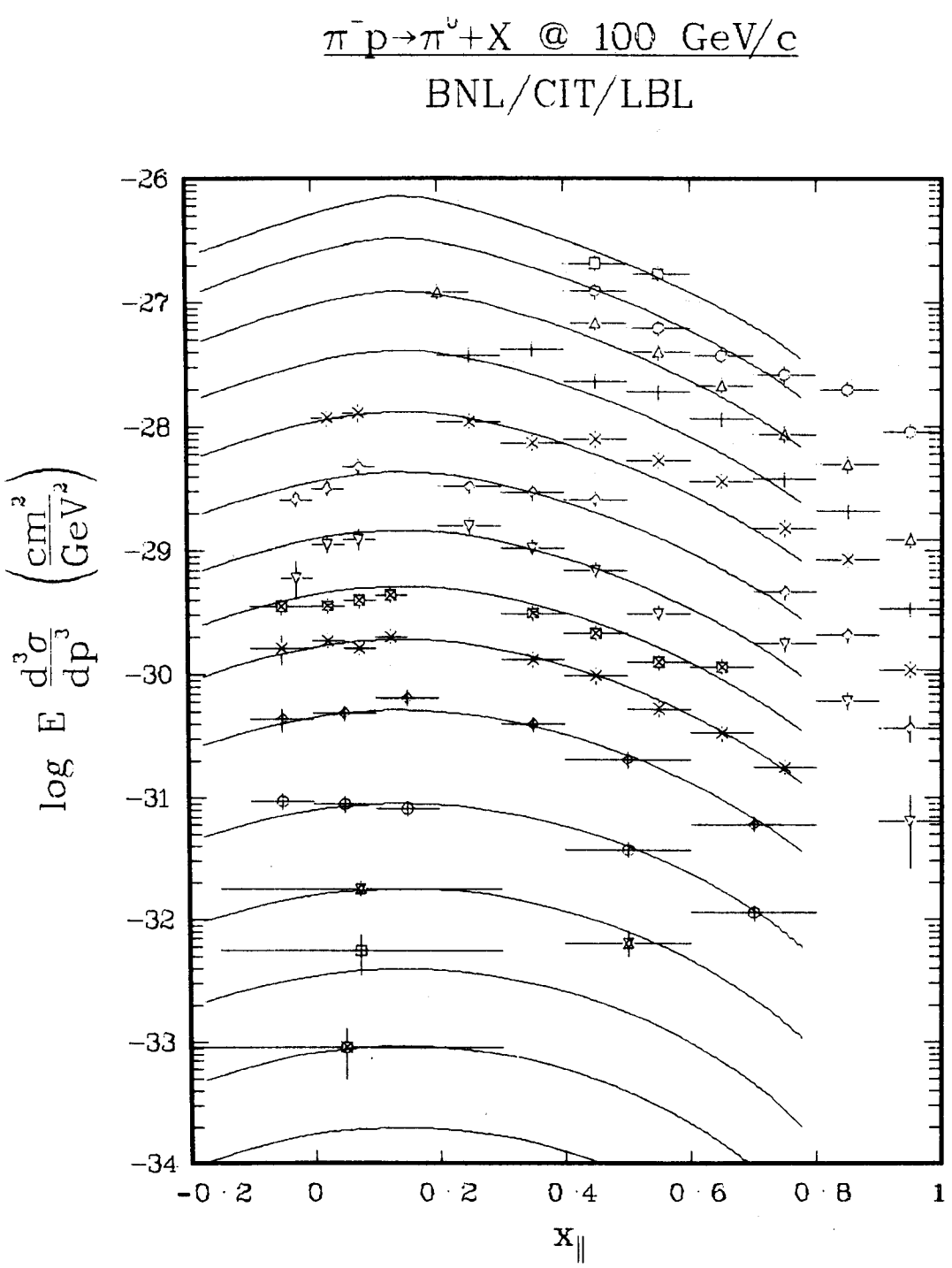

Fig. A3-3a.

XBL 789-11426

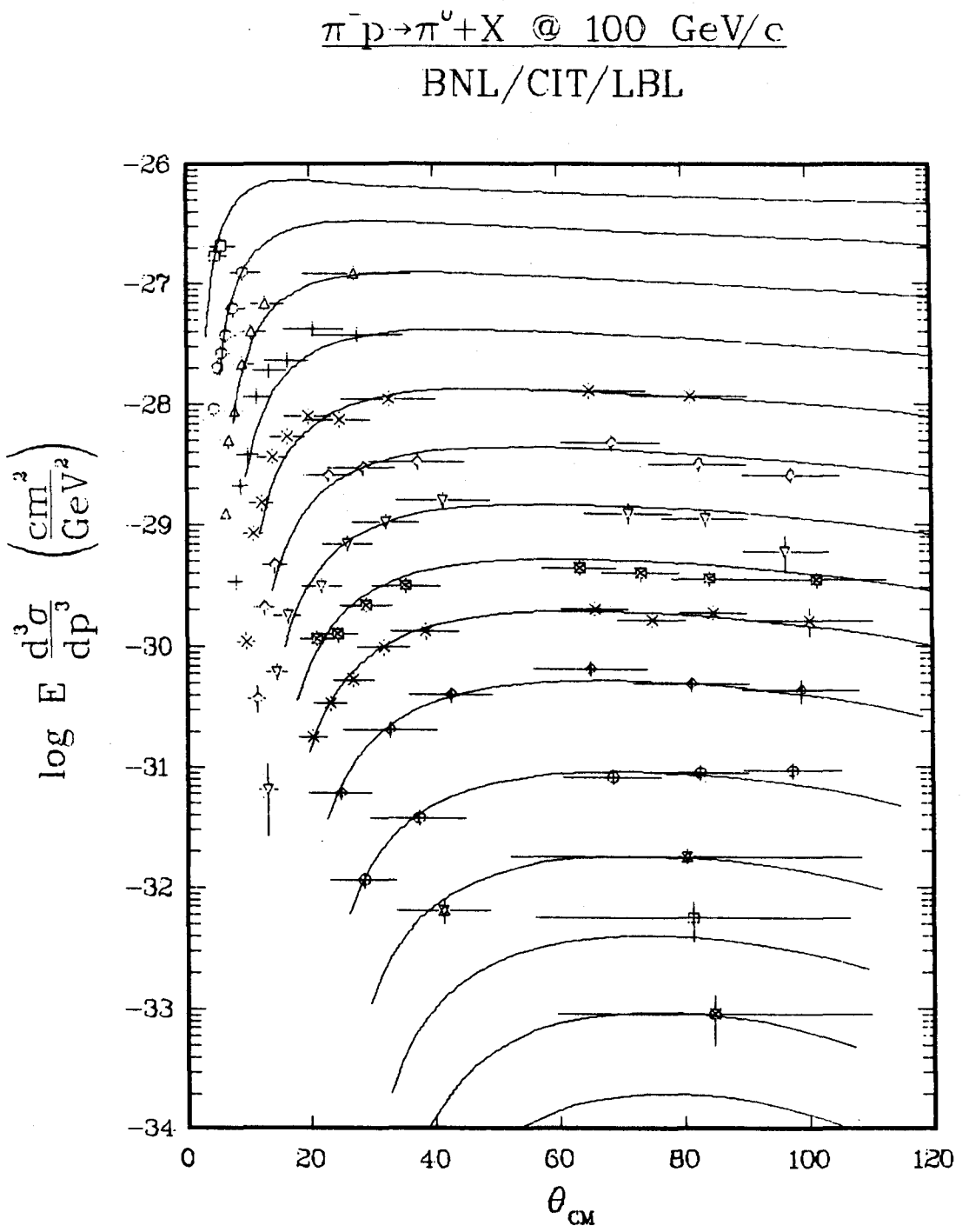

Fig. A3-3b.

XBL 789-11427

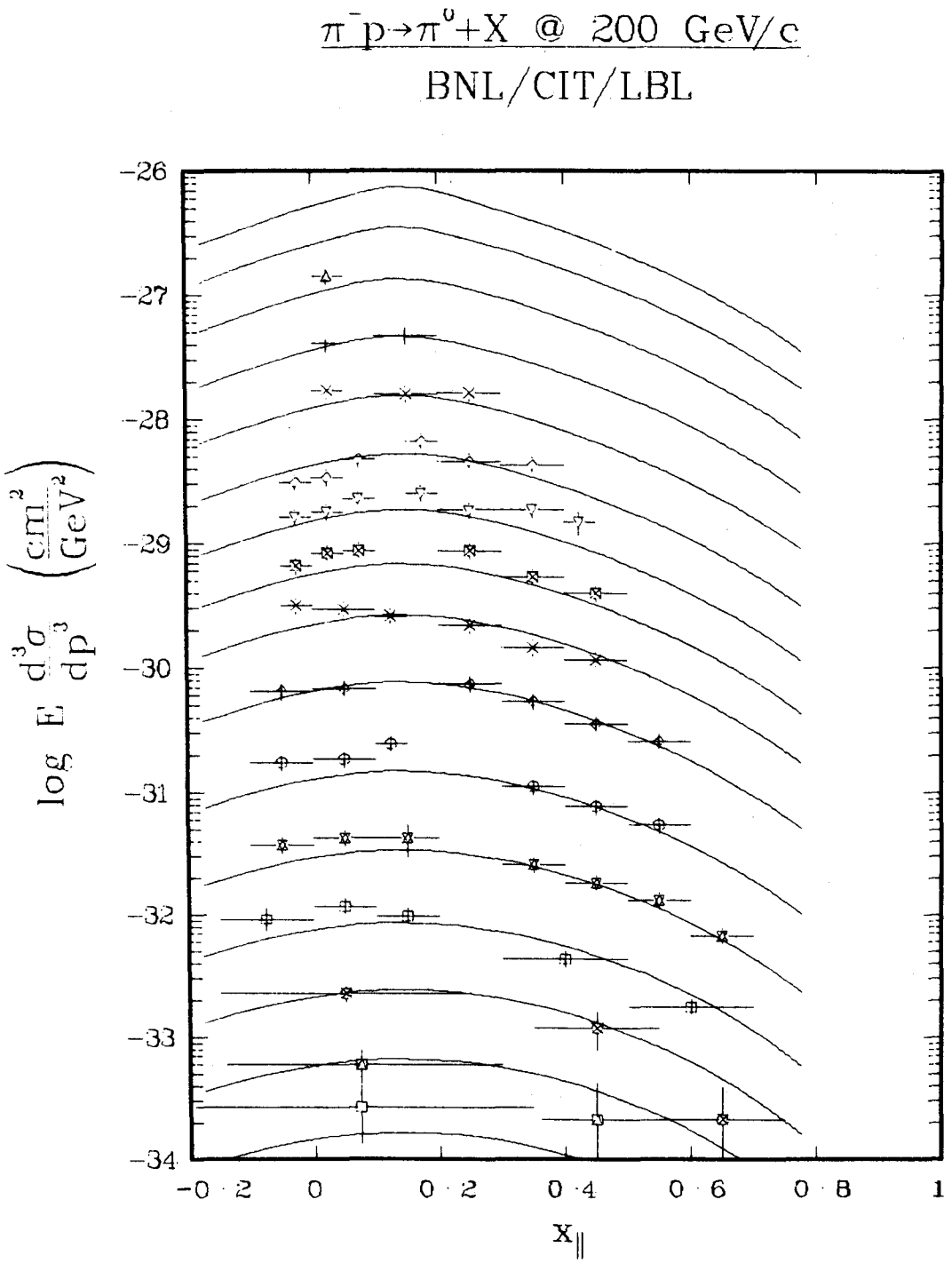

Fig. A3-3c.

XBL 789-11428

$\pi^- p \to \pi^0 + X$ @ 200 GeV/c

BNL/CIT/LBL

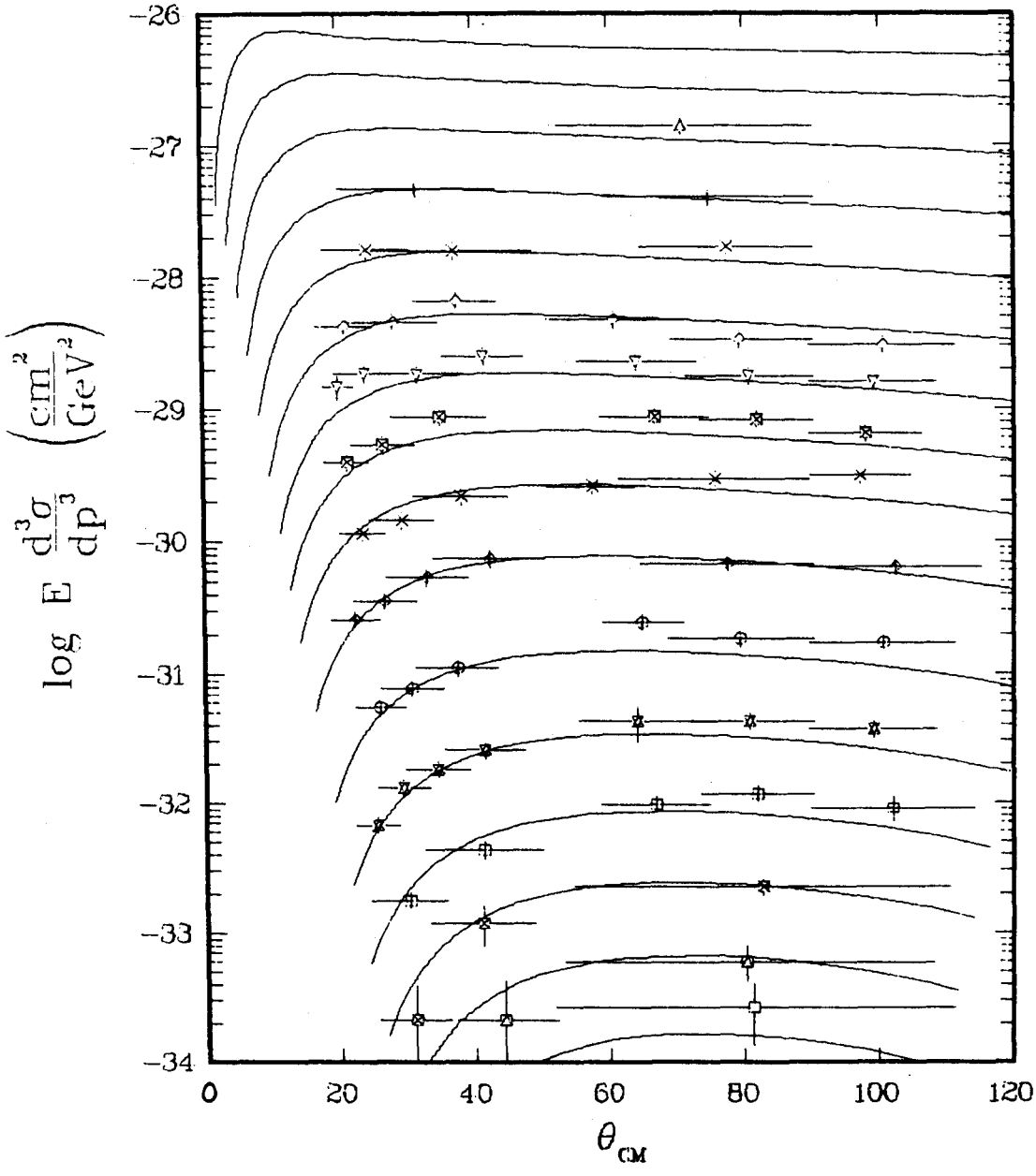

Fig. A3-3d.

XBL 789-11429

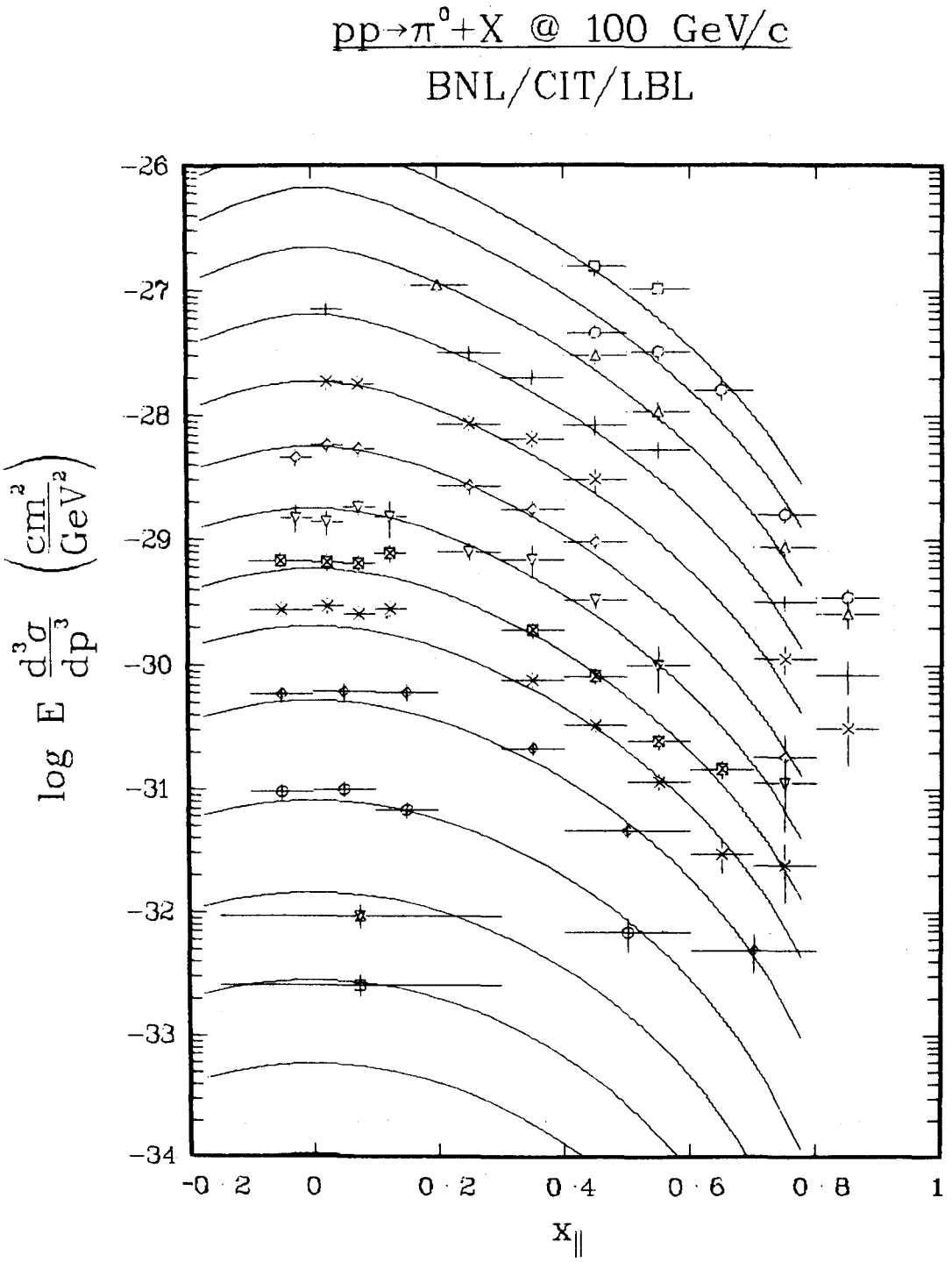

Fig. A3-4a.

XBL 789-11430

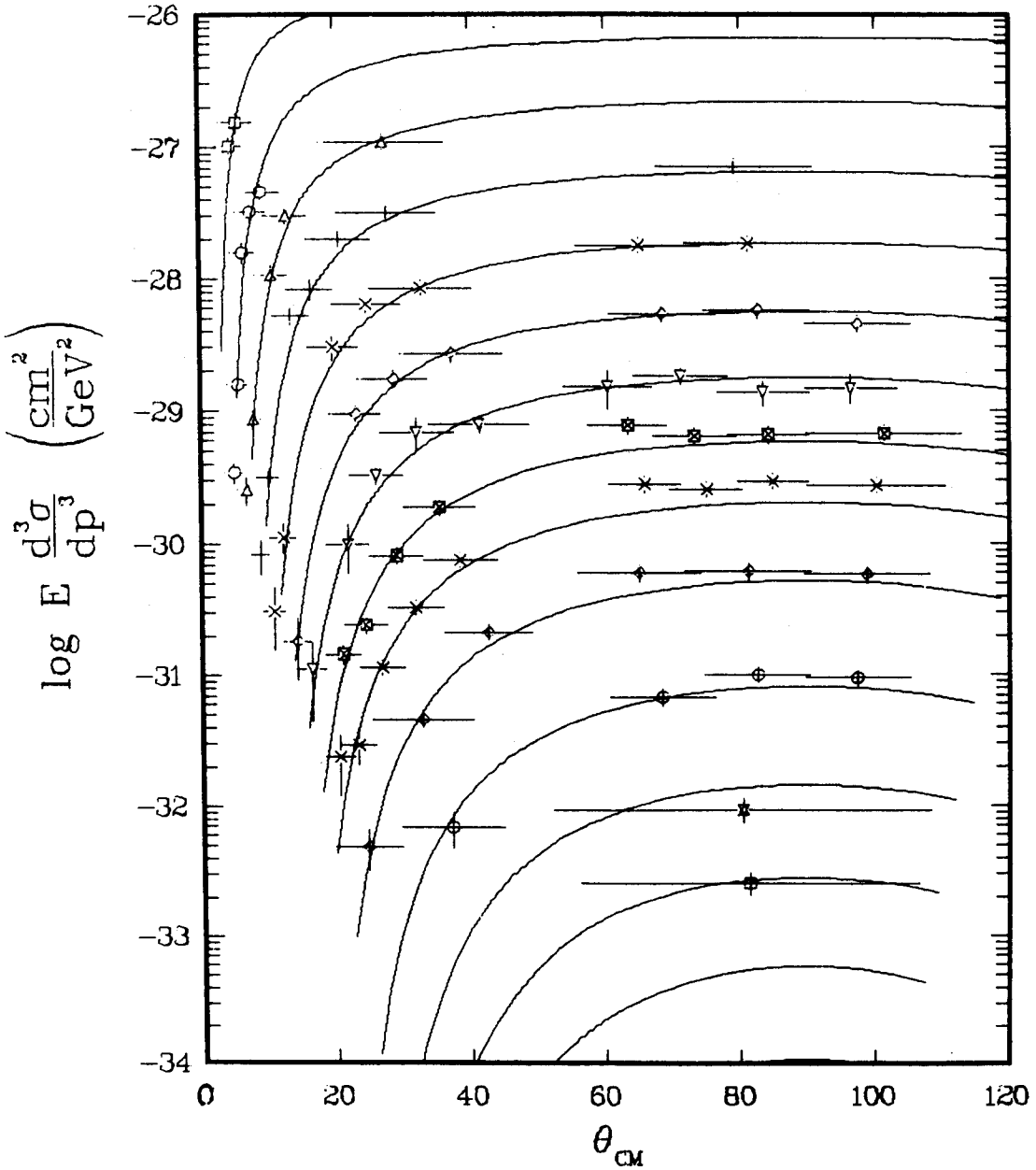

Fig. A3-4b.

XBL 789-11431

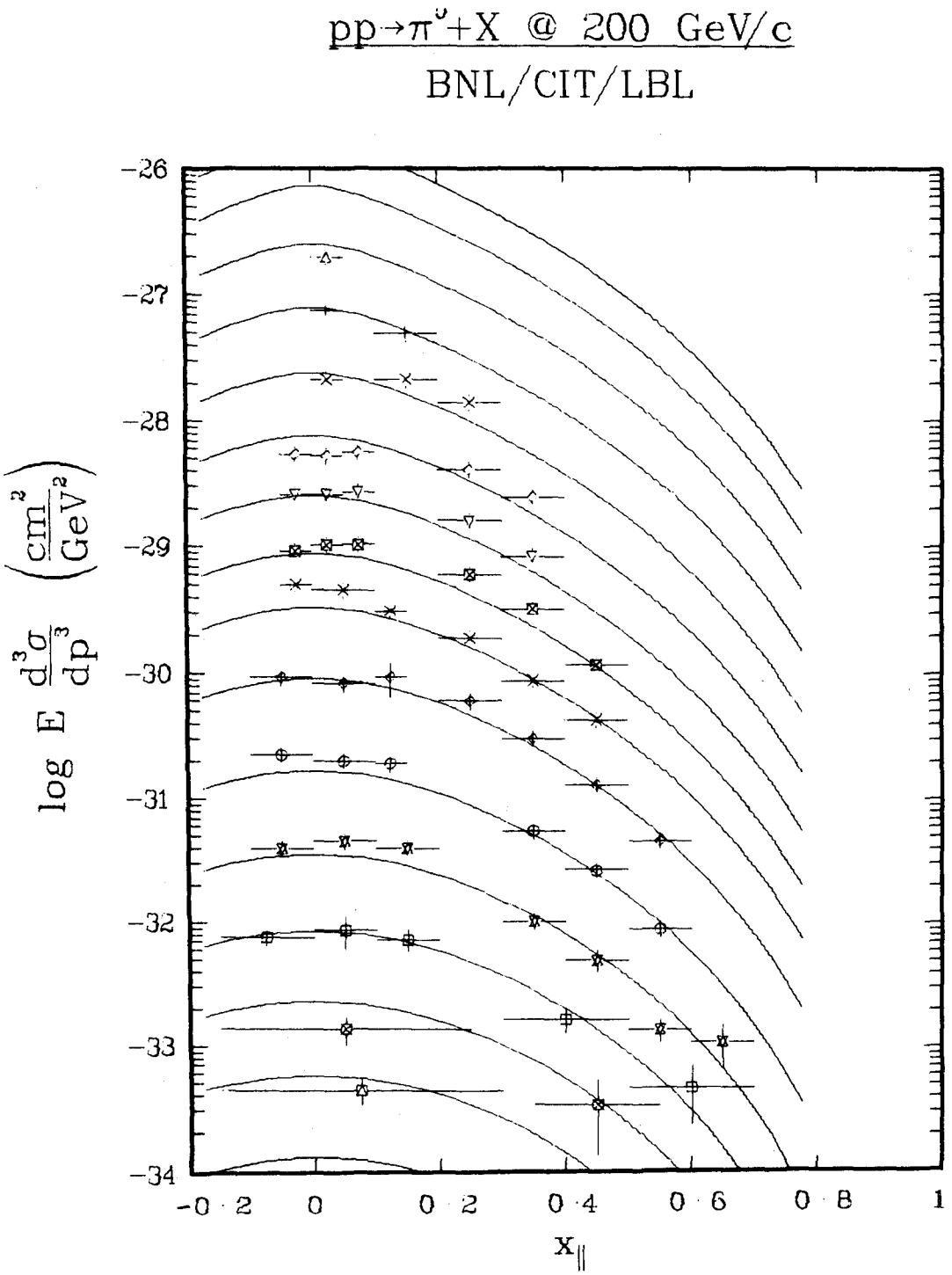

Fig. A3-4c.

XBL 789-11432

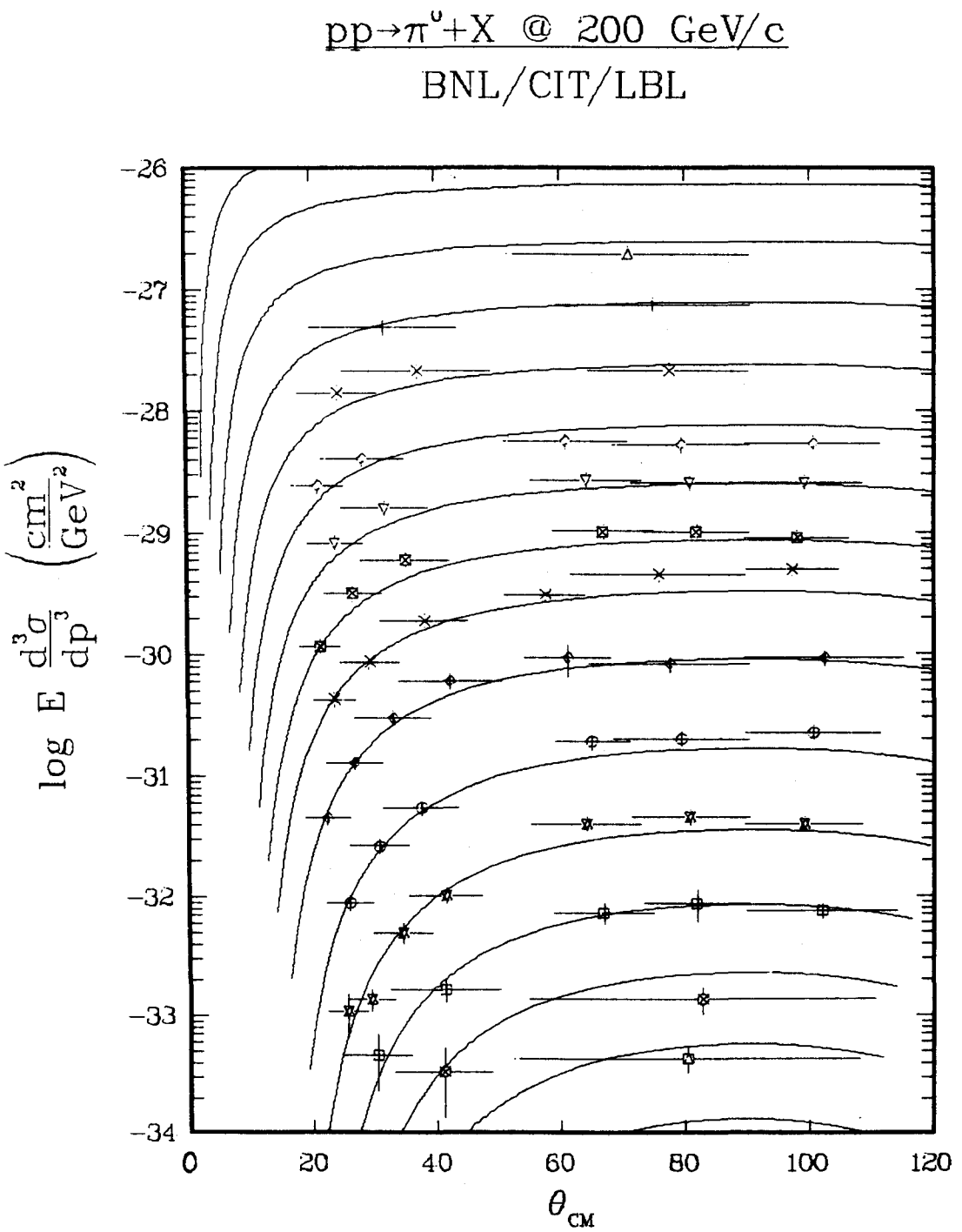

Fig. A3-4d.

XBL 789-11433

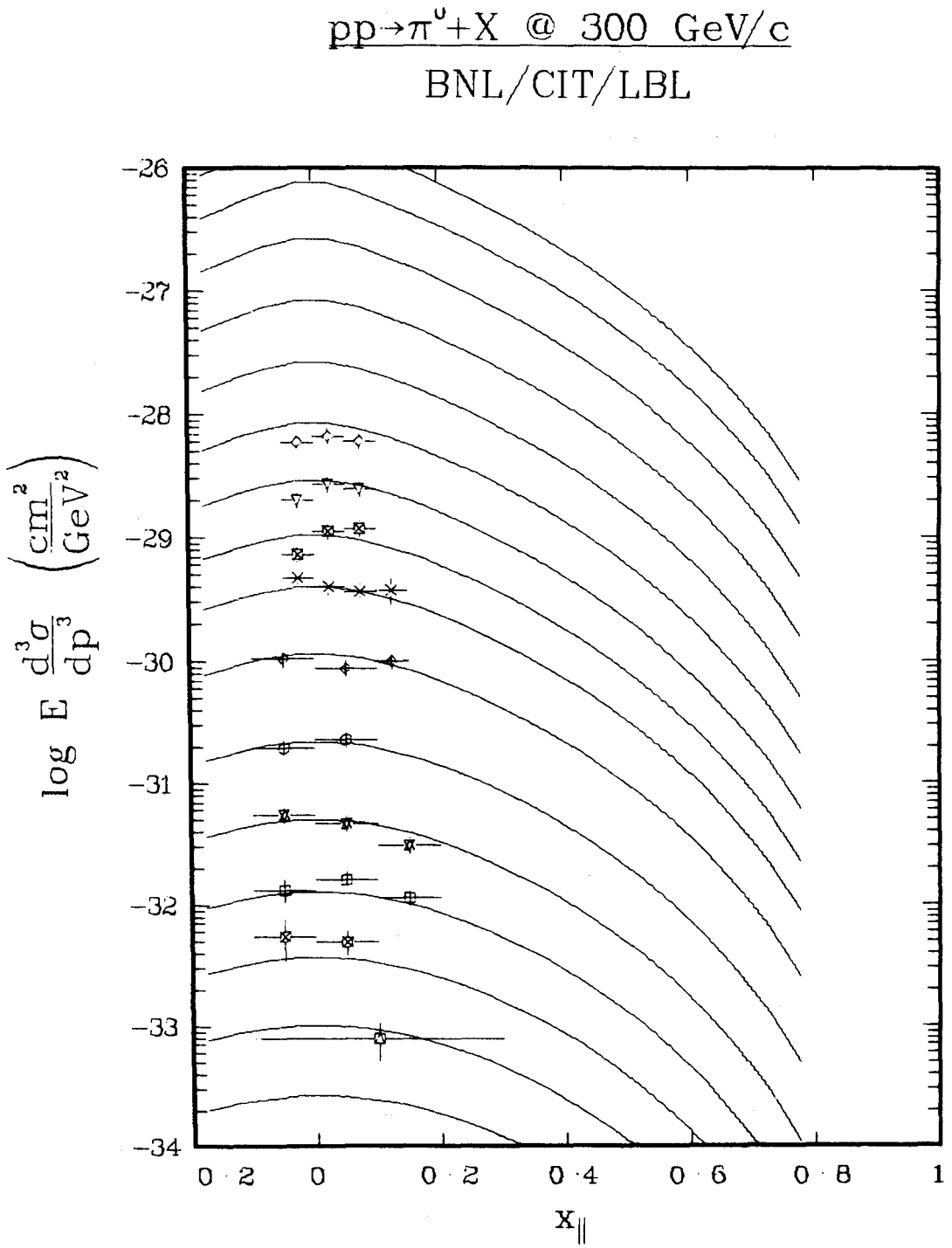

Fig. A3-4e.

XBL 789-11434

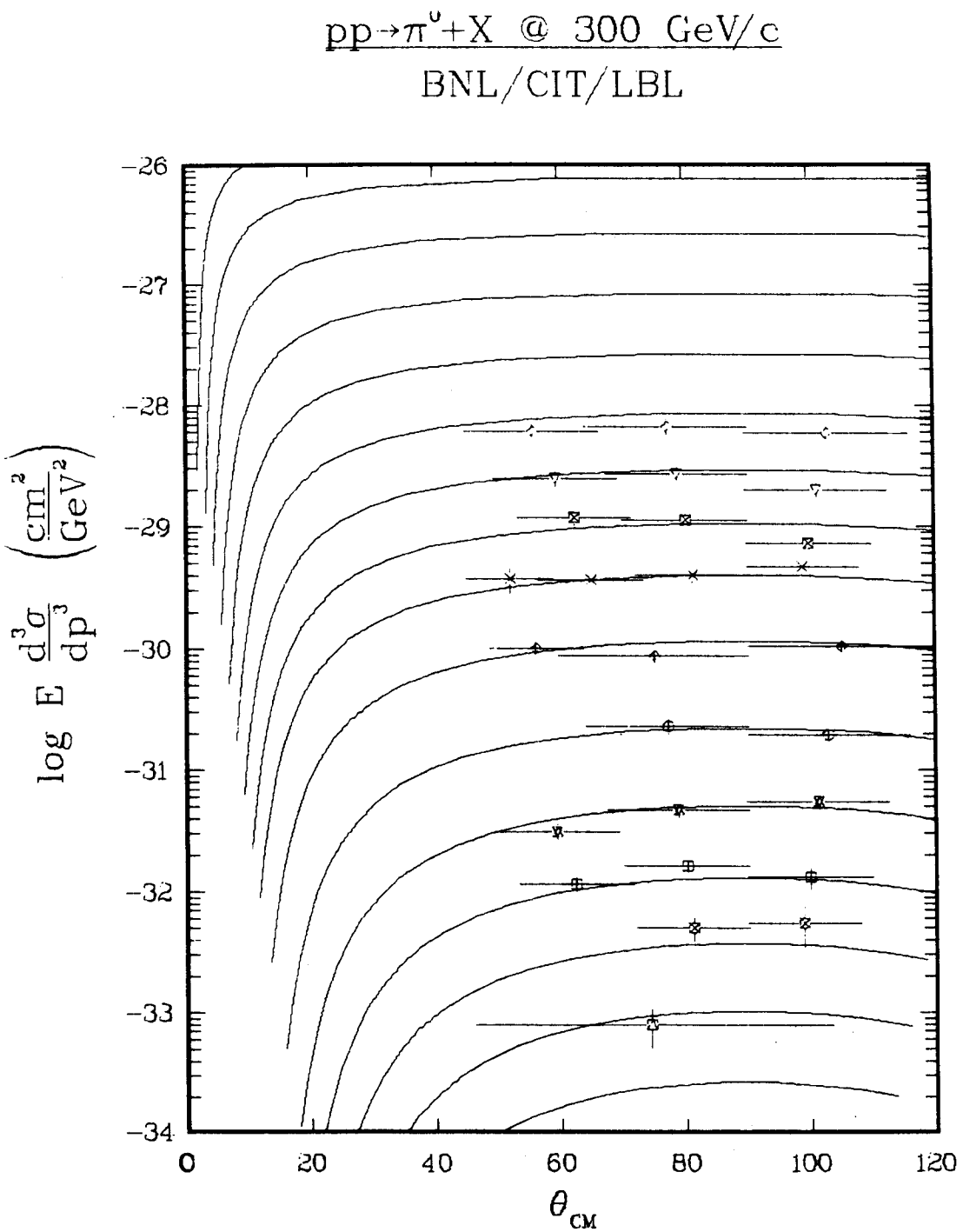

Fig. A3-4f.

XBL 789-11435

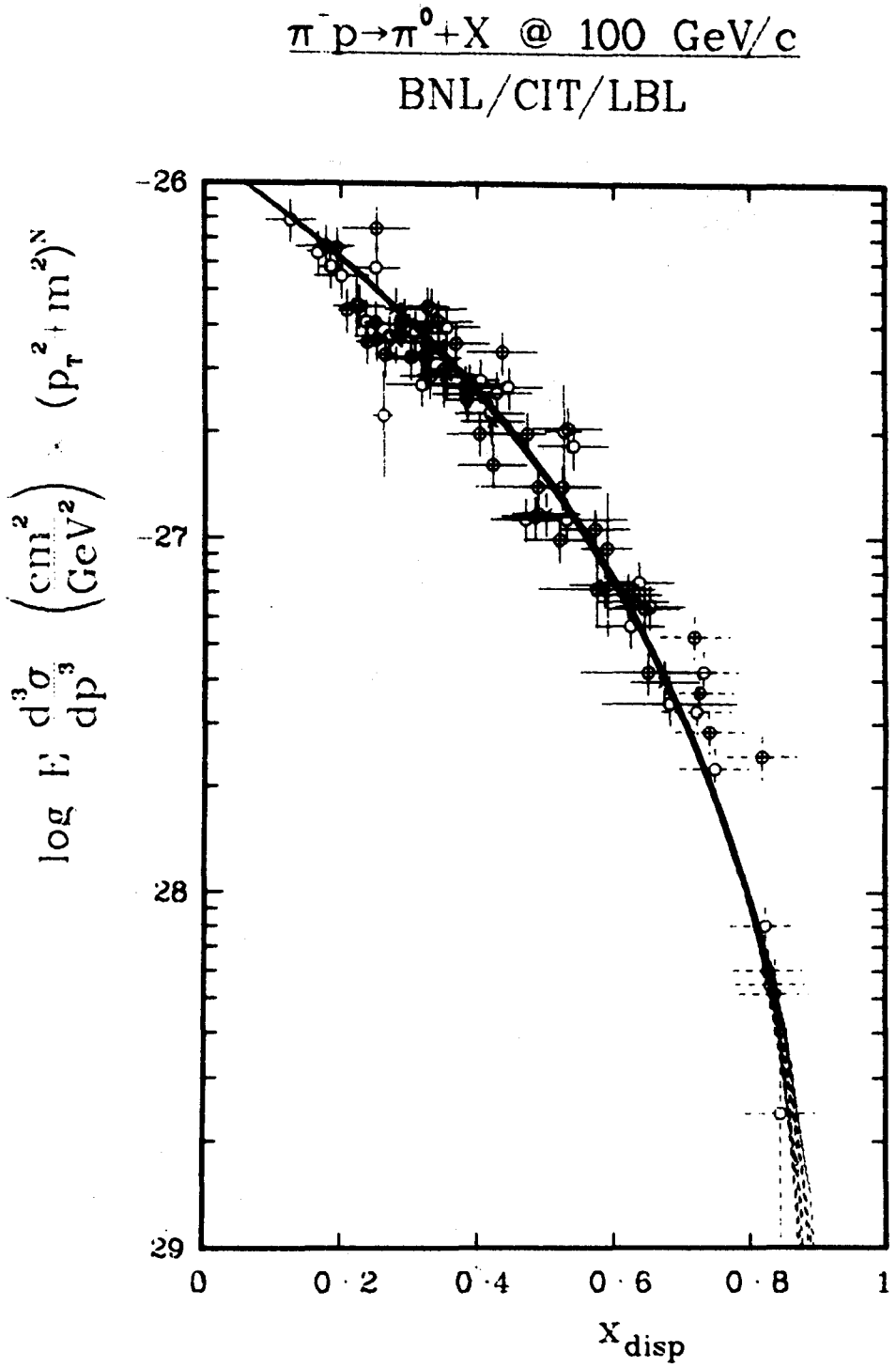

Fig. A3-5a.

XBL 789-11441

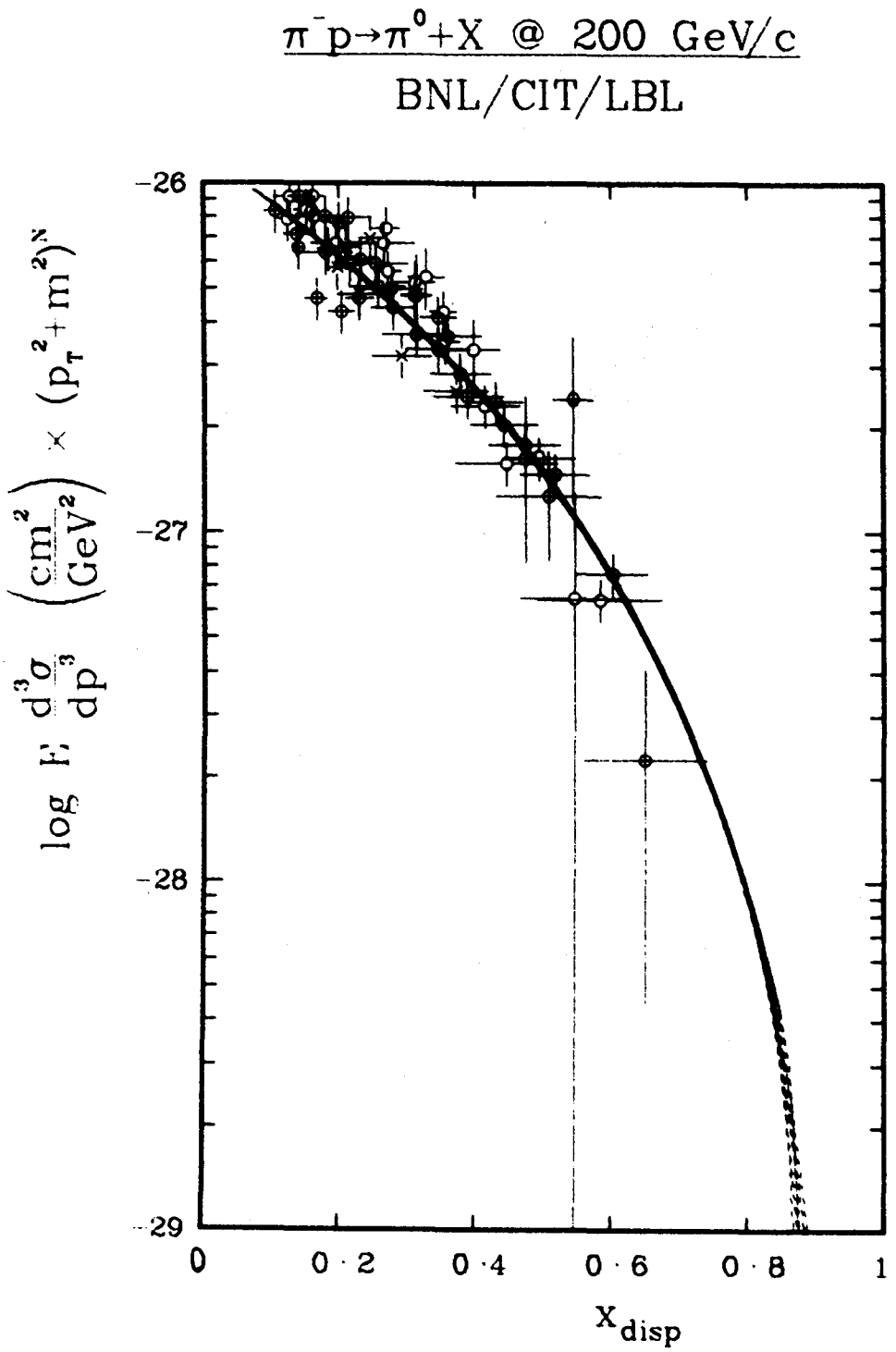

Fig. A3-5b.

XBL 789-11416

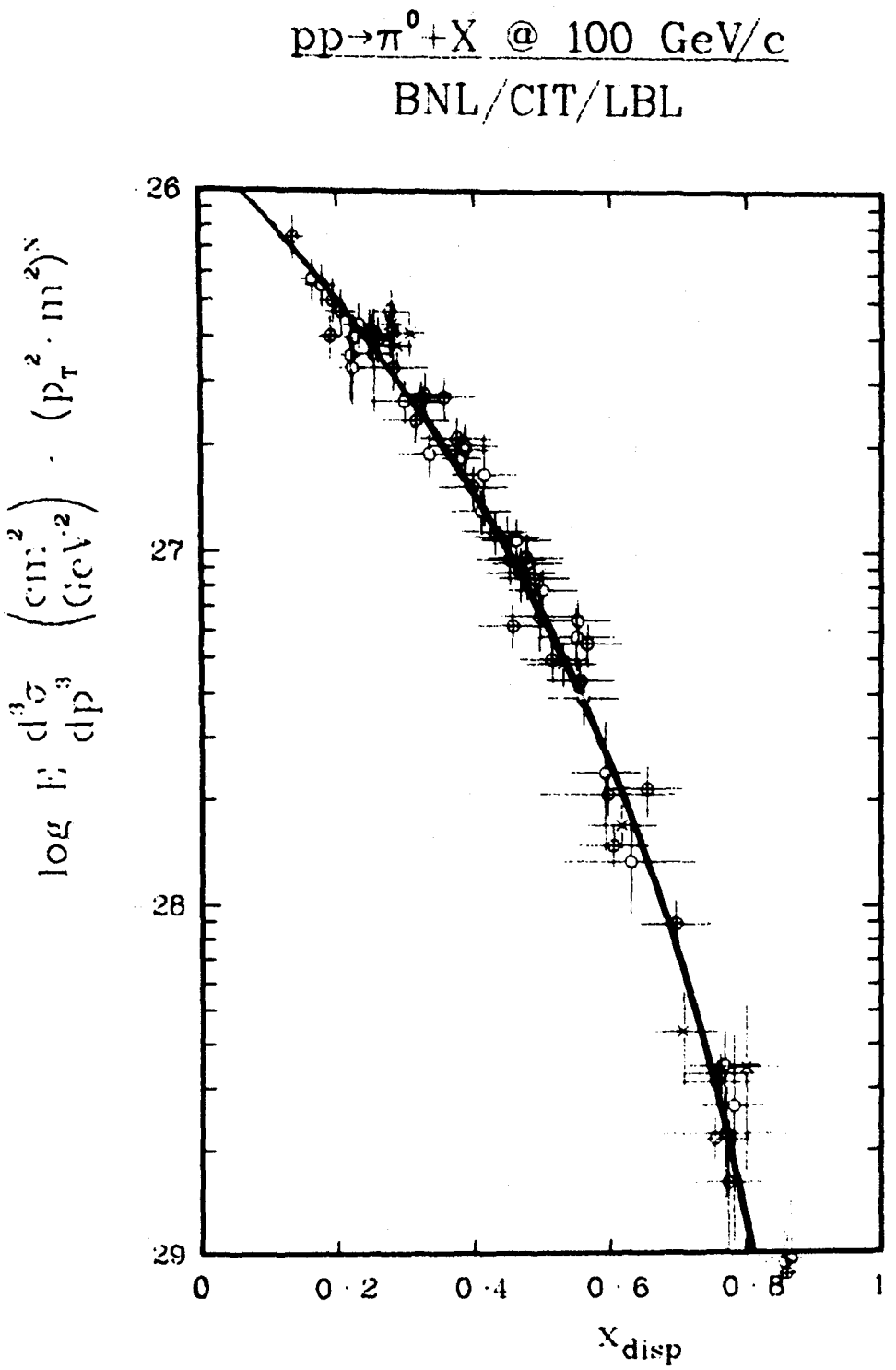

Fig. A3-6a.

XBL 789-11417

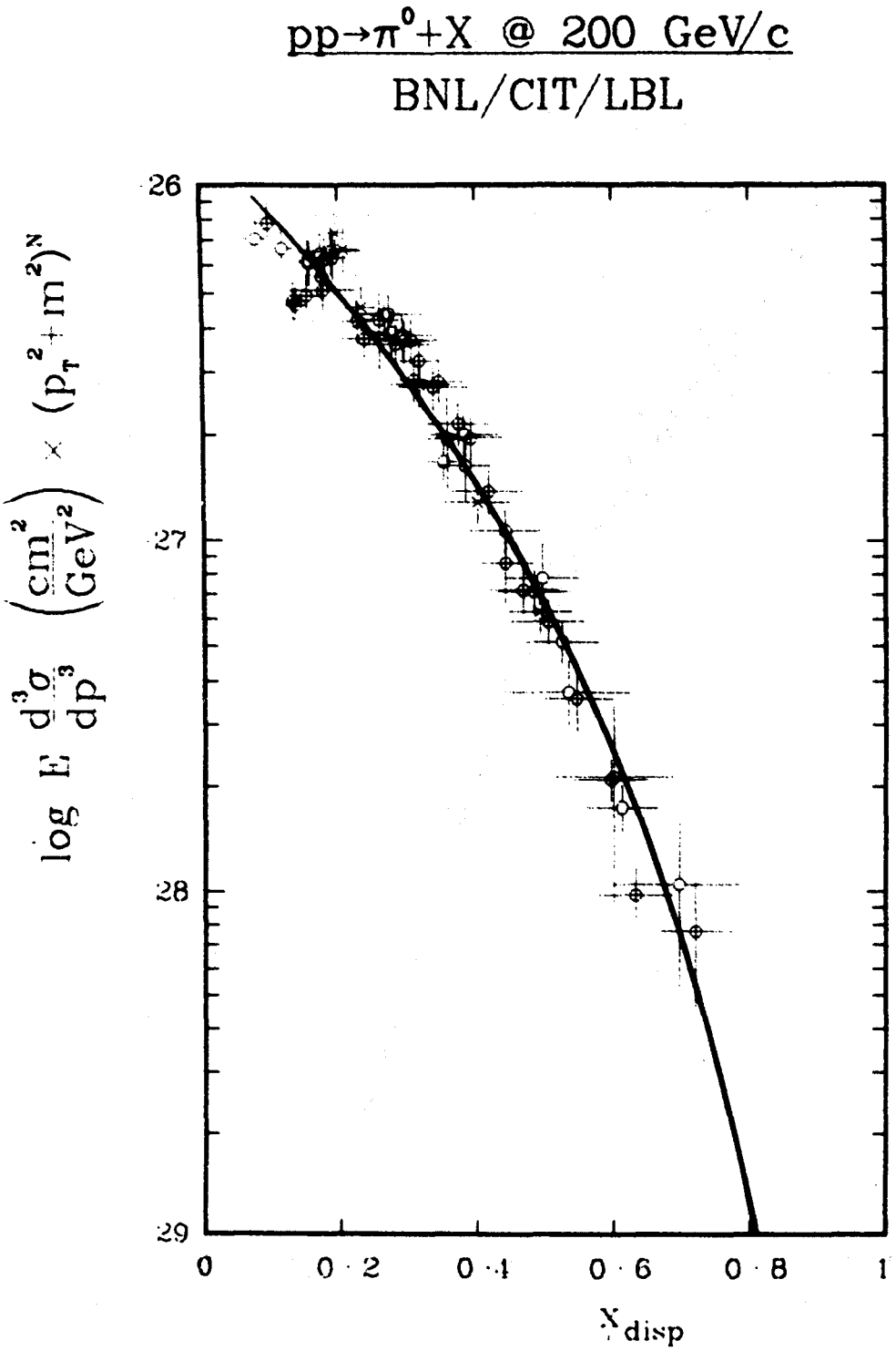

Fig. A3-6b.

XBL 789-11418

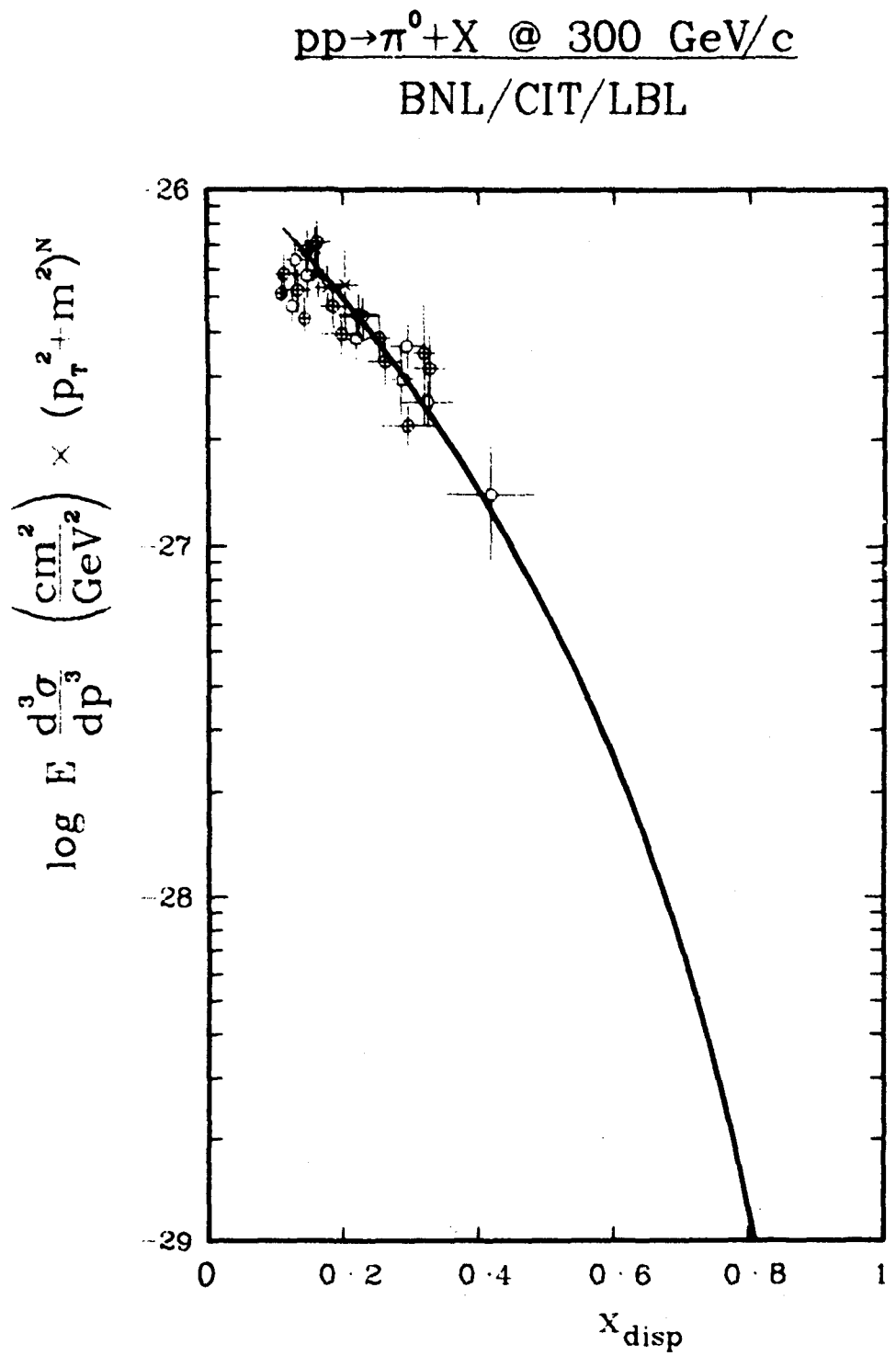

Fig. A3-6c.

XBL 789-11419

☆ U.S. GOVERNMENT PRINTING OFFICE: 1978-689-058/(F)39